Thermalization and Information Scrambling in Phases of Quantum Matter

by

Ceren B. Dag

A dissertation submitted in partial fulfillment
of the requirements for the degree of
Doctor of Philosophy
(Physics)
in the University of Michigan
2021

Doctoral Committee:

Professor Luming Duan, Co-Chair, Tsinghua University
Associate Professor Kai Sun, Co-Chair
Associate Professor Emanuel Gull
Assistant Professor Jordan Horowitz
Associate Professor Xiaoming Mao
Professor Georg Raithel

Ceren B. Dag

cbdag@umich.edu

ORCID iD: 0000-0003-0492-1651

To each and every kid in the world who daydreams about being a scientist one day, and to parents who could help their kids achieve their dreams, like my parents.

Acknowledgments

When people ask me of my PhD experience, I describe it with only one word: *transformative*. Ceren today and Ceren six years ago are approximately orthogonal to each other. What made PhD a transformative experience for me, was mainly the challenges that I needed to overcome one by one, and indeed you grow with challenges. So, at some point I learned to embrace and learn from them, instead of giving up. The first few years were the years of adaptation for me which I can unify under the theme of *being an independent researcher*. This was not only an adaptation to a different stage in my career, but also an adaptation to living in a different country. The final year was packed with *action for future*, i.e., post-doctoral applications, interviews, wrapping up the final projects of PhD, writing my thesis, starting to collaborate with other researchers. Time in between is called *sweet spot* where most of fun happens.

Let me start by thanking my advisors, Luming and Kai for their support throughout my PhD. They always encouraged me in my path to be an independent researcher and provided me a work environment where I could grow. Observing their unique insights of physics along the way was a very valuable learning experience for me. I cannot thank enough for their patience and calm attitudes in their supervision of my PhD.

I started to work on my PhD with Luming the first summer right after my first academic year which was completely occupied by courses. I had an opportunity to visit Tsinghua University in Beijing, China that summer (2016!) and had an office in the Institute for Interdisciplinary Information Sciences. This was the time that I started to study cold atom physics, and my starting topics were the methods of generating synthetic fields and spin-orbit coupled Bose-Einstein condensates. Later the same year, I continued to explore the field of cold atoms focusing on spinor Bose-Einstein condensates. I would say that my first work in spinor condensates which led to my first publication in the group, set the course of my PhD. This is mostly because of the freedom that Luming provided to me. It is fair to say that I was trained by Luming to find *the interesting physics* that I could theorize and could also be experimented in laboratory. When you think about it, there are some important constraints there; and exactly those constraints put me on the path to explore, think outside of the box, and find the project that matched my skill set at the moment while at the same time teaching me more skills, and physics. Probably one of the most challenging steps for me posed by Luming was the time when I had to decide on my second project. I still remember how victorious I felt when I had finally convinced him that the

area of information scrambling is very interesting and looks promising for future research. This free exploration that I have experienced throughout my PhD is partially the reason why today one of the unifying themes of my thesis is information scrambling. None of them would happen without Luming.

Unfortunately Luming left UM around the time when I was finishing up my third year. It was also the time that I was wrapping up my second paper with him, and getting prepped for my first Boulder Summer School experience (the one on quantum information!). It is a fun fact that at the time of writing this section of my thesis, I am actually doing my second Boulder Summer School (on cold atoms)! The first was luckily in Boulder, but the second one is held on Zoom due to obvious reasons. Probably one of the most fortunate events that happened to me during my PhD is that I started to be mentored by Kai. Kai did not only teach me so much interesting physics, but he also gave me very valuable career advice along the way. Without his constant support, I would not be able to navigate through the final year hassle of postdoctoral applications and interviews. It is easy for PhD students to get lost in the challenges, and this was certainly true for me too. However, Kai's excitement for physics is contagious and working with him revived my excitement too. It is not an understatement that his belief in me helped me believe in myself that I, too, can belong to academia after all. Kai is one of the most open-minded physicists that I have ever encountered: whatever problem that I brought to him, and whichever project I chose to commit my time to, he always expressed genuine interest for the problem and encouraged me to explore further, regardless of whether my project topics match his main research topics. The entire experience taught me a great deal about how to mentor my own students in the future.

There are so many others to thank in this adventure. First of all, I thank all my committee members for their advice along the way and making my dissertation process smooth. I had a very fun experience of my thesis presentation with friends and family in the audience too. I specifically thank Jordan for his thorough reading of my dissertation and his long list of typos, suggestions and comments. Thanks to his input, now I see much better the connections between quantum and classical nonequilibrium physics.

I still find the advice of Shengtao Wang and Yong Xu given to me in the early years of my PhD very helpful. I learned a lot when I was working with them on the topics of spinor and spin-orbit coupled Bose-Einstein condensates. I also had very fruitful exchanges with Tanvi Gujarati, Yukai Wu and Zhengyu Zhang. In the second part of my PhD, I met Heqiu Li, Xiaohan Wan and Francesco Serafin in Kai's group. I had many fun and fruitful discussions with Heqiu on topological states.

Xiaoming Mao was also my academic advisor in PhD and her advice for my academic success, especially in the beginning of my PhD, was very helpful. In the last year and a half,

I had the opportunity to take a part in the study group of Xiaoming and Kai where I learned a lot about the topological mechanics and in general the role of topology in physics.

In my fifth year, I was half-time funded by a part-time research project which was related to my PhD, although indirectly. I thank Christine Aidala for giving me the opportunity to study differential geometry in thermodynamic spaces and information geometry, which was part of MCube Foundations of Thermodynamics and Statistical Physics Project. I actually started to learn information geometry from Jun Zhang in the Department of Mathematics and Psychology in my first year. Information geometry did not take a part in my dissertation, however it was very formative throughout my PhD and I hope to make use of it in the future.

I took my quantum field theory (QFT) courses with Finn Larsen and I still remember: it was during his second QFT course when I needed to decide what to do with my PhD after Luming left the country. If I did not enjoy learning renormalization group so much, I would probably not dare working with Kai at all. Finn encouraged me many times in the beginning of my PhD to work with Kai and gave me helpful advice along the way about academia and research. I cannot thank him enough.

I spent a lot of time in the National Magnetic Laboratory in Florida and learned a lot from Paul Myles Eugenio and Oskar Vafek in many different condensed matter topics. I suppose, it was them talking about twisted bilayer graphene all the time was the reason why I found myself in that field after all. My work related to this field did not get into my dissertation either, however this field will likely be part of my future research.

Ozgur Mustecaplioglu was my undergraduate advisor and my collaborator during my PhD. My interest in nonequilibrium physics is heavily affected by him. In Ozgur's group I met brilliant people who touched my academic life in some way or another, and I thank all of them for interesting discussions. My first work with Ozgur, which is in the field of quantum thermodynamics, was published at the end of my first year of PhD. Later we extended our work to more realistic platforms and other potential applications.

In the last year of my PhD, I had a great opportunity to collaborate with Jad C. Halimeh and Philipp Uhrich from Philipp Hauke's laboratory at Trento University, and I am very happy that our work turned into the last chapter of my dissertation. I also thank Amos Chan for teaching me so much about random quantum circuit theory in our current collaboration.

Last but not least, none would happen without the constant support of friends. I guess I did make a life here in the US in the last six years of my life after all! Finally, I thank my family back in Istanbul for their support when I am away. Seeing them proud makes me proud too. In the middle of the pandemic, job search and thesis preparation, I also got married. There is nothing like sharing my passion for physics with my partner for life. I am very lucky to have you Paul, and Aslan our cat, by my side.

Table of Contents

Dedication ii

List of Tables ix

List of Figures x

List of Appendices xvi

Abstract xviii

Chapter 1: Introduction 1

1.1 Quantum Phase Transitions . . . 3

1.1.1 Transverse-field Ising Model . . . 4

1.1.2 Bose-Einstein Condensates and the Bose-Hubbard Model . . . 6

1.2 Nonequilibrium Quantum Physics . . . 23

1.2.1 Equilibration, Thermalization and Absence Thereof . . . 25

1.2.2 Quantum Revivals, Light Cone Bounds and Information Scrambling . 31

1.2.3 Dynamical Phase Transitions . . . 37

1.3 A Brief Outline of the Dissertation . . . 38

Chapter 2: Equilibration and Thermalization in the Integrable Models 41

2.1 Introduction . . . 42

2.2 Classification of Dynamical Behaviours under Sudden Quench of Spin-1 Spinor Condensate . . . 45

2.3 Eigenstate Thermalization Hypothesis in Spin-1 BEC . . . 52

2.4 Existence and Absence of Quantum Collapse and Revivals . . . 63

2.5 Conclusions and Discussion . . . 71

Chapter 3: Detection of Information Scrambling in Cold Atoms 74

3.1 Introduction . . . 74
3.2 The Ladder-XX Model . . . 76
3.3 The OTOC Properties and Level Statistics . . . 78
3.4 OTOC Detection Protocols . . . 87
3.4.1 Initial state preparation . . . 88
3.4.2 The interference measurement . . . 91
3.4.3 The interferometric scheme . . . 93
3.5 Conclusions . . . 95

Chapter 4: The Connection Between Information Scrambling and Quantum Phase Transitions 96
4.1 Introduction . . . 96
4.2 Method . . . 98
4.3 Model and the Results . . . 103
4.4 Conclusions . . . 106

Chapter 5: Topologically Induced Prescrambling 108
5.1 Introduction . . . 109
5.2 Demonstration of Topological Origin . . . 114
5.3 Topological Edge Physics Encoded in the Out-of-time-order correlators . . . 117
5.3.1 Transverse-field Ising Model . . . 117
5.3.2 Exact solution . . . 122
5.3.3 Robustness against varying the boundary conditions . . . 124
5.4 The Interplay between Topological Order and Scrambling . . . 124
5.4.1 Coherence times of prescrambling plateaus . . . 125
5.4.2 Dynamical decomposition method . . . 128
5.4.3 Effect of scrambling on dynamic phase diagrams . . . 135
5.5 Conclusions and Discussions . . . 137

Chapter 6: Probing Criticality in the Transient Quench Dynamics 139
6.1 Observation of Dynamical Quantum Phase Transitions in a Spinor Condensate 139
6.1.1 Introduction . . . 140
6.1.2 Results . . . 143
6.2 Dynamical crossover in the transient quench dynamics of short-range transverse field Ising models . . . 146
6.2.1 Introduction . . . 147
6.2.2 Methods . . . 151

6.2.3 Dynamical Crossover in the integrable TFIM 153
6.2.4 Dynamical crossover in the nonintegrable TFIM 164
6.2.5 Conclusions 171

Chapter 7: Dynamical Criticality in the Quasi-Stationary Regimes 173
7.1 Introduction 174
7.2 The quasi-stationary temporal regime in chains with boundaries 176
7.3 Quench dynamics in the integrable TFIM 177
7.4 Nonintegrable TFIM 181
7.5 Conclusions 185

Chapter 8: Conclusions, Outlook and Future Directions 186

Appendices 192

Bibliography 269

List of Tables

2.1 The regions of the sudden quench map for the ferromagnetic case. 50
2.2 The dynamic behaviors corresponding to the regions of the sudden quench map for the ferromagnetic case. 51

B.1 Exponential fit parameters for the Lyapunov-like exponents at $L = 8$. 198
B.2 Power-law scaling fit parameters at $L = 8$. 198

F.1 Fit parameters for the universal scaling law with different ultraviolet temporal cutoffs, part I. 257
F.2 Fit parameters for the universal scaling law with different ultraviolet temporal cutoffs, part II. 258
F.3 Fit parameters for the universal scaling law with a different initial state. . . 258
F.4 Fit parameters for the scaling law of the near-integrable model in the vicinity of the transition. 265
F.5 Fit parameters for the system-size scaling of single-site observable at $r = 1, 3, 6$ at the DCP. 266

List of Figures

1.1 A pictorial representation of how to condense an atomic gas to its BEC phase 7
1.2 Full phase diagram of spin-1 ferromagnetic condensate with respect to q, the Zeeman parameter, and m, the magnetization density. 14
1.3 The ground state energy gap of ferromagnetic condensate for $m = 0$. 15
1.4 The ground state phase transition and the energy gap for ferromagnetic spinor condensates when magnetization density is $m = 0.8$. 16
1.5 Full phase diagram of spin-1 antiferromagnetic condensate with respect to q, the Zeeman parameter, and m, the magnetization density. 18
1.6 Light cones of (a) integrable and (b) nonintegrable TFIM at a system size of $N = 36$ computed via t-DMRG. 33
1.7 Measurement schematic of dynamical phase transitions type-I. 36

2.1 The ground state phase transitions for spinor condensates. 47
2.2 Eigenstate occupation numbers (EONs) and eigenstate expectation values (EEVs) in spinor condensates. 48
2.3 The sudden quench map for the ferromagnetic spinor condensate. 49
2.4 The sudden quench map for the anti-ferromagnetic spinor condensate. 50
2.5 A cross section from the sudden quench map of ferromagnetic spinor condensate. 52
2.6 Another cross section from the sudden quench map of ferromagnetic spinor condensate. 54
2.7 The system size scaling of the support, ... at $q_f = 3$. 56
2.8 The system size scaling of the support, ... at $q_f = 0.65$. 57
2.9 The participation ratio values of the eigenspectrum for a ferromagnetic spinor condensate. 58
2.10 System size scaling of averaged participation ratio of low-PR and high-PR eigenstates. 60
2.11 The sudden quench dynamics for a quench from $q_i = -3$ to $q_f = -0.5$. . . . 63
2.12 (a) The overlap matrix with respect to eigenstates α and β, (b) 64

2.13 The sudden quench dynamics for quenches (a) from $q_i = -3$ to $q_f = 0.5$ and (b) from $q_i = 4.1$ to $q_f = 2$. 68
2.14 The effective dimension scaling for various quenches. 69

3.1 A schematic of the proposed optical superlattice for the ladder$-XX$ model. 77
3.2 The average ratio of level spacings. 80
3.3 The OTOC of the ladder-XX model at $h = 1$ between two distant operators 81
3.4 (a) The exponential and (b) power-law decay of OTOCs 83
3.5 The dynamical exponent γ with respect to the OTOC contour values η . . . 85
3.6 A demonstration of wavefronts for a system size of (a) $L = 8$ and (b) $L = 6$. 86
3.7 Initial state preparation at $h = 1$. 89
3.8 (a) The schematic that illustrates the circuit for OTOC measurement 92
3.9 The measurement circuit for the interferometric approach 94

4.1 Phase diagram based on the OTOC saturation values 102
4.2 The OTOC saturation values for a periodic-boundary chain with $N = 14$ size and a short-time of 104

5.1 The schematic of dynamic phase boundaries determined by OTOC time-average $\bar{F}$ with respect to control parameter h and temperature T. 110
5.2 The schematic of infinite-temperature OTOC evolving in time t for a quantum system 113
5.3 Long-time average of OTOC for XXZ model for edge-spin operators $W = V = \sigma^z_{\text{edge}}$ 116
5.4 Transverse-field Ising model at infinite-temperature. The OTOC time-average of the edge spin operators σ^z_1 via real-time OTOC dynamics 118
5.5 (a) The OTOC dynamics $F(t)$ with respect to tJ. 119
5.6 (a) The second derivative of the OTOC time-average 121
5.7 A pictorial representation of the Hamiltonian Eq. (5.8) 121
5.8 Coherence times of prescrambling plateau 126
5.9 Comparison of $\bar{F}$ and its diagonal contribution $\bar{F}_{diag}$ at different non-integrability breaking term strength Δ/J. 134
5.10 Coherence times of the edge spins based on OTOC of (a) $\Delta/J = -0.5$ and (b) $\Delta/J = -2$ 135
5.11 (a) OTOC time-average of edge spin for the nonintegrable Ising model . . . 136

6.1 The predicted A_{dip} (depth of the first dip in spin oscillations) and the long-time average 144

6.2 The observed signature of DPT. 145
6.3 (a) Circles (triangles) represent the observed occurrence time of the first dip 146
6.4 Single-site nonequilibrium response for different system sizes and transverse fields for the integrable TFIM. 152
6.5 Decay rates f_Φ for integrable TFIM in dynamically-ordered $(h_c - h)/h_c > 0$ and -disordered $(h_c - h)/h_c < 0$ regimes. 154
6.6 Scaling of the decay rate function $\exp(f_\Phi) - C_0$ for integrable TFIM in dynamically-ordered $(h_c - h)/h_c > 0$ regime. 157
6.7 Scaling of the decay rate function $\exp(f_\Phi) - C_0$ for integrable TFIM in dynamically-ordered $(h_c - h)/h_c > 0$ regime for system size $N = 480$ for different κ. . . . 158
6.8 The error functions for a system size of $N = 480$ at (a) $h = 0.5$ and (b) $h = 9.9 \times 10^{-6}$. 159
6.9 The scaling in the vicinity of the crossover for integrable TFIM with respect to reduced control parameter h_n 160
6.10 The real time dynamics for the dynamically-disordered regime at $h_f = 1.2$. 163
6.11 Angular frequency scales with $-h_n$ with a power-law exponent 165
6.12 (a) The nonintegrable TFIM with $\Delta/J = -1$ for different $h/J = 1.2, 1.95, 2.5$ 166
6.13 (a) Decay rate of the first term in the fit function Eq. (6.13) 168

7.1 The nonequilibrium response $C_r(t)$ in the TFIM with open-boundary conditions 175
7.2 Nonequilibrium phase diagram for $\Delta = 0$ (a) for different sites $r = 1, 3, 6, 9, 12$ 178
7.3 Universal scaling in the integrable TFIM for quenches from $h_i = 0$ to the vicinity of the QCP for different sites 180
7.4 MFT results for $\Delta = -0.1$. 182
7.5 $t-$DMRG results for nonintegrable TFIM 184

A.1 The microcanonical ensemble thermal prediction with respect to different energy intervals 193
A.2 (a) The hopping parameter J for the mapped single particle model 194

B.1 Error bars of the out-of-time order correlators with disorder strength 196
B.2 The difference $|F^{\text{ex}}_{i=6}(t) - F^{\sim}_{i=6}(t)|$ for Haar-distributed random states. 197
B.3 (a) Semi-logarithmic plot for σ^z_1 with σ^z_5 (blue-pentagrams), σ^z_6 (red-circles) and σ^z_7 (orange-diamonds) observables in a system size of $L = 7$. 197
B.4 (a) The EON (eigenstate occupation number) distributions $|c_\beta|^2$ with respect to eigenenergies E_β 199

C.1 The OTOC saturation values for an open-boundary chain with $N = 13$ size . 202

C.2 OTOC saturation value (Eq. (3), blue line) and its ground state contribution (Eq. (5), orange line) . . . 204
C.3 The OTOC phase diagram (via Eq. (3)) for odd-numbered chains while the x-axis is the spin interaction strength . . . 204
C.4 Ground state value contribution (Eq. (5)) to OTOC for (a) odd-numbered $N = 13$ and (b) even-numbered $N = 14$ chains . . . 205
C.5 The difference between the OTOC saturation values (via Eq. (3) in main text) and the ground state contribution for the phase diagram . . . 206
C.6 (a) Matrix elements of observable σ_z^i of a bulk spin for a ground state . . . 207
C.7 (a) The time-average of OTOC signal over a time interval of $tJ = 20$ (blue circles) . . . 209
C.8 OTOC saturation value (Eq. (3), blue line) and its ground state contribution (Eq. (5), red-circles), for $h/J = 0$ . . . 210
C.9 Real-time dynamics of OTOC at (a) $J_z/J = 0.5$ and (b) $J_z/J = 4$ at $N = 14$. 212

D.1 Diagonal contribution in the Ising model and non-interacting fermionic model after dynamical decomposition is applied. . . . 220
D.2 Coherence time computation of the integrable Ising model deep in the non-trivial phase $h/J = 0.3$. . . . 221
D.3 The scaling of OTOC, F with the system size N at the transition point determined by the second derivative of the OTOC. . . . 222
D.4 The operator ansatz tested on the Ising model. . . . 224
D.5 Real time dynamics of OTOC with both edge (red-solid) and bulk (blue-dotted) spins in nonintegrable transverse-field Ising model . . . 225
D.6 Nonintegrable transverse-field Ising model OTOC results. . . . 225
D.7 The OTOC time-average of bulk spins in the case of $\Delta/J = -0.5$ integrability breaking term. . . . 226
D.8 (a) Coherence times of the edge spins based on OTOC at $\Delta/J = -2$, deep in the topologically non-trivial phase . . . 226
D.9 Demonstration of the time-dependence of the phase diagram for the model with $\Delta/J = -0.1$ at $N = 14$ system size. . . . 227
D.10 The scaling parameters for the ground state phase transition of the model with $\Delta/J = -2$, calculated via DMRG. . . . 228
D.11 The Binder cumulant calculated for the Ising model with $\Delta/J = -2$. . . . 228
D.12 (a) The saturation value for long times and different system sizes ($N = 8$ to $N = 14$) are plotted for the gapless phase of the XXZ model. . . . 229

D.13 The coherence times of prescrambling in the gapped phase of the XXZ model, $J_z/J = 5$ for different system sizes. 230

E.1 Quench dynamics of $\overline{\rho_0}$ in the lab and the corresponding theoretical predictions derived from numerical simulations of the quench dynamics 232
E.2 $C(t)$ nonequilibrium response of the middle spin of an open chain $N = 30$, . 235
E.3 (a) Single-site observable $C(t)$ and OTOC $F(t)$, both defined at a single site, for different system sizes N for integrable TFIM at $h/J = 0.5$; 240
E.4 (a) The differences between rescaled observables with two different temporal cutoffs 241
E.5 (a-b) Ground state energy gap analysis with respect to system size N to determine the equilibrium QPT. 242
E.6 (a) The decay rate $f_{\Phi,2}$ and (b) the angular frequency ω of the fit function for the dynamics of nonintegrable TFIM at $\Delta/J = -1$. 243

F.1 Benchmarking mean field theory (MFT) analysis. 247
F.2 Nonequilibrium responses of $\sigma^z_{N/2}$ (spin in the middle of the chain), σ^z_6 (spin close to the boundary) and the total magnetization, when (a) $\alpha = 10$, (b) $\alpha = 4$, (c) $\alpha = 3$ and (d) $\alpha = 2$. 250
F.3 The nonequilibrium responses of $C_{r=6(t)}$ for different α and different system sizes (see legend). 251
F.4 Exact diagonalization results for the coherence time of 252
F.5 The spatial profiles of the edge mode $\gamma^1 = \phi_1^+$ at $h = 0.5$ 253
F.6 The single-site dynamical phase diagrams with an ultraviolet temporal cutoff of $t^* = 10$ for 254
F.7 The single-site dynamical phase diagrams with an ultraviolet temporal cutoff of $t^* = 20$ 255
F.8 The single-site dynamical phase diagrams with an ultraviolet temporal cutoff of $t^* = 2\alpha\Delta x/v_q$ 256
F.9 The single-site dynamical phase diagrams with an initial state as the ground state of an initial Hamiltonian with $h_i = 0.1$ and an ultraviolet temporal cutoff of $t^* = 10$ 259
F.10 The scaling behavior in the vicinity of the transition 260
F.11 $C_{r=6}(t)$ for quenches from $h_i = 0$ (blue-solid) or $h_i = 0.1$ (dashed-red) to $h = 0.999$ 260
F.12 The nonequilibrium response of integrable TFIM in the vicinity of the transition 263
F.13 The nonequilibrium response of integrable TFIM (a) at DCP $h = 1$ and . . 264

F.14 Mean-field nonequilibrium responses of a near-integrable model 265
F.15 Different boundary conditions are compared for the integrable TFIM 266
F.16 The dynamic order profile of the nonintegrable TFIM with $\Delta = -1$ in logarithmic scale. 267

List of Appendices

Appendix A: Thermalization in the Integrable Models **192**
A.1 Microcanonical Window Selection 192
A.2 Mapping of a Spinor Hamiltonian onto a Single Quantum-Particle Hopping Model 193

Appendix B: Detection of Information Scrambling in Cold Atoms **195**
B.1 Error bars on OTOC for the disordered XX-ladder 195
B.2 Error bounds on Haar-distributed initial states 195
B.3 The exponential and power-law fitting parameters 196
B.4 Details on the experimental initial state preparation 198

Appendix C: The Connection Between Information Scrambling and Quantum Phase Transitions **201**
C.1 Energy-time relation and finite-size effects 201
C.2 Operator Ansatz Demonstrated 205
C.3 Comparison of real-time dynamics with theory prediction in short times . . . 208
C.4 OTOC with odd number of spins and periodic boundary conditions 209
C.5 The remarks on the saturation value of OTOC 210
C.6 Density-matrix renormalization group computations 212

Appendix D: Topologically Induced Prescrambling **214**
D.1 Methods Explained 214
D.2 Derivation of Fermionic OTOC 216
D.3 The relation between OTOCs and two-time correlators 219
D.4 Further results on the Ising Model 221
D.5 Further results on the nonintegrable Ising models 223
D.6 Further results on the XXZ model 229

Appendix E: Probing Criticality in the Transient Quench Dynamics **231**

E.1 Observation of Dynamical Quantum Phase Transitions in a Spinor Condensate 231
E.2 Dynamical crossover in the transient quench dynamics of short-range transverse field Ising models . . . 234
E.2.1 Periodic vs. open boundaries . . . 234
E.2.2 Mapping to noninteracting fermions in quench dynamics . . . 235
E.2.3 Vanishing dynamical order for one-point observables . . . 239
E.2.4 Comparison between fixed and parametric temporal cutoffs in the open chain . . . 240
E.2.5 Equilibrium QPT for the nonintegrable TFIM . . . 241
E.2.6 Error bar calculations . . . 243
E.2.7 The rest of the fit parameters of the nonintegrable TFIM . . . 244

Appendix F: Dynamical Criticality in the Quasi-Stationary Regimes 245
F.1 Methods . . . 245
F.1.1 Mean-field theory (MFT) Analysis . . . 246
F.1.2 t-DMRG calculations . . . 248
F.2 The quasi-stationary regime in long-range interacting TFIM . . . 248
F.3 Numerical evidence on quasi-stationary regime not being related to strong-zero modes . . . 251
F.4 Temporal cutoffs . . . 253
F.5 Independency of the results from the initial states . . . 258
F.5.1 Analytical expression for the edge magnetization in the vicinity of the transition . . . 261
F.6 Nonequilibrium response in the close vicinity of the transition . . . 262
F.7 Details on the near-integrable model and the associated fit functions . . . 264
F.8 Robustness of the quasi-stationary regime . . . 266
F.9 t-DMRG results in detail . . . 267

ABSTRACT

Understanding how quantum matter behaves when driven out of equilibrium is one of the key focuses in quantum physics. Thanks to impressive progress in the control and precision achieved in quantum synthetic matter over the past decades, the nonequilibrium quantum many-body physics has become one of the most active research areas today, especially after the experimental realization of Bose-Einstein condensates and optical lattices, which allows us to directly observe and study nonequilibrium quantum matter with great accuracy and controllability. In this dissertation, I explore the rich landscape of nonequilibrium quantum many-body physics and how quantum phase transitions, both symmetry-breaking and topological, can be extended to the nonequilibrium setting.

In the first part of the dissertation, I focus on spinor Bose-Einstein condensates as an isolated quantum many-body system, and reveal their various dynamical behaviors, including quantum collapse and revivals, thermalization and nonthermal equilibration with no revival even though the system has finite degrees of freedom. In contrast to typical integrable systems, which usually do not thermalize, we find that spinor condensates have a parameter range in which the system thermalizes via the Eigenstate Thermalization Hypothesis (ETH). We show that this observation is linked to the presence of *rare* nonthermal states whose fraction vanishes with system size, and contributes to the notion of thermalization via weak ETH.

Next, I explore a dynamical process that is complementary to thermalization in isolated quantum systems: information scrambling, which could be probed via out-of-time-order correlators (OTOC). I propose a nonintegrable, disordered and quasi-1D spin model, the ladder$-XX$ model, for a feasible detection of information scrambling in a cold atom simulator. This chapter poses a fundamental question: *'What are the signatures of quantum*

phases and phase transitions in isolated interacting systems driven out-of-equilibrium?" I study the ladder-XX model in both clean and disordered potentials, and characterize different nonequilibrium phases, i.e., ergodic and many-body localized, of the model based on the decay properties of OTOCs. Emergent light cone shows sublinear behaviour, while the butterfly cones drastically differ from the light cone by demonstrating superlinear spread of information with a velocity that is bounded by the light cone velocity.

In the second part of the dissertation, I continue to search for answers to the question posed above, however this time with a particular focus on symmetry-breaking and topological quantum phase transitions. I pin down a universal mechanism underlying the relation between information scrambling at any temperature and quantum phases at low temperatures. Our method points to key ingredients to dynamically detect long-range order in gapped phases through OTOCs for symmetry-breaking quantum phase transitions and Z_2 topological order associated with Majorana zero modes localized at the edges. Our results pave the way to an intriguing observation that phases of quantum matter could protect the information from scrambling and thermalization, even when the system is interacting and nonintegrable.

Finally, I explore and propose utilizing short-time transient temporal regimes and single-site probes to detect the phases and phase transitions in quantum matter. These studies reveal a dynamical crossover and a dynamical phase transition, respectively for periodic and open-boundary chains. In both cases, a nonequilibrium scaling law appears in the vicinity of the crossover/transition with associated exponents that differ from the analytical predictions for long times. Feasibility of detecting such dynamical criticality in experimental systems are discussed.

Chapter 1

Introduction

Here we are, after more than two millennia of pondering about the nature of *things* [1]. On this path of understanding *matter*, there are few stories as important as that of the modern atomic theory [2–14]. In our everyday experience though, *matter* is macroscopic with conductors and insulators in a crude classification [15]. Macroscopic matter is composed of an innumerable amount of constituents, i.e., nuclei and electrons. To describe the motion of electrons in matter, one needs to abandon the treatment of individual particles and rather work with ensembles of them. Such statistical mechanic approach is the bedrock of our understanding of the collective behavior of constituents in matter [16–18]. Either fermionic [17] or bosonic [16], the *collective* quantum matter, or a quantum many-body system [18], would be described in equilibrium with the tools of quantum statistical mechanics [19]. Similar to solids, liquids and gases in our everyday experience, the quantum many-body systems exhibit phases with different orderings in equilibrium [18]. Some well-known examples are quantum gases and liquids, i.e. superconductors and superfluids [20, 21]. Quantum phases and their phase transitions are going to be introduced in the first section of this Chapter. Although the examples are plenty, we will in particular focus on the quantum phases and phase transitions of the systems that are studied in this dissertation.

This dissertation is a continuous application of Schrödinger's and Heisenberg's formula-

tion of mechanics [10, 11, 13, 14] to better understand the collective quantum matter *away from the equilibrium*. By eliminating the assumptions that the system is already in equilibrium and the dynamics is sufficiently slow to satisfy the adiabatic theorem [22] and not to drive it out of equilibrium, we start to explore an uncharted territory of physics. Arguably one of the most important motivations behind these fundamental theoretical questions is our ability to experimentally probe *nonequilibrium quantum matter*. Quantum synthetic matter can be used as an umbrella term that includes modern quantum simulators where model Hamiltonians are implemented and tested in very controlled environment with high levels of precision [23–25]. These include neutral cold atoms [26, 27], ion traps [28, 29], superconducting circuits [30], photonic systems [31], quantum dots and others [23, 24]. The quantum many-body systems could be driven out of equilibrium experimentally with quenches, ramps and periodic driving [32], some of which are going to be detailed in the next sections. We observe that two overarching themes typically appear in nonequilibrium quantum matter, (i) integrability of the Hamiltonian [33] and (ii) the presence/absence of interactions. While nonintegrability implies the presence of interactions, the opposite is not true: the presence of interactions does not always mean that the system is nonintegrable. How static properties of a Hamiltonian like its energy spectrum, its equilibrium quantum phases and emergent order parameters upon symmetry breaking, affect the nonequilibrium response will be a persistent question that I will be exploring in this dissertation. We are going to see that the nonequilibrium response of an isolated quantum system provides us with information [32, 34, 35] on (i) whether the local observables could equilibrate [36], exhibit quantum recurrences [37], thermalize [38–40]; (ii) how the decay properties of correlators probe the energy level statistics [41, 42], e.g., ergodic and many-body localized phases [43], correlation spread and bounds on correlation speed [44]; (iii) how both the steady-states and transient regimes of local observables and correlators could probe low temperature quantum phases [35], symmetry-breaking and topological.

1.1 Quantum Phase Transitions

Symmetry and *topology* are two paradigms in our understanding of matter in equilibrium. The former is the founding element of Landau's theory of critical phenomena [45], where symmetry is broken or preserved determines the phase of matter and there is a continuous transition between two phases, e.g., a second-order phase transition. Meanwhile, the classification according to the topology of the ground states is our current understanding on the phases of matter and their transitions where symmetry remains the same across the transition boundary, but a topological invariant, i.e., Chern number, of the ground state changes [46, 47].

Symmetry-breaking phase transitions between symmetry-broken and -preserved phases are associated with local order parameters where the order parameter is nonzero and zero, respectively. The critical point where the continuous transition occurs is also where the correlation length diverges and a field theoretic approach becomes applicable with coarse-grained microscopics, and hence universality classes that are equipped with universal critical exponents [45, 48]. Physics of critical phenomena is arguably one of the most intuitive principles that also connect theory with experiment: Although the underlying microscopic structure could differ greatly from one material to another, in the vicinity of the critical point one observes the same handful of critical exponents that describe the same long-wavelength physics if the compared materials belong to the same universality class.

As the temperature decreases, $T \to 0$, if a nonanalyticity is established in the ground state energy in the thermodynamic limit, the phenomenon is called a *quantum phase transition* (QPT), which holds strictly at $T = 0$ [49]. Continuous quantum phase transitions have a vanishing energy gap Δ between their ground and their first excited states at the quantum critical point, and scaling behavior of the gap provides information about some of the critical exponents,

$$\Delta \sim J \left| \frac{h - h_c}{h_c} \right|^{z\nu}, \tag{1.1}$$

where z and ν are the dynamical critical exponent and the correlation length ξ critical exponent, respectively, and individually defined as $\Delta \sim \xi^{-z}$ and $a\xi^{-1} \sim |(h - h_c)/h_c|^{\nu}$ where a is the unit lattice spacing; J is the energy level; h is the control parameter; h_c is the quantum critical point; and $(h - h_c)/h_c$ is the reduced control parameter. While sometimes there exists a finite-temperature phase transition that extends from a quantum phase transition, this is not always true. A relevant example of this in the dissertation is the transverse-field Ising model (TFIM) in one dimension, which also goes under the name of transverse-field Ising chain (TFIC). For concreteness, we state the Hamiltonian of the TFIM when its interactions are long-range,

$$H = -\sum_{r \neq l} J(r - l)\sigma_r^z \sigma_l^z + h \sum \sigma_r^x, \tag{1.2}$$

where σ_r^i, $i = x, y, z$ are Pauli spin matrices at site r [50] in a one-dimensional chain. $J(r - l) = J_0/|r - l|^{\alpha}$ is power-law decaying interactions with α rate coefficient. For $\alpha \to 0$, Eq. (1.2) reduces to the integrable all-to-all coupled Lipkin-Meshkov-Glick (LMG) model [51]; and for $\alpha \to \infty$ it reduces to integrable nearest-neighbor TFIM [49]. This long-range model has a quantum phase transition with a corresponding finite-temperature phase transition only when $\alpha \leq 2$ [52]. Therefore, the locally-connected (or short-range) TFIM with nearest-neighbor terms which is going to be extensively studied in this dissertation, hosts only quantum phase transitions. Henceforth, we will focus on the locally-connected TFIM, $l = r + 1$ in Eq. (1.2).

1.1.1 Transverse-field Ising Model

In this subsection, we will review the bullet points of the relevant section in Ref. [49] where the rest of the content can be found in detail.

When the transverse field is zero, $h = 0$, the model is classical with product states as its eigenstates. In particular, the ground states are spin-up or -down polarized states, $|\uparrow\uparrow \cdots \uparrow\rangle$

or $|\downarrow\downarrow\cdots\downarrow\rangle$ with exact two-fold degeneracy in energy. In the opposite limit where $h \gg |J|$, the ground state is a product state but in the $x-$basis.

TFIM with nearest neighbor couplings only is an integrable model and can be solved exactly via mapping to noninteracting fermions [49]. The mapped fermionic model is called the Kitaev chain [53], which will be detailed in Chapter 5 together with the mapping. The TFIM Hamiltonian is invariant under Ising (Z_2) symmetry, $\sigma_i^z \to -\sigma_i^z$ and $\sigma_i^x \to \sigma_i^x$ with the symmetry generator $\mathbb{P} = \prod_i \sigma_i^x$.

In the limit where $h \ll J$ but $h \neq 0$, nonzero h will mix the ground states and the degeneracy will be approximate in systems with finite sizes. However the degeneracy will become exact as the system size increases to the thermodynamic limit. Hence, the ground state in this limit is still two-fold degenerate, while there is a unique ground state in the opposite limit where $h \gg J$. This is a heuristic way of observing the presence of a quantum phase transition between two quantum phases, because the nature of the ground states changes from one limit to another.

One would notice that the Ising symmetry maps degenerate ground states into each other in the limit $h \ll J$. In fact this mapping is more general than the ground states in the TFIM, and it is applicable throughout the energy spectrum. The details and the consequences of this symmetry property in the nonequilibrium response will be extensively studied in Chapter 5.

A system in thermodynamic limit will always choose one state or another in the ground state, while the entire Hamiltonian still preserves the symmetry. This is called *spontaneous symmetry breaking* [45,48] and it is one of the most ubiquitous physical phenomena in physics appearing in fields ranging from condensed matter to high energy physics. In the context of TFIM, the system spontaneously breaks the Z_2 symmetry in the limit $h \ll J$. We will in particular focus on the impact of spontaneous symmetry breaking on the nonequilibrium response in Chapter 4.

The quantum phase transition of the TFIM lies at the point $h_c = J$ separating two quantum phases, a quantum ferromagnet at $h < h_c$ and a quantum paramagnet at $h > h_c$. Study-

ing the spatial correlations with respect to the ground states reveal the properties of these phases. (i) In the ferromagnetic phase, $\langle \sigma_i^z \sigma_j^z \rangle = N_0^2$ for large distances $|i-j| \to \infty$ where $N_0 \neq 0$ is the spontaneous magnetization of the ground state, and similarly $\langle \sigma_i^z \rangle = \pm N_0$. When $h = 0$, $N_0 = 1$, and N_0 decreases as h increases, however remains nonzero until $h = h_c$. (ii) In the paramagnetic phase, the spatial correlations over large distances decay exponentially $\langle \sigma_i^z \sigma_j^z \rangle \sim e^{-|r_i - r_j|/\xi}$, implying that there is no ferromagnetic order in a quantum paramagnet. (iii) At the critical point $h = h_c$, the spatial correlations decay as a power-law over large distances. In this dissertation, I will study observables and various correlators, e.g., two-point correlators, two-time correlators, out-of-time-order correlators (OTOC), in the magnetically ordered and disordered phases and in the vicinity of the quantum critical points of the TFIM and other Ising-like chains driven out of equilibrium.

Finally, let us point out that there are two obvious ways of breaking integrability in the TFIM: (i) introducing a longitudinal field $h_z \sum_i \sigma_i^z$, (ii) introducing next-nearest neighbor terms, i.e., $\Delta \sum_i \sigma_i^z \sigma_{i+2}^z$. I focus on the latter in this dissertation, because the second method preserves the Z_2 symmetry and the quantum critical point merely shifts to favor order, while it introduces interactions that break the integrability.

1.1.2 Bose-Einstein Condensates and the Bose-Hubbard Model

The next illustration of quantum phase transitions is going to be on the Bose-Einstein condensates, e.g., superfluids.

Bose Einstein condensation (BEC) is a truly quantum phenomenon where under a critical temperature, a fraction of noninteracting Bose particles, i.e. neutral atoms with bosonic statistics [16], start to share the same wave function [54]. Dilute gases are utilized to create BEC, where the particle density at the center of a Bose-Einstein condensed gas is around $10^{13} - 10^{15}$ cm^{-3}. This number can be contrasted with the density of molecules in air under standard temperature and pressure (STP) which is 10^{19} cm^{-3}, or the atoms in a liquid or a solid, which is 10^{22} cm^{-3} or nucleons in atomic nuclei, which is 10^{38} cm^{-3} [21]. To turn

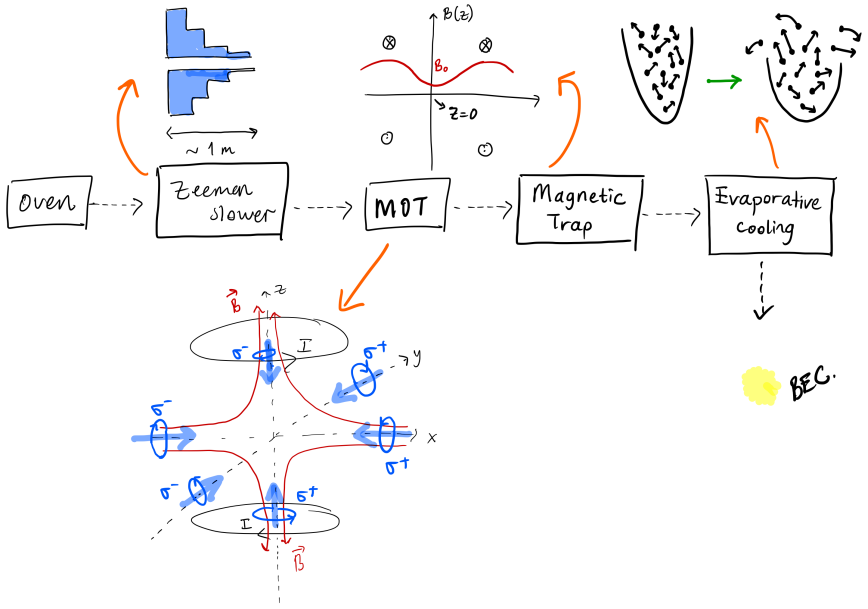

Figure 1.1: The experimental stages of how to realize Bose-Einstein condensation with Zeeman slower, magneto-optical trap (MOT), magnetic trap and evaporative cooling. See text for details on different stages.

on the interactions in a dilute gas that can form a collective quantum matter like in solids and liquids, the temperature needs to decrease at least to $\sim 10^{-5}$ K. Therefore, cooling and trapping techniques for atomic gases have been developed in last decades [55], which paved the way to the first realization of Bose-Einstein condensation [56, 57] in 1998. Dilute gases are theoretically tractable and experimentally feasible, mainly because the effective interaction can be described with only one parameter: the scattering length a_s that can be tuned through Feshbach resonances via electric or magnetic fields [21].

Cooling and trapping of dilute gases are performed with lasers and magnetic fields [21,55]. When atoms are expelled out of the oven, they have an approximate speed of 1000 ms^{-1}. In order to slow them, the experimentalists use laser cooling techniques by shooting a laser beam at the beam of *hot* atoms and making sure that atoms and laser beam are on resonance. This process introduces Doppler broadening in the spectral lines. Hence, in order to compensate for the effect of Doppler shift, atoms are let into a Zeeman slower, which

applies a spatially changing magnetic field to the atoms to cause Zeeman effect. At the end of this process, the atoms slow down to an approximate speed of 5 ms^{-1}, from where they are captured by a magneto-optical trap (MOT). The lasers that are shined on the atoms in a MOT have different polarizations induced by the inhomogeneous quadrupole magnetic field gradient. This creates a trap potential to accumulate $\sim 10^{10}$ atoms. Then the lasers are turned off and the atoms stay in a pure magnetic trap where they are exposed to a nondissipative trapping force. The magnetic trap increases the particle density, and hence it helps with the evaporative cooling process. The evaporative cooling is the last stage where the experimentalists turn on the crossed beam lasers to create a dipole trap. In evaporative cooling, they let the hottest atoms at the edge of the trap leave the trap by reducing the trap potential continuously. When the rest of the atoms recover their Maxwellian velocity distribution [19], the mean temperature decreases. The evaporative cooling process reduces the temperature of an atomic gas from tens of μK to hundreds of nK. A cartoon schematic of this process can be seen in Fig. 1.1.

As the temperature of the gas decreases, the de Broglie wavelength of the atoms increases

$$\lambda_T = \left(\frac{2\pi\hbar^2}{mkT}\right)^{1/2}.$$

When the de Broglie wavelength becomes comparable to the inter-particle spacing, Bose-Einstein condensation starts to occur. The critical temperature T_c that corresponds to the phase change from normal to condensed gas, and the associated condensate fraction in a harmonic trap are given as [21]

$$\begin{aligned} kT_c &\sim 0.94\hbar\bar{\omega}N^{1/3}, \\ N_0 &= N\left[1-\left(\frac{T}{T_c}\right)^3\right], \end{aligned}$$

where $\bar{\omega}$ is the geometric mean frequency of the trap; N and N_0 are the numbers of all particles and condensed particles in the atomic gas, respectively; k is the Boltzmann constant;

$\hbar$ is the Planck's constant and T is the temperature of the atomic gas.

When interactions and scatterings between Bose particles are taken into account, BEC dynamics follow a nonlinear Schrödinger equation, the so-called Gross-Pitaevskii equation [21, 58].

$$i\hbar\frac{\partial\Psi(r,t)}{\partial t} = -\frac{\hbar^2}{2m}\nabla^2\Psi(r,t) + V(r,t)\Psi(r,t) + U_0|\Psi(r,t)|^2\Psi(r,t), \tag{1.3}$$

where $\Psi(r,t)$ is the wave function of a single-particle state into which the condensation occurs; $U_0 = 4\pi\hbar^2 a_s/m$ is the strength of the effective potential; a_s is the scattering length for two-body $s-$wave scatterings [59] that dominate a dilute cold atomic gas and $V(r,t)$ is the external potential. While this is the case for spin-0 BEC, we can utilize the hyperfine energy structure of these cold atoms and introduce *spinor Bose-Einstein condensates*. A spinor condensate is a multi-component condensate of atoms with their spin degrees of freedom affecting the Hamiltonian of the system [21, 60]. More specifically, a spinor BEC experiences quantum spin-mixing which is initiated due to the $s-$wave scatterings of spinful Bose atoms [61]. In the next subsection, we will introduce the spinor condensates and their quantum phase transitions. In a later subsection, we will go back to the physics of spinless Bose-Einstein condensates, introduce optical lattices and the resulting Bose-Hubbard Model.

Spinor Bose-Einstein Condensates

To write down the spinor BEC Hamiltonian, we need to make some approximations in the scattering processes of cold atoms. The effective interactions between atoms in a dilute gas are assumed to be short-range contact type [60],

$$U_{\text{eff}}(r,r') = U_0\delta(r-r'), \tag{1.4}$$

where U_0 is the interaction strength and r, r' are the positions of the atoms to scatter from each other. The approximations of spinor condensates are [60],

1-*Cold-collision approximation*: all scatterings are $s-$wave scatterings, because the incident collision energy is low.

2-*Spinor gas collision approximation*: the short-range potential is rotationally invariant, so that the total angular momentum (both orbital and internal angular momenta) of a scattering pair of atoms is conserved.

3- *Weak dipolar approximation*: We neglect the spin-orbit coupling due to short-range molecular potential, so that the orbital and internal angular momenta are separately conserved.

4- *No mixing of the total hyperfine states* of the colliding atoms, so that we neglect the collisions where the atoms undergo hyperfine relaxation processes.

These approximations ensure that the $s-$wave scattering length of the colliding pair $a_{F_{\rm pair}}$ is sufficient to describe the collisions among spinor gas atoms. In addition to these approximations, quantum statistics constrain the parity of $a_{F_{\rm pair}}$. Integer spins behave like bosons, and hence they should be symmetric under the exchange of any two particles, whereas the half-integers behave like fermions, and hence they should be anti-symmetric. Therefore, the many-body wave function of identical spin$-F$ atoms will have a factor of $(-1)^{2F}$ under the exchange of any two atoms. Due to the same exchange principle, the internal spin part of the wave function has a factor of $(-1)^{2F+F_{\rm pair}}$, and the orbital angular momentum part of the wave function has $(-1)^{L_{\rm pair}}$. Therefore we have,

$$(-1)^{2F} \;=\; (-1)^{2F+F_{\rm pair}} \times (-1)^{L_{\rm pair}}, \tag{1.5}$$

which implies that $F_{\rm pair}$ must be even, when we have only $s-$wave scattering with $L_{\rm pair}=0$. These arguments simplify the interaction Hamiltonian greatly,

$$H_i \;=\; \frac{1}{2}\sum_{i,j}\delta^3(\mathbf{r}_i-\mathbf{r}_j)\sum_{\text{even } F_{\rm pair}}\frac{4\pi\hbar^2 a_{F_{\rm pair}}}{M}\mathbb{P}_{F_{\rm pair}}, \tag{1.6}$$

where $\mathbb{P}_{F_{\rm pair}}$ is the projection operator for a pair of atoms that is projected onto the total spin-$F_{\rm pair}$. There are two possible operators: the identity operator $\mathcal{I}_i$ (for the $i^{\rm th}$ atom) which

is invariant under the exchange of spin indices (being the symmetric part of the Hamiltonian)

$$\mathcal{I}_i \otimes \mathcal{I}_j \;=\; \sum_{\text{all } F_{\text{pair}}} \mathbb{P}_{F_{\text{pair}}} \tag{1.7}$$

and the angular momentum or the spin-mixing interaction operator $\mathbf{F}_i$ which is the nonsymmetric part of the Hamiltonian,

$$\mathbf{F}_i \cdot \mathbf{F}_j \;=\; \sum_{\text{all } F_{\text{pair}}} \left[\frac{1}{2}F_{\text{pair}}(F_{\text{pair}}+1) - F(F+1)\right] \mathbb{P}_{F_{\text{pair}}}, \tag{1.8}$$

where $F_i = F_j = F = 1$, since all atoms possess spin-1 in our case. Then the interaction Hamiltonian will be of the form,

$$H_i \;=\; \frac{1}{2}\sum_{i,j} \delta^3(\mathbf{r}_i - \mathbf{r}_j)\left(c_0' \left[\mathcal{I}_i \otimes \mathcal{I}_j\right]_s + c_1' \left[\mathbf{F}_i \cdot \mathbf{F}_j\right]_s\right), \tag{1.9}$$

where s reminds us that we are summing over only even F_{pair} because of the quantum statistics. The coefficients c_0 and c_1 are to be determined in the following. We notice that

$$\left[\mathcal{I}_i \otimes \mathcal{I}_j\right]_s \;=\; \mathbb{P}_0 + \mathbb{P}_2, \tag{1.10}$$

and using Eq. (1.8),

$$\left[\mathbf{F}_i \cdot \mathbf{F}_j\right]_s \;=\; \mathbb{P}_2 - 2\mathbb{P}_0. \tag{1.11}$$

If we substitute Eqs. (1.10)-(1.11) into Eq. (1.9) and equate the result to Eq. (1.6) for only even F_{pair}, we obtain the coefficients as

$$c_0' \;=\; \frac{4\pi\hbar^2}{M}\frac{a_0 + 2a_2}{3}, \tag{1.12}$$

$$c_1' \;=\; \frac{4\pi\hbar^2}{M}\frac{a_2 - a_0}{3}. \tag{1.13}$$

Let us write the identity and spin operators in terms of field operators,

$$\mathcal{I} = \sum_{m,n=-F}^{F} \hat{\psi}_m^\dagger(\mathbf{r}) I_{mn} \hat{\psi}_n(\mathbf{r}) = n(\mathbf{r}), \tag{1.14}$$

$$F_\nu = \sum_{m,n=-F}^{F} \hat{\psi}_m^\dagger(\mathbf{r}) (F_\nu)_{mn} \hat{\psi}_n(\mathbf{r}), \tag{1.15}$$

where $\hat{\psi}_{m_F}^\dagger$ is the annihilation operator that satisfies Bose statistics for the Zeeman state m_F. Hence,

$$H_i = \frac{1}{2} \int d\mathbf{r} \left(c_0' : n^2(\mathbf{r}) : + c_1' : \mathbf{F}^2(\mathbf{r}) : \right). \tag{1.16}$$

Here, :: denotes normal ordering. The total Hamiltonian in terms of field operators can be written more explicitly,

$$\begin{aligned} H &= \sum_{m=-F}^{F} \int d\mathbf{r} \psi_m^\dagger \left(-\frac{\nabla^2}{2M} + V(\mathbf{r}) \right) \psi_m + \frac{c_0'}{2} \sum_{m,n=-F}^{F} \int d\mathbf{r} \psi_m^\dagger \psi_n^\dagger \psi_m \psi_n \\ &+ \frac{c_1'}{2} \int d\mathbf{r} (\psi_1^\dagger \psi_1^\dagger \psi_1 \psi_1 + \psi_{-1}^\dagger \psi_{-1}^\dagger \psi_{-1} \psi_{-1} - 2\psi_1^\dagger \psi_{-1}^\dagger \psi_1 \psi_{-1} + 2\psi_1^\dagger \psi_0^\dagger \psi_0 \psi_1 \\ &+ 2\psi_{-1}^\dagger \psi_0^\dagger \psi_0 \psi_{-1} + 2\psi_0^\dagger \psi_0^\dagger \psi_1 \psi_{-1} + 2\psi_1^\dagger \psi_{-1}^\dagger \psi_0 \psi_0). \end{aligned} \tag{1.17}$$

We note that from now on, we skip the operator notation for simplicity in the equations $\hat{\psi}_m = \psi_m$. Since the first term in Eq. (1.17) is derived from the identity operator, we know it is the symmetric part of the interaction Hamiltonian under the exchange of two atoms. The second term, on the other hand, can be written with spin matrices for spin-1 atoms. For sodium and rubidium alkali atoms, the symmetric part of the interaction Hamiltonian is dominant over the nonsymmetric part, so that $|c_0| \gg |c_1|$ holds. This observation leads us to the so-called single mode approximation (SMA), where we assume that the condensate wave functions for each spin component $\phi_{m=-1,0,1}(\mathbf{r})$ are described by the same spatial wave function $\phi(\mathbf{r})$ [60, 61]. The spatial wave function $\phi(\mathbf{r})$ satisfies the Gross-Pitaevskii equation

which gives the spatial structure of the spin-1 spinor Bose-Einstein condensate. Then one can write,

$$\psi_m \sim a_m \phi(\mathbf{r}), \quad m = 0, \pm 1 \tag{1.18}$$

with the normalization condition $\int d\mathbf{r}|\phi(\mathbf{r})|^2 = 1$. The Hamiltonian reduces to rotationally invariant $H = \frac{c_1}{2}L^2$, which has well-known analytical solutions for both ferromagnetic $c_1 < 0$ and anti-ferromagnetic $c_1 > 0$ interaction [61]. In the next step, we apply a magnetic field to the system, which introduces linear and quadratic Zeeman effects. These terms read $\hat{\psi}_m^\dagger \left(q(L_z^2)_{mn} - p(L_z)_{mn}\right) \hat{\psi}_n$, and under SMA, they take the following form,

$$\begin{aligned} H &= c_1 \frac{L^2}{N} + \sum_{m=-1}^{m=1} \left(qm^2 - pm\right) a_m^\dagger a_m, \\ &= c_1 \frac{L^2}{N} + q\left(a_{-1}^\dagger a_{-1} + a_1^\dagger a_1\right) - p\left(a_1^\dagger a_1 - a_{-1}^\dagger a_{-1}\right) = c_1 \frac{L^2}{N} - q a_0^\dagger a_0 - p L_z, \end{aligned} \tag{1.19}$$

where the linear Zeeman term is the angular momentum operator in z-direction $L_z = n_1 - n_{-1}$ and we introduced $c_1 = c_1' N$. The SMA Hamiltonian Eq. (1.20) commutes with the linear Zeeman operator F_z, hence the eigenstates of the SMA Hamiltonian are always eigenstates of the operator L_z. We also note that the number of particles in level $m = 1$ are always equal to the number in $m = -1$, when the magnetization is set to zero. So when there is no magnetization, the linear Zeeman term will disappear, and when there is nonzero magnetization, this term will be constant throughout the time evolution. Therefore, we can safely neglect the linear Zeeman term. Therefore, the Hamiltonian reduces to

$$H = c_1 \frac{L^2}{N} - q a_0^\dagger a_0, \tag{1.20}$$

$$\begin{aligned} &= \frac{c_1}{N}(a_1^\dagger a_1^\dagger a_1 a_1 + a_{-1}^\dagger a_{-1}^\dagger a_{-1} a_{-1} - 2a_1^\dagger a_{-1}^\dagger a_1 a_{-1} + 2a_1^\dagger a_0^\dagger a_0 a_1 \\ &+ 2a_{-1}^\dagger a_0^\dagger a_0 a_{-1} + 2a_0^\dagger a_0^\dagger a_1 a_{-1} + 2a_1^\dagger a_{-1}^\dagger a_0 a_0) - q a_0^\dagger a_0. \end{aligned} \tag{1.21}$$

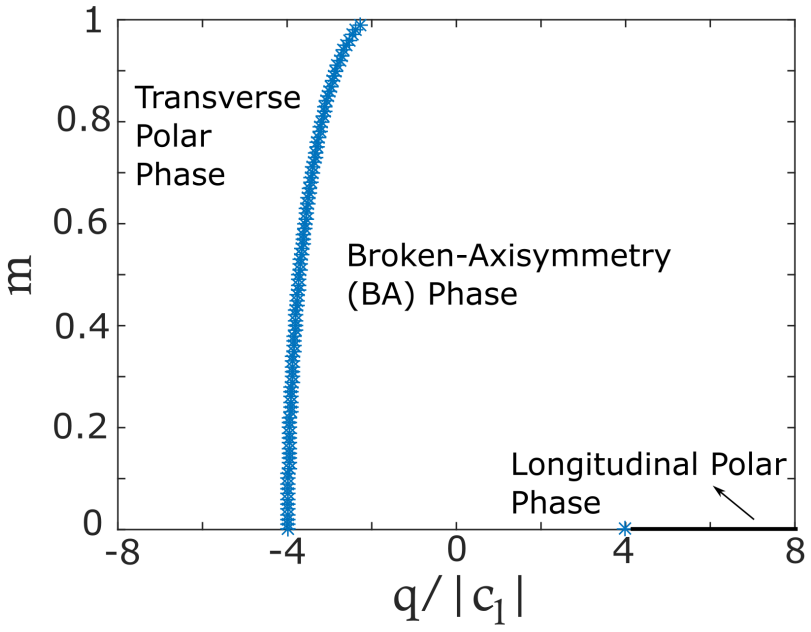

Figure 1.2: Full phase diagram of spin−1 ferromagnetic condensate with respect to q, the Zeeman parameter, and m, the magnetization density, computed via exact diagonalization of 10^4 atoms. The quantum phases are marked on the figure.

This system hosts quantum phase transitions for both ferromagnetic and antiferromagnetic interactions due to the competition between spin-mixing and Zeeman terms. For ferromagnetic interaction the phase transition is continuous, whereas for antiferromagnetic interaction the phase transition is continuous only when the net magnetization is nonzero. Otherwise, the antiferromagnetic spinor condensate has a first order quantum phase transition.

At large and positive q values the quadratic Zeeman term in the Hamiltonian Eq. (1.20) dominates the Hamiltonian and all atoms favor the hyperfine level $|m_0\rangle$. Therefore, the ground state will be of the form,

$$|\psi(q/c_1 \to \infty)\rangle \quad = \quad |\rho_{-1} = 0, \rho_0 = 1, \rho_1 = 0\rangle \, . \tag{1.22}$$

Here ρ_m is the atom density in each hyperfine level $|m\rangle$. When we take the q to large negative

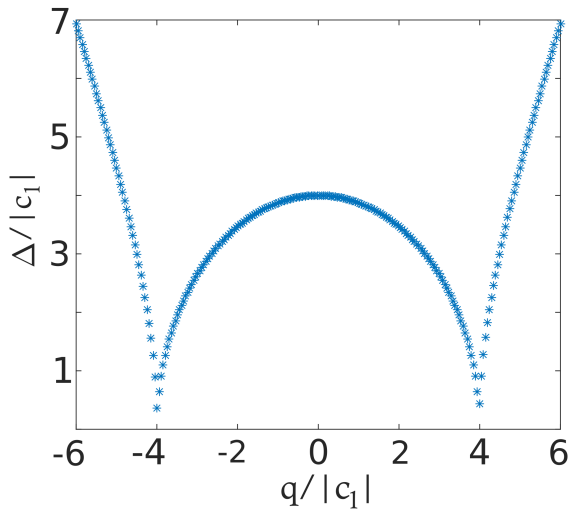

Figure 1.3: The ground state energy gap of ferromagnetic condensate for $m = 0$ and $N = 10^4$ atoms. The gap vanishes at two critical points as the system size increases, implying the presence of two second-order quantum phase transitions.

values, Hamiltonian will prevent the occupation of $|m_0\rangle$ due to minimization of energy,

$$|\psi(q/c_1 \to -\infty)\rangle \quad = \quad |\rho_{-1}, \rho_0 = 0, \rho_1 = 1 - \rho_{-1}\rangle \, . \tag{1.23}$$

As in previous section, the change in the ground states points to a quantum phase transition, as we sweep the parameter q.

When the interaction is ferromagnetic, we set $c_1 < 0$ and apply exact diagonalization to a system of 10^4 atoms. The full phase diagram of ferromagnetic condensate is given in Fig. 1.2. When there is no net magnetization $m = 0$, the ferromagnetic spinor BEC hosts two continuous quantum phase transitions between different quantum phases. A phase diagram can be seen in Fig. 2.1a in the next chapter. Here we plot the ground state energy gap of of this system in Fig. 1.3, that shows two quantum critical points that have, expectantly, vanishing gaps with increasing system size. We apply finite-size scaling analysis on one of

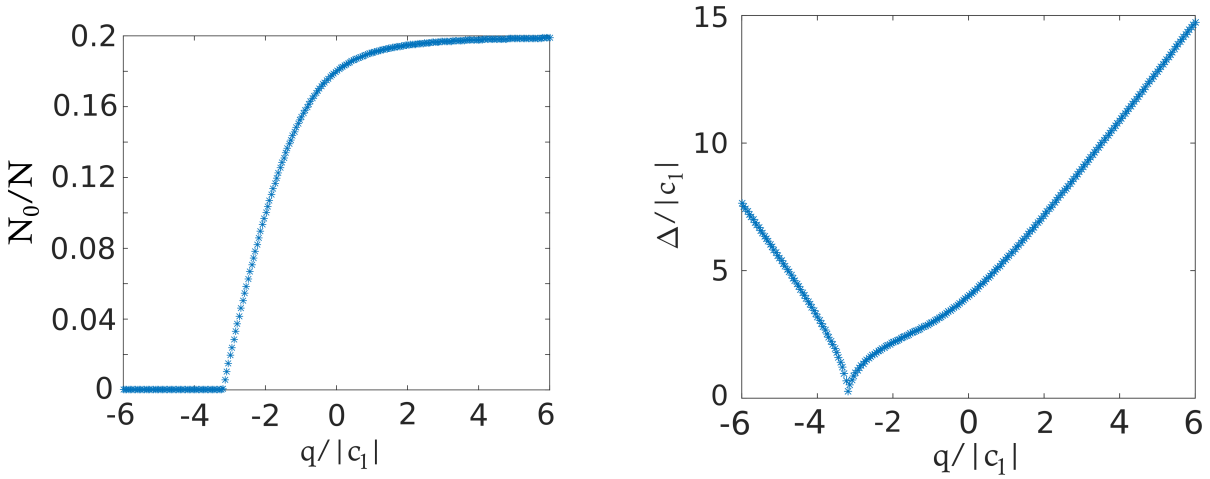

Figure 1.4: The ground state phase transition and the energy gap for ferromagnetic spinor condensates when magnetization density is $m = 0.8$ for a system size of $N = 10^4$.

these quantum critical points and find,

$$\begin{aligned} \Delta &= 5.656N^{-0.331}, \quad R^2 = 1, \\ q_c &= 8.269N^{-0.648} - 4, \quad R^2 = 1. \end{aligned} \tag{1.24}$$

Let us first observe that Δ, the energy gap, indeed vanishes in the thermodynamic limit, as we discussed in the beginning of the current Section. The critical point reads $q_c = -4$ in the thermodynamic limit. Thus, we can derive Eq. (1.1) for the ferromagnetic spinor condensate by comparing the gap and the reduced control parameter in Eq. (1.24). This comparison gives $z\nu \sim 1/2$. (i) The region where $q/c_1 > 4$ holds is the longitudinal polar phase, since all atoms in the ground state occupy the hyperfine level $|m_0\rangle$. (ii) The region where $q/c_1 < 4$ and $q/c_1 > -4$ is where the ground state breaks axial symmetry and is partial magnetized. This phase is called broken-axisymmetry (BA) phase. (iii) The region where $q/c_1 < -4$ holds is the transverse polar phase, since no atoms in this phase occupy the hyperfine level $|m_0\rangle$. If the magnetization is zero, the ground state reads $|\rho_{-1} = 0.5, \rho_0 = 0, \rho_1 = 0.5\rangle$.

When magnetization is turned on, the longitudinal polar phase disappears, while the

other quantum critical point survives to favor transverse polar phase over BA phase as the magnetization increases. A cross section at $m = 0.8$ is taken from Fig. 1.2 and the particle density at the hyperfine level $|m_0\rangle$ is plotted in Fig. 1.4a. The nonanalyticity of Fig. 2.1a at $q_c = 4$ smooths out. Correspondingly the energy at q_c gaps out in Fig. 1.4b. The quantum critical point at $q_c = -4$ in Fig. 2.1a survives but shifts. We apply finite-size analysis and find,

$$\begin{aligned} \Delta &= 4.368 N^{-0.3302}, \\ q_c &= 8.054 N^{-0.6436} - 3.2. \end{aligned} \tag{1.25}$$

The exponents are found to be the same with Eq. (1.24), giving $z\nu \sim 1/2$ as expected, because the critical exponents are universal. We also find the location of the critical point in the thermodynamic limit at $m = 0.8$ magnetization density as $q_c = 3.2$.

Finally, we turn our focus to antiferromagnetic condensates, $c_1 > 0$. When $q = m = 0$, one can write the ground state in closed form [61],

$$|\psi(q=0)\rangle = \sum_{k=0}^{N/2} A_k \, |\rho_{-1} = k/N, \rho_0 = (N-2k)/N, \rho_1 = k/N\rangle \,, \tag{1.26}$$

where the coefficients A_k are uniformly distributed across different k values [61]. Such a ground state is special and this is reflected in the phase diagram plotted in Fig. 2.1b in the next Chapter. When the net magnetization is zero, the antiferromagnetic spinor condensate hosts a first-order quantum phase transition, e.g., sudden change in the order parameter. This is not a symmetry-breaking phase transition, as the quantum phases that are connected via the first-order phase transition are longitudinal and transverse polar phases. However one can still perform finite-size scaling analysis in the vicinity of the transition. We find, $\Delta = 5.672 N^{-1}$ and $q_c = 3.311 N^{-2}$ for the energy gap and the quantum critical point, respectively. Hence, we can conclude that the gap vanishes faster compared to the ferromagnetic

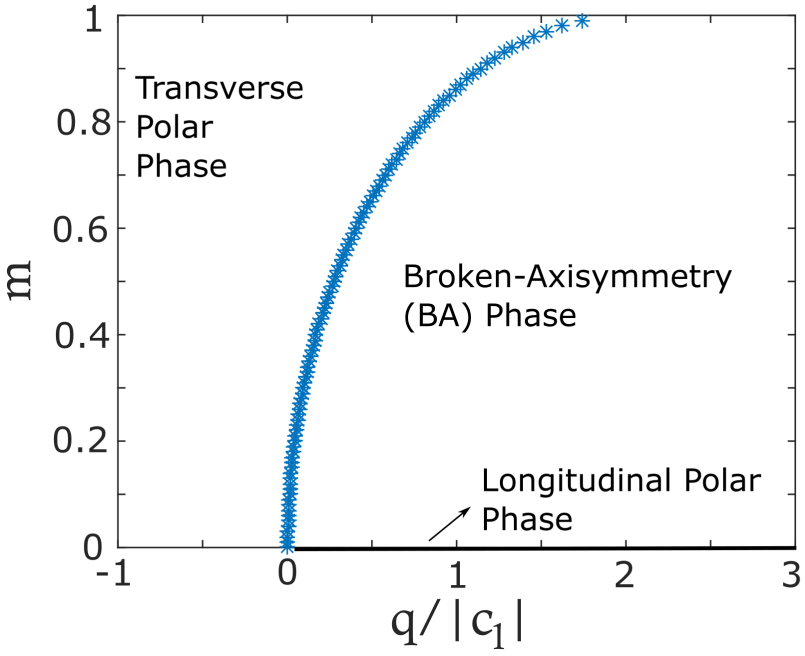

Figure 1.5: Full phase diagram of spin−1 antiferromagnetic condensate with respect to q, the Zeeman parameter, and m, the magnetization density, computed via exact diagonalization of 10^4 atoms. The quantum phases are marked on the figure.

condensate and the quantum critical point is indeed at $q_c = 0$ in the thermodynamic limit.

Introducing nonzero magnetization transforms the first-order quantum phase transition into a continuous quantum phase transition. Fig. 1.5 shows the full phase diagram for antiferromagnetic interaction where a BA phase appears with nonzero magnetization density. Perfoming finite-size scaling analysis to a cross section at $m = 0.8$ in this figure indeed reveals a second-order quantum phase transition,

$$\begin{aligned} \Delta &= 2.931N^{-0.3357}, \quad R^2 = 1, \\ q_c &= 3.752N^{-0.66} + 0.8, \quad R^2 = 1. \end{aligned} \tag{1.27}$$

The exponents are the same with that of ferromagnetic spinor condensate, leading to a $z\nu \sim 1/2$ critical exponent.

In conclusion, I demonstrated the QPTs in spin−1 spinor Bose-Einstein condensates with

different types of interactions in this subsection. In Chapter 2 we will study the quench dynamics of spinor condensates where I will establish how quench dynamics can capture the equilibrium QPTs. Later in Chapter 6, I will present how transient probes of spinor condensates could be useful to probe QPTs.

Bose-Hubbard Model

Due to light-matter interaction, the atoms in a dilute gas can experience an energy shift in the presence of an electric field, which is given as a potential [21]

$$V = -\frac{1}{2}\alpha'(\omega)\left\langle \mathcal{E}(\mathbf{r},t)^2 \right\rangle_t , \tag{1.28}$$

where $\alpha'(\omega)$ is the real part of the dynamical polarizability of the atom, ω is the laser frequency and $\mathcal{E}$ is the electric field of the laser. Dynamical polarizability of the atom depends on the detuning, Rabi frequency and the lifetime of the excited state [21]. The coupling between atoms and the coherent light, Eq. (1.28), is the heart of the optical lattice generation. If the electric field $\mathcal{E}$ has a spatial periodicity, by interfering two counter-propagating waves and time-averaging for longer times than the period of the light waves, one could produce an *optical lattice potential*. Assuming that two counter-propagating have the same frequency and linear polarization in $z-$direction, the electric field reads

$$\mathcal{E}_z = \mathcal{E}_0\cos(kx-\omega t) + \mathcal{E}_0\cos(-kx-\omega t) = 2\mathcal{E}_0\cos(kx)\cos(\omega t). \tag{1.29}$$

To substitute in Eq. (1.28), we calculate

$$\left\langle \mathcal{E}(\mathbf{r},t)^2 \right\rangle_t = 4\mathcal{E}_0^2\cos^2(kx)\int_0^{\pi/q} dt\cos^2(\omega t) = 2\mathcal{E}_0^2\cos^2(kx) = \mathcal{E}_0^2(\cos(2kx)+1). \tag{1.30}$$

Therefore, by also taking into the account $k = 2\pi/\lambda$, the spatial dependence of the potential reads

$$V(x) = V_0 \cos(2kx) = V_0 \cos\left(\frac{4\pi x}{\lambda}\right) = V_0 \cos\left(\frac{2\pi x}{d}\right), \tag{1.31}$$

where $d = \lambda/2$ is the optical lattice spacing. V_0, which is the lattice depth, depends on the intensity of the light and the real part of the atomic polarizability. The generalization to higher dimensions follows similarly, by superposing multiple sets of counter-propagating light waves depending on the lattice geometry that is desired [21, 27]. The physics of optical lattices follow closely that of solid state crystals, albeit the characteristic parameters are different due to the huge difference between interatomic distance between crystal atoms ($\sim 10^{-8}$ cm) and typical laser wavelengths (~ 600 nm). Therefore, the band theory of solid state systems and Bloch theorem apply [15].

In Chapter 3, we are going to propose an optical lattice for a spin model on a ladder geometry, which is a quasi-1D model. For this geometry, similar to a 2D square lattice, we will need two sets of counter-propagating waves. Let us also note that, in experimental setups, one could use a mirror to reflect back the light wave onto itself [62].

Upon generation of an optical lattice loaded with a dilute gas of bosonic atoms, one could write the Hamiltonian in the second quantized form,

$$\begin{aligned} H &= \int d^3x \psi^\dagger(\boldsymbol{x}) \left(-\frac{\hbar^2}{2m}\nabla^2 + V(\boldsymbol{x}) + V_T(\boldsymbol{x})\right) \psi(\boldsymbol{x}) \\ &+ \frac{1}{2}\frac{4\pi a_s \hbar^2}{m} \int d^3x \psi^\dagger(\boldsymbol{x})\psi^\dagger(\boldsymbol{x})\psi(\boldsymbol{x})\psi(\boldsymbol{x}), \end{aligned} \tag{1.32}$$

where $\psi(\boldsymbol{x})$ is the bosonic field operator, as introduced in the previous section for spinor BEC, but with no spin degree of freedom. $V(\boldsymbol{x})$ is the optical lattice potential, $V_T(\boldsymbol{x})$ is the external trap potential and the final term in Eq. (1.32) is the interaction term. A usual assumption is that the energy scale of the system is much smaller compared to the gap from

the first to the second band, and hence one can expand the field operators in the Wannier basis of the first band, $\psi(\boldsymbol{x}) = \sum_i b_i w(\boldsymbol{x} - \boldsymbol{x}_i)$. This expansion introduces the tight-binding model of an atomic dilute gas loaded into an optical lattice, which is the Bose-Hubbard model (BHM) [63, 64]

$$H = -J \sum_{i,j} b_i^\dagger b_j + \sum_i \epsilon_i n_i + \frac{1}{2} U \sum_i n_i(n_i - 1). \tag{1.33}$$

Here the algebra is $[b_i, b_j^\dagger] = \delta_{ij}$ and $n_i = b_i^\dagger b_i$ is the number operator at site i. The parameters J, ϵ_i and U can be derived in terms of the Wannier functions:

$$U = \frac{4\pi a_s \hbar^2}{m} \int d^3x |w(\boldsymbol{x})|^4, \tag{1.34}$$

$$J = \int d^3x w^*(\boldsymbol{x} - \boldsymbol{x}_i) \left(-\frac{\hbar^2}{2m} \nabla^2 + V(\boldsymbol{x}) \right) w(\boldsymbol{x} - \boldsymbol{x}_j), \tag{1.35}$$

$$\epsilon_i = \int d^3x V_T(\boldsymbol{x}) |w(\boldsymbol{x})|^2 \sim V_T(\boldsymbol{x}_i). \tag{1.36}$$

These are the onsite repulsion, the hopping strength between sites i and j, and the energy offset of site i, respectively. Wannier functions can be calculated with band theory [15]. Let us also briefly note the characteristic energy scales of the model when it is realized in an optical lattice. The recoil energy of an atom with mass m is its kinetic energy in the wake of absorbing a photon after being initially at rest, $E_R = \hbar^2 k^2 / 2m$. Stating the lattice depth V_0 in terms of the recoil energy E_R helps us observe whether the atoms tunnel freely $E_R > V_0$ or their tunneling is suppressed $E_R < V_0$. This inequality can be exactly determined if we estimate the extent of the ground state wave function of atoms localized near the potential minima by utilizing the harmonic approximation [21]. For a 1D optical lattice, the frequency of small oscillations in the vicinity of a potential minimum is $\hbar\omega_{\text{osc}} = 2\sqrt{E_R V_0}$ and the size of the ground state wave function is $a_{\text{osc}} = (\hbar / m\omega_{\text{osc}})^{1/2}$ [21]. By comparing these two equations

and using the recoil energy,

$$\frac{a_{\text{osc}}^2}{d^2} = \frac{1}{\pi^2}\left(\frac{E_R}{V_0}\right)^{1/2}. \tag{1.37}$$

Therefore, by tuning the laser frequency and intensity, we can change the tunneling amplitude of the atoms in the optical lattice. This observation can also be verified by examining Eq. (1.35). In a similar vein, we can determine how the laser frequency and intensity affect the interaction strength U, which turns out to be $U = 2\hbar\omega_{\text{osc}}a_s/(a_{\text{osc}}\sqrt{2\pi})$ [64]. As a result, optical lattices provide a very controlled environment to simulate strongly correlated physics [24, 26, 27, 64].

Finally let us very briefly mention the quantum phase transition hosted in the Bose-Hubbard model [63]. The BHM has two quantum phases: when $J > U$ the ground state is a superfluid (SF) and when $J < U$ it is a Mott insulator (MI). In the SF phase, each atom is delocalized over the lattice and the phase is gapless; while the MI phase is gapped and the ground state is a product of local Fock states with a fixed number of atoms at each site. The latter can be understood in the context of repulsive interactions. The SF-MI transition has been realized in cold atoms in Ref. [62].

In this dissertation, we utilize the hard-core boson limit of the BHM where the interaction strength is effectively infinite $U \to \infty$ and the number of bosons at each site is either $|0\rangle$ or $|1\rangle$ in Fock basis due to the noninteger filling factor f [27]. Then the BHM in hard core boson limit is exactly mapped to the $XX-$chain [65],

$$H = -t\sum_i \left(\sigma_i^x\sigma_{i+1}^x + \sigma_i^y\sigma_{i+1}^y\right) + h\sum_i \sigma_i^z. \tag{1.38}$$

The details of the mapping are given in Chapter 3 where we also extend the mapping to quasi-1D systems.

1.2 Nonequilibrium Quantum Physics

Quantum many-body dynamics is one of the most active fields of physics with vast amounts of research over the decades thanks to experimental progress in quantum simulators [66]. Since my aim in this Chapter is to prepare the reader for the rest of the dissertation, I will be focusing on select topics of quantum many-body physics out-of-equilibrium, such as equilibration, thermalization, light cone bounds, information scrambling and dynamical phase transitions. More details on the research topics of this field can be found in excellent reviews written over the years [32, 34, 35, 66, 67].

We exclusively use sudden quenches in this dissertation as a way of driving quantum many-body systems out-of-equilibrium. Sudden quench is also a limiting case of a ramp. Given that the ramp parameter is $q(t)$, a ramp reads

$$q(t) = q_0 - vt = q_0 - \frac{t}{\tau_Q}, \tag{1.39}$$

where v and τ_Q both are the ramp speed parameters in different units, either the reciprocal time (v) or time (τ_Q). The parameter q_0 is the initial q from where the ramp starts. When we ramp with $\tau_Q \to \infty$, e.g., a very slow ramp, the dynamics approach to its adiabatic limit and the ground state changes adiabatically by following the change in the control parameter $q(t)$. In the opposite limit where we perform a very fast ramp with $\tau_Q \to 0$, the ramp approaches to a sudden quench where the many-body system is excited to higher energies.

Ramps are particularly important in dynamical detection of phase transitions and mapping the phase diagrams of quantum phases in the laboratory [68–71]. As we change the control parameter q, the Hamiltonian and its eigenstates change. As long as the order parameter has time to follow the external change in the Hamiltonian, the process remains adiabatic. Since the relaxation time diverges in the vicinity of the phase transition, the dynamical evolution freezes and the system cannot equilibrate at the critical point. After the change in control and order parameters becomes comparable again, the adiabatic dynamics

resume. This mechanism is called the Kibble-Zurek mechanism (KZM) when the transition is from/to a gapped phase [70,71], which determines the scaling of freeze-out time $\bar{t}$ and the control parameter $\bar{q}$ in terms of the quench speed parameter τ_Q in the vicinity of the critical point,

$$\bar{t} \sim \tau_Q^{z\nu/(1+z\nu)}, \quad \bar{q} \sim \tau_Q^{-1/(1+z\nu)}. \tag{1.40}$$

KZM critical exponents of spin-1 spinor condensates were recently measured in the laboratory [72].

Although the most usual ramps are linear ramps [68,69], one can also engineer ramps of more complicated functional forms to achieve adiabaticity most optimally, e.g., shortcuts to adiabaticity [73]. In all these cases, one assumes that the initial state is the ground state of a Hamiltonian with an initial control parameter q_0 and that the aim is not to excite the system to its higher energy states. In the limit of sudden quenches, although one can still choose a ground state of an initial Hamiltonian as the initial state (which we will choose to do so in Chapters 6 and 7), we can set the initial state arbitrarily. Given an arbitary initial state $|\psi(0)\rangle$ and an evolution Hamiltonian H_f with eigenbasis $[E_\alpha, |\phi_\alpha\rangle]$, the initial state in the basis of the evolution Hamiltonian is $|\psi(0)\rangle = \sum_\alpha c_\alpha |\phi_\alpha\rangle$. A system that goes under a sudden quench from $|\psi(0)\rangle$ is then the time evolution of $|\psi(0)\rangle$: $e^{-iHt/\hbar}|\psi(0)\rangle$. When a measurement is performed where O is an observable, we calculate $\langle O(t)\rangle$,

$$\langle O(t)\rangle = \sum_{\alpha\beta} c_\alpha^* c_\beta \exp\left[-i(E_\alpha - E_\beta)t\right] O_{\alpha\beta}. \tag{1.41}$$

When the initial state is not a pure state, one can calculate $\langle O(t)\rangle = \mathrm{tr}(e^{iHt/\hbar} O e^{-iHt/\hbar}\rho_0)$ with the density matrix of the initial state ρ_0, c.f. Chapters 3 and 5.

There are a few different nonequilibrium responses that $\langle O(t)\rangle$ can exhibit. It can equilibrate or show quantum oscillations; if equilibration occurs, it might thermalize; depending on the locality of the Hamiltonian and the size of the system, it might demonstrate quantum

revivals. We will touch upon these processes in a quantum many-body system in the next subsections.

1.2.1 Equilibration, Thermalization and Absence Thereof

Dynamic processes in a quantum system could be very illuminating about the underlying system and the physics in play. The equilibration of quantum systems is the first example of those that we will be focusing on in this dissertation. Although the concept of equilibration is very prevalent in our everyday life in the macroscopic world, the question of how it could possibly happen in isolated quantum systems governed by the Schrödinger equation, and hence unitary time evolution attracted its first attention as early as 1929 from von Neumann [74]. Based on the principles of thermodynamics and statistical mechanics, the equilibration accompanies an increase in entropy over time, and hence the equilibrium state is the maximum entropy state [75]. However, the microscopic quantum dynamics of time-independent Hamiltonians are time-reversal invariant, and the (entanglement) entropy of pure states remains constant all times. How irreversible macroscopic dynamics could originate from reversible microscopic dynamics with an associated time-independent Hamiltonian in an isolated system on the other hand, was discussed in the context of classical statistical mechanics well before the formulation of quantum mechanics [76–81]. The analog of von-Neumann entropy of quantum mechanics is the Gibbs-Shannon entropy in isolated classical systems, and the reversible phase space trajectory of classical microscopic dynamics is replaced by the unitary evolution of wave functions in Hilbert space [82,83]. According to the early discussions in the literature [83–85], what is unique about equilibration in isolated quantum systems is (i) the quantum coherence which originates from the superposition of states and (ii) the observation that the canonical state of a subsystem in an isolated system will not be altered for different system states as the system size approaches to infinity. In the following discussion, I will detail the argument (i) as a part of the explanation for the equilibration of an isolated quantum system. Later I will briefly review the argument (ii) in

the context of subsystem equilibration and thermalization.

The notion of equilibration is defined as 'the dynamical process where a time-dependent observable evolves to some equilibrium value and remains close to this value for most times during the evolution' [67]. Note that this definition is free from an arrow of time that naturally emerges in macroscopic irreversible processes. This is reasonable, because quantum mechanics by itself does not prefer a direction for time [82]. If equilibration happens, long-time average of $\langle O(t)\rangle$ has to be equal to the value of the long-time equilibrium state. We can estimate this value straightforwardly by examining Eq. (1.41): When $t \to \infty$, there is a unique energy condition that will give a nonzero value $\langle O(t \to \infty)\rangle \neq 0$, and that is $E_\alpha = E_\beta$. If the energy spectrum is nondegenerate, the energy condition implies $\alpha = \beta$ and this leads to

$$\langle O(t \to \infty)\rangle = \sum_\alpha |c_\alpha|^2 O_{\alpha\alpha}. \tag{1.42}$$

This value is the prediction of an ensemble that describes the long-time equilibrium state of a quantum system and the ensemble is called the *diagonal ensemble* (DE) [40, 86–88]. Therefore, equilibration means $\overline{\langle O(t)\rangle}_{t\to\infty} = \langle O(t \to \infty)\rangle$, where the $\bar{\langle\cdot\rangle}_{t\to\infty}$ is the long-time average. One can notice that if a quantum system equilibrates, this implies a form of phase decoherence in Eq. (1.41). In other words, the terms in Eq. (1.41) destructively interfere in the long-time dynamics, resulting in an equilibrated (or a dephased) state.

More insights regarding the equilibration, including that of subsystems and in finite times, were reached with the rigorous proofs and results of Refs. [36, 84, 89–92]. An overview of these results and proofs can be found in Ref. [67]. Here I will quote one theorem from Ref. [36], which unified those of Refs. [90] and [91].

Definition 1 (Non-degenerate energy gaps [36, 67]). If the Hamiltonian has non-degenerate energy gaps, then any four energy eigenvalues E_k, E_l, E_m and E_n with an energy

condition of $E_k - E_l = E_m - E_n$ has to satisfy

$$(E_k = E_l \wedge E_m = E_n) \vee (E_k = E_m \wedge E_l = E_n)\,, \tag{1.43}$$

where $\wedge$ and $\vee$ stand for 'and' and 'or' logical operations. One observes that we can still treat a Hamiltonian with symmetry sectors, e.g., degenerate energy levels, while ensuring that the Definition 1 is satisfied. The cases that are eliminated by Definition 1 are when there are physically noninteracting (or uncoupled) subsystems in a model, e.g., $H = H_A \otimes \mathcal{I}_B + \mathcal{I}_A \otimes H_B$ where subsystems A and B can be for example spins in a spin chain. All systems studied in this dissertation are of interacting types, hence Definition 1 is automatically satisfied in the rest of the dissertation.

Theorem 1 (Equilibration) [36]. Given that the time evolved state is $\rho(t)$ (generalization of the pure state $|\psi(t)\rangle$ to its density operator) and its time-averaged state is $\omega \equiv \overline{\rho(t)}|_t$ over time t, if Definition 1 holds, the following quantity should be bounded for any operator O

$$\sigma_O^2 \equiv \overline{|\mathrm{tr}(O\rho(t)) - \mathrm{tr}(O\omega)|^2}|_t \leq \frac{\|O\|^2}{d_{\mathrm{eff}}}, \tag{1.44}$$

where $\|O\|$ is the operator norm, e.g., the largest singular value of O and d_{eff} is the effective dimension of the initial state

$$d_{\mathrm{eff}} \equiv \left(\sum_\alpha \mathrm{tr}(|\phi_\alpha\rangle \langle\phi_\alpha| \, \rho(t=0))^2 \right)^{-1} = \left(\sum_\alpha |c_\alpha|^4 \right)^{-1}, \tag{1.45}$$

where $|\phi_\alpha\rangle \langle\phi_\alpha|$ is the projector onto the eigenspace with energy E_α and the second term is valid when the state is pure, i.e., $\rho(0) = |\psi(0)\rangle \langle\psi(0)|$.

Theorem 1 quantifies the notion of equilibration: If the value of the time evolving observable is close enough to the value of the time average of this observable, equilibration occurs. How much close is determined by the effective dimension of the initial state d_{eff},

which was first defined in this context [36]. It is a measure of the population density of the energy levels excited by the initial state. When it is small $\mathcal{O}(d_{\text{eff}}) \sim 1$, the nonequilibrium response is composed of a few eigenstates and hence oscillatory, whereas in the case that it is large $\mathcal{O}(d_{\text{eff}}) \sim d$ where d is the dimension of the Hilbert space, a macroscopic number of energy eigenstates contribute to the dynamics, initiating equilibration. In Chapter 2, we will utilize this insight which also does not require infinitely long time evolution, and calculate d_{eff} for spinor condensates for two distinct nonequilibrium responses. The value and the system size scaling of effective dimension will help us to argue when we observe equilibration and when not in spinor condensates. Later in Chapter 3, we will again utilize the effective dimension of the initial state to demonstrate that realistic initial states prepared for experimentation scales the same with the infinite-temperature states in the system size for a system in quantum ergodic regime.

Let us also finally note that the rigorous proofs and results in the literature [67] reveal about the subsystem equilibration in quantum systems where we observe that a smaller subsystem of a large enough quantum system is not sensitive to the nature of the wave functions of the entire system [84]. In other words, the wave function could be any pure or mixed state, and yet the state of the subsystem will be always very close to a canonical state, i.e., an equiprobable mixed state. Such an irrelevance of the entire system's wave function to the state of a subsystem is a truly quantum phenomenon with no classical analogue [83]. Let us also note that Theorem 1 can be used to prove equilibration bounds for subsystems too [36, 91]. Finally, it is well-known that the entanglement entropy of the subsystems, regardless of their size, will increase in time [93, 94] and the trend of this increase is an important signature of quantum ergodicity and lack thereof. In this sense, the equilibration of subsystems in quantum systems is similar to classical systems, because (i) one could obtain a subsystem with a state drawn from the canonical ensemble, and (ii) the entropy of the subsystem increases in time up until a finite value for bounded Hilbert spaces, thus reminding of the second law of thermodynamics.

When equilibration does not occur, we observe quantum oscillations. Depending on their origins, such oscillations could tell us about the underlying system, i.e., spin mixing oscillations in spinor condensates [60,95–98] and domain-wall binding in long-range transverse-field Ising models Eq. (1.2) [99] or its ergodicity breaking mechanisms if the system is ergodic in the first place, i.e., quantum scars [100–102]. Quantum oscillations could also be the signature of a dynamical phase where the time-translational symmetry is spontaneously broken, resulting in the so-called time crystals [103–106]. In Chapter 6 we will show how transient properties of an oscillatory spinor condensate dynamics could be useful for probing the underlying quantum phase transitions.

Equilibration in quantum systems does not necessarily imply thermalization. For thermalization to occur, typically the long-time equilibrium value has to be predicted by a statistical ensemble and a few parameters, i.e., temperature, particle number [19]. In other words, the equilibrium value must be also the thermal value [40].

Here we focus on the Eigenstate Thermalization Hypothesis (ETH) as a route to thermalization in quantum many-body systems. However alternative approaches to thermalization exist and these can be found in the review articles [67]. The thermalization of an entire system must be described by the microcanonical ensemble fixing the energy of the system with a sufficiently narrow energy window on the energy spectrum [40, 107]. For subsystem thermalization, the long-time equilibrium value should be predicted by the canonical ensemble with an associated temperature that is determined by the rest of the system, because the rest of the system acts like a bath for the smaller subsystem [107]. Ref. [67] provides a straightforward guideline for subsystem thermalization which includes the following steps: (i) equilibration, (ii) subsystem and bath initial state independence, (iii) diagonal form of the subsystem equilibrium state and (iv) recovering a Boltzmann or Gibbs state for the subsystem, i.e., canonical or grand canonical ensembles. Let us note that if an extensive number of conservation laws exist in the system, the system becomes quantum integrable [33] and usually integrable systems do not thermalize to a thermal state, instead they equilibrate

to a generalized Gibbs state where additional conservation laws appear in the generalized Gibbs ensemble with Langrange multipliers [108, 109]. However, there exist integrable systems that do thermalize to thermal equilibrium values in the literature [110, 111]. Chapter 2 in the dissertation gives an example of such integrable models and numerically proves the thermalization by invoking ETH.

Conjecture 1 (ETH) [40]. The eigenstate expectation values (EEVs) $O_{\alpha\alpha}$ of a large interacting many-body system is equal to the microcanonical thermal average of O at the mean energy E_m where a narrow energy window is defined around E_m as $E_\alpha \in [E_m - \delta, E_m + \delta]$ and $\delta \ll E_m$. Here the microcanonical state could be constructed from the energy eigenstates in the narrow energy window,

$$\rho_{mc} = \frac{1}{N_{\text{int}}} \sum_{\alpha}{}' |\phi_\alpha\rangle \langle\phi_\alpha| , \tag{1.46}$$

where N_{int} is the number of states in the energy window and the notation $\sum'_\alpha$ means that we sum over the states in the energy window only. The essence of this conjecture is that one eigenstate alone, i.e., any state $|\phi_\alpha\rangle$ in the energy window, can encode the equilibrium properties of the Hamiltonian, and the states $|\phi_\alpha\rangle$ are called *thermal eigenstates*. A more precise definition for ETH can be also given:

Definition 2 (ETH, strong form) [40, 67, 107]. ETH holds if for an arbitrary initial state $|\psi(0)\rangle$, (i) the EEV $O_{\alpha\alpha}$ changes sufficiently smoothly with the energy eigenvalues E_α and (ii) the off-diagonal elements of the observable $N_{\alpha\beta}$ where $\alpha \neq \beta$ are negligibly small compared to the diagonal elements $N_{\alpha\alpha}$, assuming nondegenerate energy spectrum.

As also shown in Refs. [40, 112], a precise definition of 'sufficiently smooth' can be given and this will be presented and discussed in Chapter 2. The second condition is similar in spirit with the condition (iii) cited above for subsystem thermalization, requiring a diagonal form in the observable in the equilibrium thermal state. What makes the Definition 2 the strong form of ETH is the independence of the definition from the initial state choice [113]. This

means that for the strong form of the ETH to hold, all energy eigenstates should be thermal. Later, the weak form of the ETH is introduced to explain thermalization in the presence of *rare fluctuations* or *rare nonthermal states* [114]. In Chapter 2, it is going to be shown that the spinor condensates have such rare nonthermal states in their energy spectrum for some parameters and that the fraction of the rare states in the spectrum vanishes in system size. Based on the works in the literature [114] and our results in Chapter 2, we restate the definition of the weak ETH as,

Definition 3 (ETH, weak form). The weak form of the ETH holds, if (i) for typical eigenstates in the energy spectrum, the EEV $O_{\alpha\alpha}$ changes sufficiently smoothly with the energy eigenvalues E_α; (ii) the fraction of the rare nonthermal eigenstates vanishes in system size, meaning that there could be nonthermal states existing but they are a vanishingly small part of the spectrum, and hence they are rare, and it requires fine-tuning to probe them in the thermodynamic limit.

Based on Definition 3, we observe that a finite-size system that satisfies the weak form of ETH, but not the strong form of the ETH, cannot be thermalized by all possible initial states. Due to the presence of rare nonthermal states in the spectrum, one can design a state, either realistically or not, to probe the rare region in the energy spectrum and the resulting dynamics cannot thermalize, and even maybe cannot equilibrate.

1.2.2 Quantum Revivals, Light Cone Bounds and Information Scrambling

Finite-size quantum many-body systems typically reveal their system size in their nonequilibrium response. After enough time, the time-evolving state of a finite-size system may go back to the initial state, which is called *a quantum revival* and this nonequilibrium response is predicted by *quantum recurrence theorem* [37]. Such finite-size effects are important to detect, as often times, especially in solid-state physics, one strives to understand the physics independent of the system size, i.e., by applying finite-size scaling analysis. However, the

physics of finite-size effects are as interesting as lack thereof.

The reason why finite-size systems exhibit finite-size effects is because of the propagation of excitations across the system. When we suddenly quench a system with an *initial state in nonequilibrium*, we pump energy into the system and excitations to higher energy levels are created. Any observable that exhibits quantum revivals probe the propagation of these excitations to the edges of the system and their reflection back to the location of the observation. We will see many examples of quantum revivals in this dissertation, i.e., in Chapter 2 we will observe them in spinor condensates. Although the spinor condensates are effectively all-to-all coupled systems, we will show that the timescale of quantum revivals diverge with increasing system size, confirming that they are indeed quantum revivals, probing an *effective* system size. Later in Chapter 6, we will return back to quantum revivals in the context of a locally interacting spin chain, short-range (non)integrable TFIM. We will see that one can utilize the time range before finite-size effects kick in to predict the dynamic behavior in the thermodynamic limit. In this sense, we will focus on many different occasions of finite-size effects to demonstrate that it might be really helpful to recognize them with concrete examples, such as (i) to argue for an equilibration interval [67] (Chapter 2), (ii) to numerically estimate the coherence times of edge spins [115] in infinite time (Chapter 5), (iii) to determine a universal temporal regime in a nonequilibrium response (Chapter 6), (iv) to estimate when cluster theorem [116] breaks down in a finite-size system (Chapter 7).

Arguably, one of the most intuitive dynamical behaviors emerging in locally connected quantum many-body systems is the light cone bounds of information spread [44]. The Lieb-Robinson bound is the natural result of the geometry and limited connectivity of the underlying lattice, i.e., lattice with only nearest-neighbor couplings. It is a remarkable extension of finite velocity of light as the upmost velocity bound in relativistic quantum mechanics [48, 117] to nonrelativistic quantum mechanics where there is an emergent light cone speed that cannot be exceeded by the excitations of the system, solely due to the nature of the interactions in the Hamiltonian.

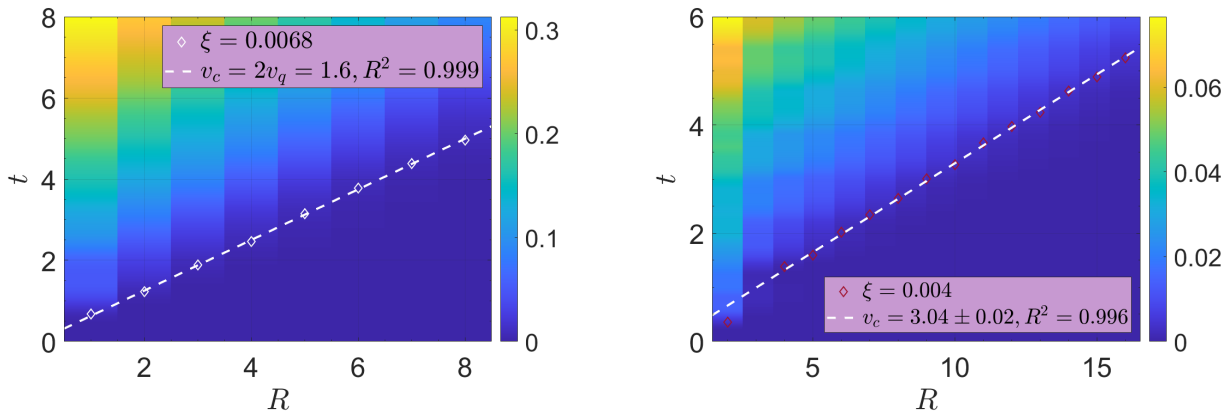

Figure 1.6: Light cones of (a) integrable and (b) nonintegrable TFIM at a system size of $N = 36$ emerging from the fluctuations of the equal-time two-point correlators (coded in colors) that are computed via t-DMRG. (a) The integrable TFIM calculated at transverse field $h/J = 0.4$ exhibits a linear light cone with numerically extracted correlation speed of $1.6J$. (b) The nonintegrable TFIM with interaction strength $\Delta/J = -1$ calculated at transverse field $h/J = 0.75$ exhibits a linear light cone with numerically extracted correlation speed of $3.04J$. In a light cone figure, $x-$ and $y-$axes stand for the spatial distance R and time t, respectively. The circles are the data points corresponding to the contour threshold ξ and the fitted dashed lines are the best fits to the data. R^2 in the legend is the correlation coefficient of the fit; v corresponds to the extracted light cone velocity at its associated threshold value ξ.

Theorem 2 (Lieb-Robinson bound) [44, 67]. Given a Hamiltonian with finite range interaction and strictly local observables W and V, there exists a finite group velocity v called the Lieb-Robinson (or light cone) speed and the following bound holds,

$$\|[W(t), V]\| \leq A \|W\| \|V\| \exp(-(x - v|t|)), \tag{1.47}$$

where x is the distance between the support of the observables and A is a positive constant.

The essence of Theorem 2 is that (i) the operator spread, e.g., spread of correlations across spacetime $W(t) = e^{-iHt/\hbar} W e^{iHt/\hbar}$, has a finite speed for a Hamiltonian with finite range interactions, meaning that there is a well-defined *information light cone* that partitions the spacetime of excitations into regions: timelike, lightlike and spacelike [59]. (ii) The probability of excitations following a spacelike trajectory is exponentially suppressed, i.e., correlation functions cannot grow significantly outside of the light cone. Light cone bounds of systems with different statistics and interaction types and ranges have been studied extensively in the literature with analytical and numerical methods [118–125], and in a laboratory [126, 127].

Figs. 1.6 give examples of linear light cones in the spacetime of the short-range TFIM where left and right panels are for the integrable and nonintegrable cases, respectively. Integrability is broken by introducing next nearest neighbor couplings, c.f. Eq. (5.15) for the Hamiltonian. These figures depict the fluctuations of equal-time two-point correlators [121, 126, 128, 129], $\left\langle \delta\sigma_z^r(t) \delta\sigma_z^{r'}(t) \right\rangle$ where $\delta\sigma_z^r(t) = \sigma_z^r(t) - \langle \sigma_z^r(t) \rangle$ for pairs of $(r', r \neq r')$ running from $t = 0$ to some time t that reveals the functional form of the light cone. Then, we determine the contours of very small amplitude ξ, that sets the onset of fluctuation growth $\left\langle \delta\sigma_z^r(t) \delta\sigma_z^{r'}(t) \right\rangle > 0$ for $t > 0$. Numerically one can study a set of light cones with different ξ. To eliminate this arbitrariness we choose ξ with the best goodness of fit, R^2 value. In Chapter 3, we will show that other types of correlators, i.e., out-of-time-order correlators (OTOC) that will be explained below, could exhibit light cone bounds in disordered spin

systems [130–132].

Information scrambling is a dynamical process that is complementary to the processes that we have discussed so far. It quantifies the operator spread, and probes the timescales of local operators being nonlocal [133–136]. Its associated timescale, that is the scrambling time, is when an initially local operator becomes the most nonlocal given the bounds on the Hilbert space dimension. This timescale is typically different than the thermalization timescale of the system [137, 138]. In other words, scrambling is the process where initially local correlations become lost to local probes in yet reversible and unitary quantum evolution. A natural probe for information scrambling (operator spread) is some form of the commutator between $W(t)$ and V, as appeared in Lieb-Robinson bound Eq. (1.47), Theorem 2 above. Observing only the commutator, i.e., $\mathrm{tr}(e^{-\beta H}[W(t), V])$, at an inverse temperature β turns out to be featureless [139]. The next possibility is to look at the second moment of the commutator, that is the commutator square,

$$C_\beta(t) = -\frac{1}{Z}\mathrm{tr}(e^{-\beta H}\left|[W(t), V]\right|^2), \tag{1.48}$$

where Z is the partition function. This quantity is called out-of-time-order commutator [140–144]. Let us note that the norm in Eq. (1.48) is Frobenius norm. For unitary and hermitian operators one can cast the out-of-time-order commutator to out-of-time-order correlator (OTOC) [145],

$$F_{W,V}(t) = \mathrm{tr}\left(e^{-\beta H}W(t)VW(t)V\right). \tag{1.49}$$

There are multiple proposals for scrambling detection in different media [146–155] and measurements in laboratory [156–161]. In Chapter 3, we will focus on a proposal of scrambling detection on cold atoms.

OTOCs have been found to be useful not only in the detection of quantum chaos [132, 140, 142–144, 150, 162–166], but also lack thereof [131, 139, 158, 162, 167–169], i.e., many-

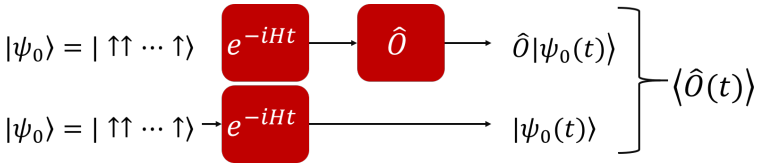

Figure 1.7: Measurement schematic of dynamical phase transitions type-I. $|\psi_0\rangle$ is the initial state and $\hat{O}$ is an order parameter observable.

body localization (MBL) [43, 170–177]. MBL is an extension of single-particle Anderson localization [178] in disordered medium to systems with interactions [170]. A many-body localized system cannot thermalize via ETH, exhibits logarithmic spreading of entanglement as opposed to linear spreading of entanglement in ergodic phase [93], has eigenstates with area-law entanglement, does not show nonzero DC conductivity and could retain some memory of local initial conditions [43]. Again in Chapter 3, we will study the ergodic and MBL regimes of a disordered quasi-1D locally connected spin system from the perspectives of energy level statistics and information scrambling. Furthermore, OTOCs exhibit not only light cone dynamics, but also butterfly cones which are the wavefronts associated with the scrambling time [130–132]. This observation will be explained in detail in Chapter 3, as well.

Information scrambling and OTOCs have also shown to be more broadly useful than just being a probe for quantum chaos and MBL, [179–182]. In particular, a new branch of research emerged in the field of information scrambling that focuses on the detection of equilibrium and dynamical phase transitions through OTOCs Refs. [160, 161, 181, 183–191] including Chapter 4. This line of works brings together the research on information scrambling and quantum chaos with the research on dynamical phase transitions where the latter will be detailed in the next subsection. Chapters 4 and 5 will focus on explaining why a connection exists between quantum phase transitions and OTOCs, and how OTOCs at infinite-temperature could probe topological phase transitions associated with Majorana edge modes, respectively.

1.2.3 Dynamical Phase Transitions

Criticality, defined under the Landau paradigm [192], is one of the milestones in our understanding of matter, providing us with a framework to classify microscopically diverse phenomena into a handful of universality classes with their associated critical exponents [45,193]. Thanks to recent impressive progress in the control and precision achieved in quantum synthetic matter [94,126,156,194–197], not only have concepts from equilibrium quantum physics been extended to the out-of-equilibrium realm such as with dynamical phase transitions (DPTs) [198–202] and dynamical scaling laws [200,203–207] where Chapter 6 is an example, but there have also been concerted efforts to probe equilibrium quantum critical points and universal scaling laws through quench dynamics [181,203,205,208–212] including Chapters 2 and 6 in this dissertation, or with infinite-temperature initial states [186, 187, 213]. Such techniques obviate the need for undertaking the usually difficult task of cooling the system into its ground state over a range of its microscopic parameters in order to construct its equilibrium phase diagram.

Two different but related types of DPTs have been defined in the literature [199,214–217]. A type-I DPT arises when the quench dynamics undergoes a nonanalytic change with respect to a system parameter in a quenched Hamiltonian [199, 214–217]. Whereas, a type-II DPT appears when one global order parameter under the quench Hamiltonian has a nonanalytic singularity in its time evolution, i.e., the Loschmidt echo [199,201,202,206,214,216,217]. In this dissertation, we will exclusively focus on the former definition, when it is applicable.

A measurement schematic of DPT-I can be seen in Fig. 1.7. Typically the initial state is chosen as a product state, because product states are easier to prepare in a laboratory, and the observable is set as the order parameter of the quantum phase, i.e., $O = M = \sum_i \sigma_i^z$ total longitudinal magnetization for TFIM. After a transient temporal regime, time evolving order parameter equilibrates and the steady state values across the transition point become a probe of the equilibrium phase transition [35]. In Chapters 6 and 7, we will extend this idea to single-site observables in chains with different boundary conditions, as

single-site observables are experimentally achievable with modern quantum simulators [195]. Particularly in Chapter 6, we will show that the transient temporal regimes could be useful to extract quantum critical points by exhibiting a dynamical crossover, eliminating the need to reach long time steady-state regimes. In Chapter 7 we will focus on quasi-stationary temporal regimes to detect quantum critical points in an open chain. In both Chapters, we will pay special attention to dynamical scaling laws in the vicinity of the crossover or transition, and extract the exponents of these scaling laws. Remarkably, these dynamical scaling law exponents will significantly differ from the analytical predictions that are valid in equilibrium at infinite-time limit. The mechanism that leads to such truly nonequilibrium critical exponents is the critical slowing down and the divergence of the relaxation time in the vicinity of the transition or crossover.

1.3 A Brief Outline of the Dissertation

Having discussed the preliminaries of the dissertation in detail and drawn an outline in the previous Sections, here let us briefly summarize the rest of the Chapters, which appeared elsewhere either as a publication or a preprint.

Chapter 2, published in Ref. [218], studies the nonequilibrium responses of spin-1 spinor Bose-Einstein condensates in the wake of a sudden quench, finds that spinor condensates can thermalize via ETH, although they are integrable systems and can equilibrate while showing no sign of quantum revival, although the system has finite degrees of freedom. This chapter also proposes that quench dynamics could probe the underlying QPT in spinor condensates for both ferromagnetic and antiferromagnetic interactions.

Chapter 3, published in Ref. [219], proposes a detection mechanism for information scrambling in cold atom quantum simulators and studies the scrambling properties of this exper-

imentally feasible model in different dynamic regimes, e.g., ergodic and MBL in disordered potentials. It finds that the ladder$-XX$ model in its ergodic regime exhibits power-law decay in OTOC and logarithmic decay in the MBL regime. The light cone extracted from OTOC exhibits sublinear propagation of excitations.

Chapter 4, published in Ref. [220], puts forward an analytical framework to calculate the infinite-time steady-state value of OTOCs, finds conditions on the initial state and the observable based on the analytical expression that are required to probe QPT via OTOCs and applies the method to a critical spin chain, the $XXZ-$chain. This method renders the connection between QPTs and information scrambling universal.

Chapter 5, published in Ref. [187], generalizes the method devised in the previous Chapter to infinite-temperature OTOCs, explains why OTOCs of edge observables are susceptible to topological phase transitions associated with Z_2 topological order and Majorana edge modes. When integrability is broken, full scrambling is prevented and a new timescale in the scrambling dynamics emerges with a long-lived plateau called the *prescrambling plateau*.

Chapter 6, published in Refs. [221] and [222], utilizes the transient temporal regimes to probe QPT and find dynamical scaling laws in the vicinity of the transition or crossover. The first Section, Ref. [221], presents experimental data on the spinor condensates where the amplitude and the timescale of the first dip in the oscillatory behavior acts like an order parameter across a first-order QPT. The second Section, Ref. [222], studies the decay rates of the transient temporal regime and proposes a dynamical order parameterlike quantity to reveal a dynamical crossover in the short-range TFIM with single-site observables.

Chapter 7, in peer-review [223], proposes utilizing single-site observables close to the edge in an open-boundary chain to initiate a quasi-stationary regime, probe quantum critical

points and extract an associated dynamical critical exponent in the vicinity of the transition. Remarkably, the critical exponent is robust to changes in the initial state, observable location and weak integrability breaking, resulting in a notion of universality in the vicinity of the transition.

Although not directly related to my dissertation, multiple other publications emerged from other collaborations during my PhD in the fields of quantum thermodynamics [224–226], quantum computing with microwave photons [227] and Quantum Hall Effect [228].

Chapter 2

Equilibration and Thermalization in the Integrable Models

Thermalization of isolated quantum systems is a long-standing fundamental problem where different mechanisms are proposed over time. We contribute to this discussion by classifying the diverse quench dynamical behaviours of spin-1 Bose-Einstein condensates, which includes well-defined quantum collapse and revivals, thermalization, and certain special cases. These special cases are either nonthermal equilibration with no revival but a collapse even though the system has finite degrees of freedom or no equilibration with no collapse and revival. Given that some integrable systems are already shown to demonstrate the weak form of eigenstate thermalization hypothesis (ETH), we determine the regions where ETH holds and fails in this integrable isolated quantum system. The reason behind both thermalizing and nonthermalizing behaviours in the same model under different initial conditions is linked to the discussion of 'rare' nonthermal states existing in the spectrum. We also propose a method to predict the collapse and revival time scales and find how they scale with the number of particles in the condensate. We use a sudden quench to drive the system to non-equilibrium and hence the theoretical predictions given in this chapter can be probed in experiments on spinor Bose-Einstein condensates.

2.1 Introduction

Understanding if and how isolated quantum systems driven out-of-equilibrium thermalize has practical implications as well as being interesting from a fundamental point of view. Being able to explain the thermalizing dynamics in an isolated quantum system is the key to have thermal quantum baths with finite size [229, 230]. Thermalization of quantum systems also sheds light on how Statistical Mechanics emerge from unitary dynamics of quantum mechanics [196, 231]. At the opposite side, nonthermalizing quantum systems might be useful to store quantum information in the protected degrees of freedom [43, 232].

Study of thermalization of isolated quantum systems has a long history that starts with the development of quantum mechanics itself [74] and can be understood in the context of Eigenstate Thermalization Hypothesis (ETH) for isolated systems [38–40, 66, 107]. In this search to understand quantum thermalization, analogue concepts which are important in the thermalization of classical systems have been drawn such as the integrability of the system [108, 233]. In this chapter, we study dynamics of the spin-1 spinor Bose-Einstein condensate (BEC) system under single-mode approximation (SMA), which is known to be a quantum-integrable model [234] based on its mean-field calculations [97, 235]. The consensus is that quantum-integrable systems do not thermalize according to statistical ensembles, but they obey the predictions of generalized Gibbs ensemble which takes into account the conservation laws in the system Hamiltonian [108] in the aim of maximizing the entropy of the system under study [236]. However, it has also been shown that the non-integrability does not always point to thermalization [208, 237–239] and some integrable systems, e.g., Lieb-Liniger model and integrable spin chains, do show thermalization in the form of weak ETH [110, 111, 114]. In fact, it seems that what differentiates a quantum integrable system from a non-integrable one in the context of thermalization is not that the system can thermalize or not, but instead having 'rare' nonthermal eigenstates in the spectrum that do not disappear in the thermodynamic limit [114]. Our results on spinor condensate model support this idea of quantum thermalization for a specific region of Hamiltonian parameters, where we observe

a spectrum composed of mostly 'typical' thermal states with some 'rare' nonthermal ones. The exact diagonalization of spin-1 condensate under the SMA for realistic condensate sizes provides us the opportunity to dig into the whole spectrum of eigenstates and determine the regions where ETH is applicable based on the condition in Ref. [40]. Then we show that these regions in the spectrum are composed of 'typical' thermal eigenstates that lead to vanishing fluctuations and shrinking support in the thermodynamic limit [110, 114]. We apply some other ETH indicators, as well, such as the scaling of eigenstate expectation value differences [113, 173] and the scaling of the maximum divergence from the microcanonical ensemble average [239] with the system size. The scaling exponents match with each other and all of them point to the observation that in the thermodynamic limit spinor condensates thermalize for certain initial conditions (but not for all initial conditions), implying the weak form of ETH. Given the fact that ultracold atoms provide a highly controllable and a sufficiently isolated system [66], we show that a spin-1 spinor condensate under the SMA could be a testbench to observe the predictions of ETH for certain sudden quench parameters and the transition between thermalization and nonthermalization without a need to add a non-integrable perturbation to an integrable Hamiltonian [238,240,241]. In fact, being able to see this transition without breaking the integrability of the model hints at that thermalization is not directly tied to non-integrability [238]. Instead, it might be more relevant to consider the localization properties of the spectrum to observe thermalizing behaviour in isolated quantum systems [173, 241]. Therefore, by invoking the analogy between our model and the single quantum-particle hopping model and hence calculating the participation ratios [242] that is a widely-used tool for Anderson models [178], we show that the most localized eigenstates in the spectrum (excluding the edges of the spectrum) are also the 'rare' nonthermal eigenstates that cause nonthermalization behaviour in the system.

Quantum collapse and revivals are well-known phenomena observed in different systems spanning from light-matter interactions in Jaynes-Cummings model [243] to Bose-Hubbard models in optical lattices [208, 244] and the matter wave field of a BEC [194]. This kind of

behaviour is also expected in discrete and finite systems due to the recurrence theorem [37]. The possibility that spin-1 BEC under the SMA might also demonstrate collapse and revivals has been suggested in Ref. [61, 245] and a detailed analysis of collapses with specific initial Fock states in this model has been given [246]. These full-quantum model studies did not take the Zeeman effects into account, partly because the model without Zeeman effects has rotational symmetry and is analytically solvable via the introduction of angular momentum-like operators in the Fock basis [61]. On the other hand, the experiments of the spinor BECs make use of the quadratic Zeeman effect as a control parameter to sweep across the well-established phase transitions [60, 247, 248] that spinor BECs have in their mean-field representation [249]. With the introduction of quadratic Zeeman effect, at the mean-field level the physics is mapped to an analytical pendulum-like model [97]. Some of the mean-field predictions have been experimentally verified [250]. However, the mean-field model cannot capture the quantum collapse and revivals of the full-quantum Hamiltonian. In the second part of our chapter, we calculate the time scales for quantum collapse and revivals in the spin-1 condensate model in the parameter region where they exist and show that under realistic conditions and condensate sizes the system equilibrates around its thermal value, validating the ETH for our model. Finally, we discuss some particular parameter regions where we observe only equilibration but not thermalization without quantum revivals in any time-scale of the evolution. This is somewhat unexpected given the fact that our model is a discrete system with finite degrees of freedom and the initial information tends to recur in long-time scale for finite-size systems.

2.2 Classification of Dynamical Behaviours under Sudden Quench of Spin-1 Spinor Condensate

The interaction Hamiltonian for a spin-1 BEC in the second-quantization picture takes the form [60]

$$\hat{H}_{\rm int} = \frac{1}{2}\int d\mathbf{r}\left(c_0' : \hat{n}^2(\mathbf{r}) : + c_1' : \hat{F}^2(\mathbf{r}) :\right), \tag{2.1}$$

where :: denotes the normal ordering. The coefficients in the interaction Hamiltonian depend on the scattering length and the atom mass through

$$\begin{aligned} c_0' &= \frac{4\pi\hbar^2}{M}\frac{a_0 + 2a_2}{3}, \\ c_1' &= \frac{4\pi\hbar^2}{M}\frac{a_2 - a_0}{3}, \end{aligned} \tag{2.2}$$

where a_0 and a_2 are the scattering lengths [21] corresponding to a total spin 0 and a total spin 2 of the colliding atoms. The operators in the interaction Hamiltonian are defined by

$$\begin{aligned} \hat{n}(\mathbf{r}) &= \sum_{m,n=-1}^{1} \hat{\psi}_m^\dagger(\mathbf{r}) I_{mn} \hat{\psi}_n(\mathbf{r}), \\ \hat{F}_\nu(\mathbf{r}) &= \sum_{m,n=-1}^{1} \hat{\psi}_m^\dagger(\mathbf{r}) (F_\nu)_{mn} \hat{\psi}_n(\mathbf{r}), \end{aligned} \tag{2.3}$$

where $\hat{\psi}_{m_F}$ $\left(\hat{\psi}_{m_F}^\dagger\right)$ is the Bose field operator for the Zeeman state m_F. I_{mn} and $(F_\nu)_{mn}$ are the identity and spin-1 matrices, respectively and $\nu = x, y, z$ in the angular momentum operator $\hat{F}_\nu$. Also note that $\hat{F}^2(\mathbf{r}) = \hat{F}_x^2(\mathbf{r}) + \hat{F}_y^2(\mathbf{r}) + \hat{F}_z^2(\mathbf{r})$ in Eq. (2.1) and the identity matrix I_{mn} results in the density operator $\hat{n}(\mathbf{r})$ for the condensate. A detailed derivation of these equations are given in the Introduction Chapter.

For sodium or rubidium alkali atoms, we have $|c_0'| \gg |c_1'|$, so the symmetric part of the interaction Hamiltonian dominates over the non-symmetric part. This observation leads to the so-called single mode approximation (SMA), where we assume that the condensate

wave functions for each spin component $\phi_{m=-1,0,1}(\mathbf{r})$ are described by the same spatial wave function $\phi(\mathbf{r})$ as in $\hat{\psi}_m \sim \hat{a}_m\phi(\mathbf{r}),\ \ m = 0, \pm 1$ [60, 61, 249, 251]. Then the spatial wave function $\phi(\mathbf{r})$ satisfies the Gross-Pitaevskii equation which gives the spatial profile of our spin-1 Bose-Einstein condensate. With the normalization condition $\int d\mathbf{r}|\phi(\mathbf{r})|^2 = 1$, the interaction Hamiltonian reduces to rotationally invariant $H_{\text{int}} = c_1\hat{L}^2/2N$, where $\hat{L}$ is the spin-1 angular momentum operator, $c_1 = c_1' N \int d\mathbf{r}|\phi(\mathbf{r})|^4$ and N is the total atom number, which has well-known analytical solutions [61]. In the experiment, an additional magnetic Zeeman field is added to the system, which results in a competition between different terms in the Hamiltonian and drives phase transitions [248]. The linear Zeeman term proportional to $\hat{L}_z = \hat{n}_1 - \hat{n}_{-1}$ commutes with the other terms in the Hamiltonian, and its effect is to conserve the magnetization. It has no influence on spin dynamics and therefore can be dropped [248]. Adding the quadratic Zeeman term, the Hamiltonian reduces to

$$\begin{aligned} H_{\text{int}} &= c_1\frac{\hat{L}^2}{N} - q\hat{a}_0^\dagger\hat{a}_0 = \frac{c_1}{N}(\hat{a}_1^\dagger\hat{a}_1^\dagger\hat{a}_1\hat{a}_1 + \hat{a}_{-1}^\dagger\hat{a}_{-1}^\dagger\hat{a}_{-1}\hat{a}_{-1} - 2\hat{a}_1^\dagger\hat{a}_{-1}^\dagger\hat{a}_1\hat{a}_{-1} \\ &+ 2\hat{a}_1^\dagger\hat{a}_0^\dagger\hat{a}_0\hat{a}_1 + 2\hat{a}_{-1}^\dagger\hat{a}_0^\dagger\hat{a}_0\hat{a}_{-1} + 2\hat{a}_0^\dagger\hat{a}_0^\dagger\hat{a}_1\hat{a}_{-1} + 2\hat{a}_1^\dagger\hat{a}_{-1}^\dagger\hat{a}_0\hat{a}_0) - q\hat{a}_0^\dagger\hat{a}_0. \end{aligned} \tag{2.4}$$

Spin-1 BEC Hamiltonian with the quadratic Zeeman term gives rise to different phases observed at the ground state due to the competition between quadratic Zeeman effect and spin-mixing interaction [250]. An adiabatic passage from one phase to another can create highly entangled states from product states as proposed in Ref. [248] and quite recently implemented in Ref. [252]. Fig. 2.1 shows the ground state quantum phase transitions by observing the order parameter $\langle N_0\rangle$, the number of particles in Zeeman sublevel $|m = 0\rangle$, by varying the quadratic Zeeman coefficient q. In the rest of the chapter, we study the dynamics of the system under a sudden quench, i.e., we start from the ground state of the initial Hamiltonian H_i, which is H_{int} (Eq. (2.4)) with an initial quadratic Zeeman term q_i, and abruptly quench the Zeeman field to a final value q_f with the final Hamiltonian denoted as H_f. The dynamics and thermalization behaviour of the system are then investigated.

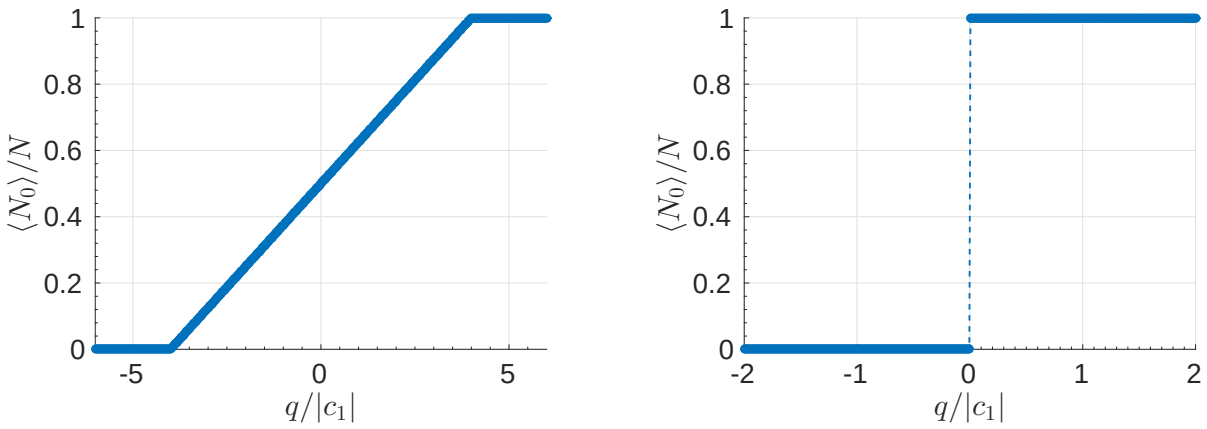

Figure 2.1: The ground state phase transitions for (a) ferromagnetic and (b) antiferromagnetic interactions for $N = 10^4$ particles in the condensate and zero total magnetization.

Both the sudden quench and the measurement of $\langle N_0\rangle$, which is used as the main observable in our study, can be readily performed in experiment [72, 250, 253, 254].

We now show how a dynamical phase transition (DPT) might be arising for spinor condensates via the sudden quench based on an alternative definition of DPTs that takes the time-average of dynamical response as the order parameter [197, 217]. In our study, we start with the ground state, $|\psi(0)\rangle$ of the initial Hamiltonian H_i with $q = q_i$. After a sudden quench of the Zeeman coefficient q to the value q_f, the initial state can be expressed as

$$|\psi(0)\rangle = \sum_{\alpha} c_\alpha |\psi_\alpha\rangle , \tag{2.5}$$

where $|\psi_\alpha\rangle$ are the eigenstates of the final Hamiltonian H_f. The number of atoms in the Zeeman sublevel $|m = 0\rangle$ can be written as

$$\begin{aligned} \langle N_0(t)\rangle &= \langle\psi(t)| N_0 |\psi(t)\rangle , \\ &= \sum_{\alpha,\beta} c^*_\alpha c_\beta e^{-i(E_\alpha - E_\beta)t} N_{0,\alpha\beta}, \end{aligned} \tag{2.6}$$

where $N_{0,\alpha\beta} = \langle\psi_\alpha| N_0 |\psi_\beta\rangle$ and E_α are the energy of the eigenstates $|\psi_\alpha\rangle$ under the final

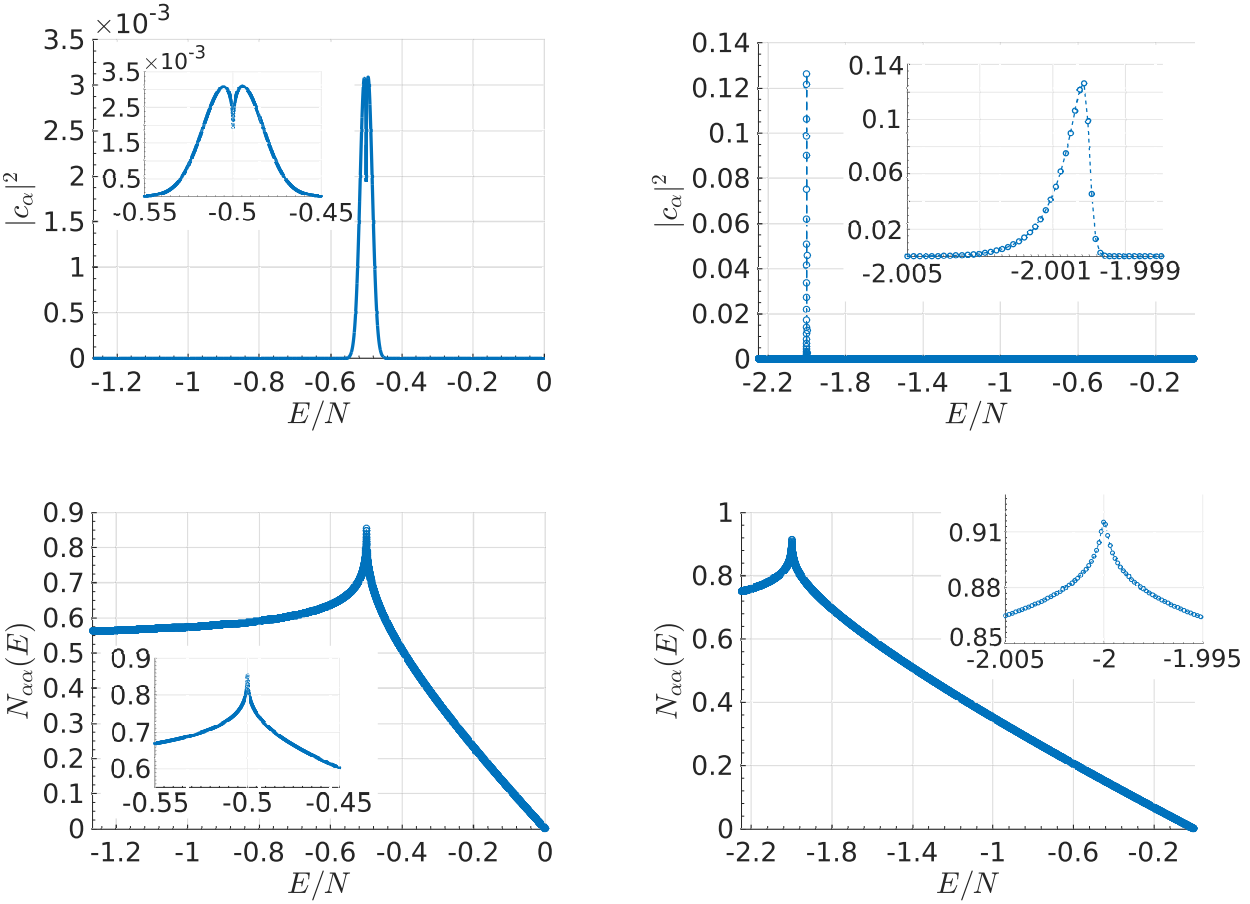

Figure 2.2: Eigenstate occupation numbers (EONs) $|c_\alpha|^2$ for a ferromagnetic quench at (a) $q_i = -3$ to $q_f = 0.5$ and (b) $q_i = 4.1$ to $q_f = 2$ (focused on non-zero sections of the eigenspectrum in the insets) and their corresponding eigenstate expectation values (EEVs) (focused on the nonlinear kink region in the insets) $N_{\alpha\alpha}$ at (c) and (d), respectively for a particle number of 10^4 with respect to the energy density E/N.

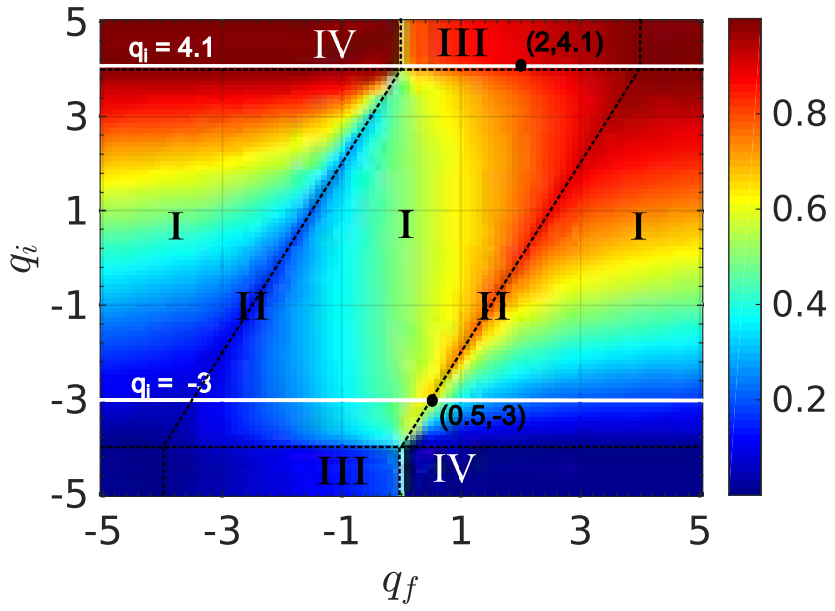

Figure 2.3: The sudden quench map for the ferromagnetic case with q_f and q_i on the x and y axes, respectively for 5×10^3 particles. Color labels $\overline{\langle N_0(t)\rangle}$ in the long time limit.

Hamiltonian H_f. The long-time average of $\langle N_0(t)\rangle$ then should follow the diagonal ensemble prediction [40, 66, 87],

$$\overline{\langle N_0(t)\rangle}_{t\to\infty} = \sum_\alpha |c_\alpha|^2 N_{0,\alpha\alpha}, \tag{2.7}$$

if the equilibration happens or when the phase coherence diminishes. In order to visualize this quantity, in Figs. 2.2a and 2.2b we plot the eigenstate occupation numbers (EONs) $|c_\alpha|^2$ for certain sudden quench parameters (seen in the caption). EONs represent windows in the eigenspectrum where we are allowed to peak into when we make a measurement. Figs. 2.2c and 2.2d are plots of the corresponding eigenstate expectation values (EEVs) $N_{0,\alpha\alpha}$. What we expect to see in the long-time average of a sudden quench experiment is the summation of EEVs weighted with EONs as shown by Eq. (2.7).

Each point on sudden quench maps (Figs. 2.3 and 2.4) corresponds to the prediction of diagonal ensemble (equilibration value if it happens, or the time-average of the dynamic response of the system) when a sudden quench is applied to the ground state from an initial Hamiltonian with q_i to a final Hamiltonian with q_f. Note that there are different regions

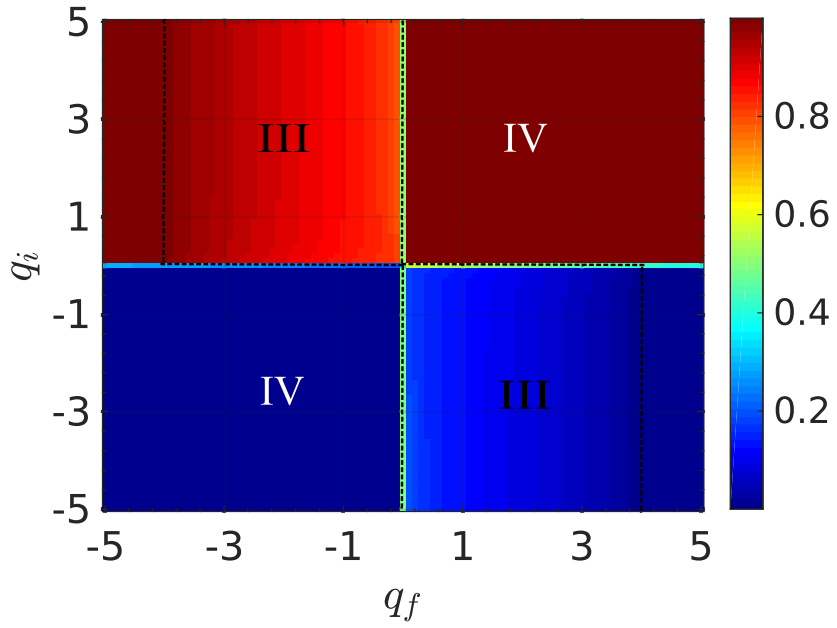

Figure 2.4: The sudden quench map for the anti-ferromagnetic case with q_f and q_i on the x and y axes, respectively for 5×10^3 particles. Color labels $\overline{\langle N_0(t)\rangle}$ in the long time limit.

Region	Boundaries
I	$\lvert q_i\rvert < 4$, all q_f except traces
II	$\lvert q_i\rvert < 4$, traces of q_f
III	$q_i > 4$ & $0 < q_f < 4$ or $q_i < -4$ & $-4 < q_f < 0$
IV	the rest of the map

Table 2.1: The regions of the sudden quench map for the ferromagnetic case.

on both maps and the ferromagnetic sudden quench map is more diverse than the anti-ferromagnetic one when the ground state is chosen as the initial state of the non-equilibrium process. Due to the symmetry embedded in the Hamiltonian for both interactions, one can obtain point symmetric version of Fig. 2.3 (reflection with respect to the origin of the plot) with anti-ferromagnetic interaction when the initial state is set as the most-excited state of the Hamiltonian.

These maps capture the ground state phase transition points of both FM ($q = \pm 4$) and AFM ($q = 0$) cases. In Fig. 2.4, the upper half ($q_i > 0$) of the map plane reveals two different regions with transition points at $q_f = -4$ and $q_f = 0$. Similarly for the lower half ($q_i < 0$), we observe two regions with the transition points at $q_f = 0$ and $q_f = 4$. In Fig. 2.3, for $|q_i| > 4$

Region	Dynamic Behaviour
I	ETH valid, well-defined collapse and revivals
II	nonthermal equilibration, collapse, no revival
III	no equilibration, no collapse or revival
IV	no non-equilibrium evolution

Table 2.2: The dynamic behaviors corresponding to the regions of the sudden quench map for the ferromagnetic case.

we see a similar behaviour to Fig. 2.4 with transition points either at $q_f = 0$ and $q_f = 4$ (for $q_i > 4$) or at $q_f = -4$ and $q_f = 0$ (for $q_i < -4$). In between $|q_i| < 4$, the two transition points gradually shift as q_i increases. In later sections, we are going to show that the sudden quench maps also show us when we do and do not expect a thermal behaviour in our system, similar to the non-equilibrium phase diagram given for Bose-Hubbard model in Ref. [208]. Additionally it will provide us a way to predict types of the dynamical behaviour in different time scales. To give an idea of the regions on the maps, we summarized them in Tables 2.1 and 2.2. Although the non-equilibrium behaviour of these regions will be explained in detail in the rest of the section, we shortly list them here. Region I is where the system equilibrates around its thermal prediction after a collapse with a well-defined time-scale. It is also a region where we observe clear quantum revivals due to finite-size effects. Region II demonstrates nonthermal equilibration after a collapse, but no clear collective-revival is observed for these points on the map. We do not see equilibration, collapse or revival for the region III, instead we observe an oscillatory behaviour around the system's PDE value due to the interference of a small number of modes of the system. Finally in region IV, the initial state turns out to be already in equilibrium with the quench Hamiltonian, giving us practically a constant behaviour for all times.

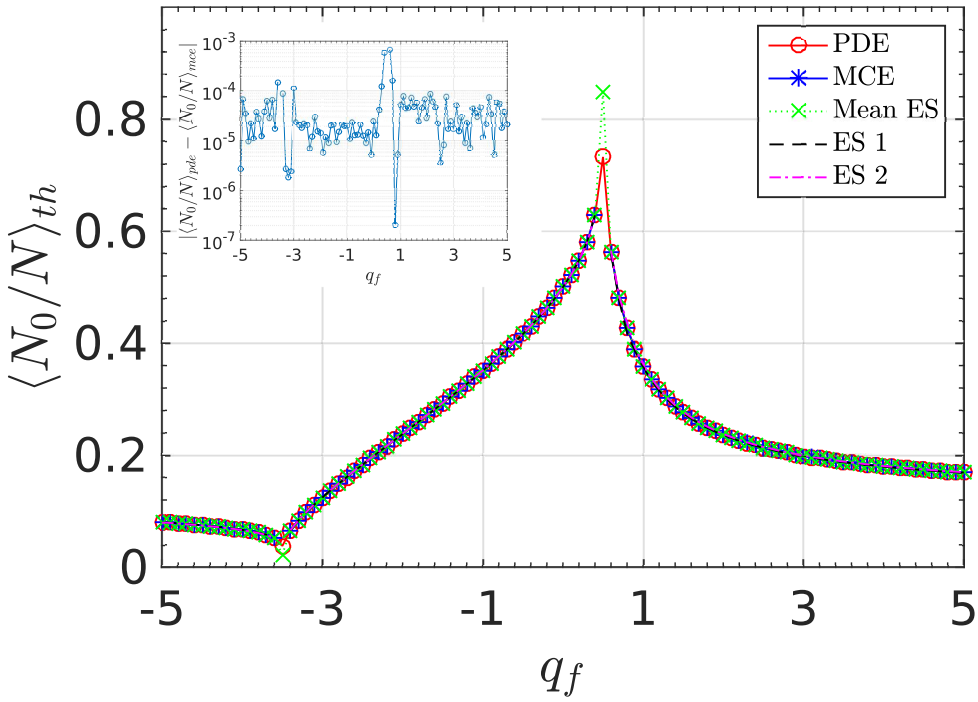

Figure 2.5: The comparison of mean values predicted by diagonal ensemble (PDE), microcanonical ensemble (MCE), the eigenstate corresponding to the mean energy of the system (Mean ES) and arbitrary eigenstates in the microcanonical energy window (ES 1 and ES 2), when the sudden quench is applied from $q_i = -3$ to different q_f values on the x-axis for ferromagnetic case. Each data point is obtained with a simulation of 10^4 particles. The inset shows the difference between the diagonal and the microcanonical ensemble predictions when it is possible to define a valid energy interval for the microcanonical ensemble.

2.3 Eigenstate Thermalization Hypothesis in Spin-1 BEC

When a system that is driven out-of-equilibrium equilibrates around a thermal value predicted by a statistical ensemble, the process is called thermalization. For isolated interacting bodies, microcanonical ensemble describes the equilibrium predictions. In this context, ETH is a possible pathway to thermalization and explains the match between the equilibration value predicted by the diagonal ensemble after a quench (Eq. (2.7)) and the microcanonical thermal value [40].

The microcanonical ensemble is a statistical ensemble with a sufficiently narrow energy

interval that describes the equilibrium properties of an isolated system [255]. In order to check the prediction of the microcanonical ensemble, we seek to define a narrow energy window around the mean energy of the eigenspectrum. Refs. [40, 87, 112] emphasize the approximate linearity of the EEVs in the microcanonical energy window in order to define a finite and narrow energy window which will also ensure the validity of ETH. Based on this idea, they state the following condition (which has been derived for the eigenstate thermalization to happen by Ref. [256])

$$(\delta E)^2 \left| \langle N_0 \rangle'' (E) / \langle N_0 \rangle (E) \right| \ll 1, \tag{2.8}$$

where δE is the energy window, $\langle N_0 \rangle (E)$ is the EEV behaviour of the system $N_{0,\alpha\alpha}$ as a function of the energy and $'$ denotes the differentiation with respect to energy. Another possibility implemented in Ref. [40] is to define the window based on a sensitivity analysis where the size of the energy window chosen does not affect the thermal prediction of the microcanonical ensemble (see Appendix A.1 for a demonstration of this method for our model). We generate the finite and narrow microcanonical energy windows for our model with a combination of these two ways. Figs. 2.5 and 2.6 show the regions where the thermal prediction of diagonal ensemble (PDE) matches the prediction of microcanonical ensemble (MCE), mean energy eigenstate (Mean ES) and two arbitrary eigenstates (ES 1 and ES 2) in the microcanonical energy window when it is possible to define one for a sudden quench from $q_i = -3$ and $q_i = 4.1$ to various q_f spanning from -5 to 5, respectively. It is important to note that the match happens only when the EON window coincides with the approximately linear or constant parts of the EEV plot. See Fig. 2.2 for the cases where the match does not happen, so that the system fails to thermalize. Hence, we conclude that the relaxation in the matching cases represents thermalization via ETH, when we disregard the finite-size effects, e.g., a quantum revival, which will be discussed in the next section.

In order to strengthen the argument that we see a nonthermal behaviour only when EON

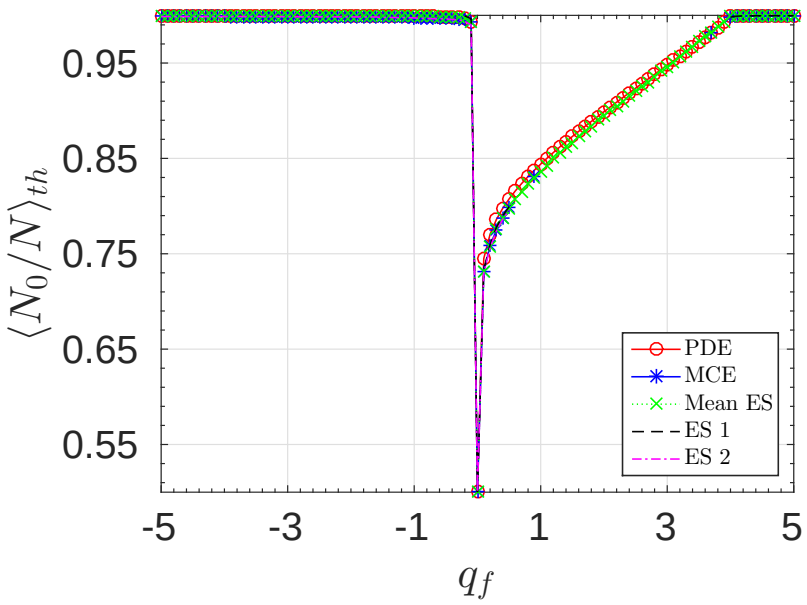

Figure 2.6: The comparison of mean values predicted by diagonal ensemble (PDE), microcanonical ensemble (MCE), the eigenstate corresponding to the mean energy of the system (Mean ES) and arbitrary eigenstates in the microcanonical energy window (ES 1 and ES 2), when the sudden quench is applied from $q_i = 4.1$ to different q_f values on the x-axis for ferromagnetic case. Each data point is obtained with a simulation of 10^4 particles.

captures the non-linear 'kink' behaviour in the EEV spectrum, we look at a couple of ETH indicators. These indicators are also used to determine the form of ETH observed in the system, e.g., weak or strong, if there is thermalization and they require an energy interval over the spectrum. It is possible to define a microcanonical ensemble energy window at the linear region of the spectrum with the methods mentioned above, while such a window is not well-defined for the kink region. Since we want to compare two cases, we define a fixed energy interval around the center of the spectrum. The first ETH indicator that we applied is the system size scaling of average EEV differences [113,173]. An EEV difference is defined as

$$r_n = |\langle\psi_{n+1}| N_0 |\psi_{n+1}\rangle - \langle\psi_n| N_0 |\psi_n\rangle|, \tag{2.9}$$

for random eigenstate $|\psi_n\rangle$ chosen in the energy interval and its adjacent state $|\psi_{n+1}\rangle$. Regardless of the interval size, when the interval encompasses the linear region as for $q_f = 3$

in Fig. 2.7, we obtain the N^{-1} scaling with $R^2 = 1$. Therefore the average of differences between EEVs vanish in the thermodynamic limit $N \to \infty$. Other indicators are: the ETH noise or fluctuations [110, 114]

$$\sigma_{N_0} = \left(\frac{\sum_{\psi_n \in \delta E} \left[\langle \psi_n | N_0 | \psi_n \rangle - \langle N_0 \rangle_{mc,\delta E} \right]^2}{N_{\text{int}}} \right)^{1/2}, \tag{2.10}$$

where the N_{int} is the number of eigenstates in the chosen interval, $\langle N_0 \rangle_{mc,\delta E}$ is the microcanonical prediction defined in the energy interval of δE and $|\psi_n\rangle \in \delta E$ are the eigenstates in the energy interval; the support of the eigenstate distribution in the energy interval [110,114],

$$s_{N_0} = \max_{\psi_n \in \delta E} \langle \psi_n | N_0 | \psi_n \rangle - \min_{\psi_n \in \delta E} \langle \psi_n | N_0 | \psi_n \rangle , \tag{2.11}$$

and the maximum divergence from the microcanonical ensemble prediction [239],

$$r_{\max} = \max_n | \langle \psi_n | N_0 | \psi_n \rangle - \langle N_0 \rangle_{\text{mc},\delta E} |, \tag{2.12}$$

in Fig. 2.7 across the energy interval chosen. We obtain N^{-1} scaling with $R^2 = 1$ for all these ETH indicators for the aforementioned case. The extracted scaling exponent of the support Eq. (2.11) clearly indicates in the thermodynamic limit all of the eigenstates in the energy interval contribute the same amount to the expectation value. Furthermore the rest of the ETH indicators, Eqs. (2.10) and (2.12), reveals that all of the EEVs in the energy interval converge to the microcanonical energy prediction $\langle N_0 \rangle_{\text{mc},\delta E}$ as $N \to \infty$. Also note that N^{-1} scaling is not surprising, since the dimension of the Hilbert space is in the order of N for our model.

The observation that all of the ETH indicators vanish in the thermodynamic limit for the linear regions of the spectrum implies that ETH holds, even in the strong sense because of the shrinking support [114]. However this is not the case when the energy interval contains

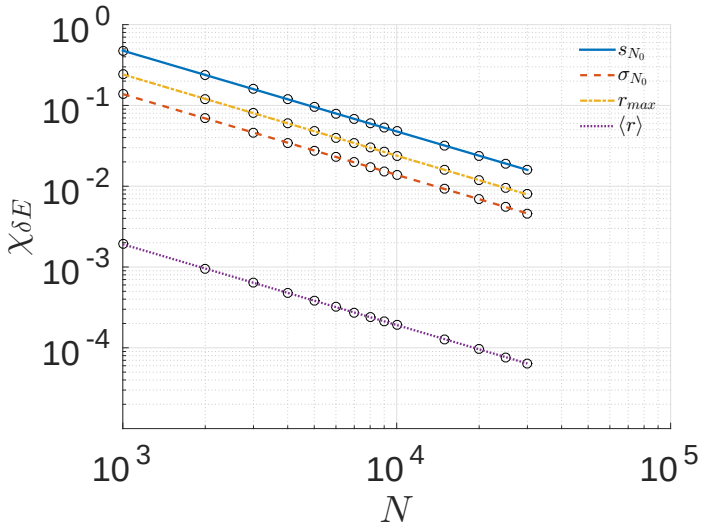

Figure 2.7: The system size scaling of the support $\chi_{\delta E} = s_{N_0}$ (solid-blue), the fluctuations (or the ETH noise) $\chi_{\delta E} = \sigma_{N_0}$ (dashed-red), the maximum divergence of EEV differences from the MC prediction $\chi_{\delta E} = r_{\max}$ (dashed-dotted orange) and the average EEV difference $\chi_{\delta E} = \langle r_n \rangle_{\delta E}$ (dotted purple) for a fixed energy interval when the interval is chosen right at the middle of the spectrum for $q_f = 3$. All of the scalings show a trend of N^{-1} with $R^2 = 1$ where R is the correlation coefficient.

the kink region as seen in scaling plots for $q_f = 0.65$ in Fig. 2.8. The scaling relation for the support shows that the support still exists in the thermodynamic limit when the kink region appears in the window. Therefore, we conclude that the kink region is composed of nonthermal states that do not vanish in the thermodynamic limit. Hence when the spectrum contains the kink region, the whole spectrum will never have a shrinking support, violating the strong form of ETH. Similarly, we observe a non-vanishing ETH noise when the kink exists in the energy interval (dashed line in Fig. 2.8). In literature, the fluctuations are expected to vanish away in the thermodynamic limit for the weak form of ETH to hold [114]. However, we see that they do not disappear when the interval includes the kink eigenstates. This matches with the fact that we do not see thermalization when the initial state overlaps with the kink eigenstates. Therefore, we can clearly conclude that the kink eigenstates are nonthermal states that cause nonthermalization when the initial state is chosen carefully to overlap with them (Regions II and III on sudden quench maps). As a result, we argue that when the kink region exists in the spectrum ($|q| < 4$) not all initial states can lead

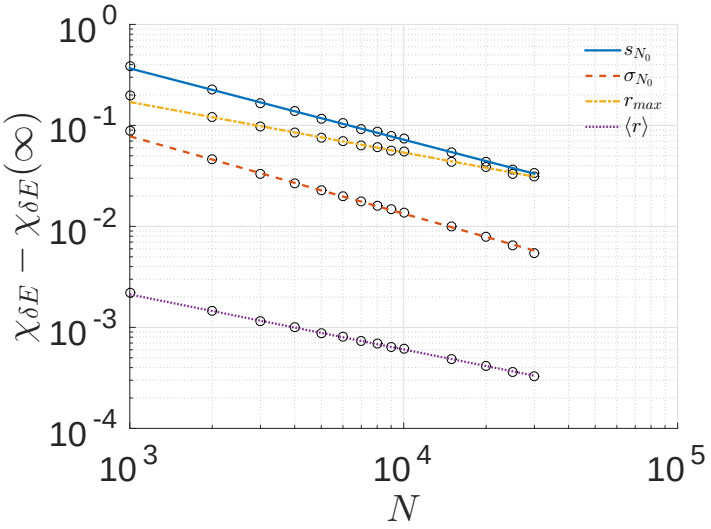

Figure 2.8: The system size scaling of the support $\chi_{\delta E} = s_{N_0} = 0.07 + 48N^{-0.71}$ (solid-blue) with $R^2 = 0.9997$, RMSE $= 10^{-3}$, SSE $= 10^{-5}$, the fluctuations (or the ETH noise) $\chi_{\delta E} = \sigma_{N_0} = 0.02 + 15.5N^{-0.77}$ (dashed-red) with $R^2 = 0.9994$, RMSE $= 10^{-4}$, SSE $= 10^{-6}$, the maximum divergence of EEV differences from the MC prediction $\chi_{\delta E} = r_{\max} = 0.04 + 5.4N^{-0.5}$ (dashed-dotted orange) with $R^2 = 0.998$, RMSE $= 10^{-3}$, SSE $= 10^{-5}$ and the average EEV difference $\chi_{\delta E} = \langle r_n \rangle_{\delta E} = 10^{-3} + 0.1N^{-0.55}$ (dotted purple) with $R^2 = 0.9996$, RMSE $= 10^{-6}$, SSE $= 10^{-10}$ for a fixed energy interval when the interval is chosen right at the middle of the spectrum for $q_f = 0.65$. Here $\chi_{\delta E}(\infty)$ stands for the offset value of the fitting. The RMSE and SSE stand for root mean square error and sum of squares of error, respectively.

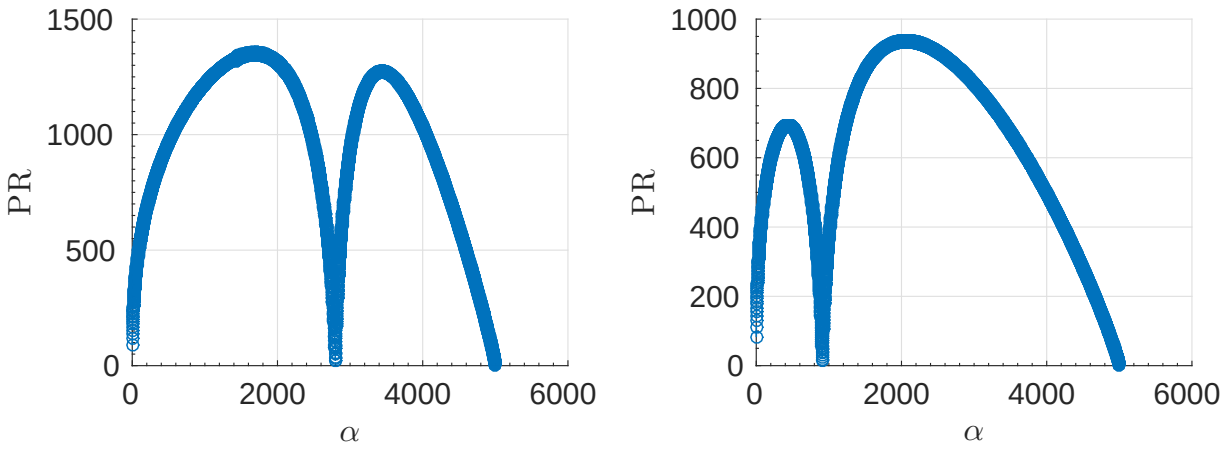

Figure 2.9: The participation ratio values of the eigenspectrum for a ferromagnetic Hamiltonian with (a) $q_f = 0.5$ and (b) $q_f = 2$ for a particle number of 10^4. The eigenstates are ordered ascending in energy from the ground state ($\alpha = 1$) to the most excited state.

the system to thermalization even in thermodynamic limit. However due to the rarity of these nonthermal states, most of the initial states will result in thermalization (Region 1 on sudden quench map Fig. (2.3). Therefore, the weak form of ETH holds for $|q| < 4$, and otherwise ETH holds in the strong sense (based on the shrinking support for all spectrum) since kink region disappears when we choose $|q| > 4$.

In order to understand why there is a nonlinear structure in the EEV plot, which basically results in a nonthermal behaviour in the dynamics, we compute other quantities which can provide more information on the eigenspectrum structure of the model. The spinor Hamiltonian in Eq. (2.4) can actually be mapped to a single quantum-particle Hamiltonian with nearest-neighbor hopping and onsite potentials on a finite lattice. The Fock basis $|N_{-1}, N_0, N_1\rangle = \{|0, N, 0\rangle, |1, N-2, 1\rangle, \cdots, |N/2, 0, N/2\rangle\}$ with zero total magnetization in our spinor Hamiltonian can be mapped to a basis of different lattice sites in the language of a single hopping particle in 1D lattice. Then the interaction terms $a_0^\dagger a_0^\dagger a_1 a_{-1}$ and $a_1^\dagger a_{-1}^\dagger a_0 a_0$ realize the nearest-neighbor hopping as can be seen when we do the operation $a_1^\dagger a_{-1}^\dagger a_0 a_0 |0, N, 0\rangle = \sqrt{N(N-1)}\,|1, N-2, 1\rangle$. The rest of the terms in Eq. (2.4) impose an

onsite potential. The tight-binding Hamiltonian for the mapping could be stated as

$$H_m = \sum_{i=1}^{N/2-1} J(i)\left(c_{i+1}^\dagger c_i + \text{h.c.}\right) + \sum_{i=1}^{N/2} \eta(i) c_i^\dagger c_i, \tag{2.13}$$

where $J(i)$ are real hopping coefficients that are a function of site position and $\eta(i)$ are the onsite potentials that depend on the site positions as well. The lattice size $N/2$ is the dimension of the Fock space. Here the exact dependence of J and η parameters on the positions of the sites in our imagined lattice is determined through the terms in the spinor BEC Hamiltonian Eq. (2.4). See Appendix A.2 for how a spinor Hamiltonian engineers the lattice parameters for the mapped Hamiltonian Eq. (2.13). This mapping reminds us of the physics of Anderson localization [178], albeit the onsite potentials $\eta(i)$ are not random. Hence, we study the participation ratio (PR)

$$P_\alpha = \left(\sum_{n=1} |\psi_{\alpha n}|^4\right)^{-1}, \tag{2.14}$$

to analyze the localization properties of the eigenstates [241, 242, 257]; here, α denotes each eigenstate and n is the Fock basis vectors. As seen in Fig. 2.9, PR has a dip around the eigenstate corresponding to the nonthermal kink eigenstate in its corresponding EEV plot, which points to lower PR values of the nonthermal states in the Fock basis when compared to other eigenstates in the spectrum. This result hints at a link between the nonthermal behaviour that we observe in the system and the Anderson-like localization [178] of the eigenstates in the Fock space. In other words, the nonthermal states of the system also seem to be the most localized states in the spectrum (excluding the edges).

In order to make this point stronger, we analyze the system size PR scaling of eigenstates with high- and low-PR values. To target the low-PR region of the spectrum, we utilize two different methods. We emphasize that low-PR region of the spectrum in Figs. 2.9 (excluding the edges of the spectrum) is also the nonthermal region as already shown with the ETH

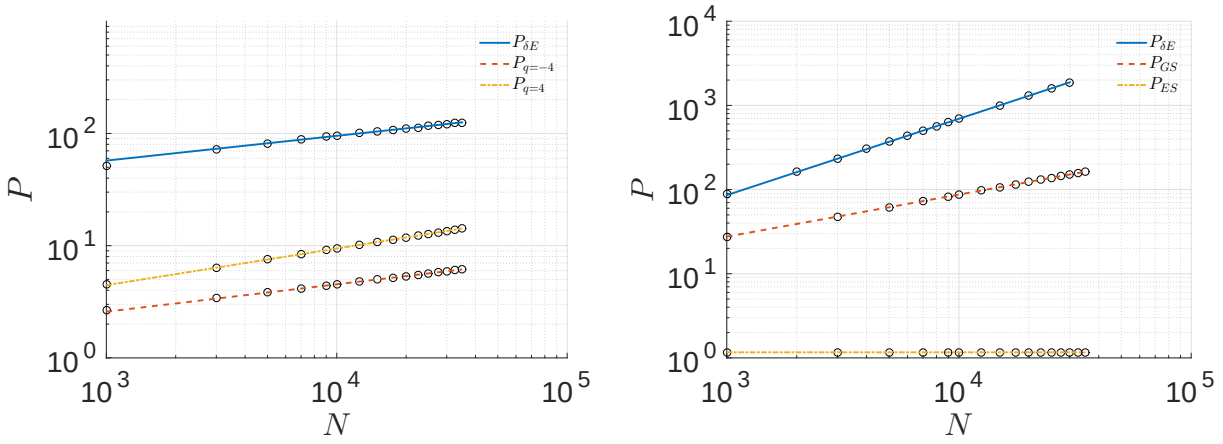

(a) (b)

Figure 2.10: System size scaling of (a) averaged participation ratio of low-PR eigenstates with a fixed energy interval of $\sim 25[c_1]$ around the most outlier (kink) eigenstate (solid blue), the ground state participation ratio at $q = -4$ (dashed red) and at $q = 4$ (dotted-dashed orange); (b) averaged participation ratio of high-PR eigenstates with a fixed energy interval of $\sim 60[c_1]$ around the center of the spectrum (solid blue) when $q = 3$ is chosen, PR of ground state (dashed red) and of the most-excited state (dotted-dashed orange) when the system is not going through one of its phase transition points e.g., $q = 1$.

indicators. There is a rapid change around the kink state which is always the extremum point of the EEV (Figs. 2.2c-2.2d) and the level spacings (Fig. 2.12c). Additionally the kink state slightly shifts in the spectrum as we increase the system size upto thermodynamic limit. So, even though we are able to detect the kink state in the spectrum with all these observations, we note that the kink state shows consistently low PR values for each system size but its scaling is not well-defined possibly due to finite-size effects. Therefore, the first method we apply is averaging over low-PR states around the most outlier (kink) state for each system size with a fixed energy interval. The solid line in Fig. 2.10a is the scaling behaviour that we observe for this method when $q = -0.65$ is chosen, which is also a q value that keeps the kink state around the center of the spectrum. The extracted scaling exponent is $\gamma \propto 0.22$ with $R^2 = 0.997$. The second method employs the phase transition points. We know that the ground state is the kink eigenstate at phase transition points when $q = 4$ or $q = -4$ is taken in the thermodynamic limit. Even though for a finite size condensate the

phase transition points are slightly off from $q = 4$ and $q = -4$ and hence the ground state is not exactly the kink eigenstate, the region around the ground state is the nonthermal kink region. This observation can be made through the difference in the PR scaling exponents of the ground state when we have $q = 4$ (or $q = -4$) and q is away from the phase transition points. Fig. 2.10b dashed line shows the scaling of the ground state when $q = 1$ which we extract $P \propto N^{0.5}$ $(R^2 = 1)$. The exponent $\gamma \propto 0.5$ is obtained for any q sufficiently far from $q = 4$ or $q = -4$. On the other hand, we obtain a scaling of $P \propto N^{0.32}(R^2 = 1)$ and $P \propto N^{0.24}(R^2 = 0.999)$ for $q = 4$ and $q = -4$, respectively. Thus, clearly the ground state is neither localized nor extended completely when the system is not at its phase transition points. However, when the system goes through its phase transitions, the ground state coincides with the low-PR region states and this provides us a way to estimate the scaling exponent of states at the low-PR region. We note that extracting a well-defined scaling only for the most outlier (kink) state in a finite-size system is difficult, but still averaging over a couple of states around it gives an idea about the localization properties of the nonthermal region. Overall the extracted scaling exponents point out to that the low-PR nonthermal kink region is not completely localized region with a scaling exponent of $\gamma = 0$, however it is the most localized region of the spectrum. The high-PR eigenstates that are also responsible of thermalization observed in the system show a scaling of $P_\delta \propto N^{0.91}$ $(R^2 = 1)$, when we choose a fixed energy interval in the middle of the spectrum for Zeeman field strength $q = 3$, (solid line in Fig. 2.10b). We observe almost the same PR scaling with exponent $\gamma = 0.9$ for single eigenstates chosen at the high-PR section of the spectrum and for different q values. Even though such an eigenstate is not completely extended with a scaling exponent of $\gamma = 1$, it is the most extended region of the spectrum. All in all, the previous analysis of the ETH indicators clearly distinguishes the thermal and nonthermal states in the system and PR analysis demonstrates a link between localization and thermalization properties of our system, even though the thermal and nonthermal states are not completely delocalized and localized, respectively.

Finally, we note the difference between the behaviours seen in regions I and IV. Although the equilibrium behaviour in region IV can be predicted by microcanonical ensemble as seen in Fig. 2.6, its cause is not related to the eigenstate localization properties. We observe almost constant dynamic evolution (or almost-no nonequilibrium evolution) for the simulations at this section, which implies that one of the eigenstates dominates the evolution. In the case seen in Fig. 2.6, it is the most-excited state that governs the dynamics for negative q_f values. The most-excited state shows a constant PR scaling with an exponent of 0 (dashed-dotted line in Fig. 2.10b). So, even though the eigenstate is perfectly localized, the initial state is already in equilibrium with the quench Hamiltonian, which leads to the thermalization. In Fig. 2.6, also note that we observe thermalization for values at $q_f > 4$ because now the initial state mostly resembles the ground state of the quench Hamiltonian instead of the most-excited state. Finally, even though we show the PDE values at region III in Fig. 2.6, we should remind the reader that the dynamics of region III does not equilibrate but shows large fluctuations around its PDE value (which will be discussed in the next section as a special case).

An important difference between the spinor BEC model and the single quantum-particle hopping model is that even though the observable $\langle N_0 \rangle$ is local in the spinor BEC case, it is a non-local observable when it is mapped onto the particle lattice. However more importantly, our model does not translate to an Anderson model with random potentials. Single quantum-particle hopping model with random potentials leads to sites with very low PR values. It is also analytically known that such a model cannot cause thermalization and satisfy ETH [258]. Therefore, based on our results with spinor BECs, we argue that engineering the potential of a single quantum-particle model should prevent the localization in the particle lattice and give rise to thermalization for global observables defined for this model.

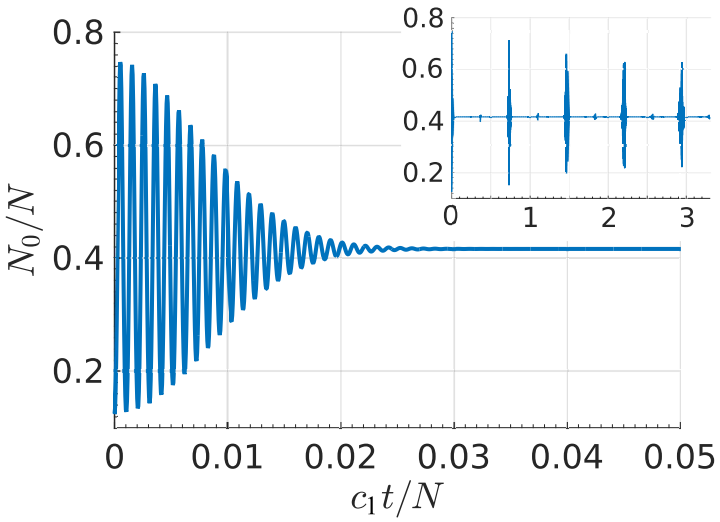

Figure 2.11: The sudden quench dynamics in the short time-scale showing the collapse in detail when there is $N = 2 \times 10^3$ particles in the condensate and x-axis is scaled with the number of particles when we quench from $q_i = -3$ to $q_f = -0.5$ for the ferromagnetic case. The inset plot shows the revivals in long time-scale.

2.4 Existence and Absence of Quantum Collapse and Revivals

In this section, we analyze the cases that demonstrate quantum collapse and revivals and derive an analytical expression to predict their time scales. Further we examine the scaling of collapse and revival times with the number of particles in the condensate to be able to present realistic predictions for the experiment. Finally we discuss 'the special cases', where we do not observe a revival or even equilibration.

Now we choose a point on the ferromagnetic sudden quench map Fig. 2.3 that thermalizes which can be detected via Figs. 2.5 and 2.6. So then, if we quench from $q_i = -3$ to $q_f = -0.5$, we observe a series of collapses and revivals in Fig. 2.11, and the equilibration value in between matches the predictions of both diagonal and microcanonical ensembles. A collapse before equilibration is what is mostly observed in experiments. We also intuitively expect to see a series of revivals due to the finite-size effects. However in order to understand how

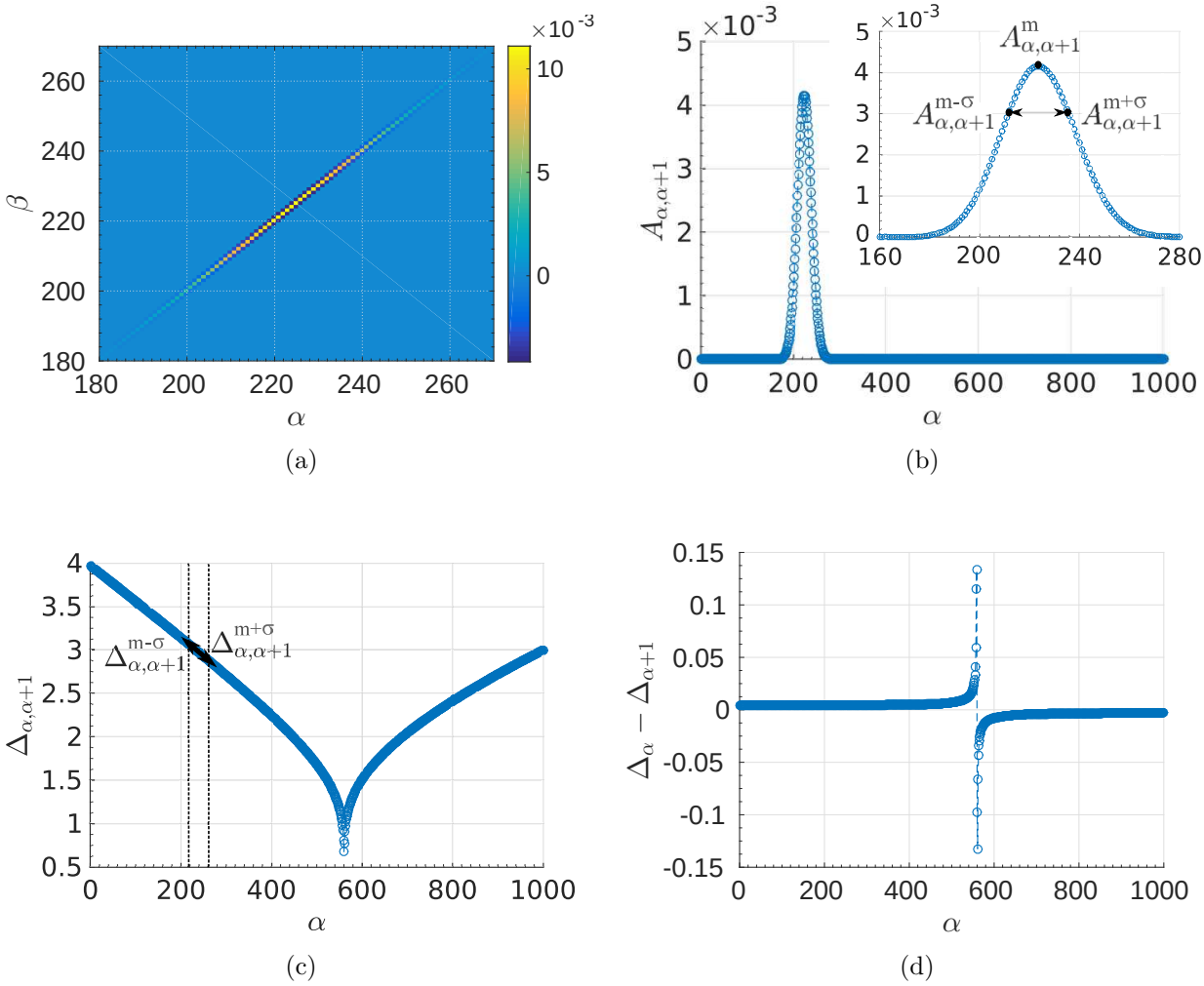

Figure 2.12: (a) The overlap matrix with respect to eigenstates α and β, (b) the first off-diagonal terms of the overlap matrix, (c) the nearest-neighbor (NN) energy gaps and (d) The difference/derivative plot of the NN energy gaps with $N = 2 \times 10^3$ particles in the ferromagnetic condensate for the quench from $q_i = -3$ to $q_f = -0.5$. The x-axis is the eigenstates α ordered ascending in energy from the ground state $\alpha = 1$ to the most-excited state.

collapses and revivals emerge in our model, let us go back to the sudden quench procedure given in the previous section and modify Eq. (2.6). Notice that $c_\alpha^* c_\beta = c_\beta^* c_\alpha$ when the coefficients are real, which is the case in our problem. Also $N_{0,\alpha\beta} = N_{0,\beta\alpha}$ in our model. Then we can regroup Eq. (2.6) as,

$$\begin{aligned} \langle N_0(t) \rangle &= \sum_{\alpha \geq \beta} c_\alpha^* c_\beta \left(e^{i(E_\alpha - E_\beta)t} + e^{-i(E_\alpha - E_\beta)t} \right) N_{0,\alpha\beta}, \\ &= 2 \sum_{\alpha \geq \beta} c_\alpha^* c_\beta \cos\left((E_\alpha - E_\beta)t \right) N_{0,\alpha\beta}. \end{aligned} \tag{2.15}$$

Eq. (2.15) tells us that the dynamics we observe in a sudden quench is the interference of sinusoidal functions weighted with some overlap. We can write Eq. (2.15) more clearly as,

$$\langle N_0(t) \rangle = \sum_{\alpha \geq \beta} A_{\alpha\beta} \cos\left(\Delta_{\alpha\beta} t \right), \tag{2.16}$$

where $\Delta_{\alpha\beta} = E_\alpha - E_\beta$ are the energy gaps, Fig. 2.12c and $A_{\alpha\beta} = 2 c_\alpha^* c_\beta N_{0,\alpha\beta}$ are the overlap matrix elements, Fig. 2.12a. We note that the diagonal terms are the most populated terms in the overlap matrix and they correspond to the diagonal ensemble prediction. In fact it is important that the off-diagonal terms vanish for thermalization to happen or they should be much smaller compared to diagonal terms. We observe this is almost the case in Fig. 2.12a, except the first and second off-diagonals still contribute to the dynamics even though they are much smaller than the diagonal terms. Fig. 2.12b shows the first off-diagonals of the overlap matrix (which we call overlap distribution in the following). This Poisson-like overlap exists when the dynamics demonstrate a series of collapse and revivals and it turns out to be important in determining the time scales of collapse and revivals in spinor condensates under SMA.

The time scale of a collapse is related to the time when the oscillating terms with an energy gap argument in Eq. (2.16) start to become uncorrelated. The terms corresponding to the farthest ends of the distribution are also the farthest in oscillation frequency. They become

uncorrelated after all the other terms get uncorrelated. From that point on, all the oscillating terms will be destructively interfering. We estimate these elements with root-mean-square of the overlap distribution as also done for collapses in Jaynes-Cummings model [243]. Ref. [107] predicts the collapse time for the Ising model as inversely proportional to the energy spread of the initial state, which is similar to our criteria and expression. The following collapse time expression produces a value of $c_1 t_c/N \sim 0.02$ for the quench simulation depicted in Fig. 2.11:

$$t_c \;=\; \frac{2\pi}{|\Delta^{m+\sigma}_{\alpha,\alpha+1} - \Delta^{m-\sigma}_{\alpha,\alpha+1}|}, \tag{2.17}$$

where $\Delta^{m}_{\alpha,\alpha+1}$ denotes the nearest-neighbour energy gap (level spacing, Fig. 2.12c) corresponding to the maximum value in the overlap distribution (Fig. 2.12b) and hence $\Delta^{m+\sigma}_{\alpha,\alpha+1}$ is the nearest-neighbour energy gap corresponding to the value which is σ farther from the mean in the distribution (cf. the inset of Fig. 2.12b). It is possible to fine-tune the predicted collapse time by taking more than 1σ of the overlap distribution. Also note that we find $c_1 t_c \sim N^{1/2}$ as the scaling of the collapse time-scale.

A quantum revival happens when all the oscillating terms become correlated with each other again. This can be measured through the difference between nearest-neighbour energy gaps corresponding to the the mean $\Delta^{m}_{\alpha,\alpha+1}$ and the closest point to mean $\Delta^{m-1}_{\alpha,\alpha+1}$ in the overlap distribution (cf. the inset of Fig. 2.12b),

$$t_r \;=\; \frac{2\pi}{|\Delta^{m}_{\alpha,\alpha+1} - \Delta^{m-1}_{\alpha,\alpha+1}|}. \tag{2.18}$$

Fig. 2.12d shows the differences between nearest-neighbour energy gaps. Note that $\Delta_\alpha - \Delta_{\alpha+1}$ are mostly flat around where the overlap distribution is nonzero. This is vital for a collective revival to occur, since otherwise terms in Eq. (2.16) will never constructively interfere at a fixed time, namely the revival time. When we have $t_r(\Delta_\alpha - \Delta_{\alpha+1}) = 2\pi$, all oscillating terms interfere constructively, creating the first revival. Both the analytical expression and

the data analysis give a revival time $c_1 t_r/N \sim 0.735$. Since the scaling of the revival time-scale turns out to be $c_1 t_r \sim N$, this value can be obtained for all sizes for the parameters depicted in Fig. 2.11. Also note that the linearly growing recurrence times is well-known in the literature [32]. The small peaks between the collapse and revivals seen in Fig. 2.4 are the small revivals contributed by the second off-diagonal terms in the overlap matrix, Fig. 2.12a. We can also predict the oscillation frequency,

$$t_{\text{osc}} = \frac{2\pi}{\Delta^m_{\alpha,\alpha+1}}, \tag{2.19}$$

by using the nearest-neighbor energy gap at the maximum point of the overlap distribution $\Delta^m_{\alpha,\alpha+1}$. There is an another interesting quantity that can be predicted in a collapse-revival picture. We observe how revivals are suppressed in a very long time scale in the inset of Fig. 2.4. This 'randomizing time' is where the initial memory of the system irreversibly gets lost. Even though a typical randomizing time is out of experimental reach, it is interesting to note that an isolated, unitary and finite-size quantum system will be eventually randomized and hence completely thermalized at the randomizing time which can be estimated via

$$t_{rz} = \frac{2\pi}{|\Delta'_{m+\sigma} - \Delta'_{m-\sigma}|}, \tag{2.20}$$

where $\Delta' = \Delta_\alpha - \Delta_{\alpha+1}$ denotes the difference between nearest-neighbor energy gaps (Fig. 2.12d) and the rest of the notation is same with the previous definitions where we use the overlap distribution for $m \pm \sigma$.

In order to give a sense of these time scales, let us fix the particle density in our condensate to 5×10^{14} cm^{-3}. Then the coefficient reads $c_1 \sim -2\pi \times 9$ Hz, which gives a realistic collapse time of ~ 0.5 s and a revival time of ~ 25 s for a condensate particle number of 2×10^3. This sudden quench experiment corresponds to a data point on Fig. 2.5, where ETH can explain the match between the thermal relaxation values predicted by diagonal ensemble and microcanonical ensemble. Therefore we can conclude that there is thermalization until the

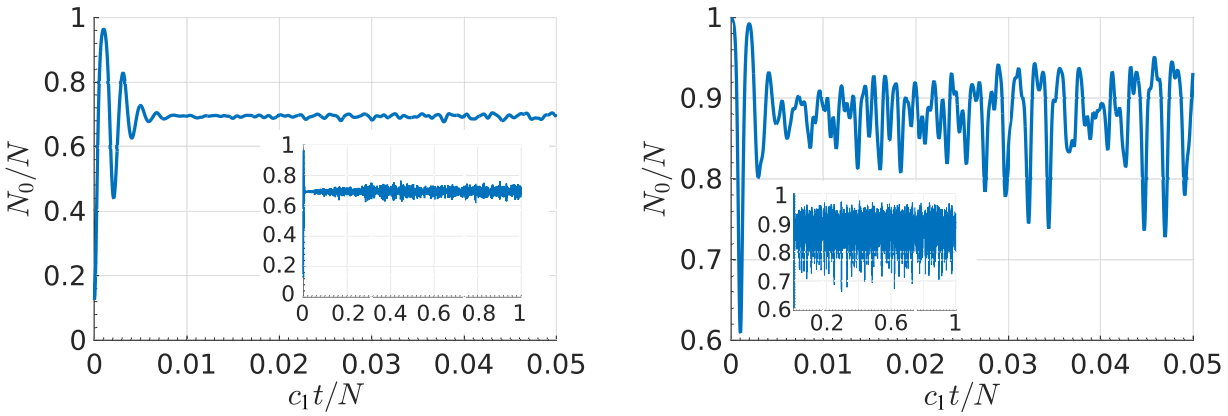

(a) (b)

Figure 2.13: The sudden quench dynamics in short time-scale (a) from $q_i = -3$ to $q_f = 0.5$ and (b) from $q_i = 4.1$ to $q_f = 2$ with insets of long time-scales for ferromagnetic condensates and $N = 2 \times 10^3$ particles.

initial memory of the system comes back with a quantum revival. Then it is important to see how the times of the collapse and the first revival scale with the number of particles in the condensate. Reminding the reader of $c_1 t_c \sim N^{1/2}$ and $c_1 t_r \sim N$ and using the estimations done for Thomas-Fermi limit in Ref. [246], we figure out that $c_1 \sim N^{2/3}$ in 1-dimension, hence $t_c \sim N^{-1/6}$ and $t_r \sim N^{1/3}$. Although SMA breaks down in large condensate limit [246] and the experiments always have finite sizes, it is still insightful to imagine the thermodynamic limit $N \to \infty$. In thermodynamic limit, a 1D spinor BEC system has a diverging revival time and a vanishing collapse time, which implies thermalization described by ETH for our model.

Now let us choose a point on the map Fig. 2.3 that does not thermalize to illustrate one of the special cases. If we quench from $q_i = -3$ to $q_f = 0.5$ (corresponding to the parameters in Fig. 2.2a and 2.2c), we observe the dynamical behaviour in Fig. 2.13a. There is a well-defined collapse whose time-scale can be predicted with the collapse criterion and the system seems to equilibrate right after the collapse. However looking at the dynamics for a longer time (inset of Fig. 2.13a) reveals that the revivals attempt to happen at different times resulting with no collective recurrence for a finite system. This is due to the broad

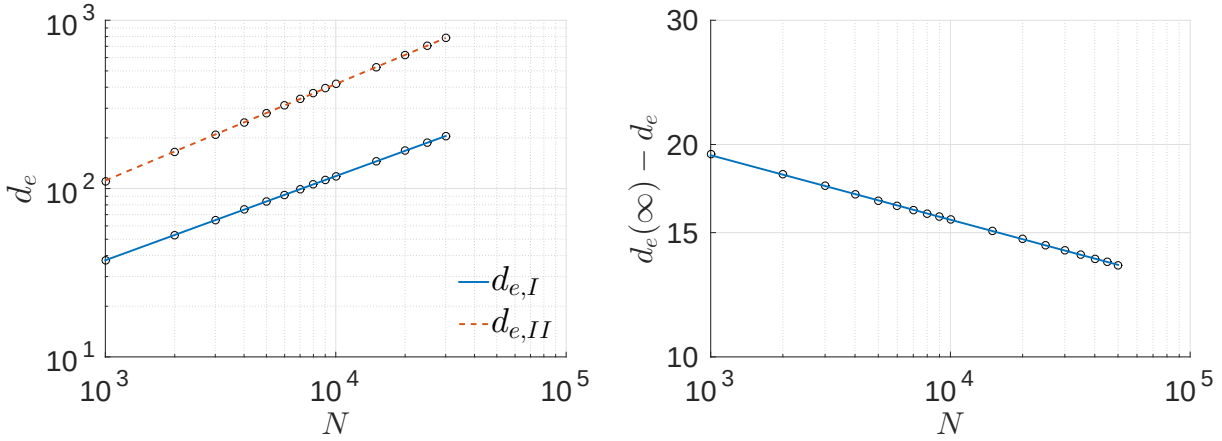

(a) (b)

Figure 2.14: The effective dimension scaling for a quench (a) from $q_i = -3$ to $q_f = 0.5$ (Region II) (dashed red) with $d_e \propto N^{0.57}$, from $q_i = -3$ to $q_f = -0.5$ (Region I) (solid blue) with $d_e \propto N^{0.5}$ and (b) from $q_i = 4.1$ to $q_f = 2$ (Region III) with $d_e = 28.3 - 36.3N^{-0.092}$ with respect to system size. The correlation coefficient is $R^2 = 1$ for all figures. $d_e(\infty)$ stands for the offset value of the fitting in subfigure b.

shape of the EON window (Fig. 2.2a). One can calculate the so-called effective dimension of the system [36, 90] under this specific quench, which is the participation ratio of the initial state in the eigenstate reference basis instead of Fock basis,

$$d_e = \left(\sum_\alpha |c_\alpha|^4 \right)^{-1}, \tag{2.21}$$

where $|c_\alpha|^2$ is the eigenstate occupation numbers as in Eq. (2.5). The effective dimension is a measure of how broad the EON window is. In order to determine if a quantum system equilibrates, one needs to look at the scaling of the effective dimension with the system size. We find a scaling of $d_e \propto N^{0.57}$ ($R^2 = 1$) for this quench (Fig. 2.14a) and in fact almost the same exponent for any other quench in region II of the sudden quench map. Therefore, we argue that in thermodynamic limit the effective dimension diverges $d_e \to \infty$ as $N \to \infty$, which leads the system to equilibration. For a comparison with region I, we calculated the effective dimension of a region I quench from $q_i = -3$ to $q_f = -0.5$ which is already shown to thermalize and hence equilibrate. As seen in Fig. 2.14b, the effective dimension is found

to be $d_e \propto N^{0.5}$ ($R^2 = 1$) and this scaling exponent is universal for all the quenches in region I. Hence, the previous argument follows. If we return to the discussion on region II dynamical behaviour, the overlap distribution (first off-diagonals in the overlap matrix) is similar in shape with Fig. 2.2a. Further computations show that the energy gap differences between neighbouring terms in the overlap distribution are different and hence they give rise to different revival times (see. Eq. (2.18) and Fig. 2.12d around the kink region) confirming the dynamical response. Also clearly the EON for this point on the map (Fig. 2.2a) is not narrow enough to avoid the kink nonthermal states, which causes nonthermalization for the system. As a result, the system only equilibrates with no collective recurrence for any finite dimensions of the system. Also note that as we increase the system size, the time-scale of the revival attempts diverges which leaves us with the equilibrated section seen right after the decay. This is the behaviour that we observe for the region II on sudden quench map Fig. 2.3.

The second special point on the map Fig. 2.3 is a quench from $q_i = 4.1$ to $q_f = 2$, which demonstrates the behaviour for region III on Fig. 2.3. Fig. 2.13b shows oscillatory behaviour around the system's PDE value for all times without any collapse or revival. The overlap distribution looks like Fig. 2.2b, however differently the first off-diagonal terms are not really smaller than the diagonal terms (EON of the system) and in fact second and third off-diagonal terms in the overlap matrix $A_{\alpha\beta}$ substantially contribute to the dynamics, too. This is in fact why we observe large fluctuations Eq. (2.16). The scaling of the effective dimension for this quench turns out to be $d_e \propto 28.3 - 36.3N^{-0.092}$ ($R^2 = 1$), which implies that in thermodynamic limit $d_e \to 28.3$ while $N \to \infty$ and the effective dimension is going to saturate at a constant value (Fig. 2.14b). This will lead to nonequilibration since the effective dimension will be so much smaller than the dimension of the Hilbert space, $d_e \ll d_H = \infty$. We note that all quenches on region III shows a universal scaling exponent with slightly different scaling parameters. As a final remark, the EON window is narrow enough to coincide only with the nonthermal kink states implying the PDE of the system is not the

thermal prediction.

2.5 Conclusions and Discussion

Spinor BEC model with SMA has an eigenstate expectation value spectrum for the observable $\langle N_0 \rangle$ (the number of particles with spin-0 component in the condensate) that shows thermalization in the context of eigenstate thermalization hypothesis in the weak form when the quadratic Zeeman term is $|q| < 4$ due to the 'rare' nonthermal states and in the strong form, otherwise. We adopted widely used ETH indicators to obtain our results, e.g., support, ETH noise (fluctuations), maximum divergence from the microcanonical prediction for an eigenstate in a fixed energy interval and the EEV differences. We studied the effect of these nonthermal states in the spectrum by driving the system out of equilibrium via a sudden quench from the ground state of an initial Hamiltonian with q_i to a final Hamiltonian with q_f. Even though this procedure allowed us to study certain initial conditions, we are able to generalize the results and predict the behaviour of the system with an arbitrary initial condition. Therefore, such a procedure is experimentally realizable and we have shown that it leads to a classification scheme of the system dynamics: the sudden quench maps, Figs. 2.3 and 2.4. Sudden quench maps give us the long-time average of the dynamical response, or the prediction of diagonal ensemble, which is valid in the long-time limit. For a region where the system does not equilibrate (e.g., Region III), the value on the map is the average of the response.

We observed that ETH is satisfied in region I with well-defined collapse and revivals where the revival time-scale is out of reach for realistic condensate sizes. For the region II, the dynamics equilibrate around a nonthermal value right after a collapse (shown via the scaling of effective dimension) due to the effect of nonthermal rare states in the spectrum. Even though dynamics at region II shows attempts for a quantum revival, not all the oscillating terms become correlated at the same time, implying the lack of a clear quantum revival. We

interpreted the thermalization seen for the region I as weak ETH, because even though the initial state does not overlap with the rare nonthermal states (kink region), these states still exist in the spectrum, even in the thermodynamic limit. Therefore, clearly not all initial states are able to thermalize the system. In fact, region II is an example of these cases. However, for the Hamiltonians with $|q| > 4$, the kink region does not exist in the spectrum even for finite-size condensates. Thus, we conclude that ETH holds in the strong sense for this set of Hamiltonians.

The system for the region III does not equilibrate or show any collapse-revival phenomena and instead oscillates, because the effective dimension saturates at a finite value whereas the Hilbert space dimension diverges in the thermodynamic limit and the main contribution to the dynamics comes from nonthermal states which also have low participation ratio values in the Fock basis. We explicitly showed that the thermal and nonthermal states in the spectrum have high and low PR values with system-size scaling exponents of ~ 0.9 and ~ 0.2, respectively. In the end, thermalization seems to be linked to the localization properties of the eigenstates. In region IV, the system thermalizes with very small amplitude collapse and revivals either at 0 or 1. The initial state is already in almost-equilibrium with the quench Hamiltonian, leading to almost-no nonequilibrium evolution for the system to pursue. For the anti-ferromagnetic sudden quench map Fig. 2.4, we always observe only the regions III and IV given that the initial state is a ground state of an anti-ferromagnetic Hamiltonian. Finally, we note that the region around $q_f \sim 0$ on both sudden quench maps is special in terms of how the thermalization value is independent of the initial state chosen. This behaviour is expected, because almost all of the eigenstates in the spectrum contribute to the observable expectation value in the same amount regardless of the system size.

Interpretation of sudden quench maps as non-equilibrium phase diagrams and the transitions between regions as the dynamical phase transitions seems possible given that these dynamical transition points originate from the equilibrium quantum phase transitions of the system. We leave the question if these transitions can be related to dynamical quantum

phase transitions (DQPTs) [259] as an investigation for future.

Spinor Bose-Einstein condensates are relatively more convenient to experiment with [60, 72, 250, 253, 254] and numerically less costly (when SMA is applied), compared to more popular models such as Bose-Hubbard model or Ising models. Here, we showed that spinor BECs can also be used as a test-bench to test the ideas on the thermalization of isolated quantum systems.

Chapter 3

Detection of Information Scrambling in Cold Atoms

Out-of-time-order correlators (OTOC), recently at the center of discussion on quantum chaos, are a tool to understand information scrambling in different phases of quantum many-body systems. We propose a disordered ladder spin model, the ladder-XX, which can be designed in a scalable cold atom setup to detect OTOC with a novel sign reversal protocol for the evolution backward in time. We study both the clean and disordered limits of the ladder-XX model and characterize different phases (ergodic-MBL) of the model based on the decay properties of OTOCs. Emergent effective lightcone shows sublinear behaviour, while the butterfly cones drastically differ from the lightcone by demonstrating superlinear behaviour. Based on our results, one can observe how the information scrambling changes in the transition from well-studied 1D spin models to unexplored 2D spin models in a local setting.

3.1 Introduction

Information scrambling has drawn much attention in the last years, not only in gravitational theories to study the information properties of black holes [133, 140, 260, 261], but also in

quantum many-body physics [130,132,139,150,162,167–169,181,262]. Even though the initial interest in scrambling was to study quantum chaos in models with gravity duals, information scrambling is, first, not limited to systems with duals, second, provides an understanding about the dynamics of any generic many-body system. Besides being a complementary approach to level-statistics [41] in the context of quantum chaos, the way that systems scramble information in time can dynamically reveal the properties of a Hamiltonian in an experiment. The tool to measure information scrambling is a correlation function, called out-of-time-order correlator (OTOC). The physics that OTOC captures is the growth of the commutator of two operators in time and this growth, also called out-of-time-order commutator, can be characterized by,

$$C_{ij}^{\beta}(t) \quad = \quad -\frac{1}{Z}\mathrm{Tr}\left\{e^{-\beta H}\left[A_i(t), B_j\right]^2\right\}, \tag{3.1}$$

for a system with a finite inverse temperature β. Here i and j denote arbitrary sites in the lattice, $A_i(t)$ and B_j are local hermitian operators for their corresponding sites and Z is the partition function. We take $j = 0$, an observable at the first lattice site in the rest of the study. The local observables of two sites at a distance initially commute, but the interactions lead the system to become more correlated in time, and the build-up of the correlations between sites-at-a-distance starts to be seen in the Heisenberg operators that no longer commute. Therefore, the initially localized operators spread across the space dimension and become as nonlocal as possible around the scrambling time. OTOCs are sensitive to conserved quantities [157,162,180], revealing the (non)integrability of the system; they also show the signatures of localized phases [139, 162, 167–169], equilibrium [220] and dynamical phase transitions [181], chaotic properties of thermal systems [140, 142, 150], e.g., exponential decay in OTOC and finally the (non-)locality and information transport of the Hamiltonian via emergent lightcones [130, 132, 150, 262]. All these theoretical discoveries on OTOCs call for experimental proposals and experiments in order to probe and eventually

utilize scrambling.

To date, there have been a number of experimental proposals [146–148, 150, 158] and realizations [156, 157, 159] on scrambling detection. In this Chapter, one of our aims is to come up with the simplest possible cold atom setup that shows a wide range of diverse scrambling phenomena and could pave the way to scalable OTOC measurements of non-integrable spin systems. The cold-atom setup is a realistic candidate to probe OTOC, mainly due to scalability and its weak coupling to the environment [66, 263]. Information scrambling could be induced by environment effects as well, and therefore it is important to differentiate the scrambling due to correlation built-up via many-body interactions in an experiment [159]. The scalability of cold atoms could be utilized to increase the size and hence the duration of transient effects in OTOC by delaying the saturation stage. The most crucial step of OTOC measurement is the evolution backward in time. We propose a novel sign reversal mechanism as an alternative to existing approaches. The convential solution to reverse the sign of a cold-atom Hamiltonian is to utilize Feshbach resonances [21, 150]. We will show that a sequence of single-spin gates can be performed via fast laser pulses [264, 265] to measure the OTOC.

In the first section, we explain our model and its cold-atom setup. Then we systematically study the level-statistics and scrambling properties of ladder-XX both with and without disorder. In the final part, we layout the scrambling detection with the preparation of realistic random states.

3.2 The Ladder-XX Model

Ladder spin models have been studied to explore their critical phenomena [266–268] and entanglement properties [269]. They are seen as useful intermediate models to understand the magnetic properties of materials while increasing the dimension from d to $d+1$ [270]. There are also natural cuprate compounds that are modelled by ladder spin models at $d = 1$ [268]

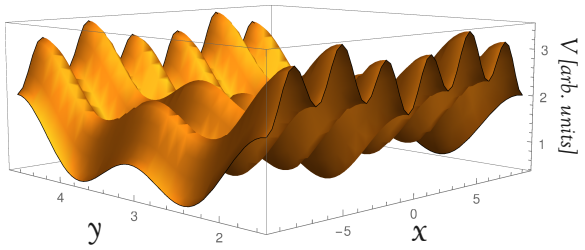

Figure 3.1: A schematic of the proposed optical superlattice for the ladder$-XX$ model where $x-$ and $y-$axes are spanned by disordered and double well potentials, respectively.

and they have been considered as candidate models to explain high-T_c superconductivity [271]. More recently ladder-spin models are studied in the context of transport [272]. We choose our chaotic ladder model as the *ladder-XX* model because of its simplicity in cold atom realization,

$$\begin{aligned} H &= \sum_{j=1,2}\sum_{i=1}^{L-1} J_{\parallel}\left(\sigma^x_{j,i}\sigma^x_{j,i+1} + \sigma^y_{j,i}\sigma^y_{j,i+1}\right) \\ &+ \sum_{i=1}^{L} J_{\perp}\left(\sigma^x_{1,i}\sigma^x_{2,i} + \sigma^y_{1,i}\sigma^y_{2,i}\right) + \sum_{i=1}^{L} h_i\left(\sigma^z_{1,i} + \sigma^z_{2,i}\right), \end{aligned} \tag{3.2}$$

with random disorder h_i which is drawn from a uniform distribution with disorder strength of $[-h, h]$. $\sigma^{x,y,z}$ are Pauli matrices for the spin$-1/2$ system, $J_{\parallel}$ is the intra-chain hopping coefficient and $J_{\perp}$ is the rung hopping coefficient. L is the system size for a single-chain and we go up to $L = 8$ in our numerical analysis with exact diagonalization.

The ladder-XX model could be realized at the hard-core boson limit of the Bose-Hubbard model [62, 64]. At the hard-core boson limit, with $U \to \infty$ and non-integer filling factor that implies every site has either 0 or 1 boson, we end up with a superfluid Hamiltonian $H_{U\to\infty} = -t_{\parallel}\sum_{i,i+1}\left(a^\dagger_i a_{i+1} + \text{h.c.}\right) - \sum_i \mu_i a^\dagger_i a_i$, that can easily be mapped to XX-chain via mapping the annihilation operator to the spin lowering operator $a \to \sigma^-$ and creation

operator to raising operator $a^\dagger \to \sigma^+$. The mapping leads us to have $J_\parallel = 2t_\parallel$, $J_\perp = 2t_\perp$ and the random chemical potential is mapped to random magnetic field strengths $\mu_i = h_i$ via $a_i^\dagger a_i - 1/2 \to \sigma^z$. Therefore, we can recover Hamiltonian Eq. (3.2) with two interacting Bose-Hubbard chains exposed to random chemical potential in the hard-core boson limit. The boson state vectors correspond to either spin down $|\downarrow\rangle$ or spin up $|\uparrow\rangle$ in the ladder-XX model. Since the filling factor is fixed in the cold atom scheme, the corresponding case in our spin model (Eq. (3.2)) has fixed total spin S_z. We set the filling factor $f = 0.5$ and the OTOC of the system is studied at the subsector $S_z = 0$.

We utilize superlattices to create random disorder in the Bose-Hubbard chains [273, 274] and to let two chains interact with each other. For the latter, we create a double well potential via choosing the laser frequencies as k and $2k$ in the y-direction with a phase difference between them ϕ, e.g., $V_y(y) = V_{1y}\sin^2(k_y y) + V_{2y}\sin^2(2k_y y + \phi)$, assuming $V_{1y} \sim V_{2y}$ so that the bosons can be trapped in the double well potential. For the random disorder, we interfere two optical fields with incommensurate frequencies, e.g., $V_x(x) = V_{1x}\sin^2(k_{1x}x) + V_{2x}\sin^2(k_{2x}x)$, where $k_{1x}/k_{2x} \in \mathbb{R}/\mathbb{Q}$ for both of the chains. When $V_{2x} \ll V_{1x}$, the disorder lattice can simulate the true random potential [273, 274]. A schematic of the optical superlattice can be seen in Fig. 3.1. One can tune the hopping coefficients $J_\parallel$ and $J_\perp$ in the ladder-XX model through the laser amplitudes and frequencies [64]; and thus access different OTOC behaviours with the simulation time of $t \propto 1/J_\parallel \propto$ 1-10 ms in laboratory. Therefore, the measurement time of OTOC is in the limits of cold atom experiments [275].

3.3 The OTOC Properties and Level Statistics

For a spin system Eq. (3.1) can be recast to the OTOC, by first setting the temperature infinite, $\beta \to 0$ and then noting that,

$$F_i^{\text{ex}}(t) = 1 - \frac{C_i^0(t)}{2N}, \tag{3.3}$$

where $C_i^0(t) = \| [\sigma_i^z(t), \sigma_1^z] \|_F^2$. Since the Pauli matrices are hermitian, norm-2 (Frobenius norm) could be utilized to rewrite Eq. (3.1). N is the dimension of the Hilbert space and the superscript ex stands for the exact value of the out-of-time-order correlator. Eq. (3.3) is measurable given a $\beta = 0$ initial state is prepared. In general, calculating an expectation value with respect to the infinite temperature state requires averaging over all eigenstates. However, we can approximate the OTOC Eq. (3.3) with smaller number of states,

$$F_i^{\sim}(t) \quad = \quad \sum_j \langle \psi_j | \, \sigma_i^z(t) \sigma_1^z \sigma_i^z(t) \sigma_1^z \, | \psi_j \rangle \, , \tag{3.4}$$

where $|\psi_j\rangle$ denotes a pure random initial state (or a mixture of random initial states) drawn from the Haar measure [130]. Haar random states are typically maximally-entangled states within a small error [276]. The error of approximating a $\beta = 0$ initial state is exponentially suppressed as the Hilbert space increases via typicality arguments [84, 277]. This procedure is numerically less expensive compared to other methods for preparing the initial state at $\beta = 0$, even though the Haar random states are hard to generate experimentally [278]. The results presented in this paper are based on averaging over more than one random initial state to obtain OTOC as precise as possible (Appendix B.2 for error bounds).

When a generalized form of Jordan-Wigner transformation [279] is applied, ladder-XX can be shown to be interacting in the spinless fermion representation. Therefore we expect to see ergodic to many-body localized (MBL) phase transition in this model [171, 173]. A common way to determine if a quantum system is chaotic is via the energy level statistics [34, 41, 171, 173]. Energy level spacings are $\delta_\gamma^n = |E_\gamma^n - E_\gamma^{n-1}|$ where E_γ^n is the corresponding energy of the many-body eigenstate n in a Hamiltonian of disorder realization γ. Each γ represents a different set of random disorder h_i drawn from uniform distribution. Then we can calculate the ratio of adjacent gaps as $r_\gamma^n = \min\left(\delta_\gamma^n, \delta_\gamma^{n+1}\right) / \max\left(\delta_\gamma^n, \delta_\gamma^{n+1}\right)$ as the indicator of the level-statistics [171, 173]: $r_\gamma^n \sim 0.53$ and $r_\gamma^n \sim 0.39$ are representative of Wigner-Dyson and Poisson statistics, respectively. If the distribution of the energy level

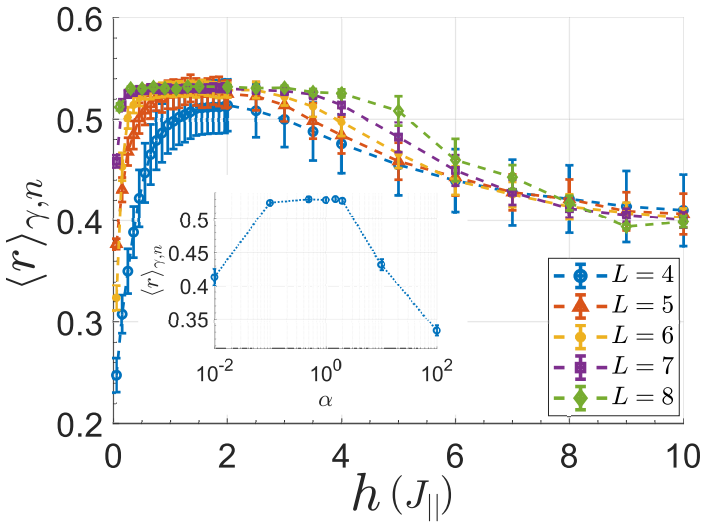

Figure 3.2: The average ratio of level spacings $\langle r_\gamma^n \rangle_{\gamma,n}$ with respect to disorder strength h. Coupling strengths are set to $J_\perp = J_\parallel$ and $\langle r_\gamma^n \rangle_{\gamma,n}$ is averaged over 5×10^3 to 10 random realizations for single-chain sizes ranging between $L = 4 - 8$. Inset: $\langle r_\gamma^n \rangle_{\gamma,n}$ at $h = 1$ $[J_{||}]$ with respect to rung interaction strength α where $J_\perp = \alpha J_\parallel$ for $L = 7$.

spacings follows Wigner-Dyson statistics through a GOE (generalized orthogonal ensemble) distribution, the model shows ergodic behaviour, whereas Poisson statistics imply a localized phase [34, 41]. Fig. 3.2 shows the average ratio values $\langle r_\gamma^n \rangle_{\gamma,n}$ varying between random field strengths of $h = 0 - 10$ for different system sizes ranging between $L = 4$ and $L = 8$ when they are averaged over 5×10^3 to 10 different random samples. The average of r_γ^n over a set of different Hamiltonians H_γ and eigenstates n, converges to $\langle r_\gamma^n \rangle_{\gamma,n} \sim 0.53$ in the presence of small disorder strength $h \lesssim 3$ $[J_{||}]$, hence implying an ergodic phase. As $h \gtrsim 9$ $[J_{||}]$, we observe $\langle r_\gamma^n \rangle_{\gamma,n} \sim 0.39$ that indicates a many-body localized (MBL) phase.

Fig. 3.3 shows how OTOC between σ_1^z and σ_7^z for $L = 7$ chain changes with respect to the rung interaction strength. In the limit $\alpha = J_\perp/J_\parallel \to 0$, the system converges to two independent XX-chains with random disorder. Whereas the opposite limit of $\alpha \to \infty$ implies a dimer phase as another integrable limit of ladder-XX. In both cases, the corresponding fermion representation becomes non-interacting, which points to single-particle dynamics with Anderson localization [162, 168]. We see a permanent revival after a decay and larger

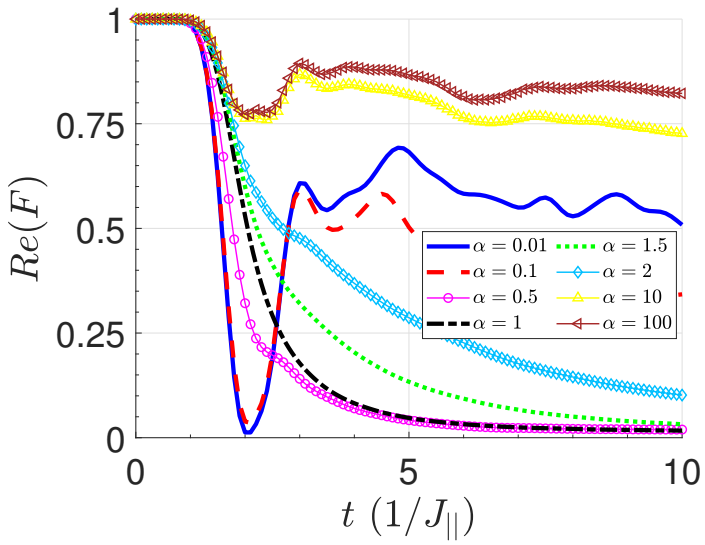

Figure 3.3: The OTOC of the ladder-XX model at $h = 1$ $[J_{||}]$ between two distant operators σ_1^z and σ_7^z in the first chain with respect to α for $L = 7$. $\alpha \sim 1$ corresponds to the interacting limit, whereas the cases $\alpha \ll 1$ and $\alpha \gg 1$ are integrable limits of the ladder-XX model. The OTOC is averaged over 100 different random samples. The plot shows the mean values, see Appendix B.1 for the error bars on the curves.

oscillations in OTOC as observed in integrable systems [142, 157]. In addition, the average level spacing ratio $\langle r_\gamma^n \rangle_{\gamma,n}$ decreases from ~ 0.53 to ~ 0.39, thus demonstrating the signature of level statistics for integrable systems (see inset of Fig. 3.2). We note that the OTOC for $\alpha \to \infty$ scrambles less than the OTOC for $\alpha \to 0$ with a small initial decay, since the model also becomes weakly-coupled throughout the x-dimension in this limit. The OTOC decays rapidly in the interacting limit around $\alpha \sim 1$ and saturates at $F(t \to \infty) \sim 0$ while showing GOE distribution with $\langle r_\gamma^n \rangle_{\gamma,n} \sim 0.53$ and hence quantum chaos in its energy levels. We set $\alpha = 1$ for the rest of our paper and study the interacting limit.

The chaotic regime of the ladder-XX model ($h = 1$ $[J_{||}]$) demonstrates a brief interval of exponential decay in early-time dynamics (Fig. 3.4a), followed by power-law tails (Fig. 3.4b) before entering into the saturation regime. The inset in Fig. 3.4b shows the Lyapunov-like exponents extracted from the data both for $L = 8$ and $L = 7$ (Appendix B.3) when we fit $\mathrm{Re}(F) = a \exp(-\lambda t)$ to the data, where a is a constant. Quantum chaotic models are expected to scramble the information fast and hence show exponential decay of OTOC [140]

before saturation. Exponential decay is a transient feature of systems with finite size and bounded operators [280], a result we observe in Fig. 3.4a. The Bose-Hubbard model [150] and time-dependent systems [162, 281] were shown to decay exponentially, whereas it is numerically hard to show the exponential decay in time-independent quantum chaotic spin chains, e.g., disordered Heisenberg model [162]. In fact, the transient exponential decay turns into power-law decay $\mathrm{Re}(F) = at^{-b}$ in Fig. 3.4b for the ladder-XX model, thus reminding us of the quasi-exponential generic form put forward by [132]. When there is no disorder, Fig. 3.4c, a decay with power-law trend is observed. There are significantly larger oscillations around the saturation value in the clean limit, however in both clean and disordered cases, the scrambling time is approximately the same. For a comparison, the power-law exponents for disordered and clean cases are $b = 2.65$ and $b = 2.76$, respectively for the observables $\sigma_1^z - \sigma_7^z$ in a system with $L = 7$. The ladder-XX model has energy and spin conservation, similar to Heisenberg model where OTOC has been observed to be sensitive to conserved quantities and show power-law decay [162]. In addition to that, ladder-XX has invariant subspaces that show ballistic transport but are not associated with local conserved quantities at the same time, hence the energy levels still show quantum chaos [272]. When random disorder is introduced, these invariant subspaces can support Anderson localized eigenstates regardless of the disorder strength [282]. We first conclude that the invariant subspaces do not change the power-law decay, however affect the saturation value of OTOC. Figs. 3.4b-3.4c show that the saturation value is much higher both in disordered $F(t \to \infty) > 10^{-2}$ and clean $F(t \to \infty) > 10^{-3}$ limits, compared to other models such as Heisenberg and transverse-field Ising models of similar sizes $F(t \to \infty) \sim 10^{-5}$ [162]. Further, we notice that the saturation value of OTOC becomes even larger when the disorder is introduced. Even though the disorder clearly resolves the degeneracies caused by symmetries, the disordered system scrambles less than the clean system. Thus, we point to Griffiths rare-region effects [283] that might also be responsible for turning exponential decay in early time into power-law later in time.

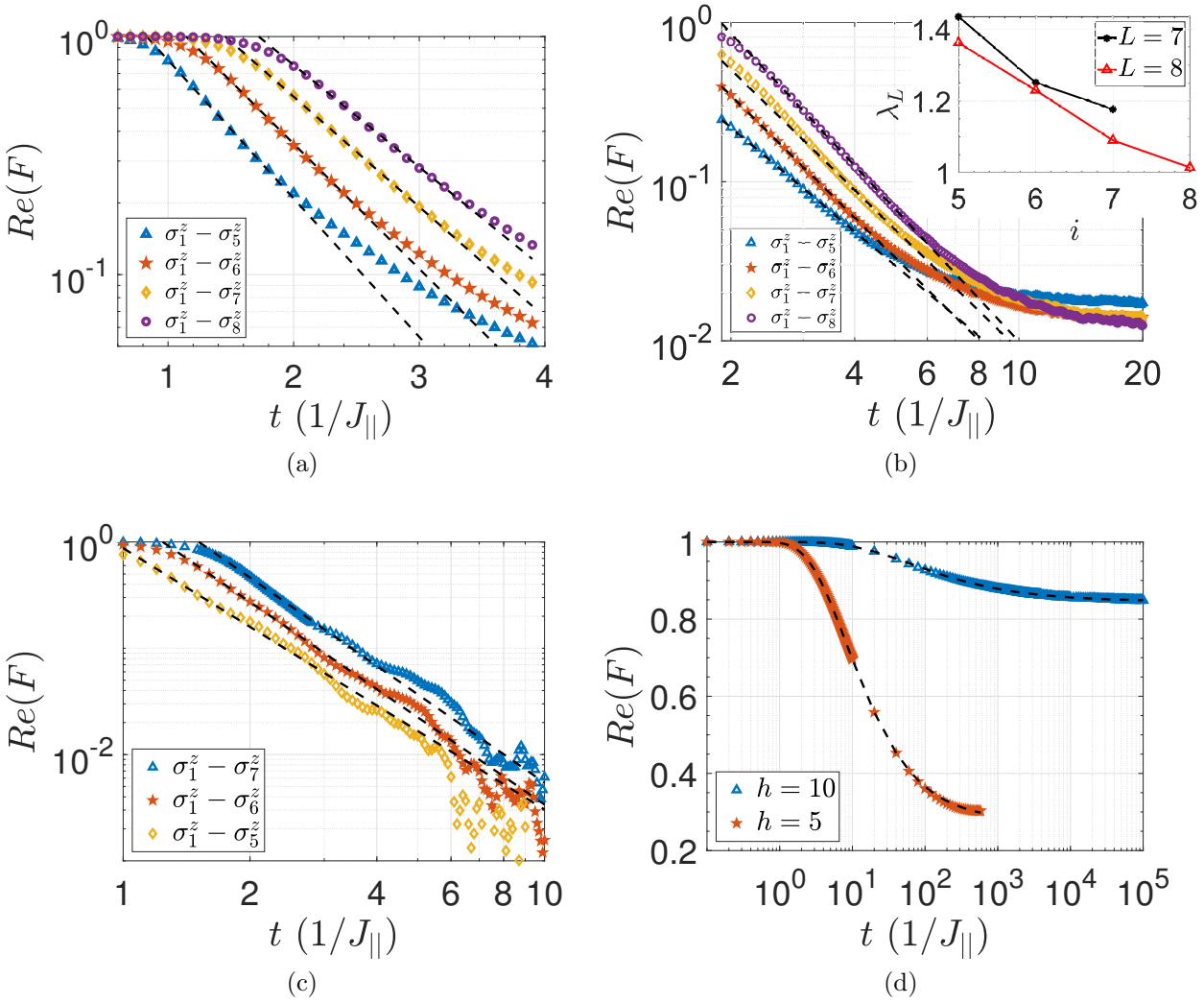

Figure 3.4: (a) The exponential and (b) power-law decay of OTOCs for σ_1^z with σ_5^z (blue-triangles), σ_6^z (red-pentagrams), σ_7^z (orange-diamonds) and σ_8^z (purple-circles) observables in a system size of $L = 8$. The inset in (b) shows the Lyapunov-like exponent extracted from exponential fitting for both $L = 7$ (black-asterisks) and $L = 8$ (red-triangles). (c) No disorder case: Only power-law decay of OTOC for σ_1^z with σ_5^z (orange-diamonds), σ_6^z (red-pentagrams) and σ_7^z (blue-triangles) observables when $L = 7$ and $h = 0$. (d) Crossover region with $h = 5$ $[J_{||}]$ (red-pentagrams) and MBL with $h = 10$ (blue-triangles) for observables $\sigma_1^z - \sigma_7^z$ with $L = 7$.

The decay becomes even slower as we increase the disorder strength h, Fig. 3.4d. The system shows no scrambling for a time interval of $t \sim 10[1/J_{||}]$ when $h = 10$ $[J_{||}]$ and differs from OTOC at $h = 5$ $[J_{||}]$ that is at the crossover region in Fig. 3.2. Even though for short times it looks like Anderson localization, simulation over long times reveals an MBL-like decay by showing a clear signature of logarithmic decay at intermediate times for both $h = 5$ and $h = 10$. By slightly modifying the general form given in Ref. [169] for logarithmic MBL decays, we find that the decay profiles in Fig. 3.4d could be fitted to $Re(F) = 1 - a\exp(-bt^c)$, where the parameter a determines the saturation value, and $c < 0$ for OTOC to decay as $t \to \infty$ and $F = 1$ as $t \to 0$. Similarly this form reduces to logarithmic decay, $Re(F) \sim 1 - \frac{a}{e} + \frac{a \times c}{e} \log\left(b^{1/c}t\right)$ for $b^{1/c}t \sim 1$. The fit parameters read $a = 0.725$, $b = 5.727$, $c = -0.812$ for $h = 5$ and $a = 0.154$, $b = 8.661$, $c = -0.519$ for $h = 10$ $[J_{||}]$. Therefore, the logarithmic decay is valid around $t \sim 10$ $[1/J_{||}]$ and $t = 10^2$ $[1/J_{||}]$ for $h = 5$ $[J_{||}]$ and $h = 10$ $[J_{||}]$, respectively. One can further see that Anderson localization lies in the limit $|c| \to 0$, which implies logarithmic decay should happen when $t \to \infty$, meaning that the OTOC does not decay at all. As a result, we demonstrate that there could be intermediate cases where the OTOC does not decay to zero, but to finite nonzero values in the MBL phase, which is possibly related to atypical eigenstates in the ladder-XX model [282].

In a lightcone figure (Fig. 3.6), each point has a set of discrete space x and time t coordinates, where the space dimension is emergent due to the nearest-neighbor couplings and defined as the distances between lattice sites in the lower leg of the ladder. The value of a point is OTOC, denoted as η. If we follow OTOC contours composed of the same η values, we obtain a series of space-time coordinates that give us a wavefront [122, 130, 262, 284]. A couple of wavefronts associated with different η values ranging between $\eta = 1$ and $\eta = 10^{-2}$ are shown in Fig. 3.6. These wavefronts are expected to reveal how the correlations spread in the system over time. The outermost wavefront $\eta \sim 1$ corresponds to the lightcone, while $\eta \sim 0$ corresponds to the butterfly cone in the literature [285]. The wavefronts that we

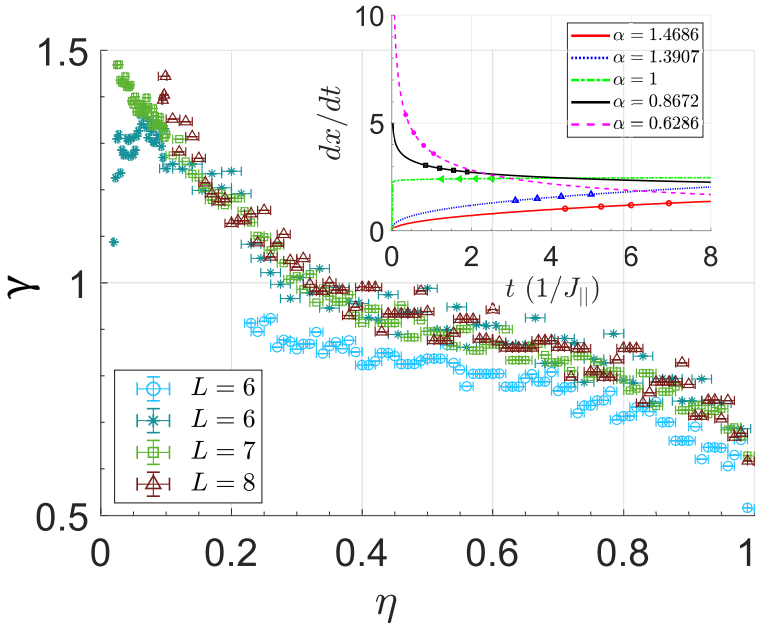

Figure 3.5: The dynamical exponent γ with respect to the OTOC contour values η extracted from analyzing data sets for $L = 6$ with observables from σ_2^z to σ_6^z (light blue-circles), with observables from σ_4^z to σ_6^z (dark blue-stars), $L = 7$ from σ_4^z to σ_7^z (green-squares) and $L = 8$ from σ_4^z to σ_8^z (red-triangles) for a random disorder strength of $h = 1$. We averaged the data over 2×10^2, 1×10^2, 1×10^2 and 1×10^1 times for first two $L = 6$, $L = 7$ and $L = 8$ system sizes, respectively. Inset: The rates of the sublinear, linear and superlinear wavefronts for a system size of $L = 7$. The markers are the data points, while the lines are the differentiation of the wavefront curves.

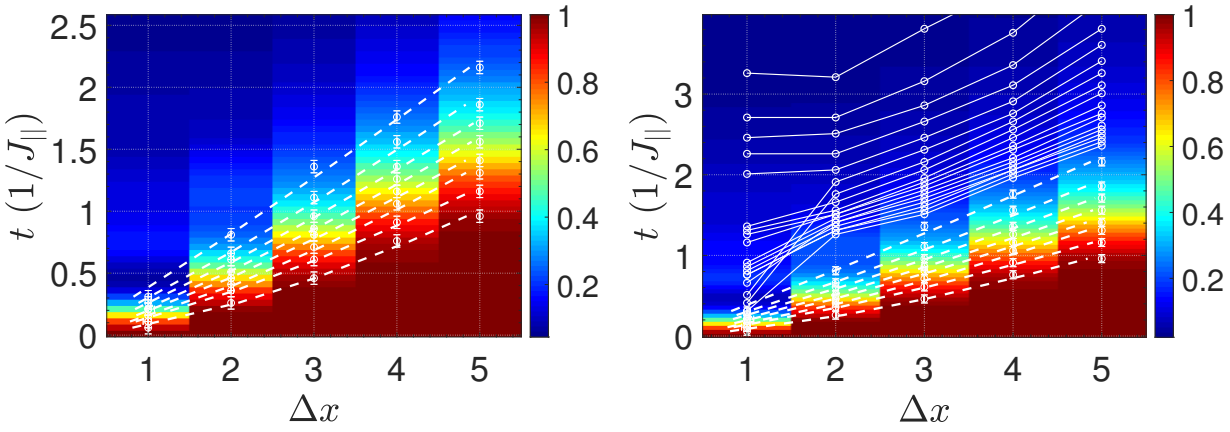

Figure 3.6: A demonstration of wavefronts for a system size of (a) $L = 8$ and (b) $L = 6$, where x-axis and y-axis are the distance and time, respectively. (a) The fitted wavefronts change from sublinear to superlinear in time between the displacements $\Delta x = 3$ and $\Delta x = 7$ units. (b) Only the sublinear wavefronts are fitted between $\Delta x = 1$ and $\Delta x = 5$ units (dotted lines), while the solid lines show irregular wavefronts appearing later in time.

extracted follow power-laws: $x \sim t^{\gamma}$ where γ is dubbed the dynamical exponent. Fig. 3.5 shows a range of γ changing from the low end of ~ 0.5 to the high end of ~ 1.5 with respect to η for different system sizes. It is not clear if γ would have a maximum in Fig. 3.5 due to the limitations in the data. We find a sublinear lightcone with $\gamma < 1$ where the spread is sub-ballistic. This observation aligns with the rare-region effects [283]. On the other hand, as the system scrambles, we observe that the wavefronts first become linear $\gamma = 1$ and then passes to a superlinear region $\gamma > 1$ in Fig. 3.5. Therefore, the butterfly cones at $\eta \sim 0$ seem to differ significantly from the lightcone at $\eta \sim 1$. The wavefront structures that demonstrate the superlinear butterfly cones can be seen in Fig. 3.6a. We plot the rates of the wavefronts in the inset of Fig. 3.5 where the sublinear lightcone ($\eta = 0.99$) initially bounds the rest. Towards the scrambling time, the linear wavefront ($\eta = 1$) seems to be the new bound on the wavefront rates. A range of sublinear wavefronts were detected in disordered Heisenberg chain before [130], implying the lightcone still differs from the butterfly cones in the dynamical exponent. Super-ballistic spread of correlations ($\gamma > 1$) has been previously observed in 1D spin chains with power-law decaying long-range interactions [122, 262, 284].

The ladder models can always be mapped to a path that passes through all the sites, e.g., zigzag or meander paths, so that 1D Jordan-Wigner transformation can be applied [286]. Such mappings bring long-range interactions due to the Jordan-Wigner strings, which could explain the super-ballistic spread appearing later in time. We note that its rate remains insignificant compared to the faster wavefronts. It is an interesting direction to see if other ladder models present similar wavefront structures. Finally, we demonstrate the irregular wavefronts appearing in the spatial region [131] when the displacement is $\Delta x = 1 - 2$ in Fig. 3.6b. The only fitted wavefronts are the sublinear wavefronts shown in Fig. 3.6b as dotted-white lines, because the wavefronts start to exhibit irregularities later in time (solid-white lines). The irregularity appears between the origin and two sites away from it, as we observe that it takes significantly greater time for the information to spread $\Delta x = 2$ units compared to $\Delta x = 1$ unit in the time interval of $t \sim 0.5$ $[1/J_{||}]$ to $t \sim 2$ $[1/J_{||}]$. Hence it seems that the information spread slows down locally and temporarily (the jump feature in Fig. 3.6b) before showing a sub-ballistic trend for $\Delta x > 2$. Furthermore, after $t \sim 2$ $[1/J_{||}]$ the jump feature is replaced by a constant line between $\Delta x = 1$ and $\Delta x = 2$ units, which points to a locally-scrambled region in the ladder while the information still spreads in the rest of the system at a finite rate. This unusual region-restricted scrambling continues until the whole ladder completely scrambles. Therefore, we conclude that different rare-region effects are at play in the ladder-XX, which calls for a more systematic future study.

3.4 OTOC Detection Protocols

The scrambling in the ladder-XX model can be detected via the interference measurement scheme on many-body states in optical lattices [94, 287] or the interferometric measurement scheme [146]. We detail both measurement schemes in the following subsections and elaborate on their advantages and disadvantages. Since both schemes need an experimental random initial state preparation, we first focus on the initial state preparation.

3.4.1 Initial state preparation

One can ideally use the whole set of Fock states to create a $\beta = 0$ initial state. However, given this process would be lengthy, we ask if using a few ($M \ll N$) randomly chosen Fock states would sufficiently mimic $\beta = 0$ initial state $\mathbb{I} \sim \sum_{j=1}^{M} |\psi_j\rangle \langle\psi_j|$, where $|\psi_j\rangle = \left\{ \left|\binom{1\ldots}{0\ldots}\right\rangle, \ldots, \left|\binom{0\ldots}{1\ldots}\right\rangle \right\}$ are Fock states for the ladder and they span the Hilbert space at half-filling. We find out that initiating an experiment with a randomly set Fock state for ~ 10 or $\sim 10^2$ times mimics the $\beta = 0$ state up to a mean error of $\sim 7 \times 10^{-3}$ or 2×10^{-3}, respectively for a system size of $L = 6$ (Fig. 3.7e). We study how the mean error scales with the sampling ratio M/N in Figs. 3.7a-3.7b for different system sizes. Here the mean of the error is calculated for the data points when the error signal $\epsilon_1(t) = |F^{\text{ex}}(t) - \frac{1}{M}\sum_j F_j(t)|$ saturates in time. The sampling ratio M/N has bounds $0 < M/N < 1$ and we observe when $M/N < 1$ the scaling is exponential and the data for all simulated system sizes could be collapsed to a single decay exponent $b \sim -2.5$ in $\epsilon_1(t) \propto a \exp(-bM/N)$, cf. Fig. 3.7a. Note that when $M/N = 1$, meaning that all Fock states are used, the error is zero up to machine precision and the OTOC is exact; and the point $M/N = 0$ is not well-defined. Except for small sizes, e.g., $L = 3$, the observed exponential scaling in Fig. 3.7a is not experimentally practical due to the increasing number of randomly-sampled Fock states. Therefore, we study the limit $M/N \to 0$ separately where we obtain power-law scaling in M/N, cf. Fig. 3.7b with $b \sim -0.5$ in $\epsilon_1(t) \propto a\,(M/N)^b$ for system sizes $L = 4 - 7$.

Remarkably, it is possible to bound the error of approximation to $\sim 10^{-2}$ with only one Fock state for $L = 7$. In fact the error decreases as a power-law with the increasing system size when only one Fock state is used to mimic the infinite temperature state (Fig. 3.7c). Fig. 3.7c shows 9 different realizations of using only one randomly-set Fock state and a single power-law curve fitted to all with $b \sim -2.26$ in $\epsilon_1(t) \propto (2L)^b$ (Appendix B.4). This observation is not utterly surprising, because a Fock state has a broad EON (eigenstate occupation number) distribution (Fig. 3.7d and Appendix B.4). An EON distribution $|c_\beta|^2$ can be defined as the overlap of the initial state with the eigenbasis of the time-evolving Hamiltonian:

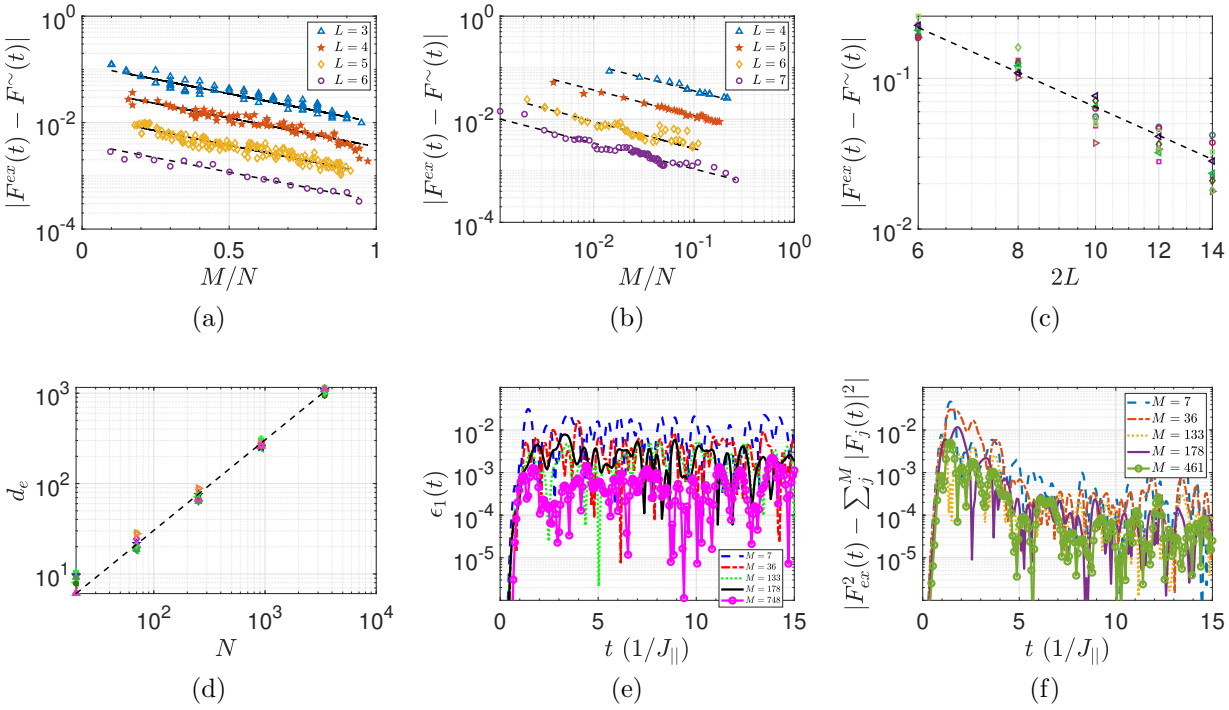

Figure 3.7: Initial state preparation at $h = 1\ [J_{||}]$. (a) The scaling of the mean error $\epsilon_1(t)$ with respect to M/N sampling ratio, where M and N are the number of randomly-sampled states and the dimension of the Hilbert space, respectively. The blue-triangles, red-pentagrams, orange-diamonds and purple-circles stand for a single-chain size of $L = 3$ to $L = 6$, where all have an exponent of $b \sim -2.5$ in the fit $\propto a\ \exp(-bM/N)$. (b) The scaling of the mean error for small M/N ratio has power-law scaling $\propto a\,(M/N)^b$ with $b \sim -0.5$ for all system sizes of $L = 4$ (blue-triangles), $L = 5$ (red-pentagrams), $L = 6$ (orange-diamonds) and $L = 7$ (purple-circles). (c) The data collapse applied to the scaling of the mean of the error $\epsilon_1(t)$ with respect to the system size for only one randomly-sampled Fock state. Each data point is a random realization where the fitted curve gives an exponent of $b \sim -2.26$ in $\epsilon_1(t) \propto (2L)^b$. (d) The scaling of the effective dimension, d_e with the Hilbert space size, N, gives linear scaling $d_e = 0.3N$, mimicking an infinite-temperature state. (e) The error signal $\epsilon_1(t)$ with respect to time, for an average of $M = 7$ (blue-dashed), $M = 36$ (red-dashed dotted), $M = 133$ (green-dotted) $M = 178$ (black-solid) and $M = 748$ (pink-circles) randomly-sampled Fock states. (f) The error signal $\epsilon_2(t) = ||F^{\text{ex}}(t)|^2 - \frac{1}{M}\sum_j^M |F_j(t)|^2|$ with respect to time, for an average of $M = 7$ (blue-dashed), $M = 36$ (red-dashed dotted), $M = 133$ (orange-dotted) $M = 178$ (purple-solid) and $M = 461$ (green-circles) randomly-sampled Fock states. Both subfigures (e)-(f) have a system size of $L = 6$.

$|\psi(0)\rangle = \sum_\beta c_\beta |\psi_\beta\rangle \to |c_\beta|^2$, where ψ_β are the eigenstates and $|\psi(0)\rangle$ is the initial Fock state. For instance, an infinite-temperature state has a uniform EON distribution: $|c_\beta|^2 = 1/N$. To be more precise, we can calculate the so-called effective dimension of the initial state, $d_e = \left(\sum_\beta |c_\beta|^4\right)^{-1}$ [36], like we did in Chapter 2 for the spinor condensates, and study the scaling of the effective dimension with the dimension of the Hilbert space. For an infinite-temperature state, $d_e = aN^\xi$ with an exponent of $\xi = 1$ and $a = 1$, which should be compared with the scaling exponent for the effective dimension of a randomly-set Fock state. Fig. 3.7d shows the data collapse on the effective dimensions of 10 different randomly-set Fock states for each system size. The fit parameters $d_e \sim 0.3N$ show that a randomly-set Fock state also gives an exponent $\xi = 1$, which more accurately demonstrates the broadness of the EON distribution. The coefficient in front is bounded for effective dimension scalings, $a \leq 1$ and we see that a randomly-set Fock state has $a \sim 0.3$. This reflects the fact that Fock state does not show uniform distribution in the eigenbasis of the Hamiltonian, and hence we have a nonzero error signal $\epsilon_1(t)$.

In conclusion, we see that the exact shape of the EON distribution is insignificant as $L \to \infty$, as long as it is a broad distribution in the eigenbasis. Therefore, only one Fock state could approximate the infinite-temperature OTOC reasonably well. We note that our analysis is valid for $h = 1$ $[J_{||}]$ disorder strength. The observation that a single Fock state could exhibit $\xi = 1$ exponent in its effective dimension scaling is possibly related to the extended eigenstates existing throughout the spectrum in the chaotic regime. Hence, whether the found power-law scaling in system size for a single Fock state as well as the exponential and power-law scalings of the error in the sampling ratio M/N, depend on the disorder strength is an interesting question for future studies and experiments. Our results also show that a few randomly-sampled Fock states could be used as an alternative approach to Haar-distributed random states in numerics to calculate OTOC with a $\beta = 0$ initial state at the chaotic regime of a model.

3.4.2 The interference measurement

$|F(t)|^2$ is the quantity to measure in the interference measurement scheme [287]. We see that $\mathrm{Im}(F(t)) \sim 0$ and $\mathrm{Re}(F(t)) \geq 0$ throughout the simulation time with the parameters used in the Chapter, thus rendering $|F(t)|^2$ a good quantity to measure. The interference measurement scheme has been proposed to probe scrambling in the Bose-Hubbard model previously [150, 183], however note that the implementation of the interference measurement further simplifies for the hard-core boson limit [287] which we utilize in the cold-atom setup of our model. The steps of the interference detection protocol follow as (Fig. 3.8a):

(i) Generate two copies of the same randomly-sampled Fock state $|\psi_j\rangle$: We can first set a 2D lattice to Mott-insulator phase with unit filling factor and then adiabatically ramp the lattice potential to a double-well potential at each site in the y-direction. This would produce $(|10\rangle + |01\rangle)/\sqrt{2}$ state for a double-well; and via suppressing the tunneling between wells in the double-wells, one can generate randomly sampled Fock states in 2D lattice at half-filling. To make two copies of the initial state, we can introduce another lattice layer in z-direction and apply the same operations of lattice potential simultaneously for both planes.

(ii) Apply $\sigma^z_{1,1}$ gate on the first spin in the lower leg in the first copy.

(iii) Apply to both copies $U(\tau)\sigma^z_{1,i}$, where $U(\tau)$ is evolution forward in time for τ and σ^z_i gate is applied to any spin i further away from the first spin in the lower leg.

(iv) *Hamiltonian sign reversal protocol*: As illustrated in Fig. 3.8b, we apply a set of gates to the lattice sites simultaneously to change the overall sign of the Hamiltonian so that we could evolve the many-body state with $-H$. Given that we shine either laser pulses [265, 288] or microwaves [289] to implement single-spin rotations, our protocol of Hamiltonian sign-reversal could be related to NMR (nuclear magnetic resonance) Hamiltonian engineering [157, 158], though with a difference of site-resolving pulses in the cold-atom setup. Remembering $R^\dagger_z(\theta)\sigma^x R_z(\theta) \to \cos\theta\sigma^x - \sin\theta\sigma^y$, $R^\dagger_z(\theta)\sigma^y R_z(\theta) \to \cos\theta\sigma^y + \sin\theta\sigma^x$, we can create sign difference in the X and Y coupling terms if we apply the $R_z(\pi)$ pulse alternating on the sites, e.g., odd-numbered and even numbered spins in the first and second legs, respectively.

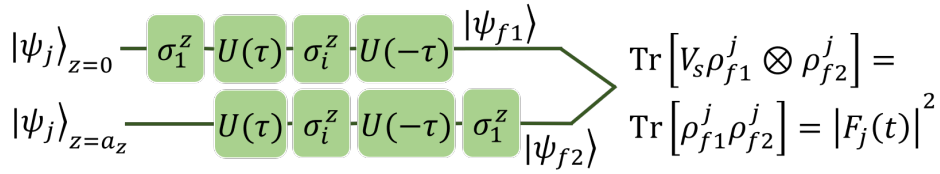

(a)

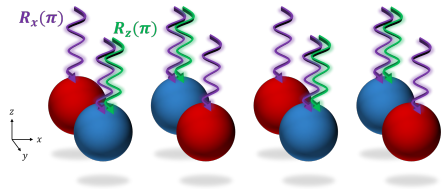

(b)

Figure 3.8: (a) The schematic that illustrates the circuit for OTOC measurement with the spin operators σ_1^z and σ_i^z. The circuit utilizes interference measurements providing $\mathrm{Tr}\left\{|\psi_{f1}\rangle\langle\psi_{f1}|\,|\psi_{f2}\rangle\langle\psi_{f2}|\right\} = |F_j(\tau)|^2$. (b) Schematic for Hamiltonian sign-reversal protocol for evolution backwards in time: red and blue spheres stand for spin up and down states, respectively. We simultaneously perform $R_z(\pi)R_x(\pi)$ gates for the odd-numbered spins in the first leg and even-numbered spin in the second leg, while only one gate $R_x(\pi)$ is applied to the rest of the spins. $R_z(\pi)$ and $R_x(\pi)$ are denoted by green and purple wiggly lines, meaning that the single-spin gates for cold-atom systems could be realized via laser pulses [265, 288] or microwaves [289].

In order to change the sign of the random disorder term, we apply $R_x(\pi)$ gate to each of the spins via utilizing $R_x^\dagger(\theta)\sigma^y R_x(\theta) \to \cos\theta\sigma^y - \sin\theta\sigma^z$. Then the gate sequence that we apply to both copies becomes,

$$\Pi_{i:odd} R_{1,i}^z R_{1,i}^x R_{1,i+1}^x R_{2,i+1}^z R_{2,i}^x R_{2,i+1}^x(\pi), \tag{3.5}$$

where $1-2$ denotes the leg number. Eq. (3.5) could be realized via a programmable acousto-optic modulator (AOM) with multiple laser outputs whose frequency differences are negligible [290] and high-resolution imaging devices that can provide single-site addressability [195, 289].

(v) Apply $\sigma_{1,1}^z$ gate on the first spin in the second copy.

(vi) Make an interference measurement between final copies $|\psi_{f1}\rangle = U(-\tau)\sigma_{1,i}^z U(\tau)\sigma_{1,1}^z|\psi_j\rangle$ and $|\psi_{f2}\rangle = \sigma_{1,1}^z U(-\tau)\sigma_{1,i}^z U(\tau)|\psi_j\rangle$ in the hard-core boson

limit [94, 287]. By measuring the swap operator on both copies [287], we can obtain $\mathrm{Tr}\{\rho_{f1}\rho_{f2}\} = |F_j(\tau)|^2$ for each $|\psi_j\rangle$ initial state where $\rho_{f1} = |\psi_{f1}\rangle\langle\psi_{f1}|$. The same measurement could be applied to the copies of initial state to check if they are identical $\mathrm{Tr}\{\rho_j^2\} = 1$. The interference measurement scheme has been applied to measure entanglement entropy [94].

(vii) Repeat the measurement protocol for M times with randomly chosen $|\psi_j\rangle$ initial states to obtain $\frac{1}{M}\sum_j |F_j(\tau)|^2$ which is equal to $|F^{\mathrm{ex}}(t)|^2$ up to an error $\lesssim 10^{-2}$ and $\sim 10^{-4}$ in decay and saturation regimes, respectively for $M \sim 10^2$ Fock states. Fig. 3.7f shows the difference between the square of the exact OTOC (Eq. (3.3)) and $\frac{1}{M}\sum_j^M |F_j(\tau)|^2$ for M randomly chosen Fock states for a system size $L = 6$.

3.4.3 The interferometric scheme

We can measure $F(t)$ with the interferometric approach [146], because the measurement of the control spin either in x- or y-basis provides the real and imaginary parts of the OTOC, respectively. Fig. 3.9 demonstrates the measurement circuit where the control spin needs to be coupled only to the first spin in the ladder. The protocol follows as:

(i) Initialize the control spin in a superposition state of $|\psi_c\rangle = (|0\rangle_c + |1\rangle_c)/\sqrt{2}$ to prepare the many-body state

$$\frac{1}{\sqrt{2}}\left[\left(\sigma^z_{1,1}\sigma^z_{1,i}(t)\,|\psi_j\rangle\right)|0\rangle_c + \left(\sigma^z_{1,i}(t)\sigma^z_{1,1}\,|\psi_j\rangle\right)|1\rangle_c\right],$$

where the ladder-XX model is simultaneously initiated in a randomly-sampled Fock state $|\psi_j\rangle$.

(ii) Apply controlled-σ_1^z operation to the first spin in the lower leg: $\left(|0\rangle_c\langle 0| \otimes \mathbb{I}_1 + |1\rangle_c\langle 1| \otimes R^z_{1,1}(\pi)\right) \otimes \mathbb{I}^{\otimes 2L-1}$.

(iii) Evolve the ladder-XX model forward in time and apply σ_i^z rotation to the spin i: $\mathbb{I}_c \otimes U(\tau)\left(\mathbb{I}^{\otimes i-1} \otimes \sigma^z_{1,i} \otimes \mathbb{I}^{\otimes 2L-i}\right)$.

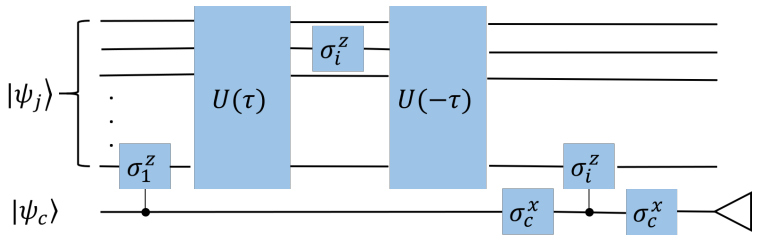

Figure 3.9: The measurement circuit for the interferometric approach [146] on the ladder-XX model with local spin observables σ_1^z and σ_i^z by using an auxiliary spin $|\psi_c\rangle$ to measure only the real part of the OTOC.

(iv) Apply Eq. (3.5) to the ladder-XX model and evolve the many-body state with $-H$ as $\mathbb{I}_c \otimes U(-\tau)$.

(v) Apply σ_c^x gate to the control spin before another controlled-σ_1^z operation, so that we have $\left(|0\rangle\langle 0|_c \otimes R_{1,1}^z(\pi) + |1\rangle\langle 1|_c \otimes \mathbb{I}_1\right) \otimes \mathbb{I}^{\otimes 2L-1}$. Further apply another σ_c^x gate to the control spin.

(vi) Make a measurement on the control spin in the x-basis to obtain the real part of the OTOC, $\mathrm{Re}\left[F_j(t)\right] = \langle \sigma_c^x \rangle = \langle \psi_j(t)| \, \sigma_c^x \, |\psi_j(t)\rangle$.

(vii) Repeat the measurement protocol for M times with randomly chosen $|\psi_j\rangle$ initial states to obtain $\frac{1}{M}\sum_j F_j(\tau)$ which is equal to $F^{\mathrm{ex}}(t)$ up to an error shown in Fig. 3.7.

Outlook. The interference measurement scheme requires two copies of the same randomly-sampled initial Fock state, which is challenging but doable. On the other hand, the interferometric approach could be realized with only one copy. However, in this measurement scheme we need to couple an auxiliary spin to the first spin and implement controlled-spin gates [291, 292] which is challenging in the current technology. Therefore both approaches have certain (dis-)advantages. An important difference that we observe in two measurement schemes are the error bounds due to the measurement output, $|F^{\mathrm{ex}}(t)|^2 = \frac{1}{M}\sum_j^M |F_j(t)|^2$ and $F^{\mathrm{ex}}(t) = \frac{1}{M}\sum_j F_j(t)$ for interference and interferometric, respectively. The error bounds are stable throughout the evolution in the interferometric approach; while they significantly lower in the saturation regime (by a factor of $\sim 10^2$) and slightly higher in the decay regime of an interference measurement. Therefore, in the case of measuring only the saturation

values of the OTOC, the interference measurement seems to be more advantageous.

3.5 Conclusions

The ladder-XX model's OTOC decay profiles and information spread show a variety of phenomena ranging from quantum chaos to MBL phase and possibly rare-region effects in the ergodic phase that we leave as a future study. We further discussed a Hamiltonian sign reversal protocol that is a novel alternative to existing approaches in cold atoms and how to apply both interference and interferometric measurements in the scrambling detection with experimental random state preparation. Our results demonstrate that the experiments could utilize only one randomly-set Fock state for sufficiently big many-body systems to reproduce infinite-temperature OTOC up to a bounded error in the chaotic regime. The ladder-XX has a more convenient experimental cold-atom setup compared to the Heisenberg chain, since it lacks Z-coupling terms, while it is still interacting due to its quasi-1D nature. Thus, it can be more easily implemented in the laboratory to further investigate scrambling and understand how scrambling changes in the transition from 1D to 2D.

Chapter 4

The Connection Between Information Scrambling and Quantum Phase Transitions

In this chapter, we elucidate the relation between out-of-time-order correlators (OTOCs) and quantum phase transitions via analytically studying the OTOC dynamics in a degenerate spectrum. Our method points to key ingredients to dynamically detect quantum phases via out-of-time-order correlators for a wide range of quantum phase transitions and explains the existing numerical results in the literature. We apply our method to a critical model, the XXZ chain that numerically confirms our predictions.

4.1 Introduction

Out-of-time-order correlators (OTOCs) [145] probe information scrambling in quantum systems of different nature c.f. Refs. [133, 134, 142, 150, 156, 162, 167] and Chapter 3, and reflect the symmetries [162, 167] as exemplified in Chapter 3 or lack thereof [133, 140, 162] of the underlying Hamiltonian. An OTOC, unlike a time-ordered four-point (or two-point) correlator [139], can determine the spatial and temporal correlations throughout the sys-

tem, thus giving rise to a bound on information spread [130, 132] as also demonstrated in Chapter 3. Through such bounds and the decay rate of an OTOC, one can dynamically detect thermal [150, 162] and localized phases [139, 162, 167–169] as again shown in Chapter 3. Recently OTOC has been numerically observed to be sensitive to phase transitions either signaling criticality in a diverging Lyapunov exponent [183] or showing signatures of symmetry-broken phases in its saturation value [181]. The latter led to more research that shows the relationship emerging in other forms, e.g., in excited states [185], or with more experimentally-relevant platforms and system parameters [293]. The interest in providing more verification for such an emergent relationship is understandable, not only because the relationship points to a practical potential for OTOC in the dynamical detection of quantum criticality, but also the underlying reason of this relationship was not understood [181]. It is indeed an intriguing question how a chaos-detecting and out-of-time ordered correlator that is contributed by presumably the entire spectrum could also probe ground state physics. The reasons of this relationship remain unknown as well as an answer to whether the relationship is universal. Motivated by these questions, here we develop a method on OTOC dynamics to obtain intuition for the emerging connection between quantum phase transitions and out-of-time-order correlators. Remarkably it is possible to dynamically decompose OTOC and show that the ground state physics is the leading order contribution to it under the criteria that our method provides. This is the origin why OTOC saturation value could detect the ground state degeneracy. Therefore, we reach the conclusion that the OTOC is sensitive to long-range order, e.g., its steady-state value presents a dynamical phase diagram, while the quasi-long range order is not visible to it, e.g., its steady-state value remains featureless in the quasi-long range ordered phase. Our method provides additional insights regarding the relationship, e.g., (i) the relationship is not restricted to already-studied models and 1D [181, 293]; (ii) the relationship can be extended to include the phase transitions in other eigenstates [185]. Hence, our theory elucidates the reasons of this *unexpected* connection, renders it intuitive and universal with further insights. To verify our method, we study the

dynamics of 1D critical XXZ chain, where there are Ising and critical XY phases.

4.2 Method

Our aim is to be able to come up with an expression that predicts the saturation value of OTOC for long times in the spirit of Eigenstate Thermalization Hypothesis (ETH) [294,295]. Complementary to the definition in previous Chapter Eqs. (3.3) and (3.4), OTOC can also be defined as

$$F(t) \;=\; \left\langle W^\dagger(t)V^\dagger W(t)V\right\rangle, \tag{4.1}$$

where V and W are local operators and the expectation value is over an initial state $|\psi(0)\rangle$. This initial state could be chosen as the ground state [156,181], or a random Haar-distributed state [130] which is also utilized in Chapter 3 to approximate an equiprobable state $\mathcal{I}$ in Eq. (4.1) [277, 296] (see Appendix C). Eventually, the original definition that is the out-of-time-order commutator $-\mathrm{Tr}\left(\frac{\exp[-\beta H]}{Z}\left[W(t),V\right]^2\right)$ [140] could be reexpressed in terms of the OTOC of operators W and V with an initial state at the inverse temperature β (see also Eq. (3.3)). Therefore we can probe the information scrambling through OTOCs [146, 150, 156, 157], as shown in Chapter 3.

Given $|\psi(t)\rangle = \sum_\alpha c_\alpha e^{-iE_\alpha t}|\psi_\alpha\rangle$, where $|\psi_\alpha\rangle$ are eigenstates of the Hamiltonian with the associated eigenvalues E_α, we define a modified initial state $|\psi'(0)\rangle = V|\psi(0)\rangle$ and have $|\psi'(t)\rangle = \sum_\beta b_\beta e^{-iE_\beta t}|\psi_\beta\rangle$ where $b_\beta = \sum_\tau V_{\beta\tau}c_\tau$ and $\langle\psi_\beta|V|\psi_\tau\rangle = V_{\beta\tau}$ are eigenstate expectation values [40]. Then the OTOC, Eq. (4.1), can be recast to a fidelity measure of 3-point function, and with the help of completeness relation $\sum_\gamma |\psi_\gamma\rangle\langle\psi_\gamma| = \mathbb{I}$, it becomes

$$F(t) = \sum_{\alpha,\beta,\gamma,\gamma'} c_\alpha^* b_\beta e^{-i(E_\beta - E_\alpha + E_\gamma - E_{\gamma'})t} W^\dagger_{\alpha\gamma} V^\dagger_{\gamma\gamma'} W_{\gamma'\beta}.$$

Now one can derive the saturation value for long times as well as dynamical features, such

as revival timescales in integrable Hamiltonians with the procedure outline in Chapter 2.

We study the saturation value at long times, since this value is expected to contain the signature of quantum phases. For long enough times, equilibration in OTOC dynamics can be obtained only when the phase decoheres. Then the equilibration value can be obtained by requiring $E_\beta - E_\alpha + E_\gamma - E_{\gamma'} = 0$. This condition can be satisfied with four different scenarios: (i) $E_\alpha = E_\beta$ and $E_\gamma = E_{\gamma'}$; (ii) $E_\alpha = E_\gamma$ and $E_\beta = E_{\gamma'}$; (iii) $E_\alpha = E_\beta = E_\gamma = E_{\gamma'}$, which is contained both in (i) and (ii); (iv) $E_\beta - E_\alpha + E_\gamma - E_{\gamma'} = 0$ with $E_\beta \neq E_\alpha \neq E_\gamma \neq E_{\gamma'}$. If a nondegenerate spectrum is assumed, i.e., $E_\alpha = E_\beta$ implies $\alpha = \beta$, the OTOC reduces to,

$$\begin{aligned} F_{t\to\infty} &= \sum_{\alpha,\gamma} c_\alpha^* b_\alpha |W_{\alpha\gamma}|^2 V_{\gamma\gamma}^\dagger + \sum_{\alpha,\beta} c_\alpha^* b_\beta W_{\alpha\alpha}^\dagger V_{\alpha\beta}^\dagger W_{\beta\beta} - \sum_{\alpha} c_\alpha^* b_\alpha |W_{\alpha\alpha}|^2 V_{\alpha\alpha}^\dagger \\ &+ \sum_{\alpha\neq\beta\neq\gamma\neq\gamma'} c_\alpha^* b_\beta W_{\alpha\gamma}^\dagger V_{\gamma\gamma'}^\dagger W_{\gamma'\beta}, \end{aligned} \tag{4.2}$$

with four terms corresponding to four conditions (i)-(iv), respectively. The last term associated with the condition (iv) can be in fact eliminated by invoking the Definition 1 in Chapter 1, e.g., the condition of non-degenerate energy gaps. However, we keep this term for completeness in the rest of the Chapter.

We note that writing OTOC as in Eq. (4.2) is useful to understand the quantum chaotic systems better, e.g., in chaotic spin chains with conserved quantities that also obey ETH, the decay of OTOC to zero is not supposed to be exponential, but inverse polynomial in system size [297] and OTOCs capture eigenstate correlations that ETH cannot [166]. These correlations can readily be seen in the first, second and the fourth terms of Eq. (4.2). See Appendix C.5 for some remarks that immediately follow from Eq. (4.2) about systems with nondegenerate chaotic spectra. Now we are going to generalize Eq. (4.2) to a form, which is more generic and allows degeneracy in the energy spectra, because a quantum phase transition usually involves energy degeneracy, e.g., degeneracy from spontaneous symmetry breaking or other sources [187]. We group all eigenstates of the Hamiltonian into degenerate

sets labeled by θ, and each state in its corresponding set is denoted by α for an eigenstate $\psi_{[\theta,\alpha]}$. The OTOC can be reorganized with the new notation, which is one main result of this chapter,

$$\begin{aligned} F(t\to\infty) &= \sum_{\theta\theta'}\sum_{\alpha\beta\gamma\gamma'} c^*_{[\theta,\alpha]}\Big(b_{[\theta,\beta]}W^\dagger_{[\theta,\alpha][\theta',\gamma]}V^\dagger_{[\theta',\gamma][\theta',\gamma']}W_{[\theta',\gamma'][\theta,\beta]} \\ &+ b_{[\theta',\beta]}W^\dagger_{[\theta,\alpha][\theta,\gamma]}V^\dagger_{[\theta,\gamma][\theta',\gamma']}W_{[\theta',\gamma'][\theta',\beta]}\Big) \\ &+ \sum_{\alpha\beta\gamma\gamma'}\Big(-\sum_{\theta} c^*_{[\theta,\alpha]}b_{[\theta,\beta]}W^\dagger_{[\theta,\alpha][\theta,\gamma]}V^\dagger_{[\theta,\gamma][\theta,\gamma']}W_{[\theta,\gamma'][\theta,\beta]} \\ &+ \sum_{\theta\neq\theta'\neq\phi\neq\phi'} c^*_{[\theta,\alpha]}b_{[\theta',\beta]}W^\dagger_{[\theta,\alpha][\phi,\gamma]}V^\dagger_{[\phi,\gamma][\phi',\gamma']}W_{[\phi',\gamma'][\theta',\beta]}\Big). \end{aligned} \tag{4.3}$$

Here, $\theta, \theta', \phi, \phi'$ denote degenerate sets while $\alpha, \beta, \gamma, \gamma'$ denote quantum states in their corresponding sets. Eq. (4.3) can determine the saturation value of OTOC accurately if the OTOC saturates at a finite time. If the OTOC does not saturate or shows transient effects, Eq. (4.3) still predicts the time-average of OTOC signal $\bar{F} = 1/\mathcal{T}\int dt F(t)$ over a time interval $\mathcal{T}$ with sufficient accuracy. In this sense, Eq. (4.3) is not limited to long-time dynamics $t\to\infty$ (see Appendix C).

We look for the criteria that the ground state subspace contribution is leading order in the OTOC saturation value Eq. (4.3). For this, we first set $W = V$ as the order parameter observable in Eq. (4.3) for convenience. Then we expand the coefficients $b_{[\theta,\beta]} = \sum_{\kappa,\tau} W_{[\theta,\beta][\kappa,\tau]}c_{[\kappa,\tau]}$ in Eq. (4.3) by using the initial state. If (i) the initial state is set to the state where the phase transition is expected to happen, e.g., the ground state(s) $c_{[1,1]} = 1$; and (ii) we apply an ansatz on the matrix elements of the observable projected on this state, e.g., $|W_{[1,\alpha][\theta,\beta]}|^2 \ll 1$, where $\theta \neq 1$ is a different energy subspace than the subspace of the ground state(s), we observe the following dynamical decomposition:

$$F(t\to\infty) = F_{\rm gs}(t\to\infty) + F_{\rm ex}(t\to\infty). \tag{4.4}$$

Here $F_{\text{gs}}(t \to \infty)$ is the ground subspace contribution, whereas the $F_{\text{ex}}(t \to \infty)$ is the contribution of higher energy excitations. When the criteria are satisfied, the latter is a correction to the ground-state physics in the OTOC in the ordered phase, and this is the second part of our conjecture. The assumption on the initial state sets the scrambling discussed in the rest of the chapter to effectively zero temperature. Whereas the operator ansatz becomes even more specific for the phase of interest. If there is a symmetry-broken long-range order to capture, the fluctuations between the matrix elements of the observable are suppressed in the ground state subspace, meaning there is at least a pair of matrix elements accumulating the order $\to |W_{[1,\alpha][1,\beta]}|^2 \sim \mathcal{O}(1)$. This modifies the operator ansatz as $|W_{[1,\alpha][1,\beta]}|^2 \gg |W_{[1,\gamma][\theta,\gamma']}|^2$ for the ordered phase. Thus, we derive the expression for $F_{\text{gs}}(t \to \infty)$ in the ordered phase as,

$$F_{\text{gs}}(t \to \infty) \sim \sum_{\beta,\gamma,\gamma'} W_{[1,1][1,\gamma]} W_{[1,\gamma][1,\gamma']} W_{[1,\gamma'][1,\beta]} W_{[1,\beta][1,1]}, \tag{4.5}$$

while the operator ansatz simultaneously implies that the OTOC is dominated by the ground state physics, $F_{\text{gs}} \gg F_{\text{ex}}$ in the ordered phase. On the other hand, the fluctuations between the matrix elements of the observable are maximal in a disordered phase, implying $W_{[1,\alpha][1,\beta]} \sim 0$ for all states in the ground state subspace, which results in $F_{\text{gs}}(t \to \infty) \sim 0$. Therefore, the OTOC is dominated by the higher energy levels in the spectrum $F_{\text{ex}}(t \to \infty)$. This result is an important insight that originates from the dynamical decomposition method and cannot be observed in real-time dynamics simulations, e.g., in Ref. [181]. In addition, the operator ansatz $|W_{[1,\alpha][\theta,\beta]}| \ll 1$ guarantees a bounded correction term $F_{\text{ex}}(t \to \infty) \ll 1$. As a result, (i) the OTOC is able to capture the degeneracy in the ground state (Eq. (4.5)) and, (ii) the correction of the excited states always remains bounded; all of which explains why the OTOC differentiates an ordered phase from a disordered one, e.g., in ground state [181] or excited-state [185] phase transitions. A mixed initial state (e.g. finite or infinite temperature) violates the initial state assumption, hence suggesting a smoothed phase boundary by

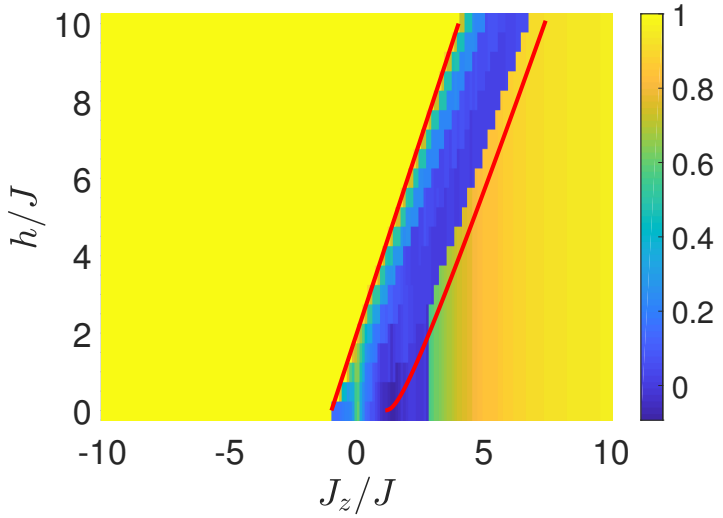

Figure 4.1: Phase diagram based on the OTOC saturation values via Eq. (4.3), x-axis is the spin interaction strength in the z-direction J_z and y-axis is the magnetic field h, for $N = 14$ system size and σ_i^z bulk spin observable, when periodic boundary conditions are set and the initial state is a ground state. The red lines are the phase boundaries based on Bethe ansatz technique for infinite-size system [65].

washing away the sharp signature at the transition point [293]. Hence the dynamical decomposition method reveals the key ingredients of the emergent connection between information scrambling and symmetry-breaking phase transitions, rendering this unexpected numerical observation [181] a fundamental connection.

Advanced numerical methods (Lanczos, tensor networks) can be employed to determine only the lowest-lying states to give the leading order term in OTOC, Eq. (4.5). In this sense, Eq. (4.5) provides us a low-cost alternative to simulating the real-time OTOC dynamics in the computation of the OTOC saturation value when we use the OTOC to probe criticality. Finally, we predict that the ground state contribution to the OTOC saturation cannot efficiently distinguish quasi-long range order from a disordered phase. Because, the quasi-long range order produces zero expectation value for the order parameter (per site): $W_{[1,\alpha][1,\beta]} \sim 0$, similar to a disordered phase, and hence $F_{\text{gs}}(t \to \infty) \sim 0$ follows with correction term dominating the OTOC saturation $F(t \to \infty)$. In the following we will provide verification for our method and theory on the 1D XXZ model.

4.3 Model and the Results

The Hamiltonian of the XXZ chain reads,

$$H = J\sum_i \left(\sigma_i^x\sigma_{i+1}^x + \sigma_i^y\sigma_{i+1}^y + \frac{J_z}{J}\sigma_i^z\sigma_{i+1}^z\right) + h\sum_i \sigma_i^z,$$

where σ_i^n are spin-1/2 Pauli matrices with energy scale set to J and hence time scale set to $1/J$; J_z/J and h are the z-axis spin coupling strength and the magnetic field strength, respectively. The red lines in Fig. 4.1 show the phase boundaries produced by an exact method (Bethe Ansatz) for an infinite-size system. Therefore, this model has three phases: two gapped Ising phases (ferromagnetic and antiferromagnetic) at large $|J_z/J|$ and a gapless XY phase with quasi-long range order for small $|J_z/J|$, i.e., the Berezinskii-Kosterlitz-Thouless transition [298, 299]. We choose the OTOC operators as σ_i^z or σ_i^x for the spin at the ith site, based on the order parameters of the ferromagnetic Ising phase ($\sum_i \sigma_i^z$), antiferromagnetic Ising phase ($\sum_i (-1)^i\sigma_i^z$), and the XY-phase ($\sum_i \sigma_i^x$). Fig. 4.1 shows the phase diagram based on the saturation values of OTOCs with σ_i^z [computed using Eq. (4.3) for a system of $N = 14$ spins]. We numerically confirm our theory with OTOC saturation values that are either nonzero or nearly zero in the Ising and XY phases, respectively. In fact, the OTOC recovers the phase boundaries of the Bethe ansatz solution: the agreement is perfect at the ferromagnetic-XY phase boundary and approximate at the antiferromagnetic-XY boundary due to significant finite-size effects (see Appendix C).

We plot two cross-sections from Fig. 4.1 in Fig. 4.2a where the lines with orange-squares ($h/J = 0$) and blue-circles ($h/J = 4$) are the saturation values, Eq. (4.3) for a short-time $tJ \sim \frac{\pi}{4}10^1$ (long-time results in the Appendix C). We also plot the leading order term in the saturation, $F_{\text{gs}}(t \to \infty)$ in Fig. 4.2a with purple-cross ($h/J = 0$) and red-diamond ($h/J = 4$) lines. The OTOC saturation exactly reduces to the ground state contribution with no correction $F_{\text{ex}} = 0$ in the Ising-ferromagnet, meaning that the saturation value in the ordered phase is exactly predicted by the Eq. (4.5). The reason follows as: the spins are fully polarized

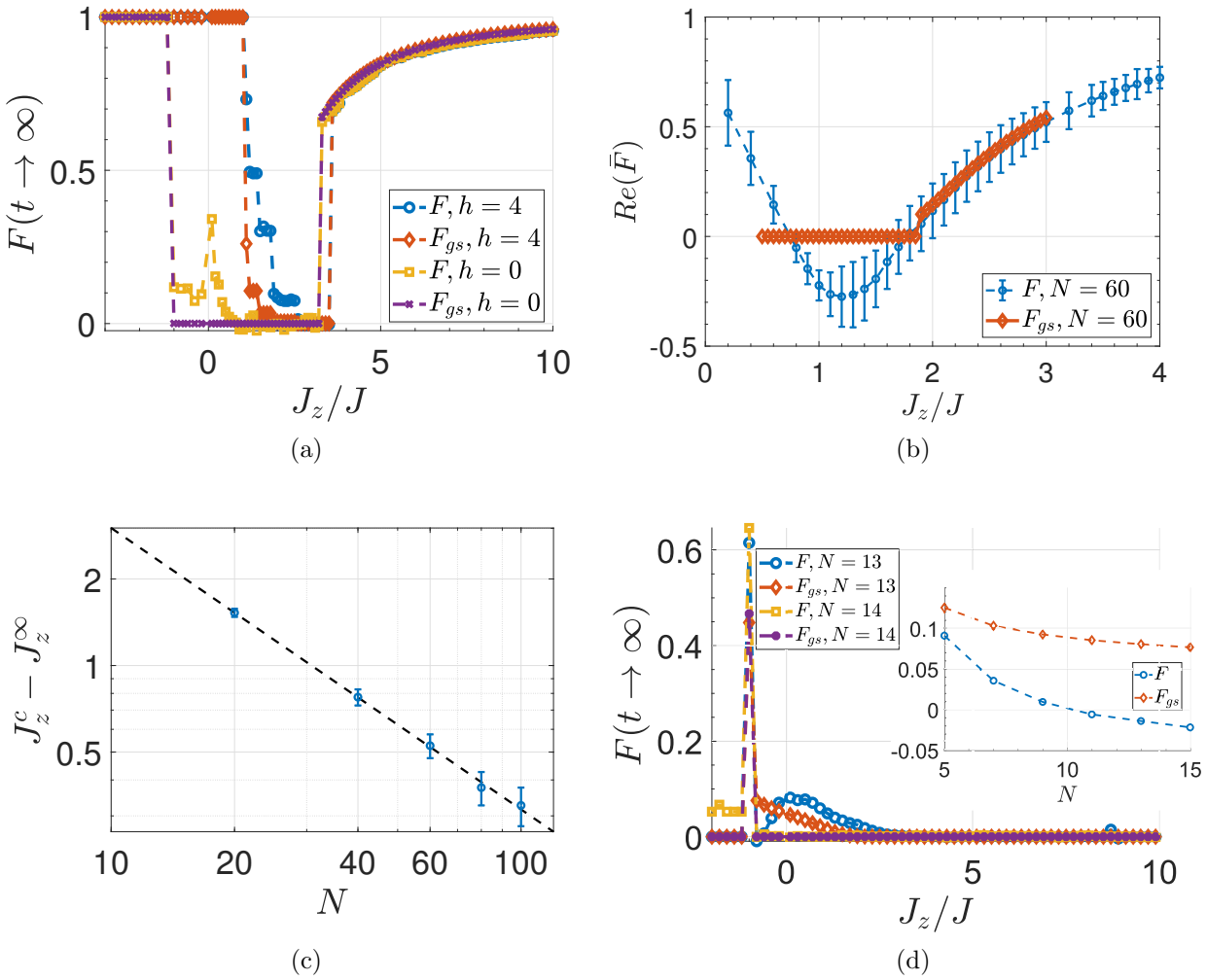

Figure 4.2: (a) The OTOC saturation values for a periodic-boundary chain with $N = 14$ size and a short-time of $tJ = \frac{\pi}{4}10^1$ at fields $h/J = 0$ (orange-squares: Eq. (4.3), purple-crosses: Eq. (4.5)) and $h/J = 4$ (blue-circles: Eq. (4.3), red-diamonds: Eq. (4.5)), for σ_i^z observable. (b) Real-time dynamics (blue-circles) averaged over a time interval $tJ = 10$, $\bar{F}$, and its ground state contribution F_{gs} (orange-diamonds) with DMRG algorithm and MPS for $N = 60$ at $h/J = 0$. (c) System size scaling of F_{gs} shows $J_z^c = aN^\xi + J_z^\infty$ with exponent $\xi = -0.98$ and $J_z^\infty = 1.02$. (d) The OTOC saturation values for σ_i^x observable at $h/J = 0$, $N = 13$ (blue-circles: Eq. (4.3), red-diamonds: Eq. (4.5)) and $N = 14$ (orange-squares: Eq. (4.3), purple-crosses: Eq. (4.5)) for time $tJ = \frac{\pi}{4}10^3$. Inset: System-size scaling of Eq. (4.3) (blue-circles) and Eq. (4.5) (red-diamonds) at $J_z/J = -0.9$.

in the ferromagnetic ground states, and they belong to the opposite magnetization sectors of the Hamiltonian which has magnetization conservation $[H, S_z] = 0$ ($S_z = \sum_i \sigma_i^z$). Since they are the only states of their corresponding magnetization sectors, the fluctuations in the matrix elements are exactly zero, $|W_{[1,\alpha][\theta,\beta]}| = 0$. This is why the system does not scramble information at all $F(t \to \infty) = 1$, even though the XXZ model is an interacting model. We emphasize that this nonscrambling is not due to integrability of XXZ model, rather it is the signature of critical order. The rotational symmetry also protects the ferromagnetic ground states from hybridizing, all of which results in no finite-size effects at the phase boundary from ferromagnet to XY-paramagnet. In the disordered-XY phase ($h/J = 0$), the ground state contribution is zero $F_{\text{gs}} = 0$, leaving the correction term to dominate the saturation value, however with a small magnitude as explained above. This is the reason of the mismatch between the OTOC saturation value and its leading order term, seen in the XY-phase of Fig. 4.2a, while we are still able to differentiate the disordered phase from the ordered phases. Finally, in the Ising-antiferromagnet the exact agreement between Eqs. (4.3) and (4.5) takes place only at the $J_z/J \to \infty$ limit. As we approach the phase boundary towards the XY-phase, the fluctuations between matrix elements gradually increase, $|W_{[1,\alpha][1,\beta]}| \to 0$ (see Appendix C), result in a nonzero but small correction term to the ground-state contribution and eventually drive the phase transition. Since the finite-size effect is significant for small sizes with exact methods, we apply density-matrix renormalization group (DMRG) algorithm with matrix product states (MPS) [300] to a system with $N = 60$ and compute the real-time dynamics averaged over a short-time interval of $tJ = 10$ shown with blue-circles in Fig. 4.2b with orange-diamonds being F_{gs}, Eq. (4.5). Note that the transition point significantly shifts towards the equilibrium phase transition point, $J_z/J = 1$. We extract the system-size scaling parameters from our DMRG computations, Fig. 4.2c and observe that the system indeed approaches to the equilibrium transition point when $N \to \infty$, $J_z^c = aN^\xi + J_z^\infty$ with exponent $\xi = -0.98$ and $J_z^\infty = 1.02$ with a power-law scaling.

We plot the OTOC with σ_i^x observable for $N = 13$ (blue-circles) in Fig. 4.2d: the OTOC

saturation remains small in all three phases and thus the OTOC can hardly distinguish the XY-ordered from XY-disordered phases. When the chains with even number of spins are used ($N = 14$, orange-squares) in the theory, we do not even obtain any difference between the phases. This is in agreement with our theoretical predictions discussed previously. Additionally, the fluctuations between the matrix elements of quasi-long range order parameter σ_i^x are always maximal regardless of the phase. Hence, we observe the mismatch between the OTOC saturation and its ground state contribution (red-diamonds $N = 13$ and purple crosses $N = 14$). The inset of Fig. 4.2d shows that the OTOC saturation value and its ground state contribution both decrease with the system size for odd-numbered chains, exhibiting that the OTOC saturation cannot capture the quasi-long range order in bigger systems and thermodynamic limit. We briefly note that the detection of the order at $J_z/J = -1$ is robust due to the massive degeneracy in the ground state at this point of different symmetry (SU(2) symmetry).

4.4 Conclusions

Our theoretical predictions on the XXZ model can be experimentally observed with cold atoms [301]. Based on the studies in the literature [181, 185, 293] and our results in the XXZ model, our method seems to be universal in explaining the reasoning behind the relationship between scrambling and the quantum criticality. In this sense, our method is an analogue of the Eigenstate Thermalization Hypothesis: It tells us the criteria of how scrambling probes criticality; though it is independent of the integrability of the system, unlike ETH. Dynamical decomposition of OTOC is a complementary tool to the real-time evolution of a state in determining the OTOC saturation value. However in addition to providing the saturation value, it also presents us the conditions for OTOC to show either order or disorder. Based on this fact, the leading order term in our theory, Eq. (4.5), could mark the phase transition points via system-size scalings. In conclusion, given that the initial state of OTOC is a state

where the phase transition is expected to happen and the off-diagonal matrix elements of the observable are sufficiently suppressed in this state (or degenerate state subspace), OTOC could be used to dynamically detect the quantum phases with long-range order and capture the symmetry-breaking quantum phase transitions.

Chapter 5

Topologically Induced Prescrambling

We report a numerical observation where the infinite-temperature out-of-time-order correlators (OTOCs) directly probe quantum phase transitions at zero temperature, in contrast to common intuition where low energy quantum effects are washed away by strong thermal fluctuations at high temperature. By comparing numerical simulations with exact analytic results, we determine that this phenomenon has a topological origin and is highly generic, as long as the underlying system can be mapped to a 1D Majorana chain. Using the Majorana basis, we show that the infinite-temperature OTOCs probe zero-temperature quantum phases via detecting the presence of Majorana zero modes at the ends of the chain that is associated with 1D Z_2 topological order. Hence, we show that *strong zero modes* also affect OTOCs and scrambling dynamics. Our results demonstrate an intriguing interplay between information scrambling and topological order, which leads to a new phenomenon in the scrambling of generic nonintegrable models: topological order induced prescrambling, paralleling the notion of prethermalization of two-time correlators that defines a time-scale for the restricted scrambling of topologically-protected quantum information.

5.1 Introduction

Out-of-time-order correlators (OTOCs) have become a widely-appreciated tool to measure the correlation build-up in space and time, and hence quantitatively characterize information scrambling in interacting many-body systems [133, 134, 142, 156, 167]. Started off as a theoretical tool to understand quantum information in a black hole [133, 261] its impact quickly expanded to a wide variety of subjects including but not limited to: quantum chaos [132, 140, 150, 157, 162], many-body localization [139, 162, 167, 169] (c.f. Ch. 3), quantum integrability [132, 157, 179, 180], quantum criticality [183] and recently symmetry-breaking quantum phase transitions in Ref. [181] and Chapter 4 in this dissertation.

For completeness, let us repeat the definition of OTOC here. At temperature $T = 1/\beta$, an OTOC is defined as,

$$F(t) \;=\; \mathrm{Tr}\left(e^{-\beta H} W^\dagger(t) V^\dagger W(t) V\right), \tag{5.1}$$

where W and V are local quantum operators and H is the Hamiltonian. At infinite temperature ($T = \infty$ and $\beta = 0$), the Boltzmann weight $e^{-\beta H}$ becomes the identity operator and thus the OTOC reads

$$F(t) = \frac{1}{M}\sum_{n=1}^{M} \langle \psi_n | W^\dagger(t) V^\dagger W(t) V | \psi_n \rangle \approx \langle \psi_h | W^\dagger(t) V^\dagger W(t) V | \psi_h \rangle . \tag{5.2}$$

Here we sum over a complete basis of the Hilbert space of dimension M, while in the second line, we use a random state $|\psi_h\rangle$ drawn from the Haar measure [130] like in Chapter 3 to approximate an infinite-temperature state in a correlation function, e.g., Eq. (5.1) [84, 85, 277, 296, 302].

The OTOC of a generic system is expected to decay to zero fast where the rate of decay carries information on the chaotic properties of the system, and to saturate at zero in long time dynamics. Saturation at zero indicates that the system scrambles information

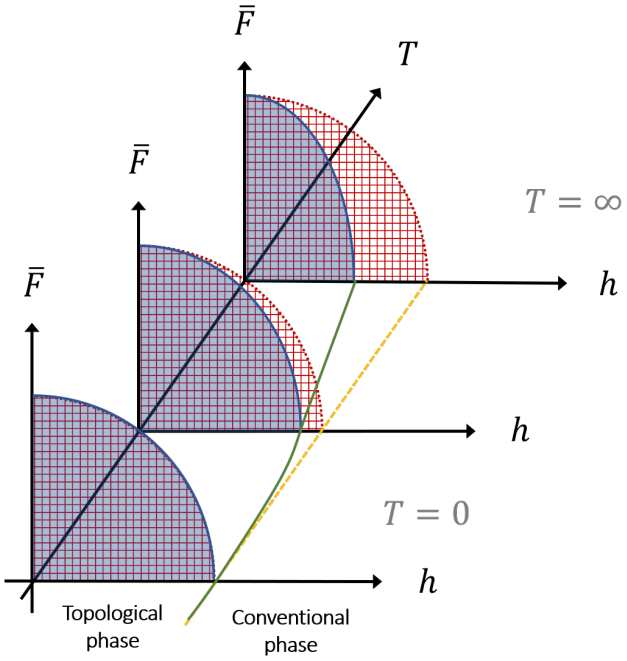

Figure 5.1: The schematic of dynamic phase boundaries determined by OTOC time-average $\bar{F}$ with respect to control parameter h and temperature T. The system experiences a topological phase transition (TPT) defined at $T = 0$ temperature from Z_2 topologically ordered phase to a trivial phase. The graphics with red-grids and solid-blue show how the topological phase survives in dynamics and at higher temperatures for integrable and generic nonintegrable models, respectively. While integrable models recover zero-temperature phase boundary at infinite temperature, nonintegrable models experience a shift that tends to destroy order quicker than at low temperature.

completely, whereas a finite saturation value points to a restricted scrambling [137]. In this Chapter, we focus on the regime starting shortly after the (initial) decay of OTOC and lasts for a time interval of $\mathcal{T}$. In the previous Chapter, we showed that the OTOC saturation value at zero-temperature exhibits order parameter-like behavior, and thus can directly probe the long-range quantum order and quantum phase transitions. In contrast to the naive intuition, where thermal fluctuations wash away low energy quantum effects at high temperature, in this chapter we observe an emergent relation between *infinite-temperature information scrambling* and *zero-temperature Z_2 topological order* in the bulk in multiple model systems, e.g., non-interacting, interacting and/or nonintegrable. The effect is robust where the qualitative features remain invariant regardless of microscopic details, e.g., integrability and symmetries. In particular, by setting W and V as local degrees of freedom localized near the edge of the system, we find that the time-average of OTOC $\bar{F} = 1/\mathcal{T} \int dt F(t)$ (or equivalently the saturation value, if the OTOC saturates) behaves like an order parameter (Fig. 5.1). It is worthwhile to emphasize that the infinite temperature OTOCs are effective tools for detecting chaos that is based on the entire energy spectrum [132, 140, 150, 157, 162] as already demonstrated in Chapter 3. Hence it is surprising and highly not obvious that this correlator can also directly probe zero temperature physics of the ground state, such as quantum phase transitions. *Then what is the underlying physics that allows the infinite temperature out-of-time-order correlator at the edge to accurately sense the bulk ground state physics and capture the bulk phase transition? Is this a generic feature?*

Through a careful analysis, we find that this connection arises universally as long as the quantum system can be mapped to a Majorana chain (1D superconductor) [53], and $\bar{F}$ value of edge operators serves as the Z_2 topological order parameter. It is known that Z_2 topological order results in a two-fold degeneracy for all energy eigenstates of the entire spectrum; and recently it is pointed out that this degeneracy structure of Z_2 topological order has a highly nontrivial impact on dynamics at any temperature, e.g., long coherence times for edge spins in Ref. [115] while the zero modes surviving in the dynamics is dubbed as *strong zero modes*,

and pre-thermalization effect in Ref. [303]. Our results extend this impact of Z_2 topological order to information scrambling and OTOCs, opens up new avenues to dynamically detect and study topological order through utilizing information scrambling as an order parameter. Paralleling the well-known prethermalization effect appearing in simpler correlators [35, 303, 304], we find that a new time-scale appears in information scrambling when Z_2 topological order [305] exists. We name this phenomenon topologically induced prescrambling and hence define the time-scale as prescrambling time. Fig. 5.2 shows a cartoon picture of prescrambling for a generic (nonintegrable) model with solid-red line where the system experiences restricted scrambling, $\bar{F} \neq 0$, forming a plateau at τ_{presc} for a period of time $\mathcal{T}$ after the first OTOC decay and preceding the full scrambling at τ_{sc} in a topological phase. On the other hand, the purple-dotted line in Fig. 5.2 shows the expected rapid OTOC decay until scrambling time τ_{sc} for a generic system with no topological order. Prescrambling (green panel) plateau in Fig. 5.2 survives at infinite-time in the thermodynamic limit for systems with extensive number of symmetries, e.g., non-interacting and/or integrable limits, with no full scrambling occurring. Such systems might demonstrate $\bar{F} \neq 0$ in their trivial phases [162, 168] as observed in Chapter 3, nevertheless it is still possible to mark down the topological phase transition due to sharp transition signatures. We compare the infinite-temperature dynamic phase boundary with zero-temperature quantum phase boundary where topological order starts to develop in Fig. 5.1 and observe that they perfectly coincide with each other in integrable systems. Away from the integrability, the dynamical phase boundary significantly shifts away from the zero-temperature phase boundary, although the qualitative trend of $\bar{F}$ survives.

The dynamical detection of topological order has been under intensive investigation [115, 213, 303, 306, 307]. Furthermore, the topological insulators and superconductors have been studied [308–312] and classified [313] according to their non-equilibrium dynamics rather in an analogy to the classification tables for topological states of matter [314] superposed with the notion of dynamical quantum phase transitions [199, 315, 316]. Thus, understanding if

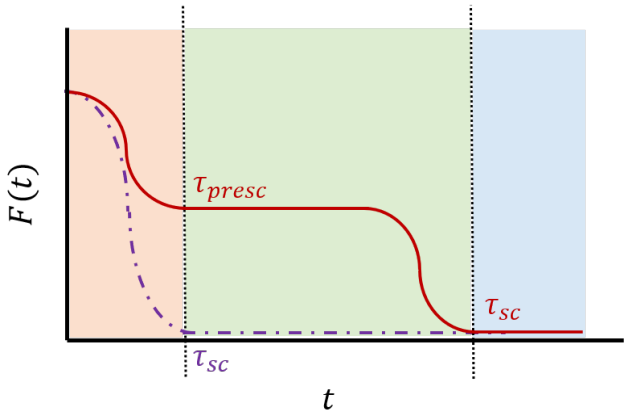

Figure 5.2: The schematic of infinite-temperature OTOC evolving in time t for a quantum system with (solid-red line) and without (dotted-purple line) Z_2 topological order. A generic system with Z_2 topological order would exhibit topologically induced prescrambling $\bar{F} \neq 0$ before fully scrambles at scrambling time τ_{sc}. We coin τ_{presc} for the prescrambling time-scale. Our study focuses on this prescrambling plateau (green panel), where the OTOC time-average exhibits order parameter like behavior (Fig. 5.1).

the information scrambling has fundamental restrictions when topological order exists is a puzzle left at the intersection of many sub-fields.

In Sec. II, we are going to detail our numerical observation around its corresponding Majorana chain and discuss about the connection between infinite temperature scrambling and $T = 0$ topological order with quantitative arguments. Later in Sec. III, we are going to show how the topological order is encoded in the saturation regime of OTOCs based on the analytical calculations in the non-interacting regime. In Sec. IV, we extend the discussion to interacting and/or nonintegrable models and demonstrate topologically induced prescrambling. Later we show how topological order persists in two separate contributions to the coherence times of the prescrambling plateaus. This will help us to explore if and how strong zero modes affect the scrambling dynamics of OTOC different than the dynamics of two-time correlators. Finally we discuss the effect of prescrambling on dynamic phase diagrams. We conclude in Sec. V and elaborate on possible questions to answer in the future.

5.2 Demonstration of Topological Origin

It turns out that the connection between infinite-temperature information scrambling and quantum phases at zero temperature has a robust topological origin. Let us demonstrate how the topological origin reveals itself in the dynamics of OTOCs with an example on 1D XXZ chain,

$$H = J\sum_i \left(\sigma_i^x\sigma_{i+1}^x + \sigma_i^y\sigma_{i+1}^y + \frac{J_z}{J}\sigma_i^z\sigma_{i+1}^z\right). \tag{5.3}$$

At $T = 0$, the model exhibits quantum phase transitions between a gapped Ising phase $|J_z| > 1$ and a critical XY-phase $|J_z| < 1$ where the spectrum is gapless [65]. We employ Haar-distributed random states $|\psi_h\rangle$ and compute $\bar{F}$ shown in Fig. 5.3.

If spin operators at the edge of the chain $W = V = \sigma^z_{\text{edge}}$ are utilized (blue-circles), the infinite-temperature OTOC saturation value behaves like an order parameter of the zero-temperature quantum phase transition, i.e., $\bar{F} \sim 0$ in the XY phase ($|J_z/J| < 1$) and increases monotonically as we enter the Ising phases ($|J_z/J| > 1$). In contrast, under periodic boundary conditions (yellow diamonds line) and for a bulk spin $W = V = \sigma^z_{\text{bulk}}$ (green left-pointing triangles), the OTOC no longer differentiates the two phases, and the transition point is smoothed out consistent with predictions from the previous Chapter.

To demonstrate the role of topological order, we rewrite the Hamiltonian of the XXZ model in the Majorana basis. First, via the Jordan-Wigner (JW) transformation [49]

$$\begin{aligned}
\sigma_i^z &= -\prod_{j<i}\left(1-2c_j^\dagger c_j\right)\left(c_i + c_i^\dagger\right), \\
\sigma_i^x &= 1 - 2c_i^\dagger c_i, \\
\sigma_i^y &= -i\prod_{j<i}\left(1-2c_j^\dagger c_j\right)\left(c_i - c_i^\dagger\right).
\end{aligned} \tag{5.4}$$

the spin Hamiltonian is mapped to

$$\begin{aligned} H &= J\sum_i \Big[\left(1-2c_i^\dagger c_i\right)\left(1-2c_{i+1}^\dagger c_{i+1}\right) - \left(c_i+c_i^\dagger\right)\left(c_{i+1}-c_{i+1}^\dagger\right) \\ &+ \frac{J_z}{J}\left(c_i-c_i^\dagger\right)\left(c_{i+1}+c_{i+1}^\dagger\right)\Big], \end{aligned} \tag{5.5}$$

which can be written in terms of the Majorana fermions $a_{2j-1} = c_j + c_j^\dagger$ and $a_{2j} = -i\left(c_j - c_j^\dagger\right)$ [53]:

$$H = -J\sum_i \left(a_{2i-1}a_{2i}a_{2i+1}a_{2i+2} + ia_{2i-1}a_{2i+2}\right) + iJ_z\sum_i a_{2i}a_{2i+1}. \tag{5.6}$$

In the Majorana basis, the spin system is mapped to an interacting Majorana chain. The XY (Ising) phase is mapped to a gapless (topological) phase, and the quantum phase transition becomes a topological transition. Same as the Kitaev chain, the topological phase in Eq. (5.6) develops Z_2 topological order and is characterized by two Majorana zero-modes localized at the two ends of the chain [53].

The physics can be understood by considering the $J_z \gg J$ limit, where Eq. (5.6) converges to the Kitaev model [53] with two zero-energy Majorana modes $\gamma_1 = a_1$ and $\gamma_2 = a_{2N}$ fully decoupled from the rest of the chain. Away from the $J_z \gg J$ limit, quartic terms in the Hamiltonian introduce interactions, but the zero-energy Majorana modes at the two ends of the chain remain topologically protected for the entire topological (Ising) phase. The existence of two Majorana modes at the two ends of the chain (γ_1 and γ_2) indicates that a zero-energy non-local fermion $d = \frac{\gamma_1 + i\gamma_2}{\sqrt{2}}$ can be defined. Because of its zero-energy nature, for an eigenstate of the Hamiltonian $|\psi_0\rangle$, another degenerate state $|\psi_1\rangle = d\,|\psi_0\rangle$ must exist with an opposite fermion parity. Therefore, in the topological phase, the edge modes are responsible for the degenerate subspaces forming not only in the ground state, but throughout the entire spectrum [53, 65]. In other words, in contrast to a conventional (Landau-type) quantum phase transition, where across the phase boundary the ground state

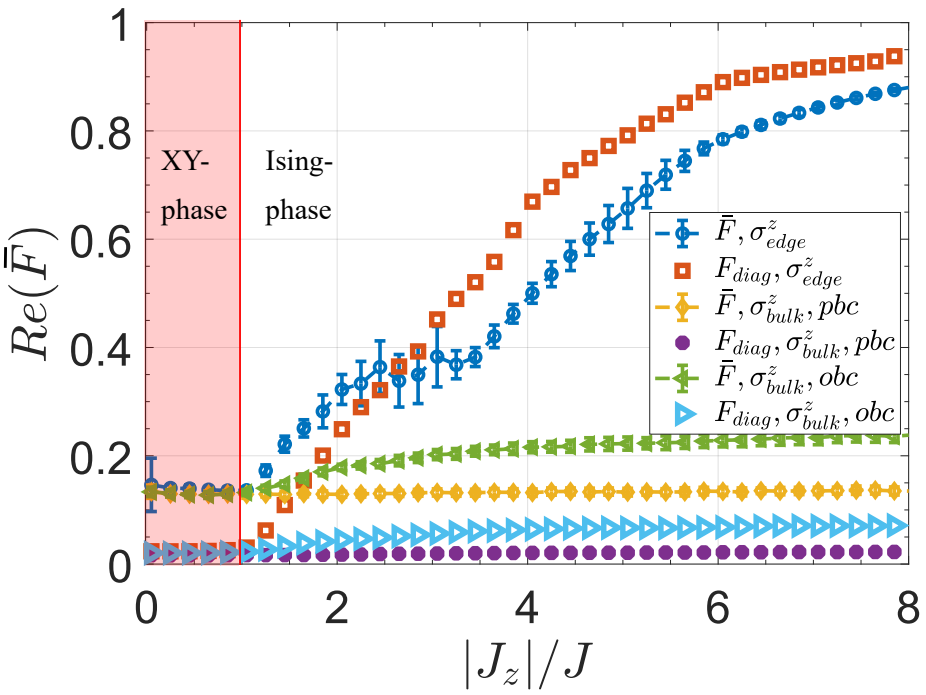

Figure 5.3: Long-time average of OTOC for XXZ model for edge-spin operators $W = V = \sigma^z_{\text{edge}}$ in blue circles and its (later explained) diagonal contribution in orange squares; for bulk-spin operators σ^z_{bulk} with periodic boundary chain (pbc) in yellow diamonds and its diagonal contribution in purple dots; with open boundary chain (obc) in green left-pointing arrows and the diagonal contribution in light-blue right-pointing arrows. System size is $N = 14$ and the time of averaging is $tJ = 800$.

changes from non-degenerate (the disordered phase) to degenerate (the ordered phase), Z_2 topological order has a direct impact for the degeneracy of all eigenstates in the entire energy spectrum, i.e., two-fold degeneracy for the entire spectrum. The effect has a direct impact on measurements and dynamical quantities at any temperature [115,303] and it is in sharp contrast to a conventional phase transition that can only be detected by zooming to the ground state at low-temperature. This is the key reason why the infinite-temperature OTOC is capable of detecting a zero-temperature topological order, but not a regular Landau-type quantum order (unless it can be mapped into a topological order).

5.3 Topological Edge Physics Encoded in the Out-of-time-order correlators

In this section, we study the non-interacting limit to provide analytical arguments in the demonstration of how infinite-temperature information scrambling of edge spins encodes the existence or absence of Majorana zero modes. Later we will mark the topological phase transition point via $\bar{F}$ in this non-interacting limit.

5.3.1 Transverse-field Ising Model

We consider a non-interacting, hence analytically solvable model and directly compute the contributions of Majorana zero-modes in the infinite-temperature OTOCs with edge operators. The Hamiltonian for the transverse-field Ising model with open boundary conditions is,

$$H = -J\sum_{j=1}^{N-1}\sigma_j^z\sigma_{j+1}^z + h\sum_{j=1}^{N}\sigma_j^x. \tag{5.7}$$

Eq. (5.7) has a critical point at $h = 1$ that separates a ferromagnetic ordered phase from a disordered phase. The time-average of OTOC $\bar{F}$ with σ_1^z at $\beta = 0$ is shown with the lines

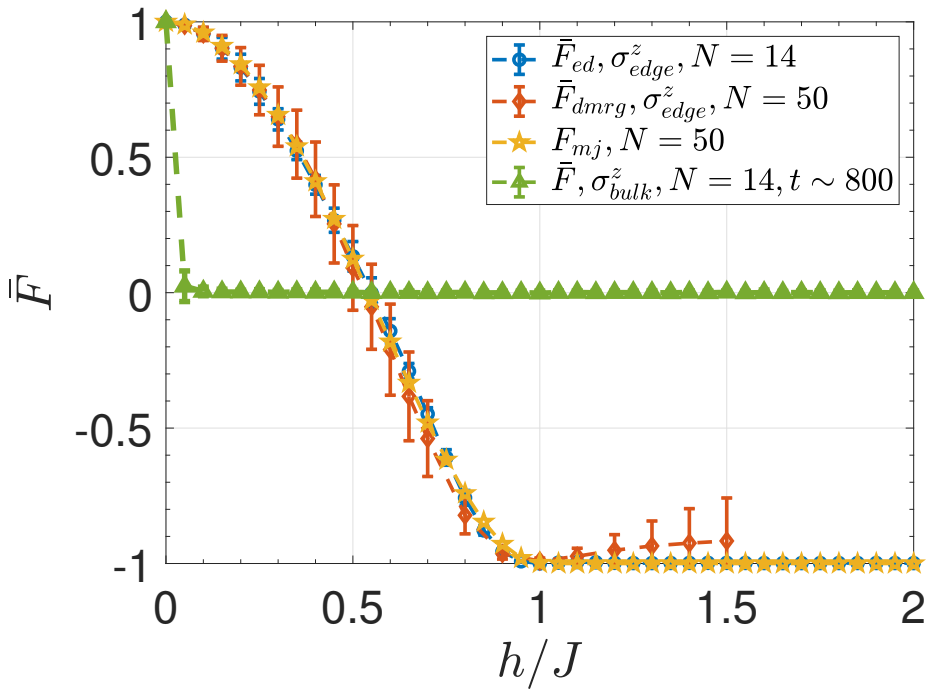

Figure 5.4: Transverse-field Ising model at infinite-temperature. The OTOC time-average of the edge spin operators σ^z_1 via real-time OTOC dynamics (blue circles) at $N = 14$ and (orange diamonds) at $N = 50$ where we used MPS (see Appendix D.1) for a time interval $tJ = \frac{\pi}{4}10 \sim 7.85$. The yellow-pentagrams show F_{11} based on Eq. (5.9) where the Majorana edge states are extracted from H_{BdG} matrix at $N = 50$ at infinite time limit for a comparison with other data. The green-triangles show the OTOC time-average of the bulk spin operator σ^z_7 at $N = 14$ for a time interval $tJ = \frac{\pi}{4}10^3 \sim 800$.

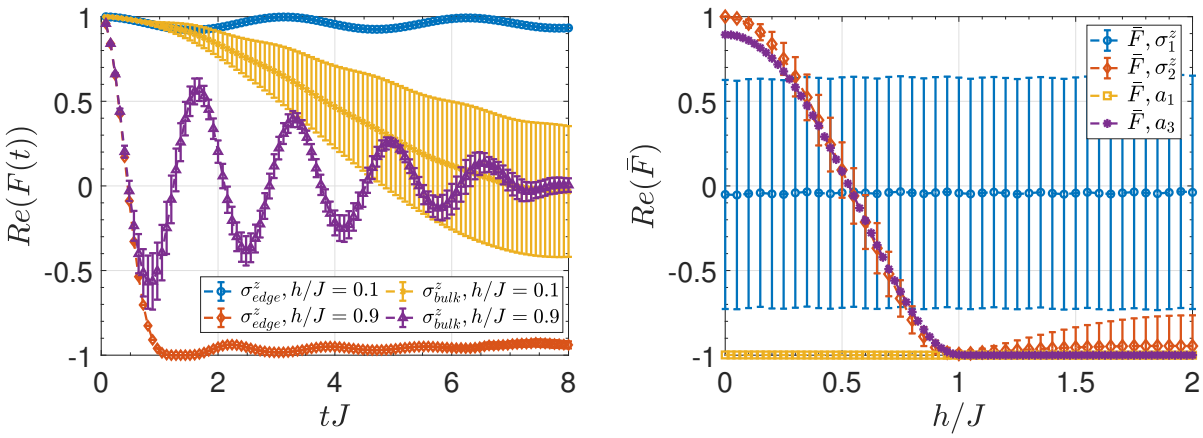

(a) (b)

Figure 5.5: Transverse-field Ising model at infinite-temperature. (a) The OTOC dynamics $F(t)$ with respect to tJ. Blue-circle and orange-diamond lines are the OTOC of edge σ^z_1 operator for $h = 0.1$ and $h = 0.9$, respectively. Yellow-cross and purple-triangle lines are the OTOC of bulk σ^z_{25} operator for $h = 0.1$ and $h = 0.9$, respectively. All curves are computed in t-DMRG for a system size of $N = 50$, averaged over 10 random product states to generate $\beta = 0$ results. The error bars stand for 1σ variation around the mean value of OTOC due to oscillations in this set of random states. (b) Robustness of order against changing the boundary conditions: a strong field is applied to the first spin only for $N = 13$ and $tJ \sim 8$ (blue circles); and to the edge fermions in the non-interacting fermion chain for $N = 50$ and $tJ \to \infty$ (yellow squares). The edge modes shifted to the nearest site that is free of pinning field, $\bar{F}$ of σ^z_2 spin (red-diamonds) and $\bar{F}_{33}$ of a_3 Majorana fermion (purple asterisks), respectively.

with blue-circles and orange-diamonds for $N = 14$ and $N = 50$, respectively in Fig. 5.4. The simulation with $N = 50$ spins is performed with matrix product states (MPS) in a t-DMRG (time-dependent density matrix renormalization group) method, (see Appendix D.1 for details). Here the error bars give us an information on the amplitude of oscillations in time, as we time-average the real part of the OTOC signal in a time interval of $tJ = \frac{\pi}{4}10 \sim 7.85$. For an edge spin operator σ_1^z, $\bar{F}$ behaves like an order parameter, which is $\bar{F} \sim -1$ in the disordered phase ($h > J$) and increase monotonically in the ordered phase ($h < J$). On the contrary, for a bulk spin operator, σ_7^z, this feature disappears (green-triangles in Fig. 5.4). This observation reflects that the physics captured by edge- and bulk-spin operators are different; a similar observation to what we presented for the XXZ model earlier. To further show how the real-time OTOC dynamics looks like, we contrast time-evolving OTOC $F(t)$ of edge and bulk operators in Fig. 5.5a. The OTOCs of the edge spin converge to different values at large times, depending on the value of h/J, while the OTOCs of bulk spins always converge to 0 at large t, as long as $h \neq 0$. The $h = 0$ limit is trivial for information scrambling, because the spin chain turns into the classical Ising model without quantum fluctuations or non-trivial dynamics, and thus information cannot scramble, $F(t) = 1$.

The results above can be easily understood by using the Majorana basis, which transforms the spin Hamiltonian into a non-interacting Majorana chain

$$H = -iJ \sum_{j=1}^{N-1} a_{2j} a_{2j+1} - ih \sum_{j=1}^{N} a_{2j-1} a_{2j}, \tag{5.8}$$

where we used Eqs. (5.4). A figure adapted from Ref. [53] can be seen in Fig. 5.7 which shows the cases (i) nonzero J and h where all Majorana fermions are coupled to each other; (ii) the topological superconductor phase with $h = 0$ where two Majorana fermions remain unpaired and their wave functions are depicted with red and blue lines at the edges; (iii) the trivial phase where Majorana fermions of different sites are not coupled. The topological superconductor phase is characterized by the presence of Majorana edge modes [22], and

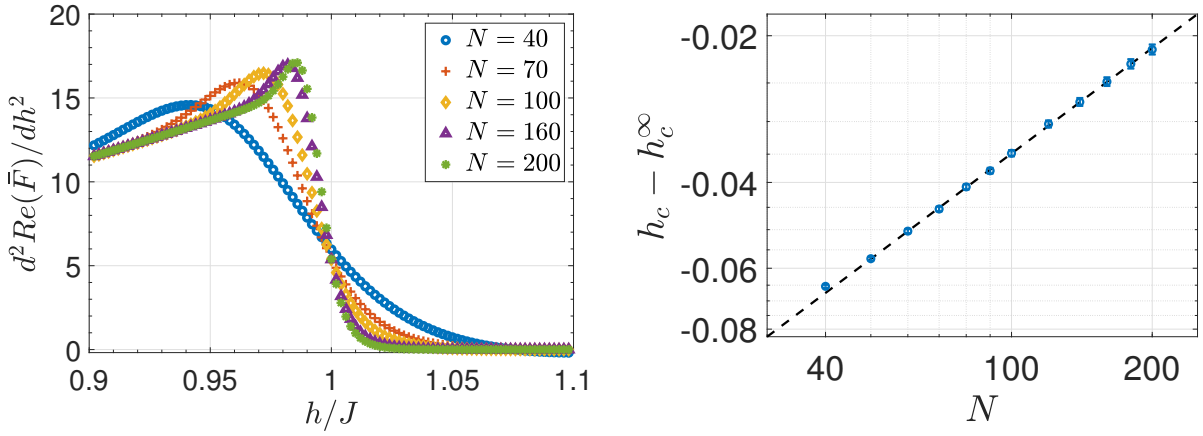

(a) (b)

Figure 5.6: (a) The second derivative of the OTOC time-average $d^2\bar{F}_{11}(t \to \infty)/dh^2$ pinpoints the phase transition point via its maximum. (b) The system-size scaling of the phase transition point gives $h_{dc} \sim N^{-0.7189} + 1.0069$ with $R^2 = 0.9996$, meaning in the thermodynamic limit the OTOC pinpoints the phase transition point as $h_{dc}^\infty = 1.0069$.

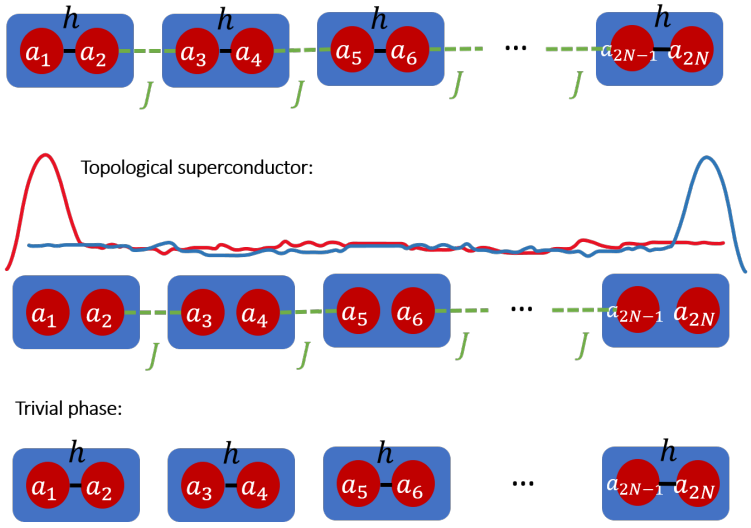

Figure 5.7: A pictorial representation of the Hamiltonian Eq. (5.8) where red circles and blue rectangles stand for Majorana and Dirac fermions, respectively. The top schematic is Eq. (5.8) for nonzero J and h. The lower two schematics are for the topological superconductor ($h = 0$) and the trivial phases ($J = 0$), respectively.

the topological phase transition between two phases lies at $h = J$, which coincides with the QPT in the TFIM.

In contrast to the XXZ model discussed above, Eq. (5.8) only contains quadratic terms, hence non-interacting, and thus can be easily diagonalized, which enables us to compute infinite-temperature OTOC saturation values $\bar{F}$ exactly. This exact solution agrees perfectly with numerical simulations in Fig. 5.4. More interestingly, as will be shown below, the analytical result exhibits that F_∞ is solely contributed by Majorana zero modes, while the contributions from all other finite energy excitations fade away at large t.

5.3.2 Exact solution

We compute the OTOC of an edge spin using the Majorana basis in this section. In the Majorana basis, the OTOC of Majorana fermions can be defined as $F_{2i-1,2i-1}(t) = \mathrm{Tr}\left(a_{2i-1}(t)a_{2i-1}a_{2i-1}(t)a_{2i-1}\right)/2^N$, where we set $W = V = a_{2i-1} = c_i + c_i^\dagger$. Since it can be easily shown that the OTOC of edge Majorana fermions must be identical to the OTOC of edge spins, $\sigma_1^z = \left(c_1 + c_1^\dagger\right) = \gamma_1$ and $\sigma_N^z = \mathbb{P}\left(c_N - c_N^\dagger\right) = i\mathbb{P}\gamma_2$, where $\mathbb{P} = \prod_j^N \left(1 - 2c_j^\dagger c_j\right)$ is the parity operator, here we focus on F_{11} with $W = V = a_1$.

The Majorana-fermion OTOC $F_{2i-1,2i-1}(t)$ can be conveniently computed by utilizing the Bogoliubov-de Gennes (BdG) basis, as detailed in Appendix D.2. With fermion operators defined for a space of double spectrum, we write the BdG Hamiltonian and calculate $F_{2i-1,2i-1}(t)$ at site i,

$$\begin{aligned} F_{2i-1,2i-1}(t) &= \left[\sum_\alpha^{2N} \left(|\psi_{\alpha,i}|^2 + \psi_{\alpha,i}\psi_{\alpha,i+N}^*\right)\cos\left(E_\alpha t\right)\right]^2 \\ &+ \left[\sum_\alpha^{2N} \left(|\psi_{\alpha,i+N}|^2 + \psi_{\alpha,i+N}\psi_{\alpha,i}^*\right)\cos\left(E_\alpha t\right)\right]^2 - 1. \end{aligned} \tag{5.9}$$

where E_α and ψ_α are eigenenergy and eigenstate of the BdG Hamiltonian, while the sum goes over all energy eigenstates $\alpha = 1, \ldots 2N$. In the long-time limit, only the non-oscillating

terms (i.e., $E_\alpha = 0$) contribute to the saturation value of $F_{2i-1,2i-1}(t)$, i.e., only zero modes need to be considered for $t \to \infty$. For $h < J$ in the Ising ordered phase, the BdG Hamiltonian describes a topological superconductor with Majorana zero modes at the two ends, Fig. 5.7, and hence we only sum over the two Majorana zero modes, e.g., $\alpha = mj$. In the disordered phase ($h > J$), the BdG Hamiltonian describes a topologically-trivial superconductor without any zero modes. Thus in the absence of zero modes, $E_\alpha = 0$, $F_{2i-1,2i-1}(t) \to -1$, explaining $\bar{F}$ approaching to -1 in the Ising model results (Figs. 5.4 and 5.5). By calculating Eq. (5.9) as $t \to \infty$, we plot $F_{11} = F_{mj}$ in Fig. 5.4 with orange-pentagrams, which matches well with the Ising model results. To conclude, the derived relation, e.g., Eq. (5.9) rigorously proves that the saturation value of an OTOC with Majorana fermions ($W = V = a_{2i-1}$) is contributed only by Majorana zero modes ($E_\alpha = 0$), while the contributions from any excited states ($E_\alpha \neq 0$) vanish at long times. Since the Ising model can be exactly mapped to a 1D Majorana chain, the infinite-temperature OTOC of the edge spins directly probes the presence or absence of the Majorana zero modes. This is one of the key conclusions in this Chapter.

Motivated by this observation, we pinpoint the phase boundary of the topological phase transition in the following. Since the OTOC $F_{11}(t \to \infty)$ has a continuous transition from topologically non-trivial to trivial phase, we focus on its second derivative $d^2\bar{F}_{11}(t \to \infty)/dh^2$ with respect to external field h. The maximum of the second derivative pinpoints the transition point, Fig. 5.6a. Then the system-size scaling provides the transition point in the thermodynamic limit as $h_{dc}^{\infty} = 1.0069$ with a power-law scaling $h_{dc} \sim N^{-0.7189} + 1.0069$ (Fig. 5.6b). For further details, see Appendix D.4. We note that the results obtained in the non-interacting limit (Ising model) are valid at the infinite time in the thermodynamic limit since topologically induced prescrambling plateau persists indefinitely (Appendix D.4).

5.3.3 Robustness against varying the boundary conditions

Although the phenomenon discussed above relies on utilizing edge degrees of freedom, all the key conclusions are robust against any local perturbations and independent of boundary conditions. Because, the physics is based on topological edge modes. To demonstrate this robustness, we vary the boundary condition of the transverse-field Ising chain by introducing a constant magnetic field (along the x direction) for the edge spin only, i.e., $h_1/J = h/J + 6$ where h_1 is the strength of the transverse field for the first site, while the rest of the spins have the same transverse field h. This strong field at the edge site introduces a strong pinning to the first spin and hence $\bar{F}$ oscillates significantly, being featureless across the phase boundary (blue-circles in Fig. 5.5b). However, if we choose the spin operator at the second site instead, the physics discussed above is recovered as shown in Fig. 5.5b with orange-diamonds. This is because such a local field cannot destroy the Majorana zero mode, which is topologically protected by the nontrivial bulk. Instead, it can only move the location of the zero modes, and thus, utilizing the second site, the conclusion remains the same. We additionally show the results for non-interacting fermion chain with an additive field affecting only the fermion at the edge. Yellow-squares in Fig. 5.5b show $\bar{F}_{mj}$ (Eq. (5.9)), the OTOC of edge Majorana mode γ_1 at the infinite-time limit, hence demonstrating no transition point. Purple-asterisks, on the other hand, show $\bar{F}_{33}$, the OTOC of Majorana mode a_3 at site $i = 2$ at the infinite-time limit, which is observed to match with $\bar{F}$ of the Ising model, implying an agreement between numerics and analytics.

5.4 The Interplay between Topological Order and Scrambling

The default expectation for generic systems in 1D is scrambling over a time interval where the OTOC decays fast or slow but saturates to a residue close to zero, both depending on the set of symmetries existing in the system and the size of the Hilbert space [139, 162, 168, 297]

as demonstrated in Chapter 3. An exception to this observation is the models that possess a symmetry-breaking phase transition with a long-range ordered phase at zero temperature regardless of the interactions as exemplified in Chapter 4, or the non-integrability [181]. However, could order in such generic systems be captured at higher temperatures, preferably at infinite temperature? Now we systematically study the detection of topological order in generic systems at infinite temperature, and show that the machinery for the detection of the topological order with simpler correlators can also be used for OTOCs. In fact, this encourages us to devise a method to show if and how the dynamical imprint of topological order on information scrambling could differ from the one on thermalization dynamics.

5.4.1 Coherence times of prescrambling plateaus

Z_2 topological degeneracy does not only slow down the scrambling process, but also temporarily freezes the dynamics for generic nonintegrable models, causing *topologically induced prescrambling*. Hence we observe that the topological order has a profound effect on the dynamics of systems [115, 303], suggesting a new time-scale for information scrambling in our case. In this section, we explore the coherence times of the prescrambling plateaus to understand the associated timescales in the thermodynamic limit.

Fig. 5.8a shows how the coherence times of the prescrambling plateau in a near-integrability model, see Eq. (5.15), ($\Delta/J = -0.1$) exponentially increase until around $N = 15$ where the increase halts, suggesting that the curves of the systems with larger sizes possibly collapse on each other. Better examples can be seen in Figs. 5.8b-5.8c of $h/J = 0.7$ of near-integrability model and deep in the non-trivial phase of the model with stronger interactions $\Delta/J = -0.5$, respectively. Therefore, prescrambling plateau has a finite lifetime in generic systems, including the vicinity of non-interacting limit. When the model becomes integrable, prescrambling plateau persists indefinitely, meaning that a system in the thermodynamic limit never scrambles. Fig. 5.8d shows the exponential increase of full scrambling decay times in the XXZ model, thus implying that the observed scrambling is a finite-size

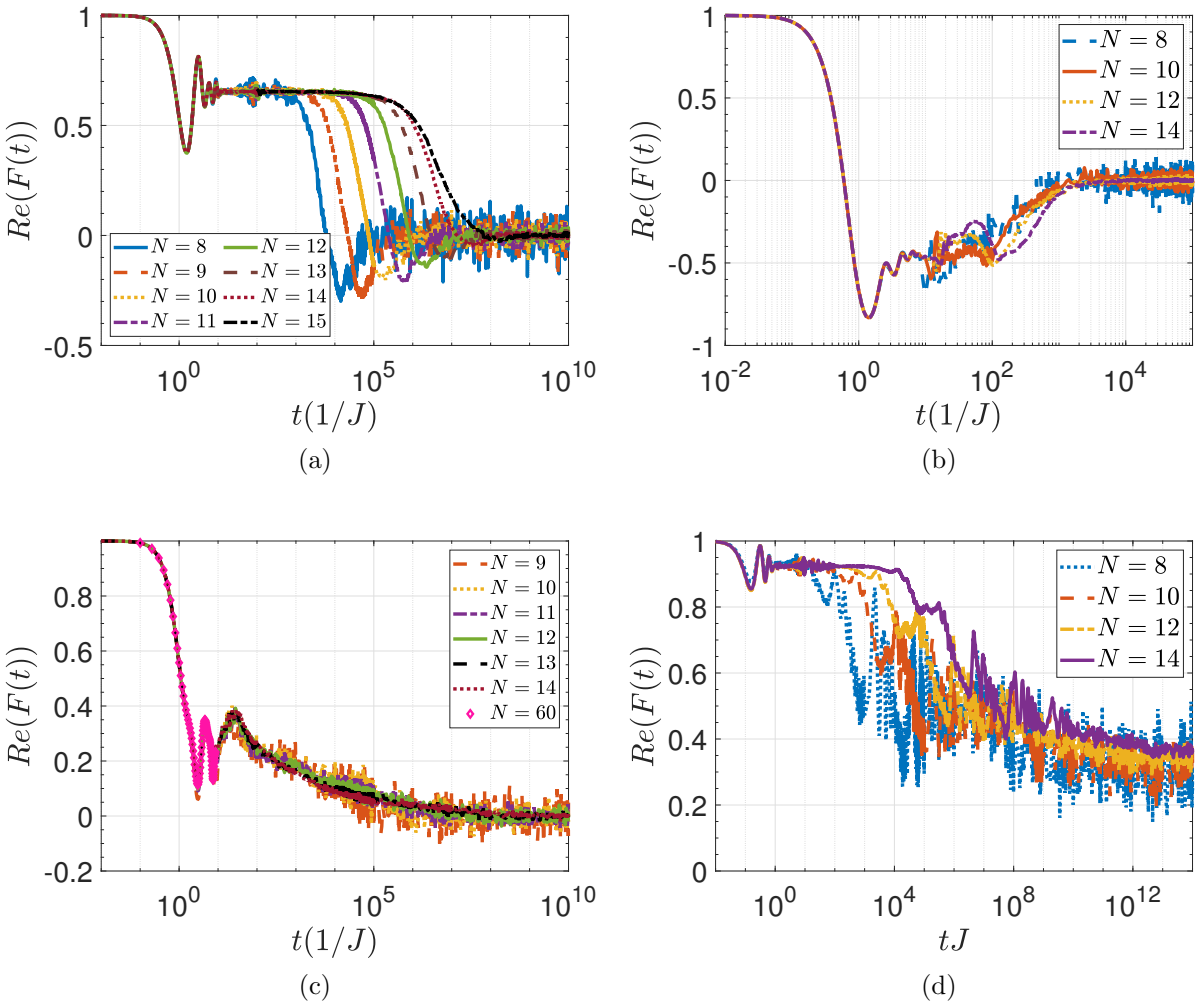

Figure 5.8: Coherence times of prescrambling plateau at (a)-(b) $\Delta = -0.1$, (a) deep in the topologically non-trivial phase $h/J = 0.3$ and (b) at $h/J = 0.7$ showing negative prescrambling plateau values; (c) $\Delta = -0.5$ at $h/J = 0.3$. $N = 60$ is computed via t-DMRG with 25 random initial states to have the infinite-temperature OTOC. (d) Prescrambling plateau deep in the topologically non-trivial phase of the XXZ model with $J_z/J = 10$ persists indefinitely.

effect. Similar behavior can be found for different J_z/J parameter (Appendix D.5), as well as the non-interacting limit (Appendix D.3).

A natural question is how a generic system could host a prescrambling plateau for mostly long but finite amount of time. Finite coherence times of edge-spin two-time correlators in generic systems have been recently based on spectrum characteristics [115]. Hence these findings should be applicable to information scrambling. The notion of easy spin flips are introduced by Ref. [115] to demonstrate that these spin flip processes destroy the perfect pairing of energy eigenstates that are caused by zero modes. Such perfect pairing, meaning exponentially close eigenstates, happen in the integrable case and is dubbed as *strong zero modes*. When integrability breaking interactions are introduced, due to the poles appearing in the perturbation theory, also called resonances, degeneracies are no longer exponentially close, but polynomially in system size. Hence there is not perfect pairing anymore, and strong zero modes turn into *almost-strong zero modes* as called by Ref. [115]. The processes of easy spin flips are the reason behind such a change in the degeneracy structure. Due to the poles in the perturbation theory, certain basis states with spin flips are equally energetically favorable with the Kramer partner. When the external transverse field is on, these states mix and one ends up with eigenstates that are comprised of not only a state and its Kramer partner as expected in a doubly-degenerate spectrum, but a state, its 'easy spin partners' and the Kramer partners of all. These now polynomially close eigenstates, depending on the external field strength as well as where the poles are, could cause bigger regions of degeneracy compared to double degeneracy. However we stress on the fact that these degeneracies are, so to speak, weaker than the degeneracies when there are no integrability breaking interactions, hence they indeed deserve the name *almost-strong zero modes*. Again we emphasize that these eigenstates are still Kramer partners of each other, as would be expected from a system that obeys Z_2 symmetry. Hence the Z_2 topological imprint is not lost, but instead reduced to a signature that could survive only for finite times. Such a profound effect on dynamics by zero modes is shown with two-time correlators by Refs. [115, 303]. Hence our

results are an intuitive extension of this effect to the dynamics of information scrambling and OTOCs. In this regard, our results demonstrate that the scrambling could be slowed down in nonintegrable systems, introducing a two-step timescale to scrambling dynamics, with the name *prescrambling*, analogizes with prethermalization as the name correctly implies. This encourages us to question how much OTOCs are really different than their simpler cousins, e.g., two-time correlators. An immediate observation shows us that Figs. 5.8a and 5.8b of the near-integrability model behave considerably different: the former has a positive-valued plateau, paralleling with the behavior of two-time correlators, whereas the latter has a negative-valued plateau. To better understand such distinct behavior appearing in OTOCs and further elaborate on related questions, we introduce a method in the next section.

5.4.2 Dynamical decomposition method

In this section, we develop a framework that can provide us more insight about detecting topological order in generic systems via OTOCs, as well as the saturation regime of OTOCs in general. Since we can already derive the OTOC saturation value analytically in the non-interacting regime (Sec. 5.3.2), we need a framework that works in nonintegrable models; a limit that is in general not analytically tractable. This framework is an application of dynamical decomposition to OTOC that is presented in the previous Chapter, and we aim to calculate $\bar{F}$ with a term that becomes the dominant contribution in $\bar{F}$ and a correction to it, as we move away from the non-interacting limit. Dynamical decomposition method is utilized in Chapter 4 to find a leading-order term in $\bar{F}$ (of arbitrary bulk spins) at zero-temperature to probe zero-temperature symmetry-breaking phase transitions. Here we generalize the idea to infinite temperature and put forward a conjecture in analogy to the Eigenstate Thermalization Hypothesis (ETH), as explained in the following. Our motivation for putting forward this method is two-fold: (i) this approach provides us an approximated solution of the saturation regime for a generic system; (ii) it also offers us a common ground to compare the saturation regime of OTOCs with the saturation regime of two-time correlators

to further understand if they differ in reflecting the dynamics of zero modes. We note why the point (ii) is interesting for our purposes: OTOCs at infinite-temperature are well-known probes of quantum chaos [132, 134, 140, 142, 162] as shown in Chapter 3, whereas two-time correlators seem to be featureless to reflect such property of the system [139, 150]. Even though intuitively related, thermalization and scrambling seem to be different from each other, motivated by their different timescales, Refs. [138, 140, 150]. Hence finding where OTOC points to additional information about the system, and where it can be reduced to two-point correlators, could prove useful to understand the relations between scrambling and thermalization. In the cases where such a reduction is possible, reminding of Wick's theorem but for OTOCs, the hope is that one can use two-point correlators instead of OTOCs to determine the scrambling in an experimental setting, because implementing an OTOC protocol is unarguably harder than measuring a two-point correlation function [146, 156, 157, 159, 210] (see Ch. 3 for the challenges of such an implementation). In the opposite situation where OTOCs provide additional information, we could know how scrambling dynamics differ from thermalization, at least for the model under study.

By utilizing the energy eigenstates as a complete basis of the Hilbert space, OTOC at infinite-temperature can be written as

$$F(t) = \frac{1}{M} \sum_{\alpha,\beta,\gamma,\delta} W_{\alpha\beta} V_{\beta\gamma} W_{\gamma\delta} V_{\delta\alpha} e^{i(E_\alpha - E_\beta + E_\gamma - E_\delta)t} \tag{5.10}$$

where $W_{\alpha\beta}$ and $V_{\alpha\beta}$ are defined as $W_{\alpha\beta} = \langle\psi_\alpha|W|\psi_\beta\rangle$ and $V_{\alpha\beta} = \langle\psi_\alpha|V|\psi_\beta\rangle$ with $|\psi_\alpha\rangle$ and $|\psi_\beta\rangle$ being the energy eigenstates with associated energies E_α, ..., E_δ. To keep the notation simpler, we do not explicitly specify the degeneracies in Eq. (5.10).

In the long time limit ($t \to \infty$), only the static terms with $E_\alpha - E_\beta + E_\gamma - E_\delta = 0$ contribute to the saturation value, while the rest of the terms dephase. Then the saturation

value, and equivalently the long time-average $\bar{F}$ of OTOC (see Ch. 4) reads,

$$\bar{F} = \frac{1}{M}\left(\sum_{\substack{E_\alpha=E_\beta,\\ E_\gamma=E_\delta}} + \sum_{\substack{E_\alpha=E_\delta,\\ E_\beta=E_\gamma}} - \sum_{\substack{E_\alpha=E_\beta=\\ E_\gamma=E_\delta}} + \sum_{\substack{E_\alpha\neq E_\beta\neq\\ E_\gamma\neq E_\delta}}\right) W_{\alpha\beta}V_{\beta\gamma}W_{\gamma\delta}V_{\delta\alpha}, \tag{5.11}$$

where $\sum_{E_\alpha=E_\beta,\, E_\gamma=E_\delta}$ implies that we take the operator matrix elements that satisfy the corresponding energy condition $E_\alpha = E_\beta$, $E_\gamma = E_\delta$. Since we look for a dominant contribution to Eq. (5.11) as the interaction strength increases, the most suitable dynamical decomposition is through a conjecture where $\bar{F}$ is dominated by the diagonal contribution. This corresponds to the contribution with the energy condition $E_\alpha = E_\beta = E_\gamma = E_\delta$ on the spectrum. A way to see why we expect our conjecture to hold is via remembering ETH. ETH, up to exceptions, i.e., [114] and Chapter 2, holds for nonintegrable systems whereas it fails for integrable systems [40]. One of the conditions of ETH is that the off-diagonal elements are suppressed compared to diagonal elements of the local observable written in the eigenbasis of the Hamiltonian. Therefore, based on the literature of ETH, we know that a local operator should dominantly populate its diagonal entries when the Hamiltonian is nonintegrable. In parallel with this argument, we numerically observe that our conjecture is indeed valid when an ansatz on the matrix elements of W and V is satisfied. This ansatz demands that the off-diagonal elements of the operators (in the eigenbasis) are suppressed with respect to the diagonal elements when the spectrum is explicitly degenerate; and can be formulated as $|W_{E_\alpha\neq E_\beta}|^2 \ll |W_{E_\alpha=E_\beta}|^2$ for both W and V, as well as $|V_{E_\alpha\neq E_\beta}|^2 \ll |W_{E_\alpha=E_\beta}|^2$ and vice versa. When the ansatz is satisfied, $\bar{F}$ simplifies to the diagonal contribution F_{diag},

$$F_{diag} = \frac{1}{M}\sum_{\substack{E_\alpha=E_\beta=\\ E_\gamma=E_\delta}} W_{\alpha\beta}V_{\beta\gamma}W_{\gamma\delta}V_{\delta\alpha}. \tag{5.12}$$

We note that the operator ansatz is the generalization of ETH's aforementioned criteria [34, 40, 67] to a degenerate spectrum. However, since we do not need to assume that the

diagonal elements of the operator matrix are a smooth function of energy $W_{E_\alpha=E_\beta} = g(E_\alpha)$, the other criteria of ETH [40] does not need to be followed, hence our conjecture does not require thermalization. This is reasonable, given that for a quantum system to thermalize strictly (in ETH sense) the saturation value should be predictable by the microcanonical ensemble in a narrow energy window on the spectrum [40]. There is not such a requirement for the saturation value of OTOCs. In conclusion, we can anticipate that our conjecture should be applicable for a wider range of systems e.g., including integrable but interacting systems.

If W and V are Majorana operators, i.e., a_{2i-1}, the only contribution to F_{diag} comes from the degenerate energy levels which contain two eigenstates with opposite fermion parity. Since the two-fold degeneracy arises in the entire spectrum, a finite F_{diag} is expected in the topologically non-trivial phase. However in the topologically trivial phase, although it could arise accidentally for some energy levels, two-fold degeneracy is generically not expected implying $\bar{F}_{diag} \sim 0$. Hence $\bar{F}_{diag}$ directly probes topological degeneracy in any system with Z_2 symmetry. Our conjecture can be rigorously proven for two-time correlation functions, where the off-diagonal contribution does not satisfy the corresponding energy condition $E_\alpha - E_\beta = 0$ and thus, must vanish in long time. Hence, the saturation value for a two-time correlator,

$$\bar{C} \;=\; \mathrm{Tr}\,(W(t)W) = \frac{1}{M}\sum_{E_\alpha=E_\beta} W_{\alpha\beta}V_{\beta\alpha}, \tag{5.13}$$

already consists of only diagonal contribution with no need to introduce an operator ansatz, unlike OTOC. For OTOC, if the operator ansatz does not hold and hence the conjecture fails, other contributions to $\bar{F}$ might exist (Eq. (5.11)), which we call *off-diagonal contribution*. Such cases, e.g., non-interacting model, clearly make the saturation regime of OTOC distinct than the saturation regime of two-time correlators, because the off-diagonal contribution becomes comparable to the diagonal contribution, and even dominates $\bar{F}$. On the other hand when the conjecture holds, and hence off-diagonal contribution sums up to ~ 0, F_{diag} becomes

the approximated solution to $\bar{F}$; and since F_{diag} (Eq. (5.12)) is related to $\bar{C}$ (Eq. (5.13)), $\bar{F}$ might be predicted by $\bar{C}$.

How F_{diag} relates to $\bar{C}$ can be seen better in the non-interacting limit. At infinite temperature, $\bar{C}$ could be utilized to straightforwardly come up with an analytical expression for F_{diag}: We calculate matrix elements of the edge operator W,

$$W_{\alpha\beta}\big|_{E_\alpha=E_\beta} = \langle\psi_\alpha| f(h)\gamma_1 \left(\frac{\gamma_1 + i\gamma_2}{\sqrt{2}}\right) |\psi_\alpha\rangle = \frac{2f(h)}{\sqrt{2}} = \sqrt{1-h^2}, \tag{5.14}$$

in the topologically non-trivial phase; $W_{\alpha\beta}\big|_{E_\alpha=E_\beta} = 0$ otherwise. Here $f(h)$ is a smooth function of magnetic field h, that can be extracted numerically for finite size systems, whereas by using $\bar{C}$ [213] we can determine an analytical expression $f(h) = \sqrt{2(1-h^2)}/2$ in the thermodynamic limit. Hence $F_{diag} = (1-h^2)^2$ can be written, while $\bar{C} = 1-h^2$ [213]. See Appendix D.3 for details and the numerical demonstration of this relation.

Now we calculate $\bar{F}_{diag}$ for three different scenarios: i) strongly interacting but integrable case (XXZ model), ii) nonintegrable models with different interaction strengths and iii) non-interacting limit; and numerically determine the bounds of our conjecture.

Strongly interacting but integrable case

We revisit the Fig. 5.3 of the XXZ model in Sec. 5.2. F_{diag} is shown for an edge-spin σ_1^z (obc) with red-squares; whereas the F_{diag} of bulk-spins σ_1^z (pbc) and σ_7^z (obc) operators are with purple-dots and light-blue right-pointing triangles, respectively. We observe that the diagonal contribution could be used to approximate $\bar{F}$ at the edge in the Ising phases, confirming the conjecture. Even though this model has interactions between Majorana fermions Eq. (5.6), it is still an integrable system which might explain why $\bar{F}$ does not completely reduce to its diagonal contribution in the long-time limit. However, the qualitative behavior is the same. The diagonal (and hence topological) contribution in the XY-phase becomes zero which is consistent with a gapless phase. Hence the sole contribution in the XY-phase is

the corrections, which shows a steady non-zero residue $\bar{F} \neq 0$. This residue seems to be a consequence of the rotational symmetry of the system, $[H, S_z] = 0$ and could be expected to vanish away in the thermodynamic limit (Appendix D.6). Since the topological order is not visible to bulk degrees of freedom, we see $F_{diag} \sim 0$ for bulk operators.

From nonintegrable cases to non-interacting limit

A generic Ising model could be introduced as,

$$H = -J \sum_{j=1}^{N-1} \sigma_j^z \sigma_{j+1}^z - \Delta \sum_{j=1}^{N-2} \sigma_j^z \sigma_{j+2}^z + h \sum_{j=1}^{N} \sigma_j^x, \tag{5.15}$$

$$= -iJ \sum_{j=1}^{N-1} a_{2j} a_{2j+1} + \Delta \sum_{j=1}^{N-2} a_{2i} a_{2i+1} a_{2i+2} a_{2i+3} - ih \sum_{j=1}^{N} a_{2j-1} a_{2j}, \tag{5.16}$$

where Δ is the next-nearest neighbor coupling between spins in Eq. (5.15) and breaks the integrability of the model. The strength Δ introduces interactions between Majorana fermions in Eq. (5.16). We focus on three different Δ values in our numerical analysis from weak to strong integrability-breaking terms (i) $\Delta/J = -0.1$, (ii) $\Delta/J = -0.5$ and (iii) $\Delta/J = -2$.

As we increase the interaction strength, $\bar{F} \sim \bar{F}_{diag}$ holds as expected from the conjecture. Fig. 5.9a compares the dynamic phase diagrams of $\Delta/J = -0.5$ and $\Delta/J = -2$ where time of averaging is fixed to $tJ = 800$ for a system size of $N = 14$. On the other hand, at the vicinity of the non-interacting limit $\Delta/J = -0.1$, $\bar{F}$ differs from its diagonal contribution $\bar{F}_{diag}$ considerably (yellow-triangles and green-circles Fig. 5.9b). Consistently, the operator ansatz in the non-interacting limit fails, leading to $\bar{F} \neq \bar{F}_{diag}$. Black-circles and red-diamonds in Fig. 5.9b show $\bar{F}$ and $\bar{F}_{diag}$ calculated at $N = 200$ in the infinite-time limit, respectively. Note that the difference is the off-diagonal contribution, which increases towards the phase boundary $h/J \to 1$ and clearly is not bounded. The off-diagonal contribution is robust, i.e., it does not vanish at infinite-time in the thermodynamic limit (Fig. 5.9b). The off-diagonal contribution also shows up in a generic model at near-integrability limit ($\Delta/J = -0.1$), seen in the observation that $\bar{F}$ diverges from $\bar{F}_{diag}$ (Sec. 5.4.1 and Appendix D.4).

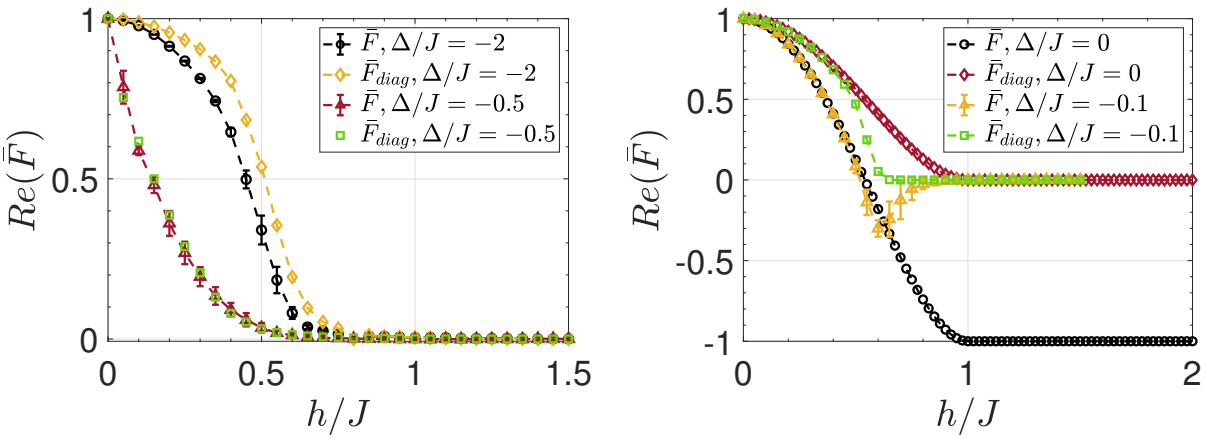

(a) (b)

Figure 5.9: Comparison of $\bar{F}$ and its diagonal contribution $\bar{F}_{diag}$ at different non-integrability breaking term strength Δ/J. (a) For a time interval of $tJ = 8 \times 10^2$ and size $N = 14$, $\bar{F}$ (red-triangles) and $\bar{F}_{diag}$ (green-squares) of $\Delta/J = -0.5$; and $\bar{F}$ (black-circles) and $\bar{F}_{diag}$ (yellow-diamonds) of $\Delta/J = -2$. Hence $\bar{F} \sim \bar{F}_{diag}$ holds for a generic nonintegrable system. (b) $\bar{F}$ (yellow-triangles) and $\bar{F}_{diag}$ (green-squares) of $\Delta/J = -0.1$ for a time interval of $tJ = 2 \times 10^3$ and size $N = 14$; and $\bar{F}$ (black-circles) and $\bar{F}_{diag}$ (red-diamonds) of non-interacting fermion model for a size of $N = 200$ at the infinite-time limit. At the vicinity of the non-interacting limit, off-diagonal contribution starts to be significant.

Outlook

In conclusion, deep in the interacting and/or nonintegrable limit, our conjecture holds and hence $\bar{F} \sim \bar{F}_{diag} \propto \bar{C}$. In near-integrability, OTOC starts to exhibit distinct behavior from two-time correlators and this becomes more apparent in the non-interacting model. We revisit Figs. 5.8a and 5.8b where the former is a point deep in the non-trivial phase with $\bar{F} \sim \bar{F}_{diag}$ (Fig. 5.9b) and hence shows similar behavior to $\bar{C}$ with a positive-valued plateau. Whereas Fig. 5.8b demonstrating a closer point to h_c gives $\bar{F}_{diag} \sim 0$, hence the OTOC time-average is mainly contributed by the off-diagonal contribution $|\bar{F}| \gg \bar{F}_{diag} \propto \bar{C}$, resulting in a negative-valued plateau.

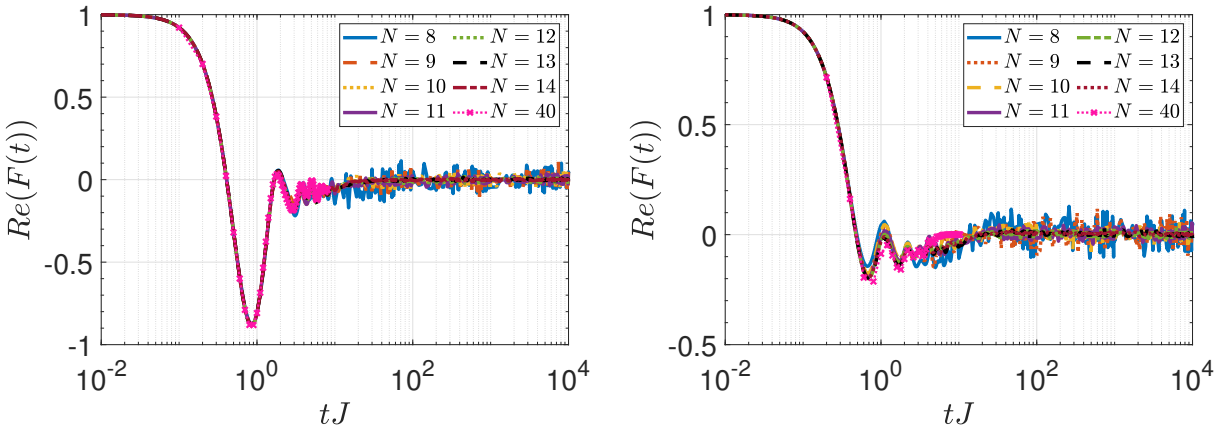

Figure 5.10: Coherence times of the edge spins based on OTOC of (a) $\Delta/J = -0.5$ and (b) $\Delta/J = -2$ closer to the critical point in their respective topological phases at $h/J = 1$ for different system sizes. The size $N = 40$ in both sub-figures is calculated via t-DMRG by averaging 10 different random product states.

5.4.3 Effect of scrambling on dynamic phase diagrams

The topological transition for $\Delta/J = -0.5$ and $\Delta/J = -2$ occurs at $h/J \sim 1.7$ and $h/J \sim 3.78$, respectively (Appendix D.5). On the other hand, Fig. 5.9a demonstrates the dynamic transition boundaries early on, $h_{dc}/J < 1$. Even though one might argue for finite-size effects, such a dramatic shift begs for additional reasons. The observation that prescrambling plateau has a finite lifetime in a nonintegrable model also suggests that the dynamic phase diagrams would significantly depend on the interval of the time-averaging (Appendix D.5 for demonstration). Hence it is not clear even if a dynamical phase transition boundary could be well-defined. Given such technical problems, instead of finite-size scaling to mark a transition point, we aim to bound the dynamic phase boundaries in these models. Figs. 5.10 demonstrate very limited prescrambling plateaus whose lifetimes are around $tJ \sim 20$ for $\Delta J = -0.5$ and $\Delta/J = -2$ at $h/J = 1$. The curves of multiple system sizes collapse on each other in a computation performed with both ED (exact diagonalization) and DMRG. Hence we can state that the dynamic phase boundary over a relatively long period of time is bounded to $h_{dc}/J < 1$, indeed suggesting a significant shift from the zero-temperature phase

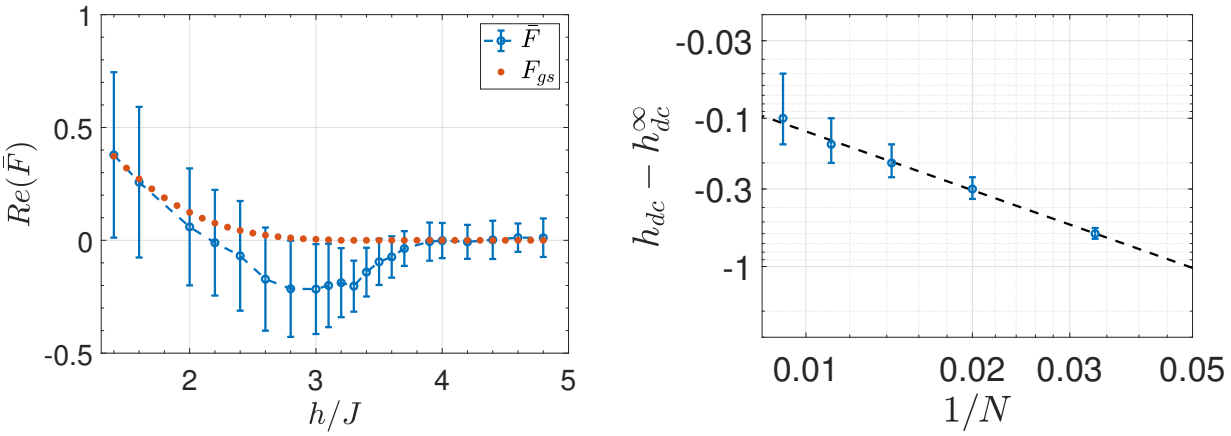

(a) (b)

Figure 5.11: (a) OTOC time-average of edge spin for the nonintegrable Ising model with $\Delta/J = -2$ at zero temperature and $N = 30$ system size. Blue-circles and orange-diamonds show $\bar{F}$ real-time average over $tJ = N = 30$ and the ground-state subspace contribution F_{gs}. (b) The system-size scaling of the critical point determined by F_{gs} as $h_{dc}^{\infty} = 3.7 \pm 0.05$. All computations in (a)-(b) are done either with t-DMRG or DMRG.

boundaries.

Such phase boundary shifts, although more mild than demonstrated here, in dynamical phase diagrams with corresponding symmetry-breaking transitions and that are initiated with polarized states in near-integrable Ising chain have been recently discussed [210]. These shifts seem to be linked to exciting the system to higher energy levels when quenched from a polarized state. Hence we can anticipate that working at infinite-temperature possibly maximizes the amount of shift from the zero-temperature phase boundary. Therefore, we lower the temperature to zero and compute $\bar{F}$ and its diagonal contribution which is simply the ground state contribution $\bar{F}_{gs}$ in Fig. 5.11a at $N = 30$ and over a time interval of $tJ = 30$. The correspondence between $\bar{F}$ and $\bar{F}_{gs}$ motivates us to apply system-size scaling on $\bar{F}_{gs}$. Fig. 5.11b demonstrates this system-size scaling which determines the critical point as $h_{dc}^{\infty} = 3.7 \pm 0.05$. Therefore the dynamical phase boundary is very close to $h_c^{\infty} \sim 3.78(2)$ that is determined by two independent methods (Appendix D.5). Hence the dynamical phase diagram based on OTOC matches fairly well with the topological phase transition boundary in low temperature, suggesting that the shift observed in Fig. 5.9a is indeed an effect from the

excited state spectrum. This is perhaps not too surprising, given the discussion on easy spin flips in Sec. 5.4.1. Since increasing the transverse field strength h (linked to spin flip operator) enhances the effect of easy spin flips on the spectrum [115], the dynamical signature of the topological order is lost well before the field value reaches the critical transition boundary h_c.

In conclusion, we demonstrate the effect of almost-strong zero modes on a dynamic phase diagram based on OTOC showing significant shift in the phase boundaries. Whether it is possible to find a functional dependence of the h_{dc} on temperature is an interesting question that can be studied systematically in future studies.

5.5 Conclusions and Discussions

We put forward a numerical observation on the XXZ model, where we showed the infinite-temperature OTOC, namely a correlator that probes the quantum chaos in interacting many-body systems, is also susceptible to ground-state phase transitions. The origin of this observation is demonstrated to be Majorana edge modes existing in the system with a systematic study of different models. This suggests the appearance of strong zero modes in the dynamics of information scrambling and OTOCs. We marked the topological phase transition in the non-interacting limit via $\bar{F}$. We further numerically studied the coherence times of the prescrambling plateaus in the nonintegrable models and demonstrated the effect of prescrambling in dynamic phase diagrams. We found that $\bar{F}$ continues to be an order parameter for the topologically non-trivial phase even in the nonintegrable limit where the dynamic phase boundary is significantly altered by the temperature. The dynamical decomposition of infinite-temperature OTOC into diagonal and off-diagonal contribution exhibits the differences and similarities between scrambling and thermalization dynamics affected by (almost-)strong zero modes.

The observations on finite topological order detected via OTOC point to edge spins that

remain local for long times in generic systems. Hence the scrambling of the edge spins with the rest of the system is negligible when the Z_2 topological order exists. Therefore, we demonstrate how topologically-protected degrees of freedom fight against being scrambled, either completely preventing (integrable systems) or restricting (generic systems) the operator spreading and thus exhibiting a clear interplay between the topological order and scrambling. Nonintegrable systems at infinite temperature are almost always expected to scramble down to zero where the decay rate depends on the symmetries existing in the Hamiltonian. However, we see that this is not always the case and the scrambling can be severely hindered by the topological protection of information. Motivated by these observations, we introduced a two-step scrambling process with the new timescale being prescrambling time τ_{presc} and the associated process, *topologically induced prescrambling*. Our conclusions in principle can be generalized to higher dimensions for topological states with similar fraction excitations and topological degeneracy [303], although the numerical verification is yet to be found.

In principle, this probe allows experimental detection of topological states without a need to cool down the system to ultra-low temperatures whether it is the OTOCs, Eq. (5.1) or two-time correlators Eq. (5.13), when the control parameter is sufficiently away from the zero-temperature phase boundary. In particular, the infinite-temperature OTOCs are experimentally more appealing than zero-temperature OTOCs [293], since it can be challenging to prepare a ground state as the initial state in certain experimental platforms.

Although surprising, the interplay between information scrambling and topological order is an intuitive observation. Beside the notion of strong-zero modes affecting the thermalization dynamics [303], the entanglement entropy of a ground state has a universal topological contribution in topologically non-trivial phases [317–319]. Moreover, the connection between OTOCs and the entanglement entropy of the time-evolved states has been introduced too [164, 168]. Hence here we make another connection that relates a dynamical quantity to a static property of the Hamiltonian.

Chapter 6

Probing Criticality in the Transient Quench Dynamics

In this Chapter, I will focus on two different models and demonstrate how to dynamically probe equilibrium quantum phase transitions in transient regimes of quench dynamics. The first section is going to be on the quench dynamics of spinor condensates, closely following the discussion on the signature of dynamical phase transitions in Chapter 2. An important difference, however, will be that we are not going to utilize the steady-state temporal regimes of the quench dynamics. Instead we are going to focus on a probe based on the oscillations that are observed in the nonequilibrium response. In the second section, we are going to turn our attention to the transverse-field Ising model and show how its exponentially decaying transient quench dynamics could be useful to probe equilibrium quantum criticality.

6.1 Observation of Dynamical Quantum Phase Transitions in a Spinor Condensate

A dynamical quantum phase transition can be characterized by a nonanalytic change of the quench dynamics when a parameter in the governing Hamiltonian is varied. Such a

transition typically only shows up in long time dynamics for extensive systems with short-range couplings. We analyze a model Hamiltonian of spin−1 atoms with effectively infinite-range couplings, and demonstrate that for this system the nonanalytic transition occurs for local observables in short time durations even when the cold atomic gas has a large system size. We experimentally realize this model Hamiltonian and observe the dynamical quantum phase transition in an antiferromagnetic spinor Bose-Einstein condensate of around 10^5 sodium atoms. Our observations agree well with the theoretical predictions. We also analyze the scaling exponent near the dynamical phase transition and discuss its relation with the excited state spectrum of the system.

6.1.1 Introduction

As already introduced in detail in Chapter 1, a dynamical quantum phase transition (DPT) is a nonequilibrium many-body phenomenon, which has recently attracted significant interests [199, 214–216]. Observing DPTs (see Sec. Sec. 1.2.3 for its definition and types) in systems with short-range couplings requires measurements of long-range correlations (e.g., infinite-range in the thermodynamic limit for type-II DPTs [217], or asymptotic long-time dynamics (e.g., infinite-time in the thermodynamic limit for type-I DPTs [210]). Recently, type-I DPTs have been observed in experiments that are modeled by a spin−1/2 long-range transverse-field Ising model (Eq. (1.2) in Chapter 1) with up to several tens of trapped ions [197] and Rydberg atoms [100], where the required observation time t is within the experimental reach because of the limited system size. As t scales up with the system size for type-I DPTs, it is challenging to confirm DPTs in large-size systems near the thermodynamic limit.

In this Section, we experimentally demonstrate the type-I DPT in a spinor Bose-Einstein condensate (BEC) with up to 10^5 sodium atoms. We start by analyzing a model Hamiltonian of spin−1 atoms with effectively infinite-range couplings. Our results show that the infinite-range couplings help type-I DPTs occur in a finite and practically short time duration

even for a system near the thermodynamic limit, which largely simplifies their experimental observations. After experimentally realizing the model Hamiltonian, we observe type-I DPT in an antiferromagnetic spinor BEC of around 10^5 sodium atoms, a massive system size compared with previous experiments [100, 197, 201]. Even in this large system size, we confirm that the DPTs could still occur in short time quench dynamics. We also measure the scaling exponents of the order parameters near the DPT, and find that they are close to the theoretical prediction.

A model Hamiltonian of N spin-1 atoms with effectively infinite-range (all-to-all) couplings takes the form

$$H = \frac{c_1}{2N}\sum_{i,j}^{N}\mathbf{F}_i\cdot\mathbf{F}_j + \sum_{i}^{N}(q(F_i^z)^2 - pF_i^z), \tag{6.1}$$

where $\mathbf{F}_i$ is the spin-1 observable for the ith-atom with its z-component denoted by F_i^z, c_1 is the spin-dependent interaction, which is positive for anti-ferromagnetic spinor BEC, and $p\,(q)$ denotes the linear (quadratic) Zeeman energy, respectively. For the infinite-range coupling, the spin coupling rate is normalized as $c_1/(2N)$, so that the energy is extensive in the thermodynamic limit, $N\to\infty$, with a finite c_1.

We realize this model Hamiltonian with a BEC of N spin-1 atoms. The spatial coherence over the whole BEC gives effectively infinite-range coupling between the atomic spin operators, although the atomic collision interaction by itself is fully local. We apply single mode approximation (SMA), c.f. Sec. 1.1.2, which decomposes the atomic field operator as $\psi_i(\mathbf{r}) \sim \phi(\mathbf{r})\,a_i$ by assuming that all spin states have the same spatial wave function $\phi(\mathbf{r})$ and a_i is the annihilation operator for the i-th spin component. The Hamiltonian for spin-1 BEC under SMA is thus [60, 320]

$$H = c_1\frac{L^2}{2N} + \sum_{m=-1}^{1}(qm^2 - pm)a_m^\dagger a_m, \tag{6.2}$$

as already noted several times in this dissertation. Here $L_\mu = \sum_{m,n} a_m^\dagger (f_\mu)_{mn} a_n$ is the BEC's total spin operator (f_μ is the spin-1 angular momentum matrix). Note that Eq. (6.2) is exactly the second-quantized form of Eq. (6.1) with $L \equiv \sum_{i=1}^N \mathbf{F}_i$ under the Schwinger representation of the spin operators.

Spinor BECs have been used to study quantum magnetism, spin squeezing [60, 248, 320, 321] and nonequilibrium dynamics as demonstrated in Chapter 2. Here, we use them as an experimental platform to study DPT with an effectively infinite-range coupling model as described by Eq. (6.1). We start from an initial state $|\psi(0)\rangle$ of the model Hamiltonian by preparing all the atoms in the hyperfine level $|F = 1, m_F = 0\rangle$ with $L_z = 0$, and the system remains in the $L_z = 0$ subspace since the total magnetization L_z is conserved. The linear Zeeman term thus has no contribution to the dynamics and can be neglected, c.f. Sec. 1.1.2. The interplay between the spin-mixing term and the quadratic Zeeman term gives rise to nontrivial dynamics [97]. We set the initial Zeeman field strength q at a value $q_i \gtrsim c_1$ so that $|\psi(0)\rangle$ is the ground state of Eq. (6.2). We then suddenly quench q to a final value q_f, c.f. Sec. 1.2. As q_f is scanned continuously, a sudden change in the quench dynamics at the phase transition point q_c can be regarded as a signature of the DPT. (See Sec. 1.1.2 for phase transition points in this model.)

Convenient detectable signals in spinor BECs are the fractional population of the spin-m_F component ($\rho_{m_F} = a_{m_F}^\dagger a_{m_F}/N$) and its average value ($\overline{\rho_{m_F}} = \langle \hat{a}_{m_F}^\dagger \hat{a}_{m_F} \rangle / N$) derived from repeated measurements. A widely-used quantity for characterizing the quench dynamics is $\langle \overline{\rho_0} \rangle_\infty$, the long-time average of $\overline{\rho_0}(t)$ in the wake of a quench. By assuming the quench occurs at $t = 0$, we can define $\langle \overline{\rho_0} \rangle_\infty = \lim_{T\to\infty} \frac{1}{T} \int_0^T \overline{\rho_0}(t)\, dt$ [201, 217], also see Sec. 1.2.3 and Chapter 2. Using $\langle \overline{\rho_0} \rangle_\infty$ as a measure, Chapter 2 showed that the model Hamiltonian (Eq. (6.1) or Eq. (6.2)) supports a DPT at $q_f = 0$. The quantity $\langle \overline{\rho_0} \rangle_\infty$, however, is difficult to measure in a lab as it requires averaging over a long evolution time t (i.e., $t \to \infty$ is theoretically required for a system in the thermodynamic limit). For spinor BECs, a large t inevitably leads to several challenges, such as significant atom losses and the invalidity of

the SMA [97, 322, 323] all of which possibly hinder an experimental observation of DPT.

To overcome this problem, we propose to identify DPT by using different parameters which can be directly measured within short time evolution and correlate unambiguously with $\langle\overline{\rho_0}\rangle_\infty$. To simulate the quench dynamics, we numerically diagonalize the model Hamiltonian (6.2) in the Fock basis $|N_1, N_0, N_{-1}\rangle = |n, N-2n, n\rangle$. Following a quench from q_i to q_f, we first find $\overline{\rho_0}(t)$ displays some oscillations. We define a quantity $A_{\rm dip} \equiv 1-\overline{\rho_0}(t=\tau_{\rm dip})$ with $\overline{\rho_0}(t=\tau_{\rm dip})$ being the value of $\overline{\rho_0}(t)$ at the first dip of the spin oscillations. By numerically solving the model Hamiltonian, we demonstrate that the dip depth $A_{\rm dip}$ is a good measure of DPT. A typical simulation result extracted from the quench dynamics at $N \sim 1\times 10^5$ is shown in Fig. 6.1 which clearly indicates that the behaviors of $\langle\overline{\rho_0}\rangle_\infty$ and $A_{\rm dip}$ are strongly correlated and they have non-analytic sudden jumps at exactly the same q_f marking a first-order DPT at $q_f = q_c = 0$. For systems with short-range couplings, the signature of DPT only shows up in long time evolution of local quantities, as the interaction effect needs to propagate over the system size. This argument is not valid for our model Hamiltonian as it has effectively infinite-range all-to-all couplings. This explains why the short time quantity $A_{\rm dip}$ and the conventional long time quantity $\langle\overline{\rho_0}\rangle_\infty$ mark the DPT equally well. In contrast to $\langle\overline{\rho_0}\rangle_\infty$, $A_{\rm dip}$ can be easily and precisely measured, because the dip time $\tau_{\rm dip}$ is short enough to avoid detrimental changes induced by long time evolution.

The details of the experimental procedure is given in Appendix E.1 with supporting data.

6.1.2 Results

Fig. 6.2 shows the observed $A_{\rm dip}$ and $\delta\rho_0(t=\tau_{\rm dip})$ as a function of q_f following a quench from positive q_i to various negative and positive q_f either crossing the dynamical transition point $q_c = 0$ or not, respectively. The results in Figs. 6.2(a) and 6.2(b) unambiguously confirm a first order DPT in our experiment, with a sudden jump of $A_{\rm dip}$ and $\delta\rho_0$ at $q_f = q_c = 0$. When q_f is positive, both $A_{\rm dip}$ and $\delta\rho_0$ remain almost at zero. Across the dynamical transition point at $q_c = 0$, $A_{\rm dip}$ and $\delta\rho_0$ jump to significant finite values and these values gradually

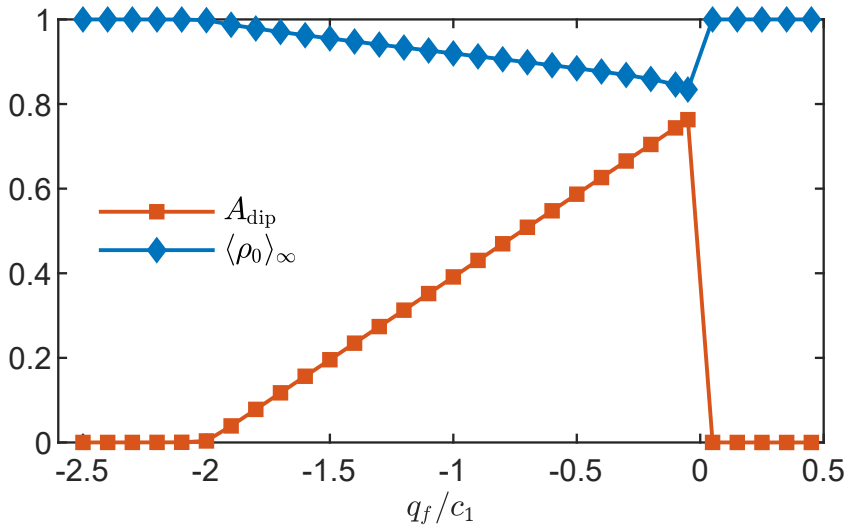

Figure 6.1: The predicted $A_{\rm dip}$ (depth of the first dip in spin oscillations) and the long-time average $\langle\overline{\rho_0}\rangle_\infty$ as functions of q_f/c_1 for $N = 1 \times 10^5$ and $q_i = 0.5c_1$ (see text). It seems that both short time $A_{\rm dip}$ and long time quench dynamics $\langle\overline{\rho_0}\rangle_\infty$ can signal DPT at the same q_f.

decrease with a linear scaling in $|q_f - q_c| = |q_f|$ when q_f is pushed to the negative region. The observed data agree very well with the theoretical prediction derived from the model Hamiltonian up to experimental uncertainty of q_f, which is about $h \times 2.5$ Hz near $q = 0$ Hz. This result demonstrates a major claim of this Section. With the measured linear scaling of $A_{\rm dip}$ in $|q_f|$ in the negative q region, its DPT scaling exponent is found to be 1, in agreement with the result from numerical simulations. The theoretical origin of this dynamical scaling exponent and its connection with the equilibrium critical exponents are interesting questions worthy of further investigation in the future.

The next important observation is the occurrence time of the first dip $\tau_{\rm dip}$. Fig. 6.3(a) compares the observed dip time $\tau^E_{\rm dip}$ with the theoretical $\tau^T_{\rm dip}$, which is predicted by the model Hamiltonian. When q_f is very close to the dynamical transition point, the measured $\tau_{\rm dip}$ is sensitive to the experimental calibration error on q_f, and there is some discrepancy between $\tau^E_{\rm dip}$ and $\tau^T_{\rm dip}$. Apart from this small region, the measured $\tau_{\rm dip}$ agrees quite well with the theoretical prediction. The theoretical dip time $\tau^T_{\rm dip}$ also exhibits an interesting power law scaling with $|q_f|$. To show this clearly, Fig. 6.3(b) displays $\tau^T_{\rm dip}$ as a function of $|q_f|$ in a log-log plot. To understand the origin of the power law scaling shown in Fig. 6.3(b), we note

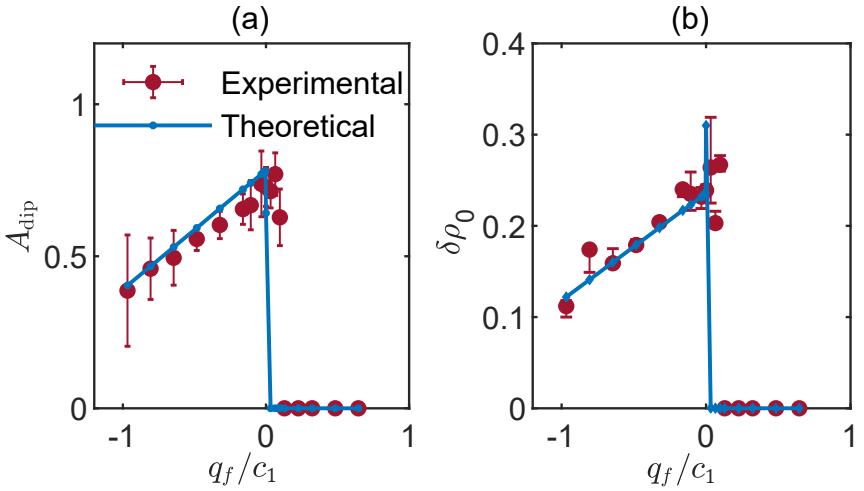

Figure 6.2: The observed signature of DPT. (a) The measured $A_{\rm dip}$ versus q_f/c_1. (b) The standard deviation $\delta\rho_0$ at $t = \tau_{\rm dip}$ versus q_f/c_1 at $c_1/h = 31\,$Hz. Circles with error bars denote the experimental data and the solid lines represent the theoretical results from numerical simulations of the model Hamiltonian (see text).

that although the quench dynamics involves the contribution of the entire energy spectrum, there are only a few eigenstates which play a dominant role when q_f is quenched across the transition. Similar to Chapter 2.4, we define an overlap function as a measure of the matrix element of ρ_0 in the basis of the final Hamiltonian and δE as the nearest-neighbor energy gap at the maximum off-diagonal term of this overlap function. We then numerically calculate the main frequency component in the oscillation of $\overline{\rho_0}$, which turns out to be $\delta E/h$. The time scale, defined by $T_{\rm osc} = h/\delta E$, also shows a power law scaling with $|q_f|$. Figure 6.3(b) shows both $T_{\rm osc}$ and $\tau^T_{\rm dip}$ as a function of $|q_f|$, which clearly indicates that the two log-log curves have similar slopes. The extracted power-law scaling exponents are -0.41 for $T_{\rm osc}$ and -0.40 for $\tau^T_{\rm dip}$, through linear fits to the log-log curves in Fig. 6.3(b). This suggests that the scaling properties of $\tau_{\rm dip}$ is mainly determined by the most dominant energy gap δE in the energy spectrum that is dictated by the initial state and the observable together.

In conclusion, this Section proposes probes originating from the transient temporal regime to dynamically detect first-order phase transition in the antiferromagnetic spinor condensates, i.e., the first dip and the associated timescale in an oscillatory nonequilibrium re-

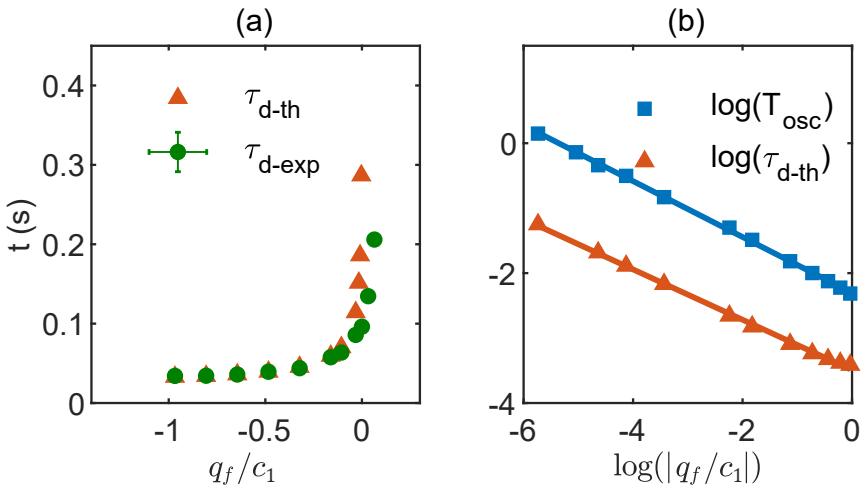

Figure 6.3: (a) Circles (triangles) represent the observed occurrence time of the first dip (the corresponding theoretical results derived from numerical simulations) as a function of q_f/c_1 at $c_1/h = 31\,\text{Hz}$. (b) The power law scaling of the theoretical dip time τ^T_{dip} and T_{osc} (the inverse of the relevant energy gap) in a log-log diagram. The extracted DPT exponents for T_{osc} and τ^T_{dip} are respectively -0.41 and -0.40, based on linear fits (denoted by the solid lines) to the log-log curves.

sponse. In the next Section, we will focus on the transient probes of the quantum criticality in the TFIM that hosts second-order phase transitions, as discussed in Chapter 1.

6.2 Dynamical crossover in the transient quench dynamics of short-range transverse field Ising models

Dynamical detection of quantum phases and phase transitions (QPT) in quenched systems with experimentally convenient initial states is a topic of interest from both theoretical and experimental perspectives. Quenched from polarized states, longitudinal magnetization decays exponentially to zero in time for the short-range transverse-field Ising model (TFIM) and hence, has a featureless steady state regime, which prevents it from exhibiting dynamical phase transitions of type-I. In this Section, we ask whether the transient regimes of such nonequilibrium processes probed by single-site observables, magnetization per site, could encode information about the underlying QPT. The decay rates of time-dependent and

single-site observables exhibit a dynamical crossover that separates two dynamical regions, ordered and disordered, both of which have distinct nonequilibrium responses. We construct a dynamical order parameterlike quantity that exhibits a scaling law in the vicinity of the crossover. Our results reveal that scaling law exponent in short times in the close vicinity of the dynamical crossover is significantly different than the one predicted by analytical theory for long times. When integrability is strongly broken, the crossover boundary turns into a region that separates two other dynamical regions that act like dynamically-ordered and -disordered regimes.

6.2.1 Introduction

The studies of dynamical criticality, phase transitions and crossovers range from dynamical detection of equilibrium criticality [66, 68–70, 181, 184, 198, 199, 204, 211, 214] (also see Ch. 4), to nonequilibrium phase transitions that might not necessarily originate from an equilibrium transition [181, 197, 198, 200, 203, 210, 217, 324, 325]. A commonly applied protocol in some of these studies is a sudden quench, which results in a nontrivial time evolution of either an observable, e.g., an (equilibrium) order parameter (OP) [181, 198, 210, 217], or Loschmidt echo [198, 199, 214, 217, 326] when the system is quenched from an initial state that is not an eigenstate of the evolution Hamiltonian. A popular choice of initial state in the current works on quench dynamics is a polarized state, due to its relevant convenience to prepare in quantum simulators [181, 198, 210, 217, 326]. Dynamical phase transitions of type-I (DPT-I) is defined when the quench dynamics equilibrate either to a thermal or a prethermal value in long times, and hence long-time average of the time-dependent observable could act like a dynamical OP, demonstrating a phase boundary. Although DPT-I is well-defined for magnetization of the long-range transverse field Ising model (TFIM) [217, 325], there is no persistent dynamic order for short-range TFIM, simply because the steady state regime of one-point observables, and likewise two-time correlators, is featureless [116, 327, 328]. The featureless steady-state for magnetization originates from the fact that this observable decays

exponentially in time as both analytically and numerically studied in the integrable TFIM [116, 128, 327–330]. In fact exponential decay is also shown to exist in the XXZ model for magnetization [331]. Therefore, one cannot dynamically detect equilibrium quantum phase transitions (QPT) of short-range TFIM quenched from polarized states by focusing on the steady-state regime of the magnetization dynamics.

Recently higher order observables are shown to exhibit steady-state regimes with a persistent dynamic order in the quench dynamics of short-range TFIM [181, 210]. Ref. [181] proposed measuring out-of-time-order correlators (OTOC) of an arbitrary single-site observable (longitudinal magnetization per site) both for integrable and nonintegrable short-range TFIM to access such steady-state regimes. Later Ref. [210] showed that two-point nearest-neighbor correlators (averaged over space) could signal a dynamical phase transition in short-range TFIM, albeit the dynamical critical point shifts to favor disorder when integrability is broken.

Motivated by the recent research interests in finding dynamical probes of equilibrium QPT in short-range Hamiltonians [181, 209, 210], in this Section we ask whether the transient regimes of short-range TFIM quenched from polarized states and probed by single-site local observables, magnetization per site, could encode information about the underlying equilibrium QPT. We stress that we focus on transient regimes of dynamics and single-site observables, instead of steady-state regimes and global observables. Let us first note that transient probes of QPT could prove useful in laboratory implementations of quantum many-body systems, given that it might be challenging to reach steady-state regimes in experimental setups that are naturally coupled to an environment and experiences decoherence (see the discussion in previous Section). Both Chapter Sec. 6.1 and Ref. [332] utilized transient signatures of the underlying QPT in the experiments on spinor condensates, e.g., the amplitude and time of the first peak/dip of an oscillatory nonequilibrium response. Furthermore, quantum simulators are ideal testbeds to study the properties and potential of single-site observables, which require only minimal resources for measurement

with technologies like quantum gas microscope [195]. Ref. [181] demonstrated that OTOC of single-site observables could be useful to probe the equilibrium QPT, however probing OTOCs in laboratory requires sophisticated protocols such as reversing the overall sign of the Hamiltonian to realize backward time evolution [146] (also see Ch. 3), or equally sophisticated alternative methods [147, 148, 153].

In our work, we focus on the single-site observables in both open-boundary and closed chains of TFIM. An open-boundary chain is experimentally more relevant, whereas the results for a periodic TFIM could be obtained by utilizing a mapping to noninteracting fermions. Open-boundary chain simulations are performed via time-dependent density-matrix renormalization group (t-DMRG). Via utilizing the representation of noninteracting fermions, we could easily reach hundreds of sites in the integrable TFIM, and compare the crossover dynamics of small and large system sizes. A crossover in integrable TFIM probed by single-site observables was analytically predicted in Ref. [116] for large times in the space-time limit. This crossover separates two distinct nonequilibrium responses where the observable decays exponentially without and with oscillations in the dynamically-ordered and -disordered regimes, respectively. Here we reveal that the scaling predicted by the analytic theory for long times ($\beta = 1/2$) in the dynamically-ordered regime, significantly changes for short times ($\beta = 1$) in the close vicinity of the crossover boundary which coincides with the equilibrium phase boundary in the integrable TFIM, $h_c = 1$. As one moves away from the vicinity of the crossover, the analytically predicted exponent is recovered, which suggests a smooth crossover between short and long time dynamics. In the dynamically-disordered regime, we find that the analytical prediction conjectured in Ref. [116] is not the only possible description of the dynamics for short times and small system sizes, e.g., $N = 48$ spins. Additionally, the angular frequency has a correction for short times and small system sizes, while we recover the analytically predicted exponent $\delta = 1/2$ for long times when we increase the system size to $N = 192$ spins.

We also find that the scaling in the vicinity of the crossover in the dynamically-ordered

regime can be described by a logarithmic function regardless of the system size and the temporal regime, e.g., short or long time dynamics. We show that this is consistent with the analytical predictions. Logarithmic form eventually becomes useful in proposing a dynamical OP-like quantity in the vicinity of the crossover. This proposal eases the experimentation of crossover physics discussed in the Section.

We note that the location of the crossover corresponds to the TFIM Hamiltonian that exhibits the fastest decay in the set of all Hamiltonians $H(h)$ across both sides of the equilibrium phase boundary, in particular for short times. Given that observables cannot show divergent decay in short-range interacting systems due to lightcone bounds, it is reasonable that all decay rates are finite. Hence our data suggests a link between the fastest decay and the equilibrium QPT, confirming Ref. [331]. We use this observation to mark the boundary between dynamically-ordered and crossover regions in the nonintegrable TFIM. We break the integrability by introducing next-nearest neighbor coupling to TFIM and study how the quench dynamics for single-site magnetization behave. After modeling the quench dynamics, we notice that three quantitatively distinct dynamical regimes emerge for the nonintegrable TFIM. The crossover boundary of the integrable TFIM enlarges into a region around the equilibrium QPT and separates two other dynamical regimes which act as -ordered and -disordered regimes of the integrable TFIM. This means that the nonintegrable TFIM exhibits a dominant trend of exponential decay in its dynamically-ordered regime; and a dominant trend of oscillatory exponential decay in its dynamically-disordered regime. We study the relevant decay rate and find that breaking integrability results in a smooth crossover, a minimum, and shifts its location from the equilibrium phase boundary to $h_c = 2.278 \pm 0.001$. The associated scaling exponent of the dynamical order parameterlike quantity reads $\beta \sim 2$, consistent with the smooth crossover of the decay rates.

In the next subsection, we introduce the models and our methods, which is followed by the dynamical crossover of the integrable and nonintegrable TFIMs, respectively.

6.2.2 Methods

In this Section, we work with TFIM with both nearest-neighbor (NN) and next-nearest-neighbor (NNN) couplings,

$$H = -J \sum_r \sigma_r^z \sigma_{r+1}^z - \Delta \sum_r \sigma_r^z \sigma_{r+2}^z + h \sum_r \sigma_r^x, \tag{6.3}$$

where σ_r^α are spin$-\frac{1}{2}$ Pauli spin matrices. TFIM preserves its gapped long range Ising ground state even when the interactions (or nonintegrability) Δ are introduced, although the transition boundary shifts to favor order as Δ increases. For all data in this Section, we fix $J = 1$ as the energy scale. Specifically we focus on the integrable model $\Delta/J = 0$ and nonintegrable model with $\Delta/J = -1$.

Since an open-boundary chain is more experimentally relevant, we study the open-boundary TFIM with matrix product states (MPS [300]). To reproduce the decay dynamics of an arbitrary site in a periodic chain we focus on the longitudinal magnetization in the middle of the chain $\sigma_{N/2}^z$ (Appendix Sec. E.2.1). Hence the observable's decay is similar to the decay of total magnetization given that total magnetization is $M = 1/N \sum_r \sigma_r^z$. We also study an arbitrary site on a periodic TFIM to utilize the mapping to noninteracting fermions and increase the system size for the integrable TFIM. To calculate single-site dynamics in noninteracting fermions, we make use of the cluster theorem similar to Ref. [116]. See Appendix Sec. E.2.2 for the details of the mapping in quench dynamics and the limitations due to cluster theorem. In both open-boundary and closed chains, we focus on the single-site dynamics of Eq. (6.3) quenched from a polarized state $|\psi_0\rangle = |\uparrow\uparrow \ldots \uparrow\rangle$: $C(t) = \langle\psi_0| \sigma_{N/2}^z(t) |\psi_0\rangle$.

In DPT-I, one studies steady-state regime where the dynamics is expected to become independent of the time. Since such steady-state regimes might exhibit oscillatory behavior, typically due to finite-size effects in small systems, often times averaging over an interval of time is employed [181, 199, 210]. Averaging over a long interval of time also makes the dynamic OP to be less sensitive to where a temporal cutoff is applied in the steady-state

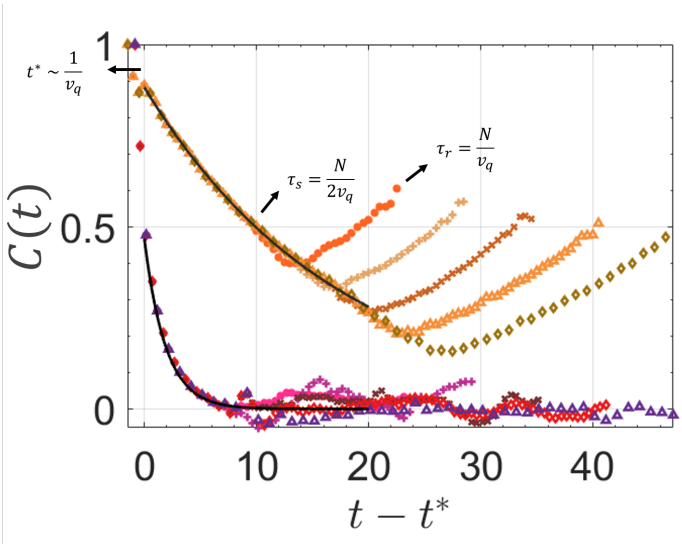

Figure 6.4: $C(t)$ for $h/J = 0.5$ upper curves with orange tones and $h/J = 0.9$ lower curves with red tones. Each set of curves have system sizes between $N = 24$ (dots) and $N = 48$ (diamonds) denoted by different markers. τ_s and τ_r are separation and revival timescales (see text). x-axis is shifted by t^*, the reference time where the exponential decay starts.

regime. This is because oscillations could alter the dynamic OP if one only uses the value at the temporal cutoff. As a result, exact location of the temporal cutoff is not significant in the construction of the dynamical OP based on DPT-I as long as the temporal cutoff is in steady-state regime. A valid temporal cutoff that can be utilized in studying DPT-I is a system-size dependent cutoff, $t \sim \alpha N$ where the interval of time-averaging is proportional to the system size [217] up to a coefficient α.

This temporal cutoff does not work for one-point observables in short-range models, because as already mentioned before, these observables are featureless in their steady state regimes, meaning that they decay exponentially to zero. If one were to use a cutoff $t \sim \alpha N$, we would simply observe a vanishing dynamic OP for one-point observables [181, 217] (see Appendix Sec. E.2.3). This observation aligns with the fact that one cannot construct DPT-I for magnetization in short-range TFIM. Hence, motivated on working in the transient regime, we turn our attention to the decay rates of the initial magnetization, which is known to exhibit a cusplike feature at the QPT for the XXZ model [331]. In order to extract the exponential decay in the thermodynamic limit with finite-size systems, which are the

only experimentally relevant systems, we find the lightcone bounds [44, 116, 333] on the magnetization per site for the finite sizes under study. The dynamics that remain in the lightcone exhibit exponential decay and show finite-size effects exponentially suppressed in the system size [334]. Fig. 6.4 shows the open-boundary integrable TFIM dynamics for $h/J = 0.5$ (orange tones) and $h/J = 0.9$ (red tones) for system sizes $N = 24 : 6 : 48$. In the lightcone, data for different system sizes collapse on each other while each separation point is roughly marked by $\tau_s = N/2v_q$ where v_q is the maximum quasi-particle velocity $v_q = \max|d\epsilon(h,k)/dk| = 2J\min(h,1)$ [116, 193, 333]. τ_s is the time for the excitations caused by the quench to reach the end of the chain, and hence τ_s probes the size of the chain. When the chosen bulk spin is not in the middle of the chain its coefficient changes $\tau_s = a/v_q$ where $N/2 \leq a < N$. Revival timescale is marked by $\tau_r = N/v_q$, which is the time for the excitations to reflect back from the boundary to the middle of the chain. The timescale t^* is the short-distance cutoff of the temporal axis defined by the lattice constant divided by velocity $t^* \sim v_q^{-1}$. Here, t^* (τ_s) serves as the ultraviolet (infrared) cutoff, below (above) which the physics is dominated by non-universal microscopic details (finite-size effects). Thus, we focus on the (intermediate) time range $t^* < t < \tau_s$, where data of different system sizes collapse on each other and universal behavior arises as shown in Fig. 6.4 with an exponential decay [116, 128, 329, 330]. The time interval that remains in the lightcone effectively simulates the decay in the thermodynamic limit.

For our periodic chain results, we are always confined to the intermediate time range due to the application of cluster theorem (Appendix Sec. E.2.2).

6.2.3 Dynamical Crossover in the integrable TFIM

Integrable TFIM hosts a crossover at $h_c = 1$ that separates two dynamical regimes. In the dynamically-ordered regime, single-site observables exhibit an exponential decay in time, whereas in the dynamically-disordered regime we observe an oscillatory exponential decay. We will systematically study the short-time nonequilibrium response of single-site observables

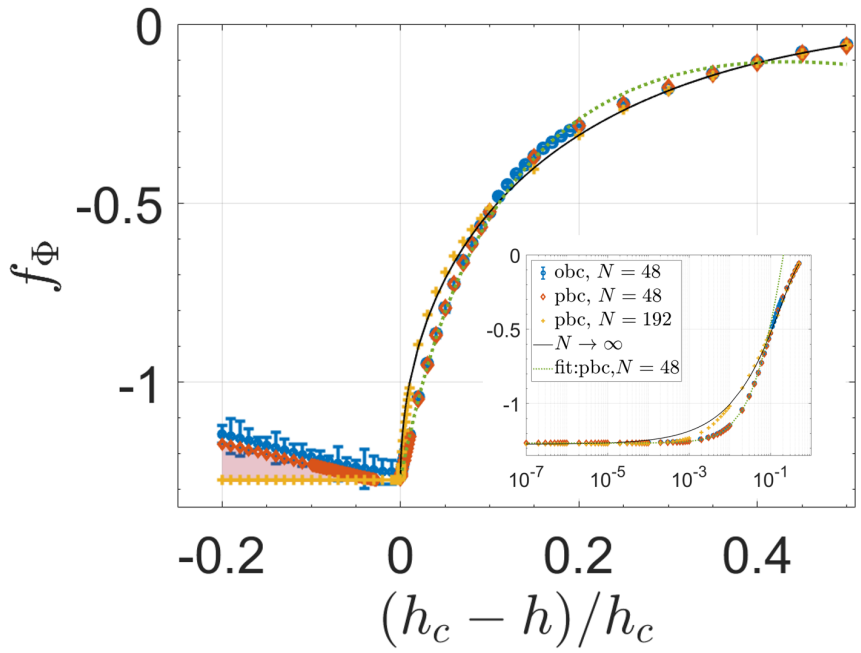

Figure 6.5: Decay rates f_Φ for integrable TFIM in dynamically-ordered $(h_c - h)/h_c > 0$ and -disordered $(h_c - h)/h_c < 0$ regimes. The inset focuses on the dynamically-ordered regime in a semilog plot. Blue-circles, red-diamonds and yellow pluses are data for system sizes $N = 48$ with open boundaries (obc), periodic boundaries (pbc) and $N = 192$ with periodic boundaries, respectively. Green-dotted line is the logarithmic fit function for the data $N = 48$ (pbc) (see text), whereas the black-solid line is the analytic result for the thermodynamic limit. In the disordered regime, the shaded region is the uncertainty for system size $N = 48$ due to short time evolution.

in the integrable TFIM in this subsection. In the following, we focus on the dynamically-ordered regime.

Decay rates

Bounded by the lightcone, we find the decay rates of magnetization per site around the crossover at $h_c = 1$. Fig. 6.5 shows how these decay rates f_Φ change with the reduced control parameter $h_n = (h_c - h)/h_c$ for system sizes $N = 48$ with both open (blue-circles) and periodic (red-diamonds) boundary conditions and $N = 192$ with periodic boundary condition (yellow-pluses). A cusplike feature is observed in Fig. 6.5, similar to the XXZ model in Ref. [331]. The dynamically-disordered regime will be explained in a following

subsection.

We first note that our two methods explained previously match perfectly for $N = 48$. Thus, one could measure the middle spin in an open-boundary chain and reproduce the results for an arbitrary site in a periodic chain. By increasing the system size to $N = 192$, we observe a convergence to the prediction by the analytic theory for the thermodynamic limit (black-solid) for $h_n > 10^{-2}$. Hence, two remarks follow: (i) Although we work with data bounded by the lightcone, the data for small system sizes, e.g., $N = 48$ still experiences finite-size effects [334], because the simulation time is restricted by the system size in the lightcone. (ii) In the close vicinity of the crossover, $h_n < 10^{-2}$, even the large systems, e.g., $N = 192$ diverge from the analytic prediction (see the inset in Fig. 6.5).

The analytic prediction is calculated based on the space-time limit derivation given in Ref. [116]. For a quench from a polarized state, the asymptotic late-time scaling reads

$$C(t) \sim \left(1+\sqrt{1-h^2}\right)^{1/2} \exp\left(t f_\Phi^\infty(h)\right), \tag{6.4}$$

$$f_\Phi^\infty(h) = -\frac{4}{\pi}\left(h+\sqrt{1-h^2}\left[\arcsin\left(\sqrt{\frac{1-h}{2}}\right)-\arcsin\left(\sqrt{\frac{1+h}{2}}\right)\right]\right). \tag{6.5}$$

For the numerics close to crossover, we propose a logarithmic fit function

$$f_\Phi = \log(\gamma h_n^\beta \exp(-h_n/\Lambda) + C_0),$$

where γ and β are free parameters to be found and Λ is the exponential cutoff coefficient which is explained below. We note that such a model for the decay rate is intuitive and describes the data in a large interval $0 < h_n \lesssim 0.4$, not only in the close vicinity of the crossover. The constant C_0 points to the observation that the decay rate is never infinite, however the largest at the crossover boundary. Hence the system thermalizes the quickest at the crossover. Further C_0 is not a free parameter, but fixed by the data itself at the crossover. Furthermore, analytical prediction for thermodynamic limit at late times gives

$C_0 = \exp(-4/\pi)$. Data follows $\log(\gamma h_n^\beta + C_0)$ in the vicinity of the crossover, while introducing an exponential cutoff [335] to the model lets us describe a bigger region of h_n as well as providing a definition for 'vicinity of the crossover', $h_n \ll \Lambda$. For example, the fit parameters for the decay rates of system size $N = 48$ depicted in the main panel of Fig. 6.5 (green-dotted line) are $\beta = 1.05$ and $\Lambda = 0.37$, meaning that the vicinity of the crossover could be defined as $h_n \lesssim 0.03$. Indeed by using the interval of $h_n \lesssim 0.03$, one can precisely determine the scaling exponent as $\beta = 1$ in the fit function $\log(\gamma h_n^\beta + C_0)$ (green-dotted line in the inset of Fig. 6.5).

We note that the logarithmic function is consistent with the analytical expression Eq. (6.5) in the vicinity of the crossover. This can be seen from the series expansions of Eq. (6.5) and the logarithmic fit function. The series expansion of Eq. (6.5) in the vicinity of the crossover is,

$$f_\Phi^\infty(h_n \to 0) \sim -\frac{4}{\pi} + 2\sqrt{2h_n} - \frac{4h_n}{\pi} + \cdots , \tag{6.6}$$

while the series expansion for the logarithmic fit function follows

$$f_\Phi(h_n \to 0) \sim \log(C_0) + \frac{\gamma}{C_0} h_n^\beta + \mathcal{O}(h_n^{2\beta}). \tag{6.7}$$

Therefore, in the close vicinity of the crossover the analytic prediction could be written as the logarithmic fit function with the parameters of $C_0 = \exp(-4/\pi)$, $\beta = 1/2$ and $\gamma/C_0 = 2\sqrt{2}$, resulting in $\gamma = 2\sqrt{2}\exp(-4/\pi)$. In the next subsection, we will see the use of logarithmic fit function in experimentation. However now let us show how it could be helpful in extracting the scaling exponent from the numerical data in the close vicinity of the crossover.

To extract the scaling exponent in the close vicinity of the crossover, we define a decay rate function $\exp(f_\Phi(h_n)) - C_0 = \gamma h_n^\beta$. Fig. 6.6 shows the decay rate function of both the numerical data and the analytical expression (black-solid). The green-dotted line is the fit to the analytical expression in the vicinity of the crossover with the expected scaling exponent of

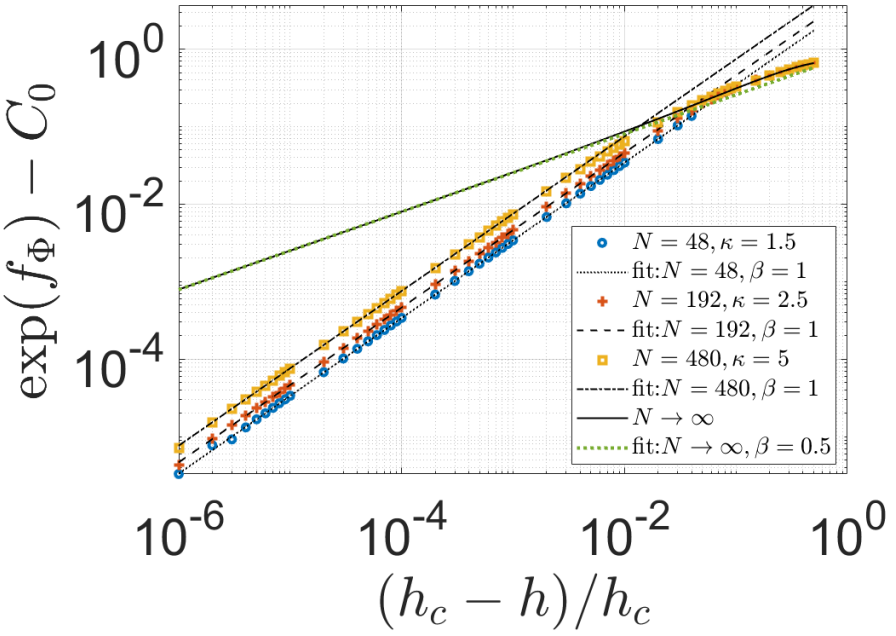

Figure 6.6: Scaling of the decay rate function $\exp(f_\Phi) - C_0$ for integrable TFIM in dynamically-ordered $(h_c - h)/h_c > 0$ regime. Blue-circles, red-pluses and yellow squares are data for system sizes $N = 48$, $N = 192$ and $N = 480$ all with periodic boundaries, respectively. Black-solid line is the analytic prediction for the thermodynamic limit and late times, whereas the green-dotted line is the fit to the analytic expression in the vicinity of the crossover with $\beta = 1/2$. The dotted, dashed and dotted-dashed lines are the fits to the numerical data in the close vicinity of the crossover with $\beta = 1$.

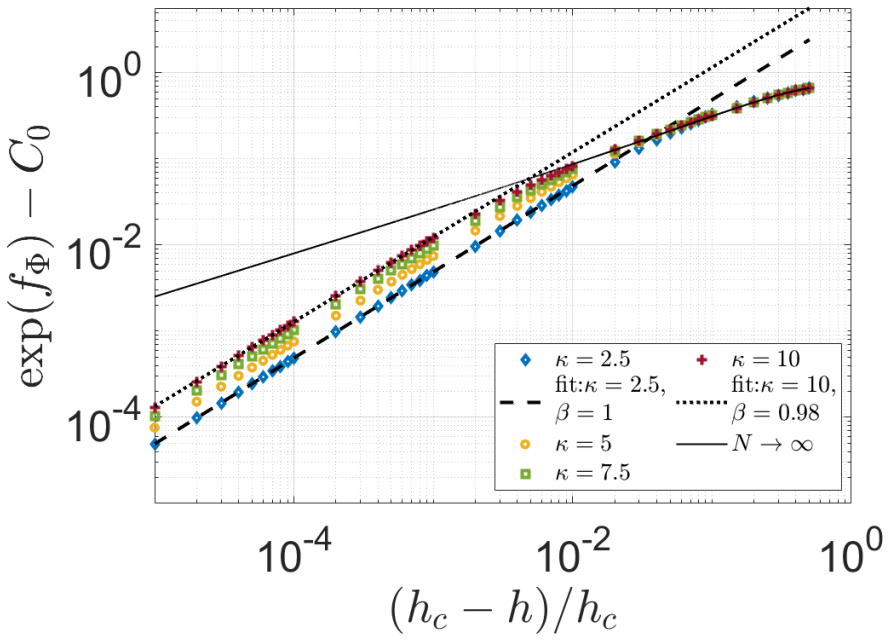

Figure 6.7: Scaling of the decay rate function $\exp(f_\Phi) - C_0$ for integrable TFIM in dynamically-ordered $(h_c - h)/h_c > 0$ regime for system size $N = 480$ for different κ. Blue-diamonds, yellow-circles, green squares and red-pluses stand for $\kappa = 2.5, 5, 7.5, 10$, respectively. Black-solid line is the analytic prediction for the thermodynamic limit for comparison with the fits (dotted and dashed lines).

$\beta = 1/2$ and coefficient $\gamma = 2\sqrt{2}\exp(-4/\pi)$. The blue-circles, red-pluses and yellow-squares depict the data for system sizes $N = 48, 192, 480$ all of which exhibit a scaling exponent of $\beta = 1$. Note that we choose the ultraviolet cutoff $t^* = \kappa v_q^{-1}$ where κ for each data set is given in the legend. Small coefficient κ implies that we focus on early-time behaviour.

As a result, regardless of system size we observe that early-time scaling exponent $\beta = 1$ is significantly different than the late-time scaling exponent of $\beta = 1/2$ in the close vicinity of the crossover. As we move further away from the vicinity of the crossover, the decay rate function at any system size converges to the prediction by analytical expression. Hence we observe a smooth crossover between different scaling exponents in Fig. 6.6, whose exact location depends on κ. To visualize the dependence on κ, we plot Fig. 6.7 where the system size is fixed to $N = 480$ for different κ. As we increase κ, we move the location of the crossover between analytical late-time and numerical early-time behaviors, to smaller h_n.

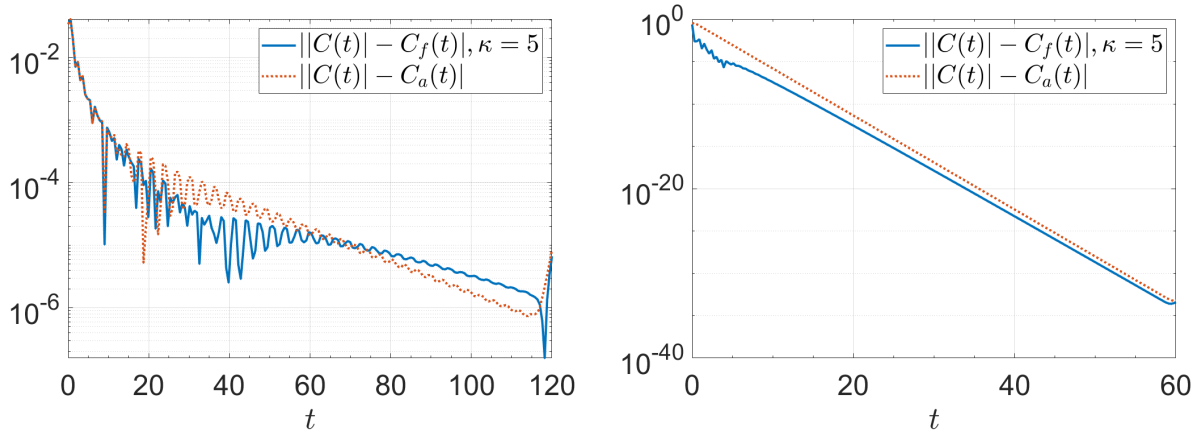

(a) (b)

Figure 6.8: The error functions, $|C(t) - C_f(t)|$ (solid) and $|C(t) - C_a(t)|$ for the fit function and the analytical expression (dotted), respectively, for a system size of $N = 480$ at (a) $h = 0.5$ and (b) $h = 9.9 \times 10^{-6}$. The fit function is calculated with $\kappa = 5$.

We observe that the numerical data mostly follows analytical prediction when h_n is sufficiently away from the crossover, resulting in a nonequilibrium response where early-time behaviour does not really differ from the analytical prediction. Hence, one can probe analytical prediction by observing early-time behaviour. Fig. 6.8a shows the difference between data and its fit function $C_f(t)$ which is named as an error function $|C(t) - C_f(t)|$ at $\kappa = 5$ for a system size $N = 480$, and similarly the difference between the data and its analytical prediction $|C(t) - C_a(t)|$ at $h = 0.5$. At early times $t < 20/J$, fit function and the analytical expression are equally successful in predicting the data. In time interval $20/J < t < 60/J$, fit function is slightly better than the analytical expression while for later times $t > 60/J$ the opposite is true, as expected.

At the other end where numerical data exhibits a distinct scaling exponent of $\beta = 1$, crossover physics at $h_c = 1$ take over with diverging relaxation time [68, 70] and one cannot reach late-time behavior in accessible times for any system size that we studied. Fig. 6.8b shows the error functions at $h = 9.9 \times 10^{-6}$ where the fit function is always better to predict the data than the analytical expression in a time interval of $t < 60/J$. This suggests that in the close vicinity of the crossover, the analytical expression fails for accessible times and

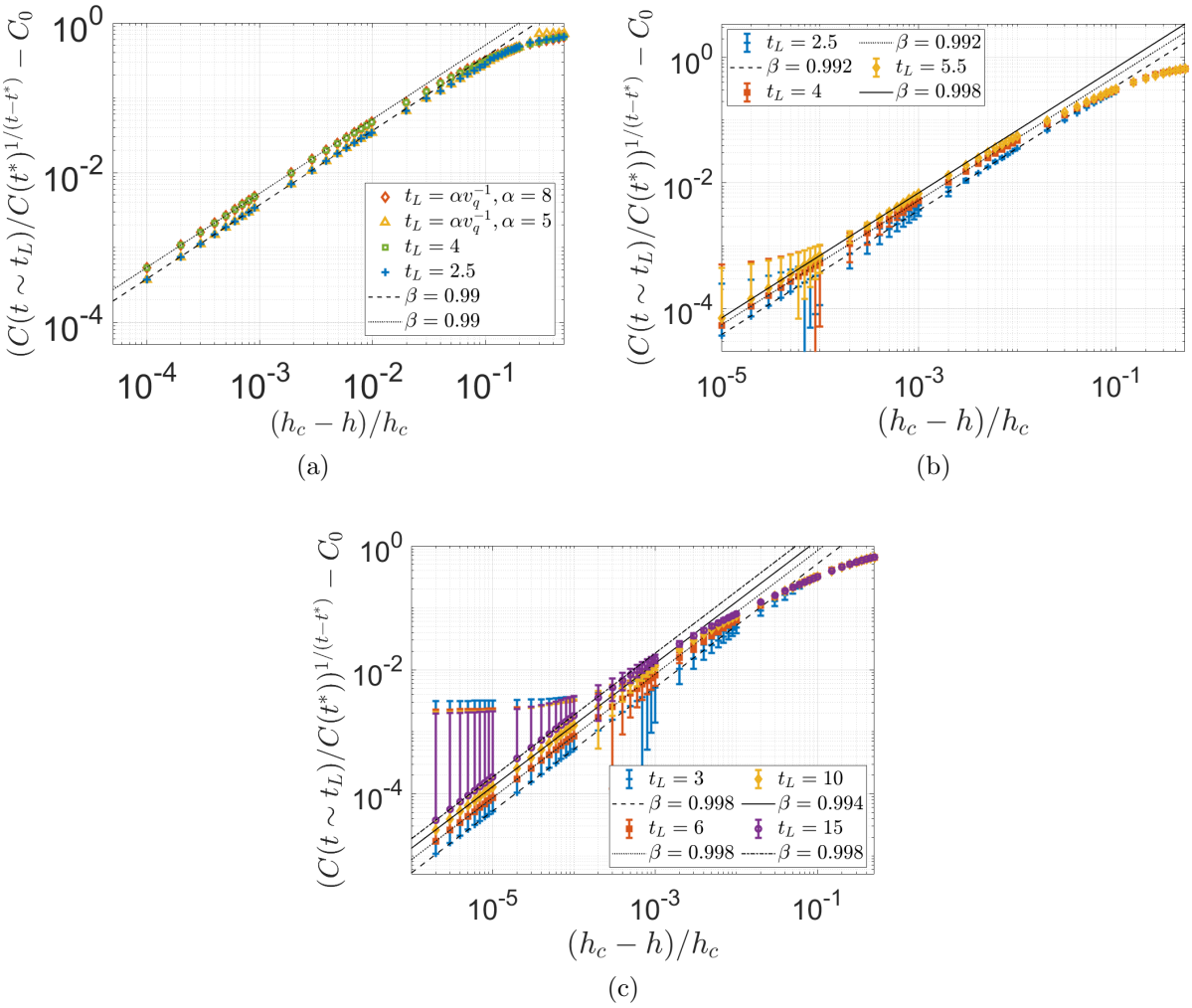

Figure 6.9: The scaling in the vicinity of the crossover for integrable TFIM with respect to reduced control parameter h_n for (a) $N = 48$ with open boundary condition (b) $N = 48$ and (c) $N = 480$ with periodic boundary condition. y-axis is rescaled correctly to obtain the scaling (see text). The temporal cutoffs are (a) either fixed at $t_L = 2.5, 4$ or parametric with $\alpha = 5, 8$; fixed at (b) $t_L = 2.5, 4, 5.5$ and (c) $t_L = 3, 6, 10, 15$. The solid, dotted, dashed and dotted-dashed lines are the fits in the vicinity of the crossover, all giving $\beta \sim 1$ for all subfigures. Error bars are explained in Appendix Sec. E.2.6.

likewise we observe a scaling exponent of $\beta = 1$ instead of $\beta = 1/2$.

Constructing a dynamical order parameterlike quantity in the dynamically-ordered regime

One can measure the decay rates of magnetization at each transverse field and probe the crossover between dynamically-ordered and -disordered regimes in TFIM. Alternatively, we aim to find a rescaling of the decaying observable $C(t)$ that can render the rescaled observable a quantity that acts like a dynamical OP in the ordered regime right in the vicinity of the crossover. One can see this procedure as a way to construct a dynamical order parameterlike quantity with the correct rescaling that is originated from the scaling behaviour of the decay rates in the vicinity of the crossover. In DPT-I, the observable naturally acts as a dynamical OP in a nonzero valued steady-state. We find that for magnetization per site in short-range TFIM one needs to correctly rescale the observable to construct a quantity alike. This, in the end, presents an alternative way of extracting the scaling exponent in an experiment, which is less laborious than measuring the decay rates directly.

Similar to how a dynamical OP in DPT-I is constructed by first choosing a temporal cutoff, we consider two different temporal cutoffs applied at a time either (i) fixed $t_L \sim$ constant or (ii) parametric $t_L = \alpha v_q^{-1}$ where α is chosen so that the dynamical response remains in the lightcone, e.g., $t_L \leq \tau_s$. Note that for all temporal cutoffs, $t_L \geq t^*$ holds. Eventually the rescaled dynamical OP-like quantity should not depend on how we choose our temporal cutoff. Furthermore, while one can average the observable for a time between the ultraviolet cutoff t^* and the temporal cutoff t_L, this would complicate the functional form of the rescaling needed and it would require more data to compute/measure. Hence, we simply measure the observable $C(t)$ at time t_L dictated by the fixed or parametric temporal cutoff.

Let us rewrite the observable in the vicinity of the crossover by substituting the logarith-

mic fit function for the decay rates in,

$$C(t) \quad = \quad C(t^*)\exp(f_\Phi(t-t^*)) = C(t^*)(\gamma h_n^\beta + C_0)^{t-t^*}. \tag{6.8}$$

The scaling of the decay rate as a function of h_n reveals a scaling for the observable in the vicinity of the crossover. This expression points out to the correct form of rescaling for the observable to make the procedure independent of the temporal cutoff. Hence the correct rescaling for the observable reads,

$$\left(\frac{C(t)}{C(t^*)}\right)^{1/(t-t^*)} - C_0 = \gamma h_n^\beta, \tag{6.9}$$

leading us to define a dynamical OP-like quantity,

$$C'(h_n) = \left(\frac{C(t)}{C(t^*)}\right)^{1/(t-t^*)} - C_0, \tag{6.10}$$

which is strictly valid in the vicinity of the crossover. Hence, one can probe the exponent by simply computing $(C(t_L)/C(t^*))^{1/(t_L-t^*)} - C_0$ which requires data points at cutoffs t^* and t_L only, assuming C_0 is fixed by numerical prediction.

Figs. 6.9 show how the dynamical OP-like quantity $C'(h_n)$ constructed based on different cutoffs scales with h_n in the vicinity of the crossover for $N = 48$ with open boundaries in (a), periodic boundaries in (b) and for $N = 480$ with periodic boundaries in (c). The colors yellow, red and blue correspond to cutoffs chosen at fixed $t_L = 2.5, 4, 5.5$ and at $\alpha = 5, 8$ for parametric $t_L = \alpha/v_q$. All data at different temporal cutoffs exhibit the same exponent $\beta \sim 1$. The differences between different temporal cutoffs are detailed in Appendix Sec. E.2.3. The error bars originate from the uncertainty in time (Appendix Sec. E.2.6). Since Fig. 6.9a is measured at temporal cutoffs, while the Figs. 6.9b and 6.9c are not, there is no error bars for Fig. 6.9a. In our data, the temporal uncertainty increases as we increase the system size, which explains the biggest error bars in Fig. 6.9c. Therefore, by measuring

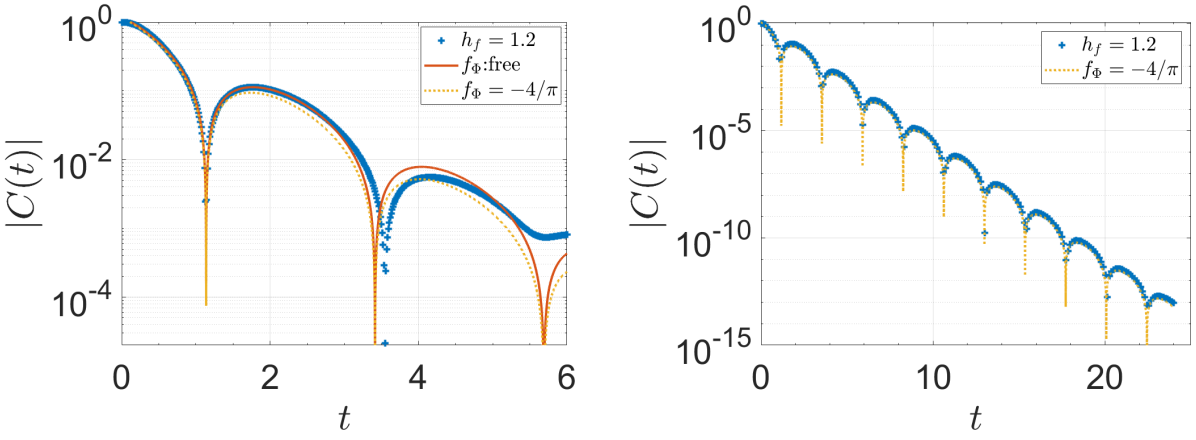

(a) (b)

Figure 6.10: The real time dynamics for the dynamically-disordered regime at $h_f = 1.2$ in (a) short-times for $N = 48$ and (b) long-times for $N = 192$. (a) The short-time dynamics is fitted with analytically predicted $f_\Phi = -4/\pi$ (yellow-dotted) and numerically the best match (red-solid) which keeps f_Φ as a free parameter. (b) For large systems, the analytical prediction matches the data excellently.

exactly at the temporal cutoffs these error bars tend to vanish away.

Dynamically-disordered regime

The analytical prediction for the dynamically-disordered regime reads $f_\Phi^\infty = -4/\pi$ in the nonequilibrium response

$$C(t) \sim (1 + \cos(2\omega t + \xi) + \cdots)^{1/2} \exp(t f_\Phi^\infty), \tag{6.11}$$

$$\omega(h) = 2\sqrt{1 + h^2} - 2, \tag{6.12}$$

where $\cdots$ means that there are subleading terms and ξ is an unknown constant. We work with a slightly simplified version of this analytical conjecture: $C(t) = \gamma \cos(\omega t) \exp(t f_\Phi)$, which also appears in Ref. [331].

We first focus on short times and small system sizes, e.g., $N = 48$ and observe that in this limit, the dynamics could be equally well described by alternative expression to the analytical prediction. Fig. 6.10a shows the dynamical response for $h_f = 1.2$ where we fit two

different curves to the data. The yellow-dotted line is the fit originated from the analytical expression where we fix the decay rate to $f_\Phi = -4/\pi$. We let f_Φ be a free parameter in the red-solid line. Therefore the latter performs slightly better than the former, especially for $t < 4/J$. We plot the scaling of the decay rates in the dynamically-disordered regime for the latter in Fig. 6.5 which turns out to be linear both for periodic and open boundary calculations. We also shade the area between the linear scaling and the constant line at $f_\Phi = -4/\pi$ to emphasize the uncertainty in the decay rates for the dynamically-disordered regime for short times and small system sizes. The corresponding scaling for the angular frequency ω is plotted in Fig. 6.11a which is $\delta \sim 0.533$ for both cases where we either fix the decay rate $f_\Phi = -4/\pi$ or let it be a free parameter. The shaded area in between is negligible.

When we increase the system size to $N = 192$, we reach longer times and the analytical expression becomes the best fit for the general trend of the data, Fig. 6.10b, as expected. In this case, the decay rate is constant at $f_\Phi = -4/\pi$ as can be seen in Fig. 6.5. The corresponding scaling for the angular frequency ω approaches to $\delta \sim 0.5$ as can be calculated from the series expansion of the analytical expression Eq. (6.12) in the close vicinity of the crossover, $\omega(h_n \to 0) \sim 2\sqrt{2}(-h_n)^{1/2} + \mathcal{O}((-h_n)^{3/2})$. The numerical demonstration of $\delta = 0.5$ is shown in Fig. 6.11b with system sizes $N = 192, 480$.

In conclusion, one observes corrections to the exponents $\delta_\infty = 1/2$ and $\beta_\infty = 0$ in the dynamically-disordered regime for short times, resulting in $\delta \sim 0.533$ and $\beta \sim 1$.

6.2.4 Dynamical crossover in the nonintegrable TFIM

Having studied the dynamical crossover observed in the transient regime for a noninteracting model, we now turn our attention nonintegrable TFIM.

We break the integrability of the model by taking $\Delta/J = -1$ in Eq. (6.3), which hosts an equilibrium QPT at $h_c \sim 2.46$ (Appendix Sec. E.2.5). Fig. 6.12a shows the sophisticated dynamical response of this model calculated with MPS for different h values in the lighcone determined by data ranging from $N = 24$ to $N = 42$. Lightcones are determined similarly by

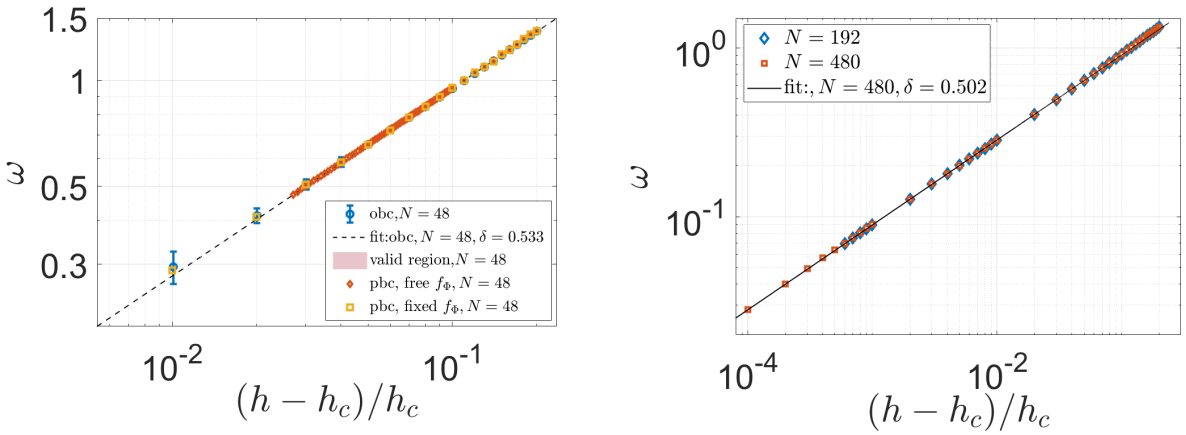

(a) (b)

Figure 6.11: Angular frequency scales with $-h_n$ with a power-law exponent of (a) $\delta \sim 0.53$ for small system sizes and (b) $\delta \sim 0.5$ for larger system sizes in the disordered regime in the vicinity of the crossover. In (a) we plot the scaling of ω for both cases where we either fix $f_\Phi = -4/\pi$ (orange-squares) or let it be a free parameter (red-diamonds). The area in between is shaded which is very negligible.

studying the separation timescales τ_s of different system sizes. Fig. 6.12b shows the presence of well-defined τ_s timescales for a range of different system sizes at $h/J = 2$.

Fit function for the nonintegrable TFIM

An important difference from the noninteracting model is the oscillations existing in both dynamically-ordered and -disordered regimes. Hence, we first aim to approximately model the dynamical response. Since oscillations are present at every h/J, a fit function that can reproduce the important features of the dynamics is,

$$C(t) = \gamma_1 \exp(f_{\Phi,1} t) + \gamma_2 \exp(f_{\Phi,2} t) \cos \omega t. \tag{6.13}$$

The dashed lines in Fig. 6.12a show how well the fit function can describe the dynamics. The first and the second terms are analogous terms for the dynamically-ordered and -disordered regimes of the integrable TFIM, respectively. Thus, an immediate observation is that there seems no sharply distinct dynamical regimes as in integrable TFIM. We study the param-

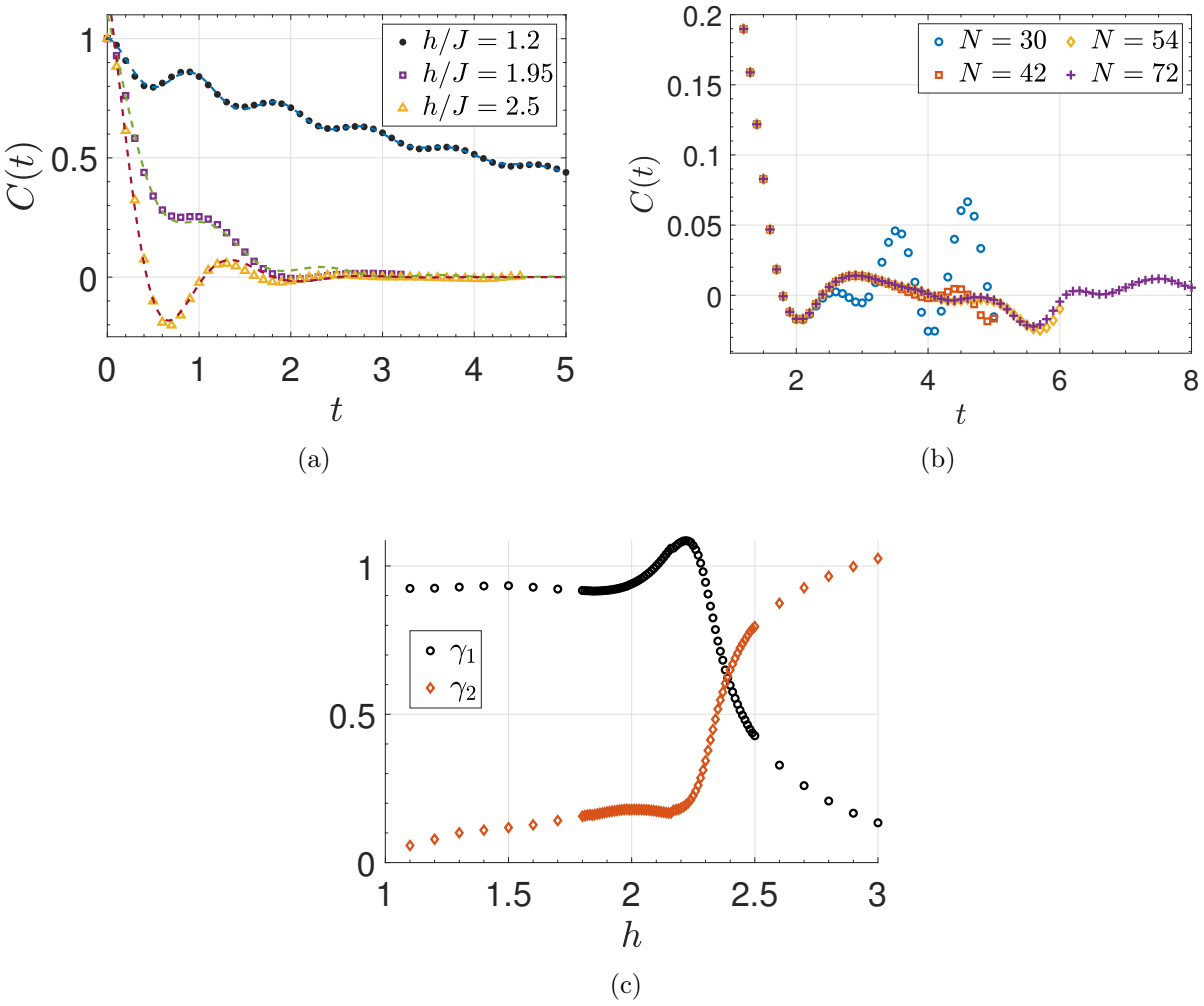

Figure 6.12: (a) The nonintegrable TFIM with $\Delta/J = -1$ for different $h/J = 1.2, 1.95, 2.5$ and dashed lines are the fit function predictions for dynamical responses. (b) Single-site observable $C(t)$ for the nonintegrable TFIM $\Delta/J = -1$ at $h/J \sim 2$ with respect to time for different system sizes between $N = 30 - 72$. (c) The coefficients γ_1 (black-circles) and γ_2 (orange-diamonds) of the fit function for the dynamics of nonintegrable TFIM at $\Delta/J = -1$.

eters γ_1, γ_2 (depicted in Fig. 6.12c) $f_{\Phi,1}$ (depicted in Fig. 6.13a), $f_{\Phi,2}$ and ω (in Appendix Sec. E.2.7) as a function of transverse field h.

By studying $\gamma_{1,2}$, coefficients of the terms, we first notice that the non-oscillatory term is dominant to the oscillatory term in the region $h \lesssim 2.3$. The opposite is true for $h \gtrsim 2.6$. Hence, even though there are not two distinct fit functions that describe two distinct regimes like in integrable TFIM, there are two limits of one fit function that exhibits distinct enough features. This behaviour seems to stem from the sharp crossover in the integrable model. This is because, the fit function reduces to one term only where $\gamma_2 = 0$ in dynamically-ordered regime and $\gamma_1 = 0$ in the -disordered regime. In this sense, with the fit function integrable and nonintegrable models are quantitatively connected to each other. Note that $\gamma_{1,2}$ intersects at a location very close to the equilibrium QPT and this is where both terms are equally significant in the nonequilibrium response. Therefore, one can separate the entire region roughly into three: (1) $h \lesssim 2.3$ where the dynamics can be approximated by only the non-oscillatory term, and hence acts like the dynamically-ordered regime in the integrable TFIM. (3) $h \gtrsim 2.6$ where the dynamics can be approximated by only the oscillatory term, and hence acts like the dynamically-disordered regime in the integrable TFIM. (2) The intermediate crossover region where both terms are important.

The fit function for the nonintegrable TFIM could be tested further with larger system size data and hence, in longer times in the future studies. Additionally, testing the fit function against nonintegrability strength Δ/J is an interesting direction for future studies. In particular, it would be interesting to study how the regions (1) through (3) change in a near-integrability model. Finally let us note that although there might be other equally accurate models to represent the dynamics of nonintegrable TFIM, the current model has the least amount of free parameters and is physically intuitive.

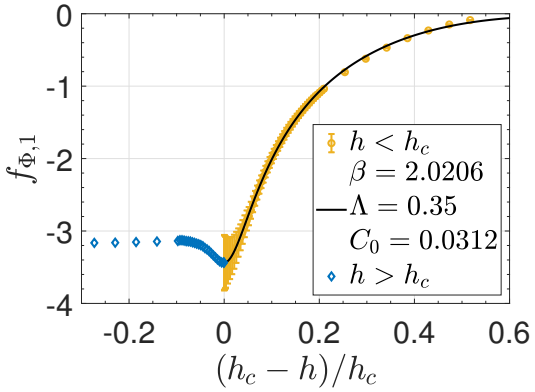

(a)

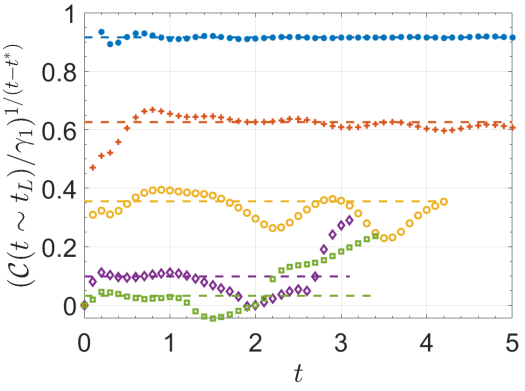

(b)

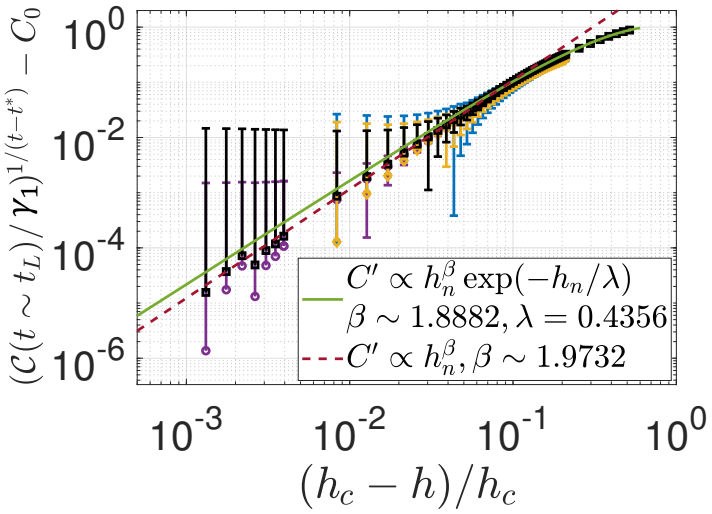

(c)

Figure 6.13: (a) Decay rate of the first term in the fit function Eq. (6.13), $f_{\Phi,1}$ shows a minimum at $h_c = 2.278 \pm 0.001$ signaling a boundary between the ordered regime (yellow-circles) that can be modeled by logarithmic function (black-solid) and crossover region (blue-diamonds). (b) Decay rate functions $\exp(f_{\Phi,1})$ shown with solid flat lines and rescaled observable data according to the method (i) (see text) around the flat lines for $h/J = 1.1, 1.5, 1.8, 2.1, 2.28$ with blue-dots, red-pluses, yellow-circles, purple-diamonds and green-squares, respectively. Data accumulates around the flat lines. (c) Power-law dynamical scaling in the vicinity of the boundary between regions (1) and (2) with an exponent of $\beta \sim 2$ with blue and yellow data at very early times $t = 0.3, 0.5$ with the rescaling method (i) and purple data at the nodes of the oscillations motivated by the method (ii) (see text). The black-squares are the decay rate function $\exp(f_{\Phi,1}) - C_0$.

Dynamical crossover region and an OP-like quantity

We focus on the decay rate of the first term, f_{Φ_1} since this is the term that governs the exponential decay of the dynamical response, whereas f_{Φ_2} controls the exponential decay of the oscillations. In this sense, f_{Φ_1} is the analogous parameter to the decay parameter in the integrable TFIM. In addition to the observation that the system thermalizes the fastest at the crossover boundary in the integrable TFIM, we notice that the minimum of f_{Φ_1} roughly coincides with the boundary between the dynamically-ordered (1) and the crossover (2) regions. Given that in the integrable TFIM, the cusplike feature emerges in short time dynamics when the nonequilibrium response changes nature, it seems that the minimum of f_{Φ_1} implies a possible boundary between the regions (1) and (2). In this regard, region (1) is where the nonequilibrium response can be approximated well enough with an exponential decay only; and region (2) is where one cannot ignore the oscillatory term anymore.

Fig. 6.13a demonstrates this minimum for f_{Φ_1}. We determine the location of the minimum as $h_c = 2.278 \pm 0.001$ which sets the boundary from dynamically-ordered (1) to the crossover (2) regions. The decay rate in the region (1) follows previously introduced logarithmic scaling in h_n (Fig. 6.13a) giving rise Eq. (6.8) to hold for the nonintegrable model, as long as the oscillations are taken care of. This could be performed in a couple of different ways, e.g., averaging over a period $\mathcal{T} = 2\pi/\omega$, working only at the nodes of the oscillations $(\pi + 2\pi n)/2\omega$ where $n \in \mathbb{Z}$ or simply rescaling the observable by substracting the oscillatory term from the observable data. Let us briefly discuss these options.

(i) The first method employed here in the main text is simple rescaling by subtracting the oscillatory term from $C(t) \to \mathcal{C}(t) = C(t) - \gamma_2 \exp(f_{\Phi,2} t) \cos(\omega t)$. Hence the rescaling of the observable $\mathcal{C}(t)$ follows similarly to Eq. (6.9). In such an expression, γ_1, γ_2, $f_{\Phi,2}$ and ω are free parameters. Fig. 6.13b demonstrates how well the rescaled data can be explained by an exponential decay when the observable is rescaled according to method (i). In the vicinity of the boundary and in early times, data coincides well with the flat lines which are $\exp(f_{\Phi,1})$. Overall, the exponential decay describes the general trend of the data in region

(1).

(ii) The second method is to choose a temporal cutoff at the nodes of the oscillations. This introduces a condition on the temporal cutoff time t_L as

$$t_L = \frac{\pi + 2\pi n}{2\omega}, \quad n \in \mathcal{Z}.$$

For sufficiently long dynamical response, this condition is not restrictive. When the condition is satisfied, the rescaled observable reduces to Eq. (6.9) with only one free parameter γ_1.

(iii) Finally one can think of averaging the observable data over a period of $\mathcal{T}$. Let us first discuss this case for the integrable TFIM. By a time-averaging integral over a period of $\mathcal{T}$ around the temporal cutoff t_L, the result reads

$$\frac{1}{\mathcal{T}} \int_{t_L-\mathcal{T}/2}^{t_L+\mathcal{T}/2} dt\, C(t^*) \exp[f_\Phi(t-t^*)] = C(t^*) \exp[f_\Phi(t-t^*)] \frac{\sinh(f_\Phi \mathcal{T}/2)}{f_\Phi \mathcal{T}/2}.$$

In the limit of $\mathcal{T} \to 0$, we recover the result with no averaging. We note that in case of averaging, one needs to rescale the observable correctly with the averaging interval $\mathcal{T}$ as well in order to construct a dynamical OP-like quantity. Although a similar procedure can be applied for the nonintegrable model, this method requires fine-tuning of t_L and the averaging interval $\mathcal{T}$ based on the free parameters ω and $f_{\Phi,2}$ to get rid of the oscillatory term in the fit function. Even though there happens to be infinite number of possible pairs of temporal cutoff and averaging interval (t_L, T) in total, there are conditions for viable sets $(t_L, \mathcal{T})$ which introduces fine-tuning. Since such a method is likely to be inconvenient both for computation and experiment, we do not discuss it further.

We plot the rescaled observable with temporal cutoff applied at $t = 0.3$ (blue) and $t = 0.5$ (yellow) in Fig. 6.13c in addition to data at a node of the oscillation with angular frequency ω (purple). The black-squares are the decay rate function $\exp(f_{\Phi,1}) - C_0$ where $C_0 = \exp(f_{\Phi,1})|_{h_c}$ at the boundary between crossover and dynamically-ordered regions. All data collapses reasonably well and can be described by a power-law scaling of $\beta \sim 2$ in the

vicinity $h_n \ll \Lambda = 0.44$, which corresponds to $h \sim 2.23$. The scaling exponent is consistent with the smooth and continuous crossover boundary. The error bars mainly stem from the fitting parameters when we model the dynamical response via the fit function Eq. (6.13) applied on our data limited to short times.

Since a single fit function can describe the data in the nonintegrable TFIM, here the observed physics clearly point out to different manifestations of the same quantum phase connected by a smooth crossover. Nevertheless finite-size scaling analysis could be applied to learn about the late-time behavior, since studying larger system sizes would provide larger time intervals remaining in the lightcone. This in turn does not only test the fit function for late times, but could also lead to more precise and accurate predictions on these emerging regions of different nonequilibrium responses as a function of transverse field.

6.2.5 Conclusions

We studied the decay rates of single-site one-point observables, magnetization per site for (non-)integrable TFIM as a function of transverse field. The integrable TFIM exhibited cusp-like feature in the decay rates at the dynamical crossover $h_c = 1$ between dynamically-ordered and -disordered regimes in early times. In the dynamically-ordered regime, the observable exponentially decays to zero, whereas the nonequilibrium response is an exponential decay superposed with oscillations in the dynamically-disordered regime. By studying the scaling of the decay rates in the vicinity of the crossover, we found a rescaling for the observable and the rescaled observable exhibited a linear dynamical scaling law with $\beta = 1$ in the ordered vicinity of the crossover in early times in contrast to $\beta_\infty = 1/2$ predicted by late time analytical expression. In the dynamically-disordered regime, we showed that both exponents $\beta = 1$ and $\delta = 0.533$ take up correction factors in early times and differ from the predictions of analytical expression $\beta_\infty = 0$ and $\delta_\infty = 1/2$.

Next we wrote down a fit function for the nonequilibrium behavior of the nonintegrable TFIM. Three regions appeared from the model where in (1) $h \lesssim 2.3$ the response is dominated

by a smooth exponential decay and hence acting like a dynamically-ordered regime; (3) $h \gtrsim 2.6$ the response is dominated by an oscillatory exponential decay and hence acting like a dynamically-disordered regime; and (2) the intermediate crossover region where none of the terms can be ignored. Hence, we observe that the point-like crossover boundary in the integrable TFIM turns into a region in the nonintegrable model. It is an interesting direction to test this model, its parameters and the region boundaries against different Δ/J. Later we focused on the decay rate of the non-oscillatory term which showed a minimum at the boundary between dynamically-ordered and crossover regions $h_c = 2.278 \pm 0.001$; and found a dynamical OP-like quantity based on temporal cutoffs in the transient regime that can probe this feature of the model after rescaling the observable. The rescaled observable exhibited a dynamical scaling law exponent $\beta \sim 2$.

Our work opens new avenues to explore nonequilibrium order, in particular with local observables, with no need for reaching the saturation regime which might be challenging for experiments as discussed in the first Section of the current Chapter. There are interesting directions for future, such as (i) whether a similar dynamical OP-like quantity could be constructed for other short-range Hamiltonians with exponential decay, e.g., the XXZ model; and (ii) whether long-range interacting TFIM [125] could exhibit similar behavior in its transient temporal regimes.

Chapter 7

Dynamical Criticality in the Quasi-Stationary Regimes

Extracting critical behavior in the wake of quantum quenches has recently been at the forefront of theoretical and experimental investigations in condensed matter physics and quantum synthetic matter, with particular emphasis on experimental feasibility. Here, we investigate the potential of single-site observables in probing equilibrium phase transitions and dynamical criticality in short-range transverse-field Ising chains. For integrable and near-integrable models, our exact and mean-field-theory analyses reveal a truly out-of-equilibrium universal scaling exponent in the vicinity of the transition that is independent of the initial state and the location of the probe site so long as the latter is sufficiently close to the edge of the chain. Signature of a dynamical crossover survives when integrability is strongly broken. Our work provides a robust scheme for the experimental detection of quantum critical points and dynamical scaling laws in short-range interacting models using modern ultracold-atom setups.

7.1 Introduction

In a global quench, the ensuing dynamics of a quantum many-body system can yield signatures of *dynamical* criticality, such as dynamical phase transitions (DPTs). Several major concepts of DPTs have been proposed [198, 214] with some of them converging [336]. One such DPT is of the Landau paradigm, i.e., it is based on nonanalytic behavior in the long-time dynamics of the local order parameter. This indicates that, in principle, such nonanalytic behavior may be used to extract equilibrium criticality that manifests itself dynamically. Indeed, it has been shown that this is possible through, e.g., out-of-time-ordered correlators [181] (also see Chs. 4 and 5) and spin-spin correlations [204, 209, 210] in the wake of a quench. Given that quench protocols in modern quantum synthetic matter setups are relatively straightforward to implement compared to the preparation of a system in its ground state, it is worth further investigating experimentally feasible methods aimed at extracting equilibrium criticality through quench dynamics.

In this spirit, we show here that the dynamics of single-site observables close to the boundary of a short-range transverse-field Ising model (TFIM) is a promising venue for the detection of a quantum critical point (QCP). Whereas a single-site observable at an arbitrary site of a *periodic* chain decays exponentially for quenches starting in the ordered phase of the nearest-neighbor TFIM [116, 128, 328], a hard-boundary condition gives rise to a quasi-stationary regime [337]. This allows one to probe equilibrium phase transitions and dynamical criticality by utilizing the degrees of freedom close to the boundaries. Although the profile of the on-site order dynamics naturally differs for each single-site observable and depends on the initial state, we observe a universal behavior in the vicinity of the transition for sites sufficiently close to the chain boundaries independently of the initial state.

The same behavior is also observed in a near-integrable model under mean-field theory (MFT) analysis, which, together with the above, suggests a universal scaling exponent in the vicinity of the transition. This observation stems from the fact that the relaxation time to the quasi-stationary value diverges as we move towards the transition point, which is

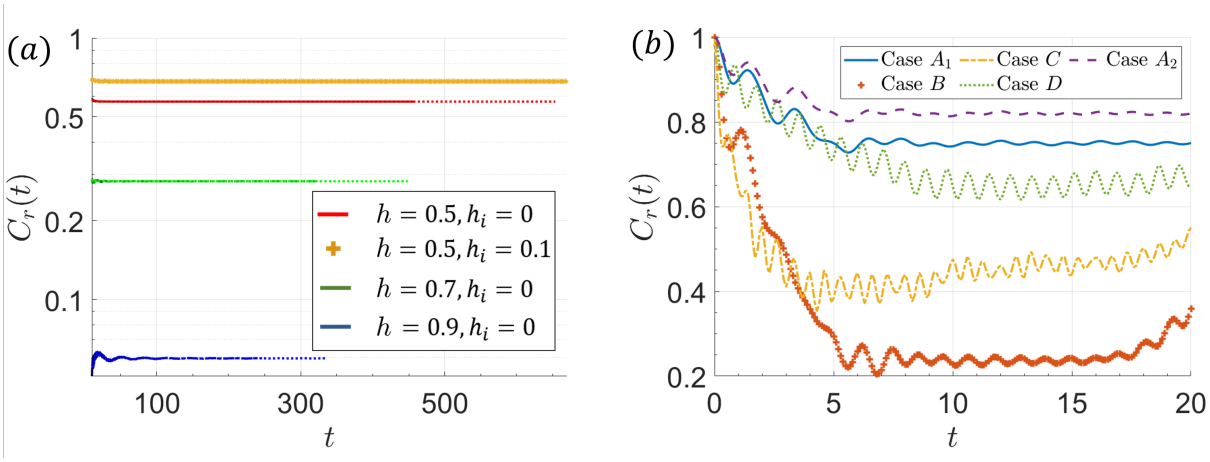

Figure 7.1: The nonequilibrium response $C_r(t)$ in the TFIM with open-boundary conditions given in Eq. (7.1) after a quench in the transverse-field strength from h_i to h. (a) Results for the integrable limit ($\Delta = 0$) for $r = 6$. Lowest three colors (blue, green, red) depict results over a range of system sizes $N = 96, 480, 960, 1440$ all of which collapse onto each other. (b) In the nonintegrable limit ($\Delta \neq 0$), five cases are considered: $A_1 : r = 3$, $\Delta = -0.1$, $h_i = 0$, $h = 0.5$, $N = 36$, $B : r = 9$, $\Delta = -0.5$, $h_i = 0$, $h = 1$, $N = 42$, $C : r = 6$, $\Delta = -2$, $h_i = 0$, $h = 2$, $N = 48$, $D : r = 12$, $\Delta = -1$, $h_i = 0$, $h = 1$, $N = 42$, and $A_2 : r = 3$, $\Delta = -0.1$, $h_i = 0.1$, $h = 0.5$, $N = 36$.

a consequence of critical slowing down. Single-site observables at different sites approach the quasi-stationary value in qualitatively the same way and independently of the initial state. Therefore, the information of the precise site location is *effectively* washed away in the vicinity of the transition. We determine the dynamical critical point (DCP) [210] in the near-integrable model, which we find to be close in value to the QCP. Furthermore, time-dependent density-matrix renormalization group (t-DMRG) calculations show a dynamical crossover when integrability is strongly broken, albeit data is inconclusive as to whether this is possibly a DPT due to numerical limitations on accesible evolution times.

We emphasize that we use the simplest possible probe, a single-site observable, in a chain with hard boundaries, which is experimentally more relevant than a periodic chain. This Chapter also forms a complementary approach to recent works on local probes in DPT [338] and other dynamical schemes for detecting equilibrium phase transitions as shown in Ref. [213] and Chapters 5 and 6.

7.2 The quasi-stationary temporal regime in chains with boundaries

The short-range TFIM with interaction strength Δ is given by

$$H = -J\sum_{r=1}^{N-1}\sigma_r^z\sigma_{r+1}^z - \Delta\sum_{r=1}^{N-2}\sigma_r^z\sigma_{r+2}^z + h\sum_{r=1}^{N}\sigma_r^x, \tag{7.1}$$

where $\sigma_r^{x,z}$ are the Pauli spin matrices on site r, h is the transverse-field strength, N is the length of the chain, and we fix $J = 1$ as the energy scale. At $\Delta = 0$, this model is the integrable nearest-neighbor TFIM. Let us consider as initial state the ground state $|\psi_0\rangle$ of H at initial value h_i of the transverse-field strength, and then we quench the latter to a value h. Even though in the case of the TFIM under periodic-boundary conditions the single-site nonequilibrium response $C_r(t) = \langle\psi_0|\,\sigma_r^z(t)\,|\psi_0\rangle$ decays exponentially [116] (also see Ch. 6), it has long been realized that open-boundary conditions stabilize a quasi-stationary regime in the integrable TFIM when $h_i < h \leq h_c$ [337] where $h_c = 1$ is the QCP. Figure 7.1a shows the quasi-stationary regime of $C_{r=6}(t)$ in the integrable TFIM for various h and systems sizes ranging between $N = 96 - 1440$ with $h_i = 0$ where the initial state is the fully z-up product state, $|\psi_0\rangle = |\uparrow\uparrow\ldots\uparrow\rangle$ (c.f. Appendix F for the methods). It is straightforward to demonstrate that this stationary regime is not thermal by simply observing the strong dependence of the stationary value on the initial state in Fig. 7.1a when $h_i = 0.1$. Since the stationary value carries the initial state information, and given the fact that this regime persists for all accessible times up to recurrences [337] at all sites $r \ll N/2$, degrees of freedom near the boundaries do not thermalize. The origin of this boundary effect is in fact independent of the integrability of TFIM, c.f. Fig. 7.1b for various nonintegrable cases up to some oscillations computed via t-DMRG, confirming the quasi-stationary nature of this temporal regime. Recurrences observed in some cases occur due to finite-size effects (see Appendix F). The stationary value again carries the initial state information. In a similar

vein, this boundary effect is observed when interactions are power-law decaying long-range interactions [339,340], also c.f. Appendix F. Therefore, our work contributes another example of a strongly nonintegrable system exhibiting nonthermal behavior [237]. We note that this boundary effect is robust against changing the hard boundaries to smooth ones [341], does not originate from strong zero modes [115], and clearly is not confined to only the edge of the chain (Appendix F). Rather, the reason is simply the geometry of the open-boundary chain where the asymmetric location of a site $r \ll N/2$ causes destructive interference between two signals, one of which reflects back from the closest edge much earlier than the other moving towards the farthest edge [337]. This stabilizes a quasi-stationary nonthermal temporal regime regardless of the integrability of the system. In the rest of our work, we will utilize this quasi-stationary regime of single-site observables to probe equilibrium phase transitions and dynamical criticality in the short-range TFIM. Unless otherwise specified, we use polarized states as initial states and set hard boundaries in our discussion.

7.3 Quench dynamics in the integrable TFIM

In equilibrium, the TFIM has two phases, i) the ferromagnetically ordered phase for $h < h_c$ and ii) the paramagnetic disordered phase for $h > h_c$. The QCP shifts to favor order upon introducing interactions ($\Delta \neq 0$). The local order parameter is the magnetization averaged over all sites, and when it is finite it indicates spontaneous symmetry breaking in the ground state.

The dynamical order parameter is set as the time-averaged nonequilibrium response, $\overline{C_r(t)} = \int_{t^*}^{t_l} dt\, C_r(t)/(t_l - t^*) \equiv \bar{C}_r(h)$, where t^* is the ultraviolet cutoff, c. f. Appendix F, and t_l is the evolution time at which the cluster theorem [116] breaks down. This breakdown time can be estimated based on the maximal quasi-particle velocity v_q: $t_l = \Delta x/(2v_q)$ where $\Delta x = N - 2r + 1$ is the distance between two spins at r and $N - r + 1$ that are symmetrically located around the symmetry center of the open-boundary chain (Appendix F). For quenches

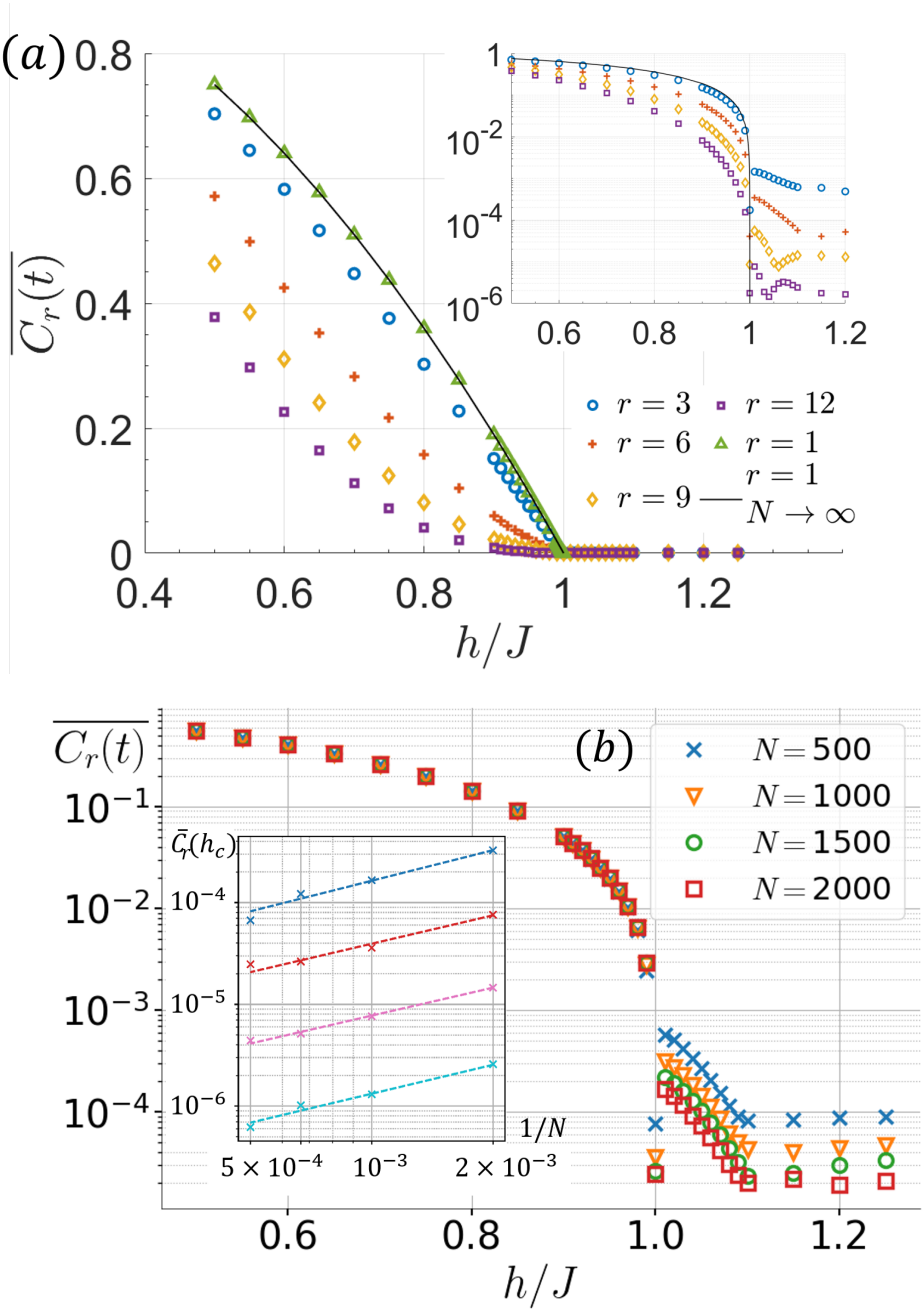

Figure 7.2: Nonequilibrium phase diagram for $\Delta = 0$ (a) for different sites $r = 1, 3, 6, 9, 12$ depicted by triangles, circles, pluses, diamonds, and squares, respectively, at $N = 1440$. Solid-black line is the analytic result for edge magnetization in thermodynamic limit. The inset shows the same plot in semi-logarithmic scale exhibiting a discontinuous behavior at the DCP. (b) For different system sizes, $N = 500 - 2000$, at site $r = 6$. The inset shows the system size scaling of the value $\overline{C_r(t)} = \bar{C}_r(h_c)$ after a quench to the QCP $h_c = 1$ for sites $r = 3, 6, 9, 12$, in descending order, with all exhibiting scaling $\propto N^{-1}$.

sufficiently far away from the vicinity of the DCP, $\overline{C_r(t)}$ matches the quasi-stationary value, as then there is no diverging relaxation time. Each single-site observable in the TFIM equilibrates around a different value in the quasi-stationary regime. This can be seen in Fig. 7.2a that depicts $\overline{C_r(t)}$ for $r = 1 - 12$, all of which have a different functional form of h. The analytic expression for the value of the quasi-stationary regime at $r = 1$, $C^{qs}_{r=1}(h) = 1-h^2$ [337] matches the corresponding numerical result in Fig. 7.2a. The inset in Fig. 7.2a shows the same plot in logarithmic scale that exhibits a clear and abrupt change in $\bar{C}_r(h)$ regardless of the value of r. Hence, the behavior of the singularity at h_c is captured by all single-site observables $r \ll N/2$. We focus on $\bar{C}_{r=6}(h)$ in Fig. 7.2b to demonstrate through finite-size analysis the presence of a transition with system sizes ranging between $N = 500 - 2000$. For $h < h_c$ the dynamic order is persistent, i.e., it has an increasing trend with increasing system size, whereas for $h \geq h_c$ the dynamic order vanishes, i.e., it has a decreasing trend with increasing system size. This observation suggests that in the thermodynamic limit, we would observe $\bar{C}_{r=6}(h) \neq 0$ for $h < h_c$ and $\bar{C}_{r=6}(h) = 0$ for $h \geq h_c$, the hallmark of a phase transition. The same behavior holds for other sites $r \ll N/2$, c. f. Appendix F, and the inset shows the system-size scaling at the QCP for different r, all of which decay as $N^{-\gamma}$ where $\gamma \sim 1$. This power-law decay is independent of the choice of ultraviolet temporal cutoff and initial state, as long as $h_i < h_c$ holds (Appendix F). Therefore, we demonstrate a DPT for different sites $r \ll N/2$ that reflects the underlying ground-state phase transition. The functional form of the dynamic order in the dynamically ordered phase varies for different r. Nevertheless, we observe that the site information is *effectively* washed away in the vicinity of the transition.

Figure 7.3a shows how the time-average $\bar{C}_r(h)$ scales with the reduced control parameter $h_n = (h_c - h)/h_c$ for different $r \ll N/2$ for quenches to the vicinity of $h_c = 1$. As we move closer to the phase transition, all sites exhibit the same scaling behavior $\bar{C}_r(h) - \bar{C}_r(h_c) \equiv \bar{C}'_r(h_n) \propto h_n^{\beta}$ where $\beta \sim 4/3$ is obtained through fit functions (Appendix F). This is a main result of our work, indicating a possibly truly out-of-equilibrium

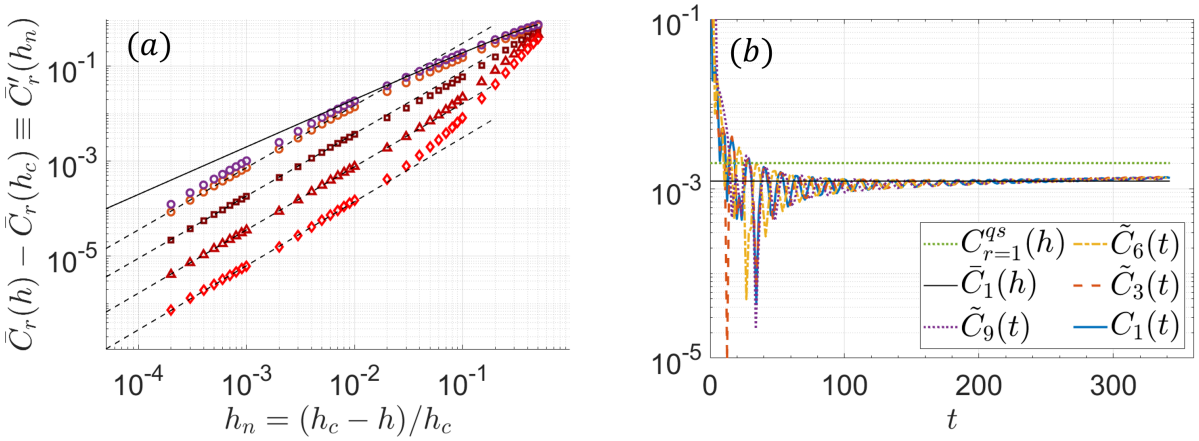

Figure 7.3: Universal scaling in the integrable TFIM for quenches from $h_i = 0$ to the vicinity of the QCP for different sites $r = 1, 3, 6, 9, 12$ (in descending order) where all exhibit an out-of-equilibrium critical exponent of $\sim 4/3$. Solid-black line is the analytic expression for the edge magnetization in the thermodynamic limit. This qualitative picture holds for different values of h_i. (b) All $C_r(t)$ for a quench from $h_i = 0$ to $h = 0.999$ for different sites collapse onto each other, up to different oscillation frequencies, when rescaled according to the fitted power-law in (a), hence resulting in a single envelope function where rescaling is denoted by tilde. The black-solid and green-dotted lines stand for the time-average $\bar{C}_1(h)$ with $t^* = 10$ and the quasi-stationary value $C^{qs}_{r=1}(h)$, respectively. All data is for $N = 1440$.

critical exponent, since it is not found in equilibrium. A comparison with the analytic expression of the edge magnetization in the quasi-stationary regime $C^{qs}_{r=1}(h)$ [337] (black-solid line in Fig. 7.3a), reveals that $C^{qs}_{r=1}(h)$ does not describe well the time-average of the data in the close vicinity of the transition. The origin of this discrepancy lies in the fact that the analytic expression is strictly valid when $t \to \infty$, whereas the relaxation time diverges in the vicinity of the transition. This means that in practice the quasi-stationary regime cannot be reached in the close vicinity of the transition, neither numerically nor in experiments. A similar effect has been observed in the periodic TFIM in Chapter 6, where the analytic expressions are derived in the $t \to \infty$ limit [116]. We do not study the region $h_n < 10^{-4}$, because the nonequilibrium response does not show true equilibration to a quasi-stationary state over accessible evolution times due to the diverging relaxation time (Appendix F). Figure 7.3b displays how nonequilibrium response functions of different sites collapse onto each other when rescaled according to the coefficients of the fit function appear-

ing in Fig. 7.3a, e.g., $\bar{C}'_r(h_n) = a_r h_n^\beta$ and $\bar{C}'_{r'}(h_n) = a_{r'} h_n^\beta$ and hence the scaling factor reads $\bar{C}'_r(h_n)/\bar{C}'_{r'}(h_n) = a_r/a_{r'}$, i.e., $\tilde{C}_{r'}(t) = C_{r'}(t) a_r/a_{r'}$. Even though the frequencies differ, all nonequilibrium responses converge to a single envelope function when rescaled, displaying a universal behavior in the relaxation to the quasi-stationary value. We emphasize that this region, where scaling at all sites $r \ll N/2$ yields the critical exponent β, still describes the *critical* relaxation regime to the quasi-stationary value, although it lasts for very long times, i.e., the time-averages in Fig. 7.3b (black-solid) would not perfectly match with the value in the quasi-stationary regime (green-dotted).

This observation can also be confirmed by the scaling change in the edge magnetization from the analytic prediction of the quasi-stationary value $C^{qs}_{r=1}(h_n) = 2h_n - h_n^2$ (Appendix F). For quenches in the vicinity of the transition, the latter scales as $C^{qs}_{r=1}(h_n) \propto h_n$. However, our numerical results show that a *critical* relaxation regime preceding the quasi-stationary state should persist indefinitely as $N \to \infty$ due to critical slowing down, leading to $\bar{C}'_{r=1}(h_n) \propto h_n^{4/3}$. Changing the initial state does not alter the numerically obtained scaling exponents of the magnetization per site in the vicinity of the transition (Appendix F). As a consequence, we demonstrate the presence of a slowed down critical relaxation regime in the vicinity of the QCP which precedes the quasi-stationary regime and results in a dynamical critical exponent of $\sim 4/3$.

7.4 Nonintegrable TFIM

We apply MFT analysis for $\Delta = -0.1$ which is a near-integrable TFIM (Appendix F for the details on MFT). This model has a QCP at $h_c \sim 1.16$ [210]. Figure 7.4a shows the dynamical phase diagram for different $r = 1 - 12$, which looks similar to the case of the integrable TFIM ($\Delta = 0$) except for a shift in the QCP to favor order, $h_c > 1$, as expected. We notice that the quasi-stationary value of the edge magnetization, which our numerical results access for quenches far away from the vicinity of the transition, can be fitted well with

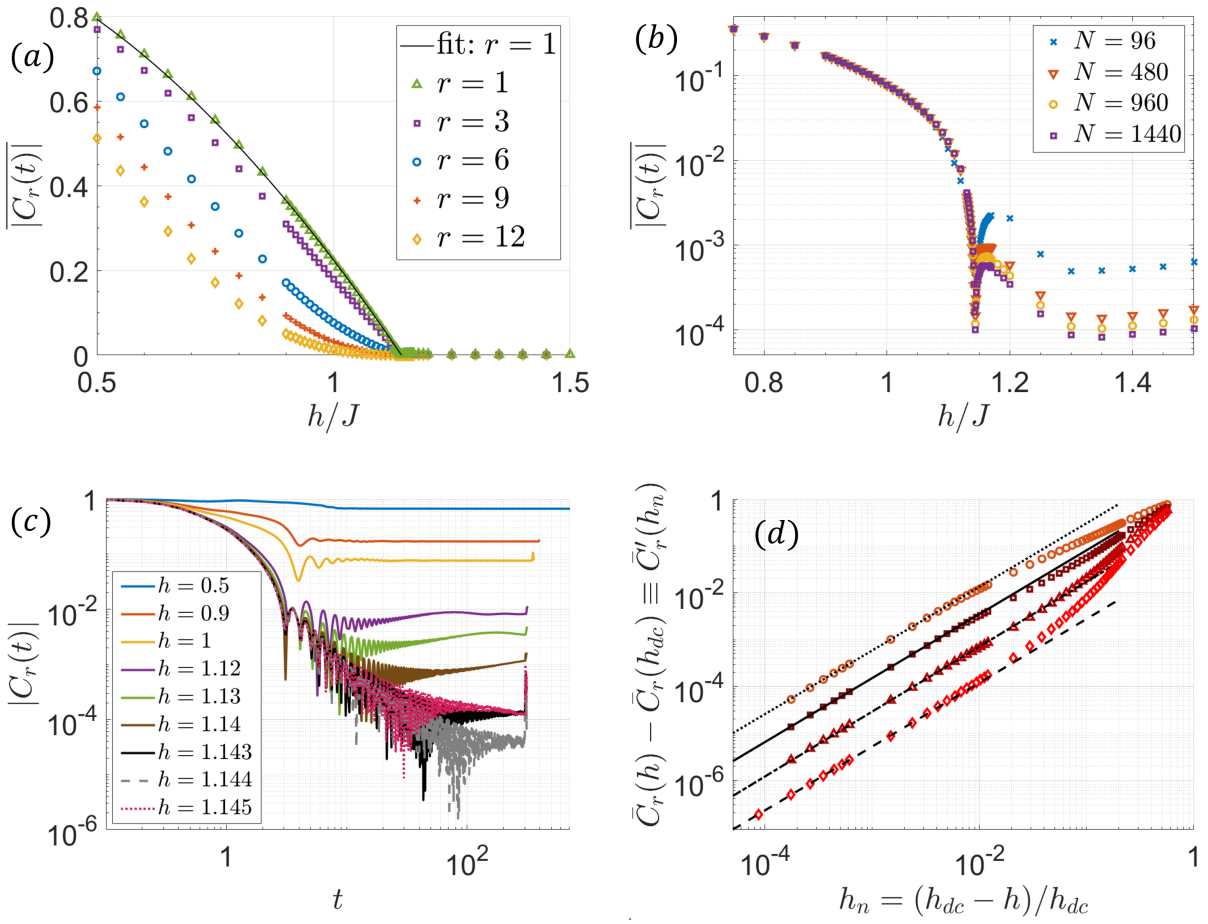

Figure 7.4: MFT results for $\Delta = -0.1$. Nonequilibrium phase diagram (a) for different sites $r = 1, 3, 6, 9, 12$ in descending order at $N = 1440$ and solid-black line is a fit function for the edge magnetization (see text), (b) for different system sizes $N = 96 - 1440$ at site $r = 6$, demonstrating the singular point. (c) Nonequilibrium response in the dynamically-ordered phase and in the vicinity of the transition at $N = 1440$ for $r = 6$. The recurrence attempts observed here imply the breakdown of the cluster theorem (Appendix F). (d) Different sites, $r = 3, 6, 9, 12$ in descending order, scale with the same exponent $\sim 4/3$ in the vicinity of the DCP at $N = 1440$ where $h_n = (h_{dc} - h)/h_{dc}$.

a functional form that is reminiscent of that of the integrable TFIM, $C^{qs}_{r=1}(h) = \alpha(h^{\nu}_{dc} - h^{\nu})$ for $h \leq h_{dc}$ and zero otherwise, where we denote the DCP as h_{dc}. We focus on $\bar{C}_{r=6}(h)$ in Fig. 7.4b where we observe a singularity at $h_{dc} \sim 1.144 \pm 0.001 < h_c$ whose magnetization decreases with increasing system size (Appendix F). Meanwhile, the same (opposite) behavior is observed in the dynamically disordered (ordered) phase, suggesting a phase transition at h_{dc}. In Fig. 7.4c we plot the nonequilibrium responses around the DCP for $N = 1440$, which shows a qualitative change in the nonequilibrium response across the DCP. For example, up until $h = 1.144$ which is denoted by the gray-dashed line in Fig. 7.4c, there is evidence of equilibration, whereas starting at $h = 1.145$, which is denoted by the pink-dotted line, the response starts to develop a low-frequency oscillatory feature seen in the downward trend of its dynamics (see Appendix F for data on $h > 1.145$). This feature is captured in Fig. 7.4b as a singularity. Based on this method, we further refine the DCP to be at $h_{dc} = 1.1437 \pm 0.0001$, which is slightly smaller than the corresponding QCP at $h_c \sim 1.16$. Although it is possible that the DCP we obtain is actually the QCP and this small numerical difference is a mere artifact of MFT, it is worth noting that MFT usually predicts a larger critical point than the physical one since it neglects fluctuations, whereas here $h_{dc} < h_c$. With h_{dc} substituted into the fit function of the edge magnetization, we obtain $\alpha = 0.78$ and $\nu = 1.89$. It is important to note that although the MFT treatment gives rise to a quasi-stationary regime for long intervals of time as seen in Fig. 7.4c for quenches away from the vicinity of the DCP, this is not conclusive evidence for infinitely long-lived nonthermal behavior in a nonintegrable model. Indeed, MFT is not expected to adequately capture thermalization as it may neglect fluctuations that are essential for the latter.

Next we study the close vicinity of the transition in the MFT data. Figure 7.4d reveals an out-of-equilibrium critical exponent $\beta \sim 4/3$ based on the fit functions in the relaxation regime for different single-site observables $r = 3 - 12$ (Appendix F), in congruence with the conclusions of the integrable case. Once again, this shows how the analytic prediction for the quasi-stationary steady state does not capture this exponent since $C^{qs}_{r=1}(h_n) \sim h_n$ as

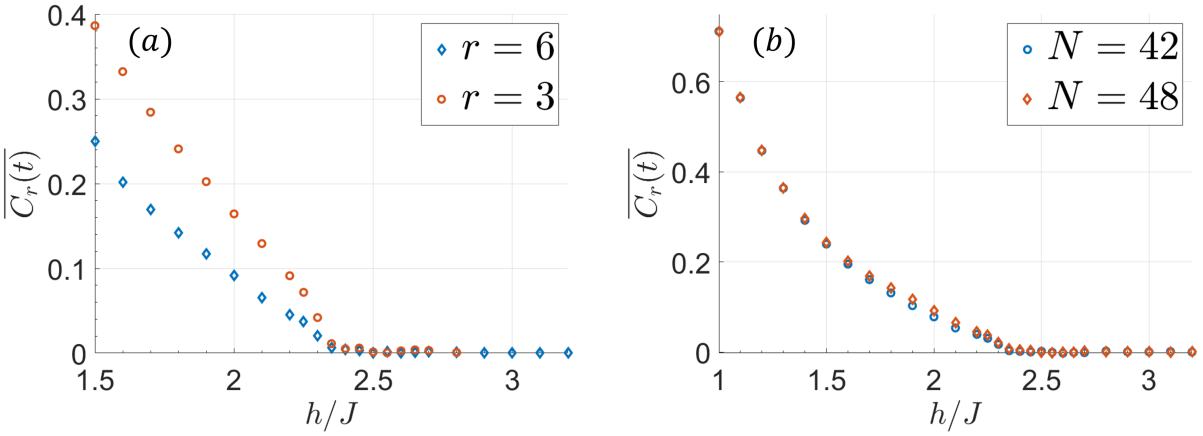

Figure 7.5: $t-$DMRG results for nonintegrable TFIM with $\Delta = -J$, (a) for different sites, $r = 3, 6$ in descending order at $N = 48$ and (b) for different system sizes $N = 42, 48$ at site $r = 6$.

$h_n \to 0$ (Appendix F). As in the integrable TFIM, a diverging relaxation time for quenches in the vicinity of the DCP gives rise to a very long-lived *critical* relaxation regime where the quasi-stationary steady state is accessible neither numerically nor in experiment.

Finally, we consider the strongly nonintegrable TFIM with $\Delta = -1$, whose QCP lies at $h_c \sim 2.46$ (see Appendix E.2.5). At such large values of Δ, MFT is inadequate, and we therefore employ t-DMRG. The latter is numerically exact, but within a given fidelity threshold the accessible evolution times are limited and far shorter than those achievable for the (near-)integrable model. Figure 7.5a shows the local order profile for $r = 3$ and 6 for $N = 48$ spins, which exhibit behavior similar to that of our previous results. Figure 7.5b focuses on $r = 6$ and exhibits the increasing trend of order with increasing system size in the dynamically ordered phase. We apply a temporal cutoff of $t_l = N/3$ for both to calculate $\bar{C}_r(h)$. Although we cannot precisely determine a DCP due to lack of data for larger times (a constraint due to increasing bond dimension with evolution time in t-DMRG), our data still suggests a dynamical crossover. Intricate details of this crossover, e.g., whether it is actually a DPT if longer evolution times are available, are not possible to discern within the limited evolution times we can achieve in t-DMRG.

7.5 Conclusions

We have studied the quasi-stationary regime and the critical relaxation to it at sites close to the edge in short-range TFIMs with open-boundary conditions. We have shown that single-site observables are able to extract quantum critical points at or near integrability. The corresponding dynamical phase transition is present independently of the measurement location and initial state. In the vicinity of the transition, a universal scaling behavior with a truly out-of-equilibrium exponent $\beta \sim 4/3$ emerges in the very long-lived critical relaxation regime to the quasi-stationary steady state.

Our setup is experimentally convenient, because (i) hard-boundary chains are a more natural setup than their periodic counterparts in experimental realizations, (ii) single-site observables are readily accessible in modern quantum simulators [195]. Further, since we have shown that the physics near the edge of the chain is independent of the initial state, so long as $h_i < h_c$, one can prepare the most convenient initial state in a lab, e.g., a polarized state. Most theoretical works have focused on periodic chains naturally to utilize the translational symmetry, which removes site-dependency of the dynamical order parameter within the ordered phase [210,325,342]. In this sense, our work complements the literature via explicitly demonstrating the potential of single-site observables in open-boundary chains. One can reproduce the periodic chain results in the middle of an open-boundary chain as shown in the previous Chapter and Appendix Sec. E.2.1, however most of the chain would actually diverge from this behavior due to the boundary effects exemplified above. Our setup does not require a precise choice of location $r \ll N/2$, yet one can probe a universal dynamical criticality in the vicinity of the transition.

Chapter 8

Conclusions, Outlook and Future Directions

In this dissertation, I explored the field of quantum many-body dynamics from a range of different perspectives, i.e., equilibration, thermalization, information scrambling, light cone bounds and dynamical criticality in a variety of systems, i.e., Bose-Einstein condensates, spin chains and ladders, and fermionic systems. I looked for answers to the question posed in the beginning of the dissertation: *'What are the signatures of quantum phases and phase transitions in isolated interacting systems driven out-of-equilibrium?"*, found signatures for dynamical detection and determined the paths of how we can extend the quantum phase transitions, symmetry-breaking and topological, to the nonequilibrium setting. All theoretical works that are performed in this dissertation with discovered predictions could be probed in experiments based on quantum simulators.

After presenting the preliminaries in Chapter 1, I explored various dynamical phenomena that are observed in spinor Bose-Einstein condensates in Chapter 2, including well-defined quantum collapses and revivals, thermalization via Eigenstate Thermalization Hypothesis, equilibration with no revivals despite of finite degrees of freedom in the system, and spin-mixing oscillations. The reason behind both thermalizing and nonthermalizing behaviours

in the same model under different initial conditions was linked to the presence of *rare* nonthermal states in the spectrum. It is an interesting and intriguing direction to see whether these rare nonthermal states could survive when the integrability of the model is broken, i.e., by introducing magnetic field in $x-$direction [343], and demonstrate quantum scarring in spinor condensates. Furthermore, I proposed a method to predict the collapse and revival timescales in the dynamics and put forward the observation that quench dynamics can probe both the ground state and excited state quantum phase transitions of the system. The experiment on the former is presented in the first section of Chapter 6 and the related Appendix Sec. E.1, while the latter has been recently explored in detail in the literature [332, 344].

Chapter 3 focused on finding a feasible spin model to detect information scrambling in a cold atom simulator and analyzing the scrambling properties of this model, that is the ladder$-XX$ model, in both clean and disordered potentials. Such properties are (i) the decay rates of the out-of-time-order correlators which exhibited power-law; (ii) the rates of information spread that are determined with the light cone which turned out to be sublinear, and butterfly cone wavefronts which exhibited a range of dynamical exponents. Advanced numerical analysis could be applied to the ladder$-XX$ model to study these properties in larger systems to test whether the results could be generalized to bigger system sizes and potentially to the thermodynamic limit. In this Chapter, I also studied realistic initial state preparation for feasibility and advanced the idea that we can use light pulses to implement the sign reversal protocol as an alternative to Feshbach resonances. The ladder$-XX$ model in disordered potentials has been shown to exhibit a crossover between ergodic and many-body localized regimes via the level-statistics in this Chapter for the first time to our knowledge. Later, these dynamical regimes along with the associated crossover [345] and in general the localization properties [346] of the ladder$-XX$ model have been studied in detail in the literature. A close cousin of OTOC is spectral form factor (SFF) [347, 348], whose time evolution has signatures of the onset of quantum chaos. Feasible methods to measure SFF [349] and alternative paths to probe quantum chaos in quantum simulators are needed,

as both the decay and steady-state properties of OTOCs capture more than the signatures of quantum chaos only. As we demonstrated in this Chapter, a disordered spin model in its ergodic regime which is determined by the energy level statistics, cannot exhibit an exponential decay for long enough times to argue for quantum chaos by OTOC. The OTOC shows clear differences in its decay properties between ergodic and MBL regimes, differentiating two dynamic regimes well, and in fact signaling the ergodic-MBL crossover [131]. However, the hallmark of quantum chaos by OTOC is an exponential decay with a Lyapunovlike exponent [144], and it is now well-known that while Floquet spin chains exhibit a robust exponential decay [162], time-independent disordered spin Hamiltonians do not, i.e. disordered Heisenberg chain [162] and the ladder$-XX$ quasi-1D spin chain in Chapter 3 [219] both of which shows a robust power-law decay instead, likely due to additional symmetries. Given such difficulties, discovering a more transparent and robust experimental probe of quantum chaos is an important and promising direction of research.

In Chapter 4, I laid down the necessary key ingredients for out-of-time-order correlators to probe ground state physics, and hence the quantum phase transitions. These key ingredients followed from an analytical framework based on predicting the steady state values of OTOCs, and this analytical framework also elucidated the numerical observations of Ref. [181]. I applied the theory to a critical Isinglike spin chain, that is the $XXZ-$model, and numerically confirmed the predictions, by also explaining why the steady-state value of OTOC is sensitive to long-range order but not to quasi-long range order. This Chapter helped us to argue for a universal connection between information scrambling and quantum phase transitions when the conditions on initial state and the observables are satisfied. Later, this connection is explored further in the literature [188, 190] as well as in Chapter 5, and is experimented [160, 161]. Whether this analytical framework could be utilized to understand how the connection survives following the quenches from the long-range ordered phase, instead of using the ground state, is an interesting direction to pursue.

Chapter 5 revealed another interesting connection between information scrambling and

the ground state physics: OTOCs of edge observables are sensitive to the presence or absence of Majorana zero modes, even at infinite temperatures. We accurately marked down the location of the topological phase transition via the steady-state temporal regime of OTOCs. When integrability is broken, the competition between information scrambling and Z_2 topological order led to a new timescale in the scrambling dynamics with a long-lived plateau of partial scrambling before full scrambling in long times. We coined the term *prescrambling* for this restricted scrambling of topologically-protected quantum information. These results extend the studies on strong zero modes in the literature [115, 303, 350, 351] to the realm of information scrambling and OTOCs. This Chapter is also the first systematic study of the effect of Z_2 symmetry on the OTOC, and in particular on its steady-state regime, in the literature to our knowledge. While the OTOCs with no symmetries and charge conservation in 1D chains have been extensively studied in the literature [163, 164, 352–354], there is much room to explore in the dynamics of OTOCs with Z_2 symmetry. Additionally, how our results in Chapter 5 can be extended to 2D fermionic systems is an interesting and promising direction of study. There have been current experimental progress in 2D quantum simulators [355–359], and there is a great interest in understanding how these nonequilibrium processes, in particular information spread and scrambling, occur in two dimensions. (i) One could study 2D topological superconductors with $p-$wave pairing [22] in nonequilibrium to see whether thermalization and scrambling probes are still useful to detect the presence or absence of Majorana zero modes in 2D. (ii) One of the most interesting physics to study in 2D is Quantum Hall Effect (QHE) [360–363] and topological insulators [364–366]. There is a recent body of works that apply quench dynamics to paradigmatic models of topological insulators, i.e. Haldane model, [308–313]. In particular, figuring out how the interplay between fractional QHE and information spread in nonequilibrium would play out, under what conditions the nonequilibrium response would be affected by fractional QHE ground state and how the scrambling properties are affected in a topological phase transition point are only a few of the exciting questions to answer in quench nonequilibrium studies in 2D.

In Chapter 6, I steered the focus from information scrambling back to thermalization, however this time with the most of the focus on the paradigmatic model of dynamical phase transitions, TFIM. While the first Section studied dynamical detection of a first-order quantum phase transition in an antiferromagnetically interacting spinor Bose-Einstein condensate both theoretically and experimentally, the second Section was exclusively on the quench dynamics of short-range TFIM. The unifying theme of both Sections was the use of transient temporal probes in dynamically detecting quantum phase transitions of the ground state. In both Sections, we revealed dynamical scaling laws in the vicinity of the transition or crossover. I explained the origin of the exponent observed in the spinor condensates based on the method put forward in Chapter 2. In the latter part of the Chapter, I showed that the decay rates of the transient regime in short-range TFIM exhibit a dynamical crossover even in short times and one could construct dynamical order parameterlike quantity with the correct scaling of the single-site observables. The exponent of the dynamical scaling law in the vicinity of the crossover significantly differed for short times from the analytical results that are strictly valid in infinite time limit. The origin of this observation is the critical slowing down and the divergence of the relaxation times in the vicinity of the crossover. Breaking integrability strongly, transformed the sharp crossover to a smooth one. Near-integrable models with weak integrability breaking only are very useful intermediate models in between integrable and strongly nonintegrable models. Studying the crossover in a near-integrable model to better understand the smoothing of the cusp in the integrable TFIM and studying this transition from a cusp to a smoothed cusp with different types of integrability breaking terms to test the universality of the crossover are interesting directions of study [367]. Additionally, as shown in Chapter 7, mean-field theory could be used for the quench dynamics of the near-integrable models, which would be useful to reach bigger system sizes and longer simulation times than we could with numerical methods like time-dependent density-matrix renormalization group. Eventually it is important to test further the nonequilibrium regions appearing around the quantum critical point with integrability breaking term by accessing

longer simulation times than what we had in this dissertation.

Finally, the Chapter 7 utilized the quasi-stationary temporal regimes that form in the nonequilibrium responses of the single-site observables near the boundary of chains. This dynamical behavior is significantly different than that of an arbitrary single-site observable in a periodic chain, or the observable in the middle of an open-boundary chain. I showed that a dynamical scaling law with a universal exponent arises in the vicinity of the transition and the exponent does not depend on the choices of the initial state, location of the single-site observable, temporal cutoffs and weak integrability breaking. Signature of a dynamical crossover survives when integrability is strongly broken. Quasi-stationary temporal regime is likely a prethermal regime for nonintegrable models before full thermalization to zero. However this idea could not be verified or refuted with our data, because (i) our t-DMRG data is limited to short times where we do not observe a full thermalization to zero, (ii) although mean-field theory results reach much longer simulation times, it is not expected that the MFT could capture full thermalization of a quantum system, as the role of quantum fluctuations is important in quantum thermalization. Let us also remember the slight shift in the dynamical critical point from the equilibrium quantum critical point in our results on the near-integrable TFIM, observed with MFT. Such a shift was also observed in Ref. [210] with MFT. Whether this shift originates from MFT or whether it can be observed with density matrix renormalization group methods is a significant question that needs to be answered in the future to fully understand the reliability of MFT in quench dynamics.

Appendix A

Thermalization in the Integrable Models

A.1 Microcanonical Window Selection

The microcanonical ensemble (MC) prediction should not depend on the size of the energy window. This constraint prevents us to calculate the MC prediction for the cases where the kink structure exists in the spectrum and the initial state is chosen in such a way that it overlaps with the kink. See Figs. 2.5 and 2.6 for these regions where the MC energy interval cannot be well-defined. This result is consistent with the condition Eq. (2.8) which does not hold for the aforementioned cases above. However the typical eigenstates of a spinor BEC system are thermal with high PR values and therefore we can compare the prediction of diagonal ensemble (PDE) (or the long-time average of dynamical response) with the MC prediction for almost any initial state. For these cases, we calculate the mean energy of the system according to

$$E_o = \sum_{\alpha} |C_\alpha|^2 E_\alpha, \tag{A.1}$$

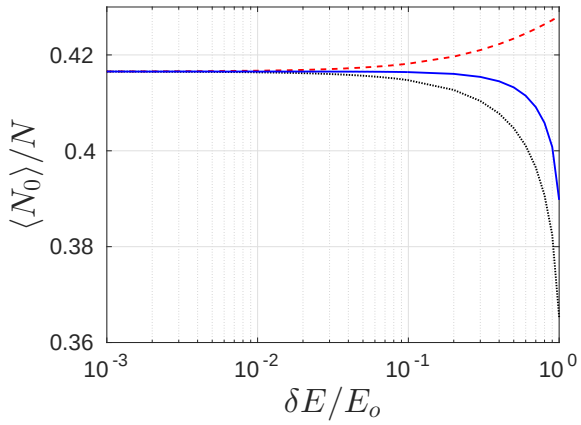

Figure A.1: The microcanonical ensemble thermal prediction with respect to different energy intervals for $[E_o - \delta E, E_o]$ (red-dashed), $[E_o - \delta E, E_o + \delta E]$ (blue-solid) and $[E_o, E_o + \delta E]$ (black-dotted) when a sudden quench is applied from $q_i = -3$ to $q_f = -0.5$ for a condensate size of $N = 10^4$.

where E_α is the energy associated with each eigenstate. Keeping in mind that the energy window should be much smaller than the mean energy $\delta E \ll E_o$, we look for the threshold window size δE_{th} that starts to affect the MC prediction. Then any $\delta E < \delta E_{\text{th}}$ gives a well-defined MC energy window. We also compare three different possibilities for the window size as $[E_o - \delta E, E_o]$, $[E_o - \delta E, E_o + \delta E]$ and $[E_o, E_o + \delta E]$. Fig. A.1 shows an example of this procedure.

A.2 Mapping of a Spinor Hamiltonian onto a Single Quantum-Particle Hopping Model

Here we show how the parameters of single quantum-particle model (Eq. (2.13)) depend on the sites of the lattice. Upon comparing with the spinor Hamiltonian Eq. (2.4), we observe that the Zeeman field strength q modifies only the diagonal terms and hence the onsite potential terms η. Therefore, the single particle Hamiltonian family that can produce the dynamics in this paper consists of only different onsite potential configurations. Fig. A.2a shows the hopping coefficients with respect to single particle lattice positions. This functional

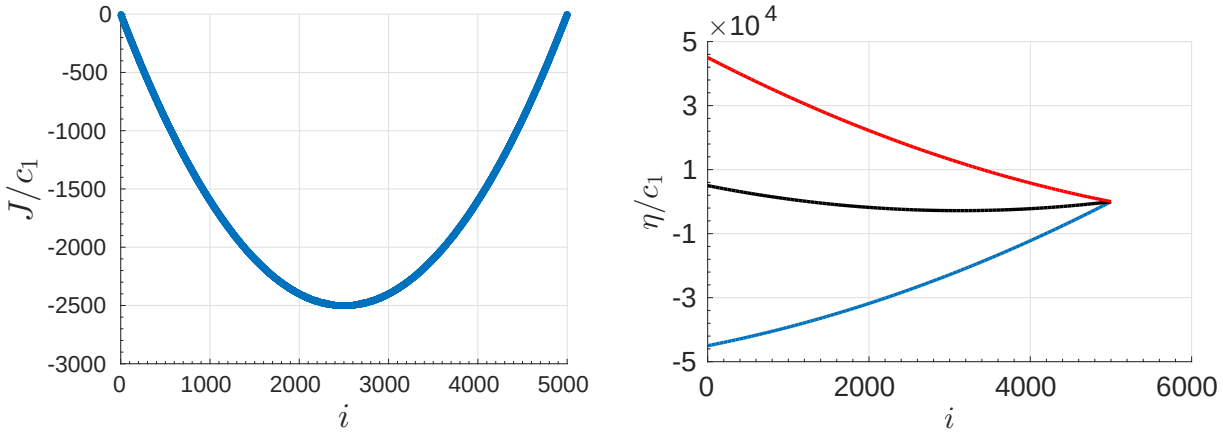

(a) (b)

Figure A.2: (a) The hopping parameter J for the mapped single particle model, (b) the onsite potential parameter η for a condensate model with Zeeman field strength $q = 4.5$ (blue-lower curve), $q = -0.5$ (black middle curve) and $q = -4.5$ (red upper curve) with respect to site position i for a condensate of size $N = 10^4$.

dependence of J onto the site positions is fixed for each spin-1 BEC Hamiltonian. Fig. A.2b shows different onsite potential configurations depending on the Zeeman field strength. The most important observation is that onsite potentials for all cases are not random, instead they are engineered potentials with respect to site positions. This property breaks the localization of single particle hopping model and hence we observe thermalization of an observable that is nonlocal for the model.

Appendix B

Detection of Information Scrambling in Cold Atoms

B.1 Error bars on OTOC for the disordered XX-ladder

Fig. B.1 shows the out-of-time-order correlators for different rung couplings with error bars in the case of $h = 1$ $[J_{||}]$ random disorder strength. The error bars are significant for smaller rung couplings where the integrable limit of the ladder-XX model resides. As the rung coupling becomes equal to intra-leg couplings, the error bars become smaller. Therefore, the scrambling that we observe in the chaotic limit is robust to different configurations with the random disorder strength of $h \sim 1$ $[J_{||}]$. The error bars are more pronounced in the decay compared to unity and saturation regimes. When we study the opposite regime of dimer phase where rung coupling is much bigger than the intra-leg coupling $\alpha \to \infty$, the error bars do not grow significantly.

B.2 Error bounds on Haar-distributed initial states

We present the error bounds on the OTOC when Haar random states are used to mimic the $\beta = 0$ initial state in Fig. B.2. Fig. B.2 shows the difference $|F_i^{\text{ex}}(t) - F_i^{\sim}(t)|$ for $L = 6$

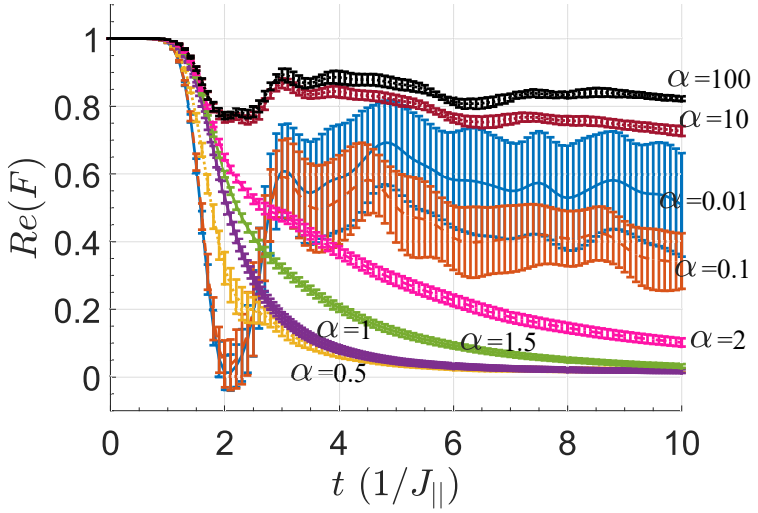

Figure B.1: Error bars of the out-of-time order correlators with disorder strength of $h = 1$ $[J_{||}]$ between two distant operators σ_1^z and σ_7^z with respect to different rung interaction strengths α where $J_\perp = \alpha J_{||}$ for $L = 7$. The OTOC is averaged over 100 different random samples. The curves are, $\alpha = 0.01$ (blue-solid), $\alpha = 0.1$ (orange-dashed), $\alpha = 0.5$ (yellow-dotted), $\alpha = 1$ (purple-solid), $\alpha = 1.5$ (green-solid), $\alpha = 2$ (pink-dashed), $\alpha = 10$ (crimson-dotted) and $\alpha = 100$ (black-dotted).

system size at $h = 1$ random disorder strength with only one random field configuration when $i = 6$ is set. The blue line stands for the case where we take only one random initial state, whereas the black line shows the case where we average over 100 such initial states. The difference is slightly more than an order of magnitude. However as seen from the other curves, the mixture of a couple of them is quite close to the case with $M = 100$. While using only one random state approximates the OTOC with an error up to 10^{-2}, one can improve the error bound via averaging over only a few states. The results are obtained in this paper with an average of 100 random states.

B.3 The exponential and power-law fitting parameters

Here we present the additional figures and fitting data that show the exponential and power-law decays.

Figs. B.3a-B.3b are for $L = 7$ system size. The lyapunov-like exponents for $L = 8$

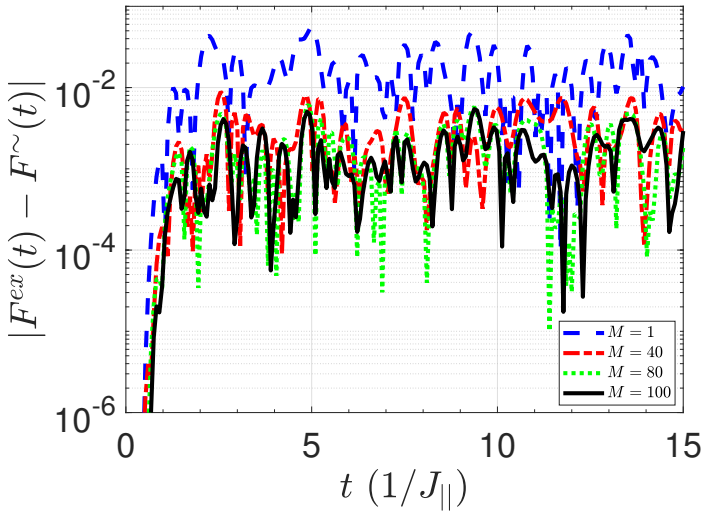

Figure B.2: The difference $|F^{\text{ex}}_{i=6}(t) - F^{\sim}_{i=6}(t)|$ for only one Haar-distributed random state (blue-dashed), averaged over 40 random states (red-dashed dotted), 80 states (green-dotted) and 100 states (black-solid). Only the real part of $F_i^{\sim}(t)$ is taken since the imaginary part is practically zero.

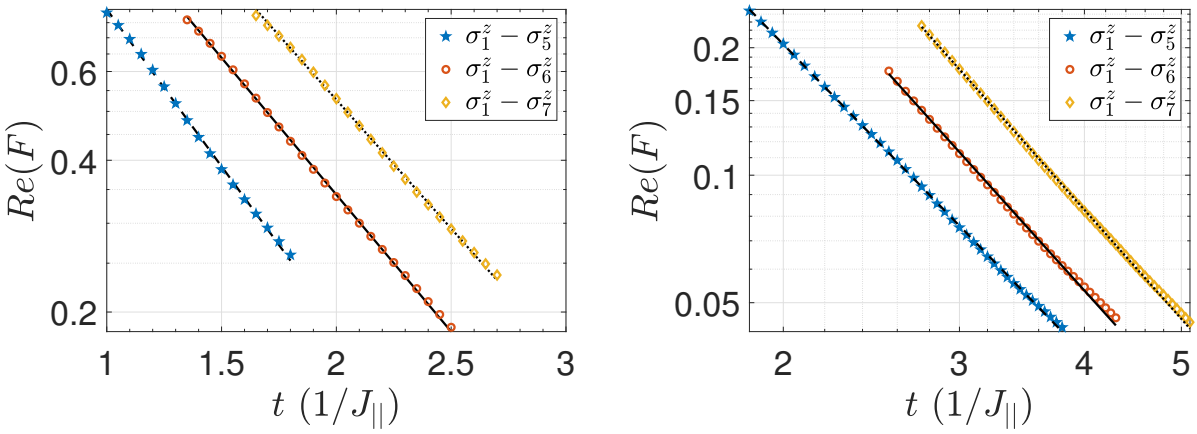

Figure B.3: (a) Semi-logarithmic plot for σ_1^z with σ_5^z (blue-pentagrams), σ_6^z (red-circles) and σ_7^z (orange-diamonds) observables in a system size of $L = 7$. The lyapunov-like exponents follow as, 1.4342 ($R^2 = 0.9989$), 1.2507 ($R^2 = 0.9996$) and 1.1767 ($R^2 = 0.9994$) for σ_5^z-σ_7^z with dashed, solid and dotted lines respectively. (b) Logarithmic plot for σ_1^z with σ_5^z (blue-pentagrams), σ_6^z (red-circles) and σ_7^z (orange-diamonds) observables in a system size of $L = 7$. The power-law exponents follow as 2.4335 ($R^2 = 0.9999$), 2.6165 ($R^2 = 0.9991$) and 2.6565 ($R^2 = 0.9997$) for σ_5^z-σ_7^z with dashed, solid and dotted lines respectively. The data is averaged over 100 different realizations of the Hamiltonian at $h = 1$ $[J_{||}]$ for both subfigures.

observable	λ	R^2
σ_5^z	1.362	0.9986
σ_6^z	1.229	0.9992
σ_7^z	1.09	0.9997
σ_8^z	1.015	0.9996

Table B.1: Exponential fit parameters for the Lyapunov-like exponents at $L = 8$.

observable	b	R^2
σ_5^z	2.1865	0.9996
σ_6^z	2.5506	0.9981
σ_7^z	2.5751	0.9976
σ_8^z	2.7636	0.9995

Table B.2: Power-law scaling fit parameters at $L = 8$.

are tabulated in Table B.1 and the relevant figure is shown in the main text. The data is averaged over 10 different random samples all at $h = 1$. The interval of data used for the exponential fitting at $L = 8$ extends from the time when OTOC starts to deviate from unity to $t \sim 2\ [1/J_{||}]$, $t \sim 3\ [1/J_{||}]$, $t \sim 4\ [1/J_{||}]$ and $t \sim 4\ [1/J_{||}]$ for σ_5^z, σ_6^z, σ_7^z and σ_8^z, respectively. The power-law fitting is applied to data seen in Fig. 3.2b (in the main text) until $t \sim 5\ [1/J_{||}]$, $t \sim 5\ [1/J_{||}]$, $t \sim 6\ [1/J_{||}]$ and $t \sim 6\ [1/J_{||}]$ for σ_5^z, σ_6^z, σ_7^z and σ_8^z, respectively. Similarly, the data used for the power-law in the clean limit, $h = 0$, is shown in Fig. 3.2c in the main text (until $t \sim 10\ [1/J_{||}]$ for all observables). The MBL decay form is applied to all data as seen in Fig. 3.2d in the main text.

B.4 Details on the experimental initial state preparation

Fig. B.4a plots the EON (eigenstate occupation numbers) distribution, $|c_\beta|^2$, for $L = 6$ and $L = 7$ for a randomly-set initial Fock state. These distributions should be contrasted with a uniform distribution of an infinite-temperature initial state. Even though they are

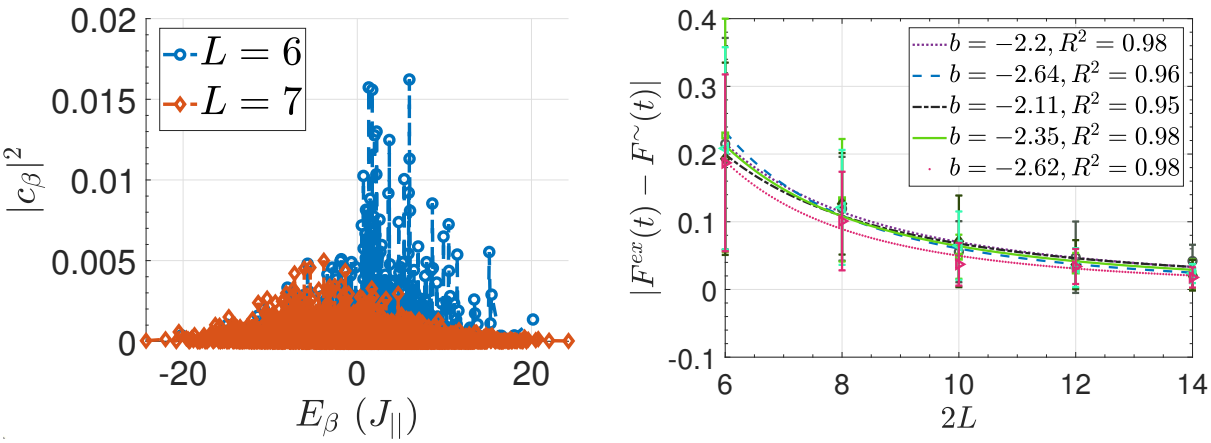

(a) (b)

Figure B.4: (a) The EON (eigenstate occupation number) distributions $|c_\beta|^2$ with respect to eigenenergies E_β for $L = 6$ (blue) and $L = 7$ (orange) sizes when only one Fock state is randomly set. (b) The scaling of the mean of the error $|F^{\text{ex}}(t) - \frac{1}{M}\sum_j F_j(t)|$ with the system size when we use only one randomly-sampled Fock state. Different curves are different random realizations with the legend showing the exponent of the corresponding power-law decay. The error bars stand for 1σ standard deviation around the mean of the error signal.

not uniform, they are still broad distributions which helps the approximation error to be bounded. As a result, as long as the initial state has a broad distribution in the eigenbasis, the exact shape of the distribution is not significant. Hence such an initial state could be used to sufficiently approximate an infinite-temperature OTOC.

Fig. B.4b shows the error ϵ_1 scales as a power-law in the system size when only one Fock state is randomly-set. This figure focuses on five realizations that were given in the main text in logarithmic scale. Here we plot the data in linear scale to also demonstrate the error bars. The error bars stand for 1σ deviation around the mean of the error signal in time. Note that the error bars increasingly become smaller as the system size increases, meaning that our initial state approximation does not only work better on average but also throughout the simulation time.

Finally we provide the exact fitting expressions for the exponential and power-law scalings of the mean error in the sampling ratio M/N. The exponential scaling parameters are, $a = 0.1218$, $R^2 = 0.9134$ $(N = 3)$, $a = 0.043$, $R^2 = 0.933$ $(N = 4)$, $a = 0.0132$, $R^2 = 0.884$

($N = 5$) and $a = 0.004$, $R^2 = 0.962$ ($N = 6$) with very close exponents $b \sim -2.5$. The power-law scaling parameters are, $a = 0.0112$, $R^2 = 0.984$ ($N = 3$), $a = 0.0037$, $R^2 = 0.991$ ($N = 4$), $a = 8 \times 10^{-4}$, $R^2 = 0.945$ ($N = 5$) and $a = 3.4 \times 10^{-4}$, $R^2 = 0.981$ ($N = 6$) with very close exponents $b \sim -0.5$.

Appendix C

The Connection Between Information Scrambling and Quantum Phase Transitions

C.1 Energy-time relation and finite-size effects

Eq. 5 in the main text clearly exhibits how the OTOC can suffer from the finite-size effects. Imagine that the finite-size lifts the degeneracy. Based on the dynamical equation of OTOC,

$$F(t) = \sum_{\alpha,\beta,\gamma,\gamma'} c_\alpha^* b_\beta e^{-i(E_\beta - E_\alpha + E_\gamma - E_{\gamma'})t} W_{\alpha\gamma}^\dagger V_{\gamma\gamma'}^\dagger W_{\gamma'\beta},$$

one would write the ground state contribution to the OTOC at zero temperature as

$$F_{gs}(t) \sim |W_{[1,1][1,2]} W_{[1,2][1,1]}|^2 \exp\left[-2i(E_{[1,2]} - E_{[1,1]})t\right]. \tag{C.1}$$

Since Eq. (C.1) is the dominant contribution to the OTOC in the ordered phase, the order will eventually be invisible to the saturation value, and it will be encoded in the frequency spectrum of the OTOC. However since this is a finite-size effect, we expect to see finite

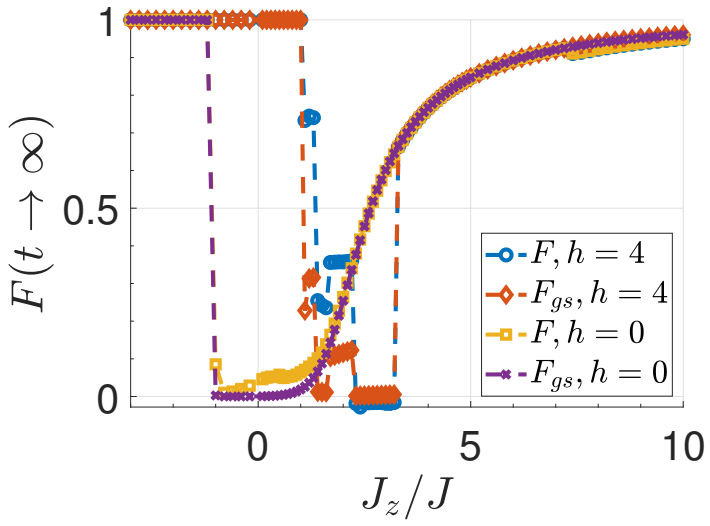

Figure C.1: The OTOC saturation values for an open-boundary chain with $N = 13$ size and a long-time of $tJ \sim \frac{\pi}{4}10^3$ at fields $h/J = 0$ (orange-squares: Eq. 4, purple-crosses: Eq. 6 and $h/J = 4$ (blue-circles: Eq. 4, red-diamonds: Eq. 6, for σ_i^z observable.

saturation value for all times in the thermodynamic limit. The period of the emerging oscillation (due to degeneracy-lifting) is $\tau = \pi/(E_{[1,2]} - E_{[1,1]})$. Then starting from $t \sim \tau/2$, the order will be invisible to the saturation value. Thus, the region where the system seems to have reached its most correlated state before the finite-size effects show up, could be defined for $t \ll \tau/2$; whereas the order will be most visible to the frequency spectrum around $t \gg \tau/2$. Further, the ground state contribution will exist in the saturation value as a non-zero effect for a time $t \sim \tau/4$, where the time-averaging will reveal the order. The relation between evolution time and energy spectrum reflects the observation that longer the time evolution, better the resolution of the energy spectrum. This, in turn, helps us to estimate the time interval of the corresponding dynamics simulation of the theory Eq. 5 (in the main text), even though Eq. 5 is explicitly time-independent.

For a phase transition that involves antiferromagnetic order, due to the doubling of the unit cell size, it is not uncommon that the finite-size contributions may oscillate as we increase the system size, depending on whether the system is composed of odd (Fig. C.1) or even (Fig. 2a in the main text) number of sites. For periodic boundary conditions, the systems

with even number of sites usually show smaller finite-size effects. In our studies, though, we observe the opposite: chains with odd number of spins experience finite-size effects less. As far as the OTOC is concerned, stronger finite size effects are expected for systems with even number of sites, since the key to obtain the OTOC saturation value is to sum over all the quantum states in the ground state subspace. In an Ising-ordered phase, an exact two-fold degeneracy is guaranteed for a chain with odd number of spins by the Kramers degeneracy theorem, because an odd number of spin-1/2 results in a half-integer total spin. For a system with even number of sites (i.e. integer total spin), such an exact degeneracy is not expected and thus the degeneracy is lifted by finite size effects more strongly than chains with odd number of spins. This explains the dramatic difference between the results of open and periodic boundary conditions at the XY-antiferromagnet boundary. We also note that the ground states belong to the $S_z = 0$ magnetization sector in the antiferromagnet, which is the biggest sector of the Hamiltonian and hence they would hybridize with each other. To alleviate the finite-size effects, we make use of the time-energy relation explained above and plot the OTOC for significantly smaller interval of time, $tJ \sim \frac{\pi}{4}10$ in the main text. This should be compared with the results of a long-time evolution $tJ \sim \frac{\pi}{4}10^3$ in Fig. B.3b. This comparison is a good example of how finite-size effects could show up in scrambling, restricting the order to short-times. We also note that even though our method is valid at the infinite-time limit, due to the energy-time relation employed in the computations it produces sufficiently good results for the real-time dynamics in a short-time evolution.

Fig. C.3 is the phase diagram of odd-numbered chains with phase boundaries dictated by the Bethe ansatz for an infinite-size chain. Even though the finite-size effects for small fields are more severe in even-numbered chains than odd-numbered chains in small systems, we note that the transition in odd-numbered chains is ambiguous. The continuous transition between XY- and antiferromagnetic phases due to the nature of the doubly-degenerate ground states in odd-numbered chains (as explained above), prevents a straightforward system-size scaling based on odd-numbered chains. Therefore we chose to focus on even-numbered chains in the

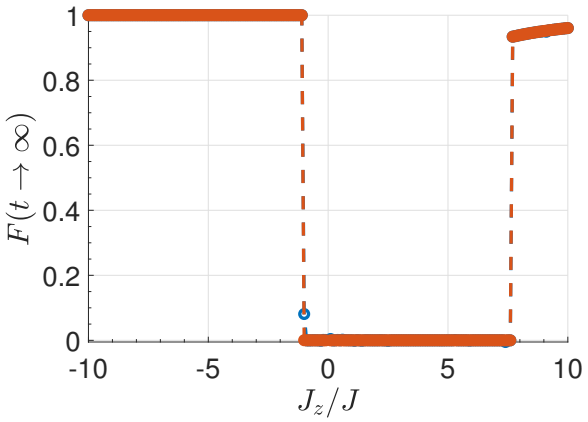

Figure C.2: OTOC saturation value (Eq. (3), blue line) and its ground state contribution (Eq. (5), orange line) for $h/J = 0$, $N = 14$ and for time $tJ \lesssim \frac{\pi}{4}10^3$. The anti-ferromagnetic order is concealed due to finite-size effects appearing in long-times.

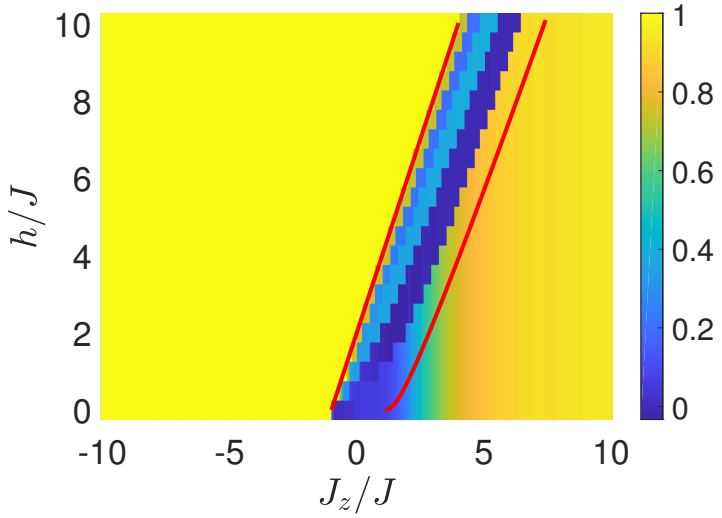

Figure C.3: The OTOC phase diagram (via Eq. (3)) for odd-numbered chains while the x-axis is the spin interaction strength in the z-direction J_z/J and y-axis is the magnetic field h/J, for $N = 13$ system size and σ_z^i where the observation spin is chosen from bulk, when open boundary conditions are set and initial state is a ground state. The time-scale where the results are valid is $tJ \sim \frac{\pi}{4}10^3$.

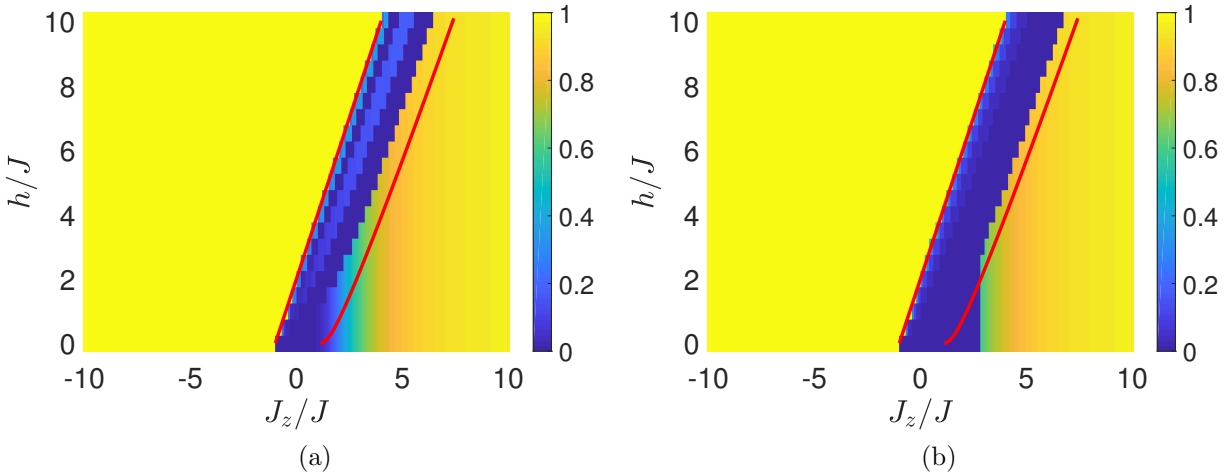

Figure C.4: Ground state value contribution (Eq. (5)) to OTOC for (a) odd-numbered $N = 13$ and (b) even-numbered $N = 14$ chains with respect to J_z/J at x-axis and field h/J at y-axis.

main text. We also note that as we compute results for bigger system sizes, the apparent odd-even effect disappears. The difference between Bethe ansatz results and the OTOC phase boundary for the anti-ferromagnetic to XY phase in high fields is also due to finite-size effects. This could be seen in Figs. C.4, where we compare the ground state value in OTOC with the exact phase boundaries. This means that the ground state contribution similarly suffers from the finite-size effects as well. Hence the results point to the effect of finite-size on the ground state manifold rather than the incapability of OTOC to probe the phase transition as precisely as exact results. It is an interesting question how the system size scaling results of OTOC and its ground state contribution would compare with the existing methods of determining the phase boundary, e.g. Binder ratio, fidelity measures, determining the energy gap, spatial correlation functions etc.

C.2 Operator Ansatz Demonstrated

Here we give the additional results of XXZ model on the relation between OTOCs and phase transitions. Fig. C.5 shows the difference between the OTOC saturation values, Fig. C.3

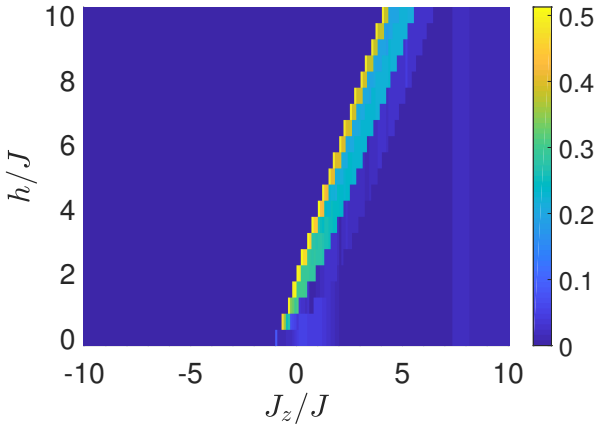

Figure C.5: The difference between the OTOC saturation values (via Eq. (3) in main text) and the ground state contribution for the phase diagram while the x-axis is the spin interaction strength in the z-direction J_z and y-axis is the magnetic field h, for $N = 13$ system size and σ_z^i where the observation spin is chosen from bulk, when open boundary conditions are set and the initial state is a ground state.

and the ground state contribution in these values, Fig. C.4a. The mismatch between OTOC saturation value and ground state contribution to it is clear in XY-phase, due to the fact that the correction term of the excitations is dominant in the XY-phase, as explained in the text.

Fig. C.6a shows the matrix elements of the long-range order bulk observable σ_z^i used in the study only for a ground state $|V_{1,\alpha}|^2$. Note how the observable's matrix elements satisfy the operator ansatz put forward in the text: in Ising-ordered phases we observe $|W_{[1,\alpha][1,\beta]}|^2 \gg |W_{[1,\gamma][\theta,\gamma']}|^2$ while in the Ising-disordered phase (XY-phase) $W_{[1,\alpha][1,\beta]} \sim 0$ and $|W_{[1,\alpha][\theta,\beta]}|^2 \ll 1$ is satisfied. Fig. C.6b shows the participation ratio (PR) value of the ground state in terms of spin basis. PR is defined as

$$P_\alpha \;=\; \left(\sum_{n=1} |\psi_{\alpha n}|^4\right)^{-1}, \tag{C.2}$$

where α are eigenstates and n are the reference basis. PR is a measure of fluctuations of a state in a reference basis. We see that the ferromagnetic ground states ($J_z/J < -1$) are more localized compared to anti-ferromagnetic ground states ($J_z/J > 1$), because of

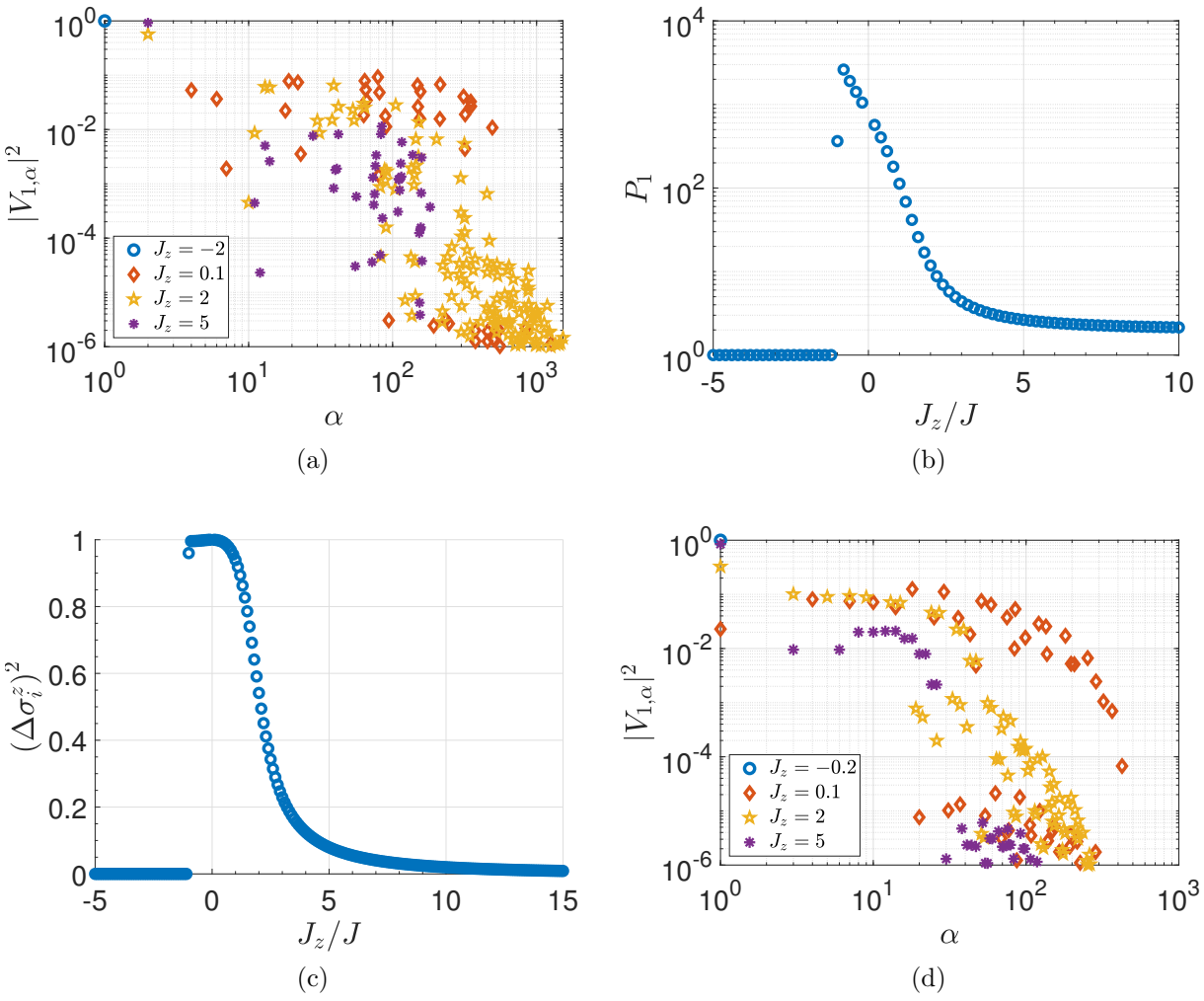

Figure C.6: (a) Matrix elements of observable σ_z^i of a bulk spin for a ground state $|V_{1,\alpha}|^2$ at $N = 14$ for various J_z: $J_z/J = -2$ (blue-circles), $J_z/J = 0.1$ (red-diamonds), $J_z/J = 2$ (yellow-pentagons) and $J_z/J = 5$ (purple-dots). (b) Participation ratio of the ground state with respect to J_z/J for a system size $N = 14$, while the reference basis is spin basis. (c) Fluctuations of a ground state at $N = 15$. (d) The matrix elements of observable σ_z^i of a bulk spin for a ground state $|V_{1,\alpha}|^2$ at $N = 13$ (odd-numbered chains) for various J_z: $J_z/J = -2$ (blue-circles), $J_z/J = 0.1$ (red-diamonds), $J_z/J = 2$ (yellow-pentagons) and $J_z/J = 5$ (purple-dots).

the subspaces that they belong to under a S_z conserving Hamiltonian. As a result, anti-ferromagnetic ground states are more susceptible to both finite-size effects (mixing in energy levels) and the effect of the rest of the terms in the Hamiltonian. This is also the reason why OTOCs are better in capturing the transition from a ferromagnet to a XY-paramagnet compared to anti-ferromagnet to XY-paramagnet. Unless $J_z \gg J$, the XX- and YY-coupling terms cause the Neel states to slightly couple to the other states in $S_z = 0$ subspace.

The operator ansatz on the matrix elements can also be seen in terms of the fluctuations in a ground state. The fluctuations of the ground state can be defined as $(\Delta\sigma_z^i)^2 = \langle(\sigma_z^i)^2\rangle - \langle\sigma_z^i\rangle^2$ where the expectation is taken over the ground state and seen in Fig. C.6c for a system size of $N = 15$. Hence, we state that the fluctuations are maximized in XY-phase, causing a dominant correction term in the OTOC saturation value. The fluctuations are zero in the ferromagnetic phase and they approach to zero in the anti-ferromagnetic phase as $J_z/J \to \infty$. Note that this is the case because an open boundary chain with odd-number of spins have two ground states with different S_z quantum numbers in the anti-ferromagnetic phase. This can be seen more explicitly in the matrix elements of an odd-numbered chain in Fig. C.6d. The operator ansatze are satisfied as expected, however note that the main contribution comes from the diagonal elements in the Ising-ordered phases, unlike in the even-numbered chains in Fig. C.6a. Finally we note that the fluctuations are always maximum for the quasi-long range observable σ_x^i.

C.3 Comparison of real-time dynamics with theory prediction in short times

Here we share a direct comparison between real-time dynamics of OTOC in short-time and the infinite-time saturation value that is predicted by Eq. 3 in the main text, to demonstrate that the analytical framework to predict the saturation value (or the time-average) is robust in finite times. Fig. C.7a shows the average of the time-signal (over a time interval of $tJ = 20$)

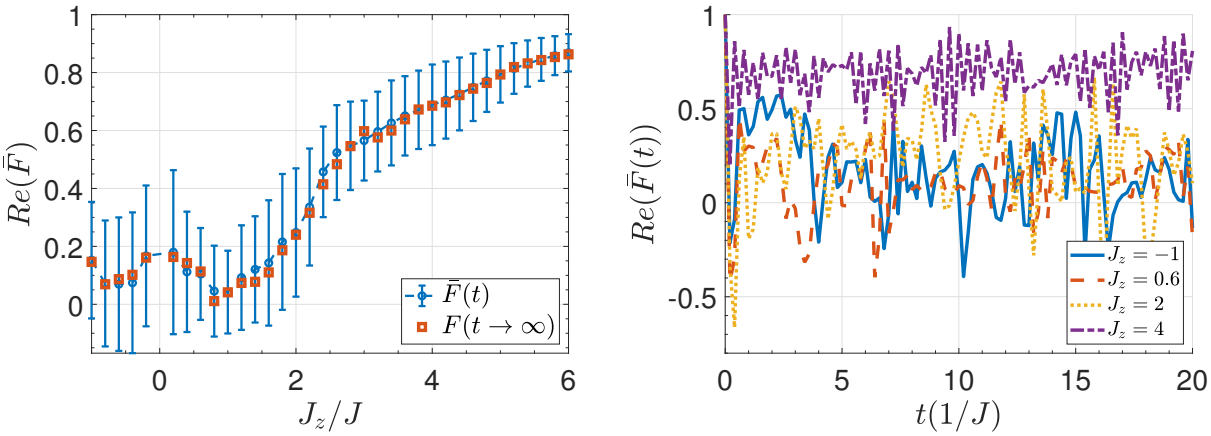

(a) (b)

Figure C.7: (a) The time-average of OTOC signal over a time interval of $tJ = 20$ (blue circles) and the extend of the oscillations around the average with the error bars; the theory saturation value prediction Eq. 3 in the main text (red squares). (b) The real-time dynamics shown for $J_z = -1$ (blue-solid), $J_z = 0.6$ (red-dashed), $J_z = 2$ (yellow-dotted) and $J_z = 4$ (purple-dashed dotted). Both subfigures are for a system size of $N = 13$ and at a zero field $h/J = 0$.

with blue circles and the extend of oscillations with the error bars around the blue circles. Some of these real-time OTOC signals can be seen in Fig. C.7b. Even though these signals are oscillatory and show transient features, our theory could predict the average of the signals with a good accuracy as seen with red squares in Fig. C.7a. Therefore, our theory is not restricted to long times. The main reason of this robustness is due to the energy-time relation we employ in the computations, hence the saturation value Eq. 3 (in the main text) changes with the interval of time-averaging even though the Eq. 3 is explicitly time-independent (see Appendix C.1).

C.4 OTOC with odd number of spins and periodic boundary conditions

We present the result for odd-numbered chain if periodic boundary condition is applied, Fig. C.8. The low values and fluctuations in the anti-ferromagnetic region are a sign of how

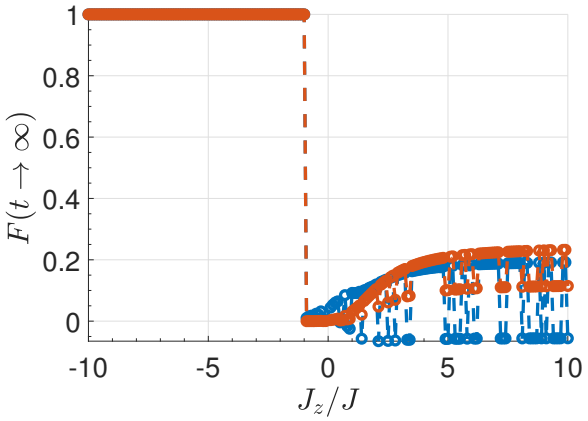

Figure C.8: OTOC saturation value (Eq. (3), blue line) and its ground state contribution (Eq. (5), red-circles), for $h/J = 0$ when $N = 13$ is set and for time $tJ \lesssim \frac{\pi}{4}10^3$ with periodic boundary conditions.

OTOC is sensitive to emerging domain walls in the ground state. Domain walls are expected in the anti-ferromagnetic ground state because of the frustration in an odd-numbered periodic chain.

C.5 The remarks on the saturation value of OTOC

Eq. 2 in main text can show why quantum chaotic spin systems should eventually decay to zero when ETH is evoked up to some approximations. When a system follows ETH, there are two criteria to satisfy: (i) $V_{\gamma\gamma'} \ll V_{\gamma\gamma}$, where $\gamma \neq \gamma'$, and (ii) $V_{\gamma\gamma}$ is a smooth function of energy E_γ, $f(E_\gamma)$ ($V_{\gamma\gamma}$ almost do not fluctuate) [40, 295]. In this case, we end up with $F(t\to\infty) \sim \sum_\alpha c_\alpha^* b_\alpha |V_{\alpha\alpha}|^3$ up to some residue due to finite-size and conservation laws [297]. (We assume $V = W$ for simplicity of the argument.) We can state,

$$\mathrm{Tr}(V\mathbb{I}) \sim \mathrm{Tr}(V\,|\psi(0)\rangle\,\langle\psi(0)|) = \langle\psi(0)|\,V\,|\psi(0)\rangle \tag{C.3}$$

because $|\psi(0)\rangle$ is drawn from a Haar-distributed ensemble (detailed in the next paragraph). Then, under the assumption of $\mathrm{Tr}\,(V) = 0$, $\langle\psi(0)|\,V\,|\psi(0)\rangle = \sum_\alpha c_\alpha^* b_\alpha = 0$. Since $V_{\gamma\gamma}$ do not fluctuate significantly via ETH's second criteria [40] and in fact the support of distribution

of $V_{\gamma\gamma}$ shrinks around the microcanonical ensemble value in the thermodynamic limit if we assume the strong form of ETH [114], $F(t \to \infty) \to 0$ for chaotic spin systems. However, in order to extract the rate of decaying to zero e.g. power-law in chaotic spin systems with conserved quantities, and/or the residue due to finite-size, one needs a more rigorous analysis where the fluctuations of the diagonal elements $V_{\gamma\gamma}$ around the smooth function $f(E)$ are included in the second assumption of ETH [297].

$\mathrm{Tr}V \sim \langle\psi\,|\,V\,|\,\psi\rangle$ holds for a pure state $|\psi\rangle$ randomly drawn from uniform distribution induced by Haar measure [277]. These so-called Haar-distributed random states, unlike random product states, are close to maximally entangled states [368]. By being close to maximally-entangled states, Haar-distributed random pure states behave as typical states on which *canonical typicality* [84, 85] could emerge. Canonical typicality is defined as the following: Consider a system U with Hilbert space dimension d_u, composed of a subsystem S with dimension d_s and its environment E of dimension d_e which is significantly larger than the system itself $d_e \gg d_s$. In a system with equiprobable states, the state of the system would be $\rho_u = \mathbb{I}/d_u$. Hence the subsystem would be in a canonical state, $\Omega_s = \mathrm{Tr}_e\rho_u$. Now if we take a pure typical state for the system $|\psi\rangle$ instead of ρ_u, the subsystem state can be written as $\rho_s = \mathrm{Tr}_e\,|\psi\rangle\,\langle\psi|$. Canonical typicality asserts that $\rho_s \sim \Omega_s$ for typical states $|\psi\rangle$. This means that typical system state $|\psi\rangle$ is locally indistinguishable from ρ_u. As stated in Ref. [84], canonical typicality emerges because of 'massive entanglement between the subsystem and the environment' which is a feature of typical states. These ideas are established in Ref. [85] and more generally in Ref. [84] via invoking Levy's lemma [277] for systems with constraint of energy conservation. Later studies showed that energy constraint on the system is not required for canonical typicality to emerge [302] and it is possible to formulate the principle for mechanical observables [296, 302]. Canonical typicality for a mechanical observable reads [277, 296]

$$P\left[\left|\mathrm{Tr}V - \langle\psi\,|\,V\,|\,\psi\rangle\right| \geq \epsilon\right] \lesssim \exp\left(-\mathcal{O}(d_u)\right), \tag{C.4}$$

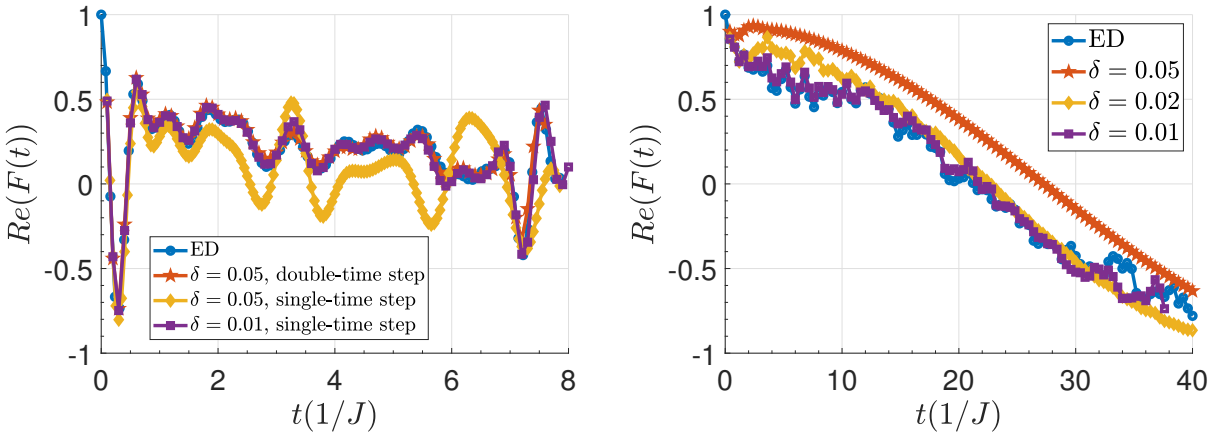

Figure C.9: Real-time dynamics of OTOC at (a) $J_z/J = 0.5$ and (b) $J_z/J = 4$ at $N = 14$. (a) Blue-circles: exact diagonalization, red-pentagons: double-time steps with $\delta = 0.05$, yellow-diamonds: single-time steps with $\delta = 0.05$ and purple-squares: single-time steps with $\delta = 0.01$. (b) Blue-circles: exact diagonalization, red-pentagons: double-time steps with $\delta = 0.05$, yellow-diamonds: double-time steps with $\delta = 0.02$ and purple-squares: double-time steps with $\delta = 0.01$. Both subfigures are at $h/J = 0$.

where ϵ is a small parameter. Hence, the probability that $\langle\psi\,|\,V\,|\,\psi\rangle$ deviates from $\mathrm{Tr}V$ decreases exponentially in the system size. Therefore, for big enough many-body systems Haar-distributed states could very well imitate an equiprobable state, $\rho_u = \mathbb{I}$ in the calculation of observable expectation values. This theory has been used in numerical studies to compute OTOCs at infinite-temperature Ref. [130] and Chapter 3.

C.6 Density-matrix renormalization group computations

In order to compute the real-time dynamics of OTOC with MPS, we first find the ground state of the system with DMRG where we limit our computation to maximum 10 sweeps and set it to initial state. Then we time-evolve the initial state approximately [369]. Note that this approach is accurate as long as the time increment δ is small enough. Fig. C.9a compares three different methods in the calculation of the OTOC at $J_z/J = 0.5$ (XY-phase).

While ED stands for exact diagonalization, single-time step means using only real time step δ and double-time means utilizing two complex time steps at a real time step in order to decrease the scaling of the error [369]. Fig. C.9b shows different δ values with double-time steps in the anti-ferromagnetic phase of the XXZ model. Due to our benchmarking results, we set $\delta = 0.01$ for our time evolution computations. For the calculation of the ground state contribution to OTOC as the leading-order term in the Ising-ordered phases, we compute the first three states with lowest energies via DMRG.

Appendix D

Topologically Induced Prescrambling

D.1 Methods Explained

To determine the degeneracy in the spectrum, we need to characterize the uncertainty in energy, ΔE. This means that we define an energy window around each energy level with ΔE as $[E_m - \Delta E, E_m + \Delta E]$ where we assume that the states remain in this window are degenerate with the state whose associated energy is E_m. This process defines an energy resolution and in a way coarse-grains the energy spectrum.

As discussed in Chapter 4 and the previous Appendix Sec. C.1, the energy resolution is related to the interval of the time-evolution. Longer time-evolution translates to finer energy resolution, resolving the smallest energy differences in the spectrum, $\mathcal{T}\Delta E \sim 1$, where $\mathcal{T}$ is the total time of the evolution. Hence anytime we simulate a system with a finite time interval, we define an energy resolution as $\Delta E = \frac{\pi}{4\mathcal{T}}$. In return, the parameter ΔE determines the degenerate subspaces in the spectrum and hence helps us to determine the diagonal contribution $\bar{F}_{diag}$ in OTOC time-average. Note that this reverse relation between the time interval and energy resolution also implies that any degeneracy lifting will be eventually captured by a long-time evolution.

We call an equation derived by the dynamical decomposition as a framework equation.

If the operator in the eigenbasis $W_{\alpha\beta}$ can be calculated analytically for an integrable system, that would present us the analytical expression of its OTOC saturation value. However, one can numerically derive the matrix elements $W_{\alpha\beta}$ too and use them in the framework of dynamical decomposition. Any brute force calculation of the OTOC saturation value requires an estimation on the time-dependent part in the dynamical Eq. (5.10), e.g. which energy pairs are equal to each other. The energy resolution ΔE is used here to define a threshold so that we could exert the degenerate subspaces on the OTOC calculation. Crudely speaking, this threshold determines whether the saturation value is contributed by the found energy set $\{E_\alpha, E_\beta, E_\gamma, E_\delta\}$. In the end, the numerical incorporation of a finite energy resolution into our framework equation that analytically determines the saturation value, also provides us the time-average of OTOC over any time interval up to dramatic transient features (see Appendix Secs. C.1 and C.3). Hence we equivalently call $\bar{F}$ both for long-time saturation value and the time-average of OTOC.

When we numerically calculate the OTOC saturation value, we do the summations in Eq. (5.11). This introduces an approximation to the final OTOC saturation value in our numerical result. We set a threshold where any term greater than the threshold is found and summed over. We determine our threshold based on the dimension of the Hilbert space, $\sim 1/M^2$, where M is the dimension of the Hilbert space. This generally bounds the error on the order of $\sim 10^{-2}$ (we remind the reader that $|F| \leq 1$).

We utilize ITensor platform in C++ environment and MPS (matrix product states) for DMRG computations [300]. To prepare infinite temperature states in MPS format, we average over random product states. We restrict the bond numbers to $m \lesssim 100$. Since the bond numbers increase rapidly as the system evolves in time, this results less accuracy for the later times. Therefore, we restrict our time-evolution with MPS at infinite-temperature to $tJ \lesssim 10$. The t-DMRG of OTOC in low temperatures or zero temperature present modest bond numbers, hence we are able to simulate OTOC at zero temperature for longer times.

D.2 Derivation of Fermionic OTOC

In order to (both analytically and numerically) solve Kitaev chain, we double the Hilbert space of single-particles and generate the BdG Hamiltonian. This Hamiltonian gives us a symmetric spectrum around energy $E = 0$ where there are two states at $E = 0$ when the chain is open due to the localized Majorana fermions at two ends. Therefore, if we derive an equation for OTOC in terms of single-particle states, via summing over only $E = 0$ states (Majorana zero modes) due to Eq. (5.9), we can calculate the OTOC in the infinite-time limit.

We work with the fermion operator in doubled space, that is, in addition to $d_i = c_i$ we also have $d_{i+N} = c_i^\dagger$, hence d_i has a dimension of $2N$ where N is the dimension of the free fermionic system without pairing terms. Note that in addition to the familiar anti-commutation relation $\left\{d_i, d_j^\dagger\right\} = \delta_{ij}$, we have $\{d_i, d_{j+N}\} = \delta_{ij}$ and $\left\{d_i^\dagger, d_{j+N}^\dagger\right\} = \delta_{ij}$. Hence, a Majorana operator can be defined as $a_{2i-1} = c_i + c_i^\dagger = \left(d_i + d_i^\dagger + d_{i+N} + d_{i+N}^\dagger\right)/2$. With this algebra in mind, we can derive

$$F_{2i-1,2i-1}(t) = \frac{1}{2^N}\mathrm{Tr}\left(a_{2i-1}(t)a_{2i-1}a_{2i-1}(t)a_{2i-1}\right). \tag{D.1}$$

After the substitution of d_i operators,

$$\begin{aligned}
F_{2i-1,2i-1}(t) &= \frac{1}{2^{2N}}\frac{1}{2^2}\mathrm{Tr}\Big[d_i(t)a_{2i-1}d_i(t)a_{2i-1} + d_i^\dagger(t)a_{2i-1}d_i^\dagger(t)a_{2i-1} \\
&+ d_{i+N}(t)a_{2i-1}d_{i+N}(t)a_{2i-1} + d_{i+N}^\dagger(t)a_{2i-1}d_{i+N}^\dagger(t)a_{2i-1} \\
&+ 2\Big(d_i(t)a_{2i-1}d_i^\dagger(t)a_{2i-1} + d_i(t)a_{2i-1}d_{i+N}(t)a_{2i-1} \\
&+ d_i(t)a_{2i-1}d_{i+N}^\dagger(t)a_{2i-1}\Big) + 2\Big(d_i^\dagger(t)a_{2i-1}d_{i+N}(t)a_{2i-1} \\
&+ d_i^\dagger(t)a_{2i-1}d_{i+N}^\dagger(t)a_{2i-1} + d_{i+N}^\dagger(t)a_{2i-1}d_{i+N}(t)a_{2i-1}\Big)\Big].
\end{aligned} \tag{D.2}$$

Since the dimension of the Hilbert space is 2^{2N}, the following identities hold:

$$\begin{aligned}
\mathrm{Tr}\left(d_i d_i^\dagger + d_i^\dagger d_i\right) &= 2^{2N} \rightarrow \mathrm{Tr}\left(d_i d_i^\dagger\right) = 2^{2N-1}. \\
\mathrm{Tr}\left(d_{i+N} d_{i+N}^\dagger\right) &= \mathrm{Tr}\left(d_i d_{i+N}\right) = \mathrm{Tr}\left(d_i^\dagger d_{i+N}^\dagger\right) = 2^{2N-1}. \\
\mathrm{Tr}\left(d_i d_i^\dagger \left(d_i^\dagger d_i + d_i d_i^\dagger\right)\right) &= 2^{2N-1} \rightarrow \mathrm{Tr}\left(d_i d_i^\dagger d_i d_i^\dagger\right) = 2^{2N-1}. \\
\mathrm{Tr}\left(d_{i+N} d_{i+N}^\dagger d_{i+N} d_{i+N}^\dagger\right) &= \mathrm{Tr}\left(d_i d_{i+N} d_i d_{i+N}\right) = \mathrm{Tr}\left(d_i^\dagger d_{i+N}^\dagger d_i^\dagger d_{i+N}^\dagger\right) = 2^{2N-1}.
\end{aligned}$$

Eq. (D.2) takes a form of

$$\begin{aligned}
F_{2i-1,2i-1}(t) &= \frac{1}{2^{2N}} \frac{1}{2^2} \sum_{k,l}^{2N} \Big[(G_{ik}(t) G_{il}(t) + G_{i+N,k}(t) G_{i+N,l}(t) \\
&+ 2 G_{ik}(t) G_{i+N,l}(t)) \mathrm{Tr}(d_k a_{2i-1} d_l a_{2i-1}) + \mathrm{h.c.} \Big] \\
&+ \frac{2}{2^{2N}} \frac{1}{2^2} \sum_{k,l}^{2N} \Big[(G_{ik}(t) G_{il}^*(t) + G_{ik}(t) G_{i+N,l}^*(t)) \mathrm{Tr}(d_k a_{2i-1} d_l^\dagger a_{2i-1}) \\
&+ \left(G_{ik}^*(t) G_{i+N,l}(t) + G_{i+N,k}^*(t) G_{i+N,l}(t)\right) \mathrm{Tr}(d_k^\dagger a_{2i-1} d_l a_{2i-1}) \Big],
\end{aligned} \tag{D.3}$$

in terms of the matrix elements of the single-particle propagators $G(t) = \exp\left(-i H_{\mathrm{BdG}} t\right)$.

The term $\mathrm{Tr}(d_k a_{2i-1} d_l a_{2i-1})$ is non-zero only when $k = l = i$ or $k = l = i + N$ where in both cases $\mathrm{Tr}(d_k a_{2i-1} d_l a_{2i-1}) = 2^{2N}$. The term $\mathrm{Tr}(d_k a_{2i-1} d_l^\dagger a_{2i-1})$, on the other hand, vanishes for $k = l = i$ and $k = l = i + N$, however survives for $k = l \neq i$ and $k = l \neq i + N$. In this case, $\mathrm{Tr}(d_k a_{2i-1} d_l^\dagger a_{2i-1}) = -2^{2N}$. Note that none of these terms survives if $k = i, l = i + N$ and vice versa. Therefore we end up with

$$
\begin{aligned}
F_{2i-1,2i-1}(t) &= \frac{1}{2^2}\Big[\left(G_{ii}(t)\right)^2 + 2\left(G_{i,i+N}(t)\right)^2 + \left(G_{i+N,i+N}(t)\right)^2 \\
&+ 2\left(G_{ii}(t)G_{i+N,i}(t) + G_{i,i+N}(t)G_{i+N,i+N}(t)\right) + \text{c.c}\Big] \\
&- \frac{1}{2}\sum_{k\neq i,k\neq i+N}^{2N} \left(|G_{ik}(t)|^2 + |G_{i+N,k}(t)|^2 + G_{ik}(t)G^*_{i+N,k}(t) + G^*_{ik}(t)G_{i+N,k}(t)\right).
\end{aligned} \tag{D.4}
$$

The unitarity condition reads $\sum_k^{2N} |G_{ik}|^2 = 1$, then

$$
\sum_{k\neq i,k\neq i+N}^{2N} |G_{ik}(t)|^2 = 1 - |G_{ii}(t)|^2 - |G_{i,i+N}(t)|^2. \tag{D.5}
$$

Furthermore, we utilize the relation $\sum_{k=1}^{2N} G_{ik}G^*_{i+N,k} = 0$ which leads to

$$
\sum_{k\neq i,k\neq i+N}^{2N} G_{ik}(t)G^*_{i+N,k}(t) = -G_{ii}(t)G^*_{i+N,i}(t) - G_{i,i+N}(t)G^*_{i+N,i+N}(t). \tag{D.6}
$$

When these relations are utilized, one can write the final result as

$$
\begin{aligned}
F_{2i-1,2i-1}(t) &= \left(\text{Re}\left(G_{ii}(t)\right) + \text{Re}\left(G_{i,i+N}(t)\right)\right)^2 \\
&+ \left(\text{Re}\left(G_{i,i+N}(t)\right) + \text{Re}\left(G_{i+N,i+N}(t)\right)\right)^2 - 1,
\end{aligned} \tag{D.7}
$$

for OTOC for a Majorana fermion of type a_{2i-1}. Given $G_{ij}(t) = \sum_\alpha \exp\left(-iE_\alpha t\right)\langle\psi_{\alpha,j}|\psi_{\alpha,i}\rangle$ where $\psi_{\alpha,i}$ means the i^{th} element of the eigenstate α of H_{BdG}, this result should eventually lead to the result stated in the main text,

$$
\begin{aligned}
F_{2i-1,2i-1}(t) &= \left[\sum_{\alpha=1}^{2N} \left(|\psi_{i\alpha}|^2 + \psi_{i\alpha}\psi^*_{i+N,\alpha}\right)\cos\left(\epsilon_\alpha t\right)\right]^2 \\
&+ \left[\sum_{\alpha=1}^{2N} \left(|\psi_{i+N,\alpha}|^2 + \psi_{i+N,\alpha}\psi^*_{i,\alpha}\right)\cos\left(\epsilon_\alpha t\right)\right]^2 - 1.
\end{aligned} \tag{D.8}
$$

D.3 The relation between OTOCs and two-time correlators

Eq. (5.13) shows that the saturation value of a two-time correlator will always be governed by the diagonal elements in the operator W. Then $W_{\alpha\beta} = \langle\psi_\alpha| W |\psi_\beta\rangle$ can be straightforwardly calculated in the non-interacting limit. Here, $|\psi_\beta\rangle$ and $|\psi_\alpha\rangle$ are even and odd parity states in a doubly-degenerate subspace that is dictated by the Majorana zero modes. We note that $|\psi_\gamma\rangle = d|\psi_\alpha\rangle = f(h)\left(\frac{\gamma_1+i\gamma_2}{\sqrt{2}}\right)|\psi_\alpha\rangle$, where $f(h)$ is a function of magnetic field h and $f(h=0) = 1/\sqrt{2}$, however decreases as $h \to 1$. The quantity that we need to calculate becomes $\langle\psi_\alpha| W f(h)(\gamma_1 + i\gamma_2)|\psi_\alpha\rangle/\sqrt{2}$. The effect appears when we use edge spins, hence

$$W = \sigma_1^z = \left(c_1 + c_1^\dagger\right) = \gamma_1 \tag{D.9}$$

$$W = \sigma_N^z = \prod_{j<N}\left(1 - 2c_j^\dagger c_j\right)\left(c_N + c_N^\dagger\right) = \mathbb{P}\left(c_N - c_N^\dagger\right) = i\mathbb{P}\gamma_2, \tag{D.10}$$

where $\mathbb{P} = \prod_j^N \left(1 - 2c_j^\dagger c_j\right)$ is the parity operator. Eqs. D.9-D.10 show the operator W in Ising, Dirac and Majorana bases, respectively. If we work with the operator Eq. (D.9),

$$\langle\psi_\alpha| f(h)\gamma_1\left(\frac{\gamma_1+i\gamma_2}{\sqrt{2}}\right)|\psi_\alpha\rangle = \frac{2f(h)}{\sqrt{2}}, \tag{D.11}$$

where we utilized $(\gamma_i)^2 = \mathbb{I}$ and $-i\gamma_1\gamma_2|\psi_\alpha\rangle = -|\psi_\alpha\rangle$ since $|\psi_\alpha\rangle$ is an odd-parity state. Similarly for Eq. (D.10),

$$if(h)\langle\psi_\alpha|\mathbb{P}\gamma_2\left(\frac{\gamma_1+i\gamma_2}{\sqrt{2}}\right)|\psi_\alpha\rangle = \frac{2f(h)}{\sqrt{2}}, \tag{D.12}$$

where we additionally use $\mathbb{P}|\psi_\alpha\rangle = -|\psi_\alpha\rangle$. Given each degenerate subspace contributes equally, we write $\bar{C} = 2f(h)^2$. A simple functional form of Eq. (5.13) is calculated as $\bar{C} = 1 - h^2$ for $h < J$ and $\bar{C} = 0$ for $h > J$ in Ref. [213]. We substitute this analytical result into Eq. (5.13) and obtain $W_{\alpha\beta} = \sqrt{1-h^2}$ for $h > J$ in the topologically non-trivial phase.

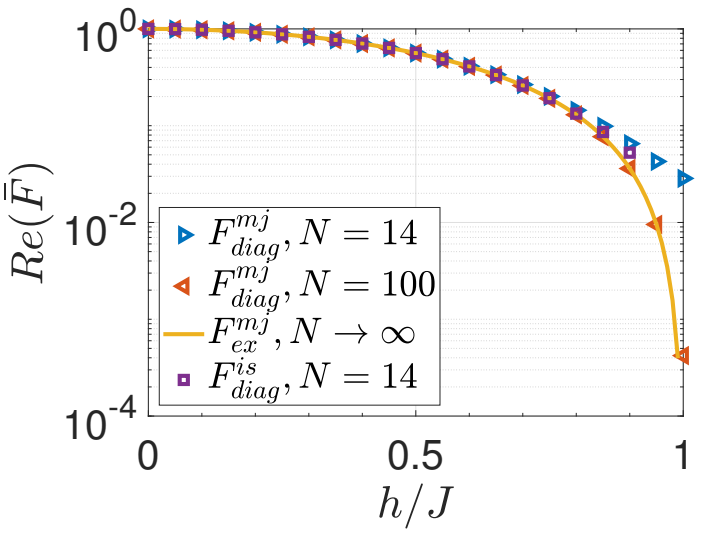

Figure D.1: Diagonal contribution in the Ising model and non-interacting fermionic model after dynamical decomposition is applied. Purple-circles show the diagonal contribution Eq. (5.12) at $N = 14$ in the Ising model (for a time interval $tJ = \frac{\pi}{4}10 \sim 7.85$), while the blue right-pointing triangles ($N = 14$) and red left-pointing triangles ($N = 100$) show Eq. (5.12) for H_{BdG} in non-interacting fermion system at infinite-time limit. The exact form is derived from the two-time correlators of Majorana fermions (solid-orange).

Hence we observe that the diagonal contribution of OTOC is a direct dynamical probe of topological order, giving a non-zero $F^{mj}_{\text{ex}} = (1 - h^2)^2$ in the non-trivial phase.

To demonstrate how $\bar{F}_{diag}$ of Ising model can match with Eq. (5.14) of non-interacting fermionic system whose calculation is purely based on Majorana zero modes, we plot Fig. D.1. Blue right-pointing triangles and orange left-pointing triangles show $\bar{F}^{mj}_{diag}$ numerically computed via Majorana zero modes from BdG Hamiltonian for system sizes of $N = 14$ and $N = 100$, respectively. Note that $\bar{F}^{is}_{diag}$ of the Ising model (purple-squares) computed at $N = 14$ for a time interval of $tJ \sim 8$ matches well with F^{mj}_{diag} at the same size, implying that F^{is}_{diag} could be used to detect the presence/absence of Majorana zero modes. The difference between $N = 14$ and $N = 100$ sizes of $\bar{F}^{mj}_{diag}$ shows how finite size effects show up near the transition point due to the divergent length scale associated with the quantum critical point. Additionally we compare $\bar{F}^{mj}_{diag}$ at $N = 100$ with the analytically derived result $\bar{F}^{mj}_{\text{ex}}$ that is denoted by solid-orange line in Fig. D.1 and observe that they match perfectly.

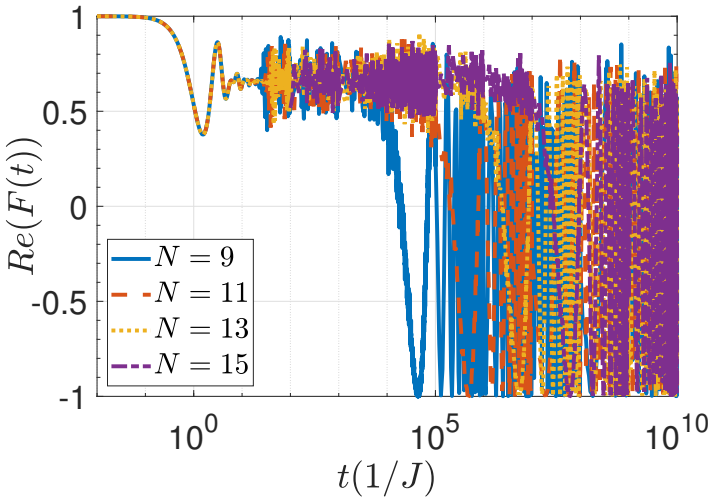

Figure D.2: Coherence time computation of the integrable Ising model deep in the non-trivial phase $h/J = 0.3$. The coherence times exhibit exponential increase with the system size which implies that prescrambling lasts indefinitely.

D.4 Further results on the Ising Model

Fig. D.2 shows that the prescrambling time-scale scales with the system size in the Ising model. Hence, in the thermodynamic limit, prescrambling continues to survive, giving a finite OTOC saturation (time-average) $\bar{F} \neq 0$ at the infinite-time limit.

Fig. D.3 shows the system-size scaling of fermionic OTOC time-average at the phase transition point that is also determined by OTOC itself. The scaling parameters of the phase transition point was already given in the main text. Here we provide the scaling parameters of the OTOC amplitude with respect to system size: $F^{\infty} \sim N^{-1.5452} - 1$, meaning the OTOC in thermodynamic limit should saturate at $F^{\infty} = -1$ in the transition point.

Now we explicitly demonstrate how operator ansatz is satisfied or violated in the integrable Ising model. For this, we plot the matrix elements $|V_{\beta\alpha}|^2$ for various β in the spectrum at different h values in Fig. D.4. Note that $|\psi_\beta\rangle$ and $|\psi_\alpha\rangle$ in $|V_{\beta\alpha}|^2$ denote states sorted according to their energies.

The first two subfigures (a)-(b) are for an edge spin operator σ_1^z, whereas the rest (c)-(d) are for a bulk spin operator. We sample the ground state (a)-(c) and a state in the middle

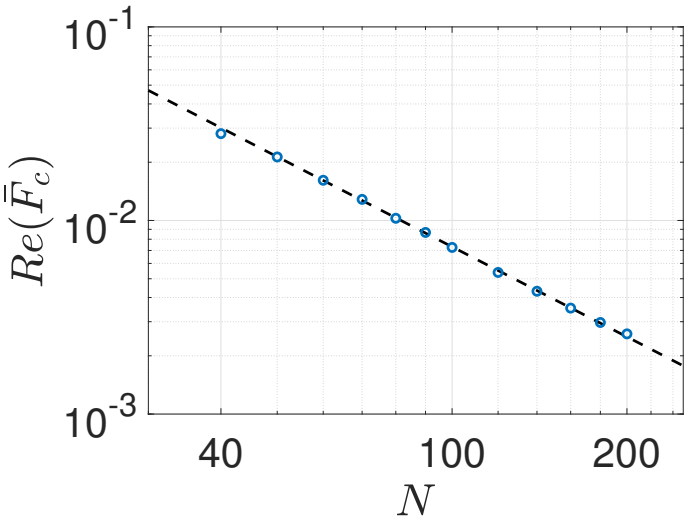

Figure D.3: The scaling of OTOC, F with the system size N at the transition point determined by the second derivative of the OTOC (see main text). The scaling parameters are: $F^{\infty} \sim N^{-1.5452} - 1$ with $R^2 = 0.9994$.

of the spectrum (b)-(d) in these subfigures. Deep in the topologically non-trivial phase, $h/J = 0.1$, we see that the operator ansatz is satisfied $|V_{E_\alpha = E_\beta}|^2 \gg |V_{E_\alpha \neq E_\beta}|^2$ for an edge spin (blue-circles). For a bulk spin, the operator ansatz is valid only in the ground state subspace with $E_\alpha = E_{gs}$, the condition put forward by Chapter 4 for the dynamical detection of symmetry-breaking phase transitions via OTOCs. This is how the edge spins preserve the topological order in the OTOC throughout the spectrum, while the bulk spins can preserve only the symmetry-breaking order. Closer to the transition point, e.g. $h/J = 0.8$, the order $|V_{E_\alpha = E_\beta}|^2$, expectantly, decreases while the off-diagonal elements $|V_{E_\alpha \neq E_\beta}|^2$ grow, which is a signature of integrability at this special non-interacting limit. Hence the operator ansatz, still in the topologically non-trivial phase, breaks down explaining how the OTOC saturation starts to be dominated by off-diagonal contribution (Fig. 3.8b where $\bar{F} \neq \bar{F}_{diag}$ in the non-trivial phase). Note that this breakdown of the operator ansatz in the ordered phase does not happen for the bulk spin that is in its ground state, Fig. D.4c. The operator ansatz in the topologically trivial phase, e.g. $h/J = 1.5$, continues to fail (compare orange-diamonds with blue-circles in Figs. D.4a-D.4b). Eventually this causes a non-vanishing OTOC time-

average $\bar{F} \neq 0$ in the trivial phase, even though this time average value has nothing to do with topological order (Sec. 5.3.2).

D.5 Further results on the nonintegrable Ising models

We first compare the scrambling dynamics of edge (red-solid) and bulk (blue-dotted) spins in real time, Fig. D.5 in the regimes of near-integrability $\Delta/J = -0.1$ and far from integrability $\Delta/J = -0.5$. The edge and bulk spins behave drastically different for significantly long times, even though the size is considerably small, $N = 14$. Hence, we can still observe the effect of zero modes in nonintegrable models, however as discussed in the main text, in a weaker form than in integrable models.

Now we plot a dynamic phase diagram for a bulk spin in Figs. D.6-D.7 and observe it is drastically different than of an edge spin: as we increase the system size, both $\bar{F}$ and $\bar{F}_{diag}$ approach to zero for all h, and hence gets even farther away from the transition point. Figs. D.6 and D.7 show the OTOC of bulk spins in the models with $\Delta/J = -0.1$ and $\Delta/J = -0.5$, respectively.

The coherence times of the edge spins at $\Delta/J = -2$ deep in the non-trivial phase (Fig. D.8a) exhibit exponential increase with the system size in Fig. D.8b up to an apparent odd-even effect. All different scaling samples collapse at around $\xi \sim 1$ for the exponent of the exponential scaling. While it is highly expected that this increase should slow down with bigger system sizes, based on our available data we cannot state that this behaviour is an example of prescrambling, instead it looks like a finite-size effect up until $N = 15$ system size. Hence it is not always easy to extract a curve collapse to demonstrate prescrambling in systems with small sizes.

Fig. D.9 demonstrates the dependence of a dynamic phase diagram on the interval of time averaging. The data is for the model at near-integrability. The result with blue-circles that is computed in a short time interval of $tJ = 10$ converges to the OTOC of non-interacting limit,

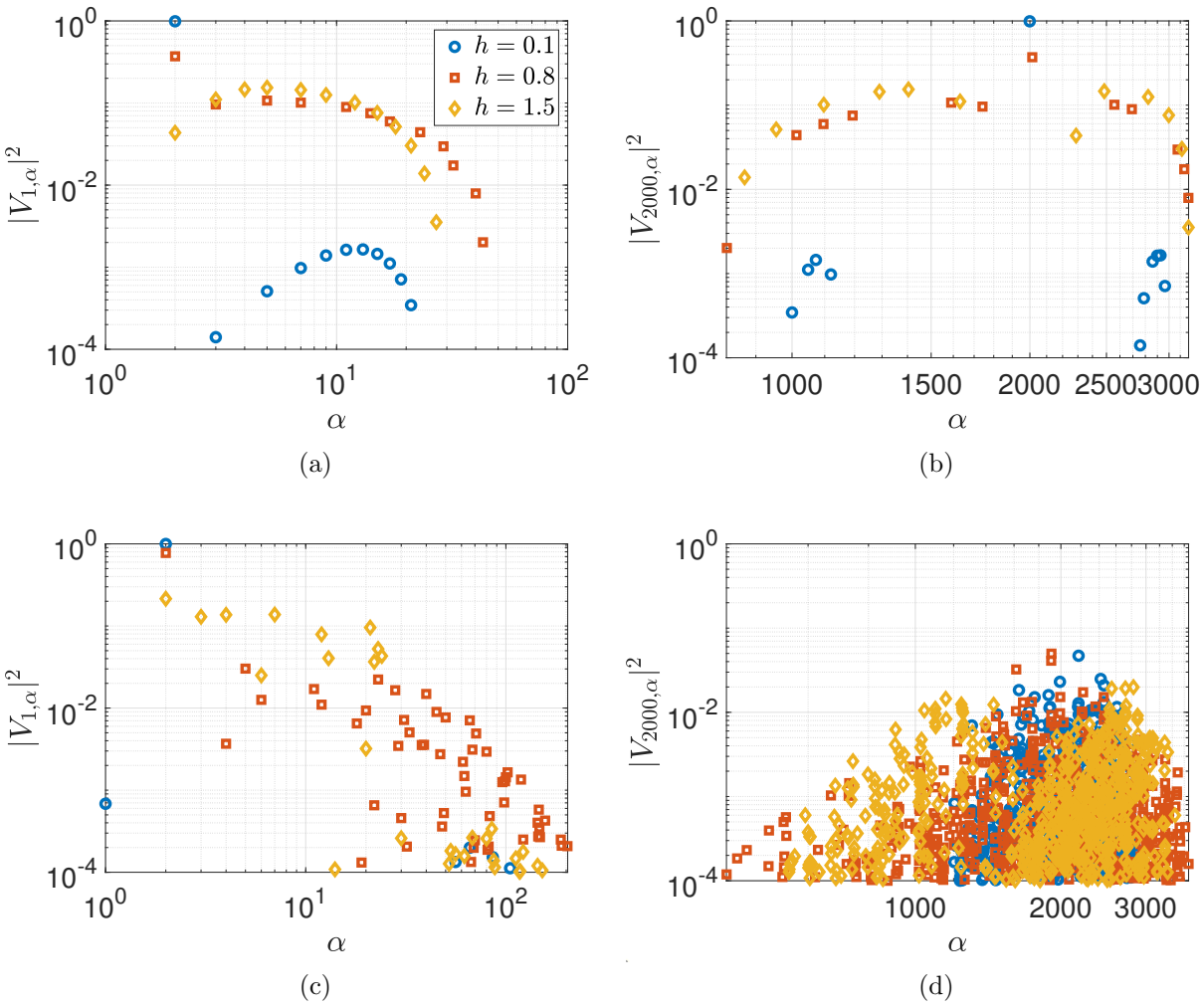

Figure D.4: The operator ansatz tested on the Ising model. Matrix elements $|V_{\beta\alpha}|^2$ are plotted for (a) $\beta = 1$ (b) $\beta = 2000$ with respect to α for an edge operator σ_1^z (open boundary); same β (c)-(d) for a bulk operator (periodic boundary) at a size $N = 12$. Blue-circles, red-squares and orange-diamonds stand for field strength $h/J = 0.1$, $h/J = 0.8$ and $h/J = 1.5$, respectively for all subfigures.

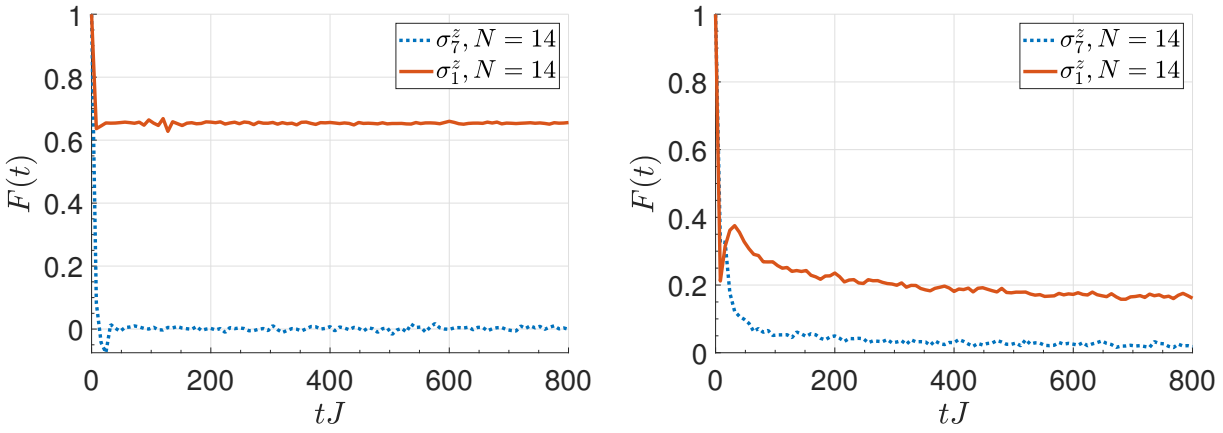

Figure D.5: Real time dynamics of OTOC with both edge (red-solid) and bulk (blue-dotted) spins in nonintegrable transverse-field Ising model at $h/J = 0.3$ for (a) $\Delta/J = -0.1$ and (b) $\Delta/J = -0.5$ with size $N = 14$.

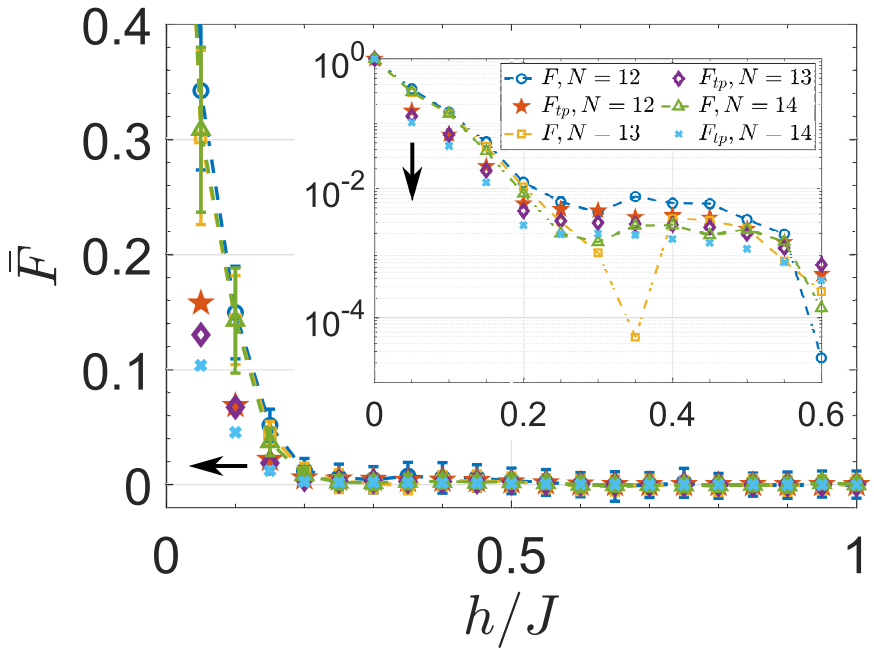

Figure D.6: Nonintegrable transverse-field Ising model. OTOC time-average of bulk spins in small integrability breaking term $\Delta/J = -0.1$ in linear and logarithmic (inset) scales. Red pentagrams, purple diamonds and light-blue crosses show $\bar{F}_{diag}$ whereas the blue circles, yellow squares and green triangles show $\bar{F}$ for $N = 12$, $N = 13$ and $N = 14$, respectively. All curves have open boundary conditions and a time interval of $tJ \sim 800$.

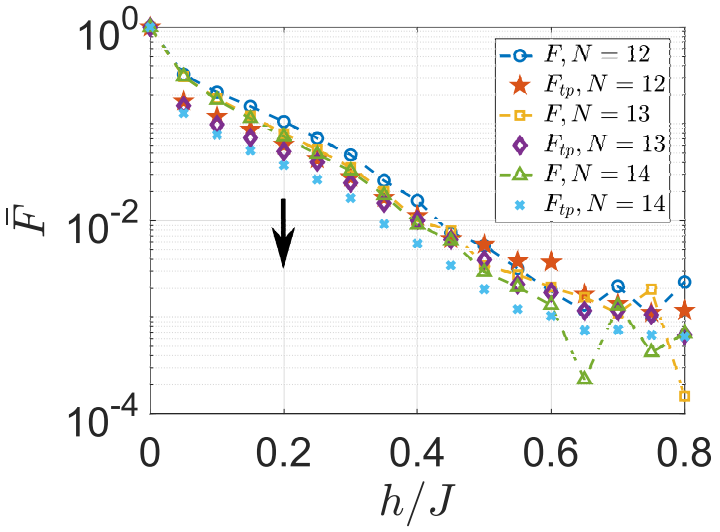

Figure D.7: The OTOC time-average of bulk spins in the case of $\Delta/J = -0.5$ integrability breaking term. $\bar{F}$ and $\bar{F}_{diag}$ for $N = 12$ (blue-circles and red-pentagrams), $N = 13$ (yellow-squares and purple-diamonds) and $N = 14$ (green-triangles and light-blue crosses). All curves have open boundary conditions and a time interval of $tJ \sim 800$.

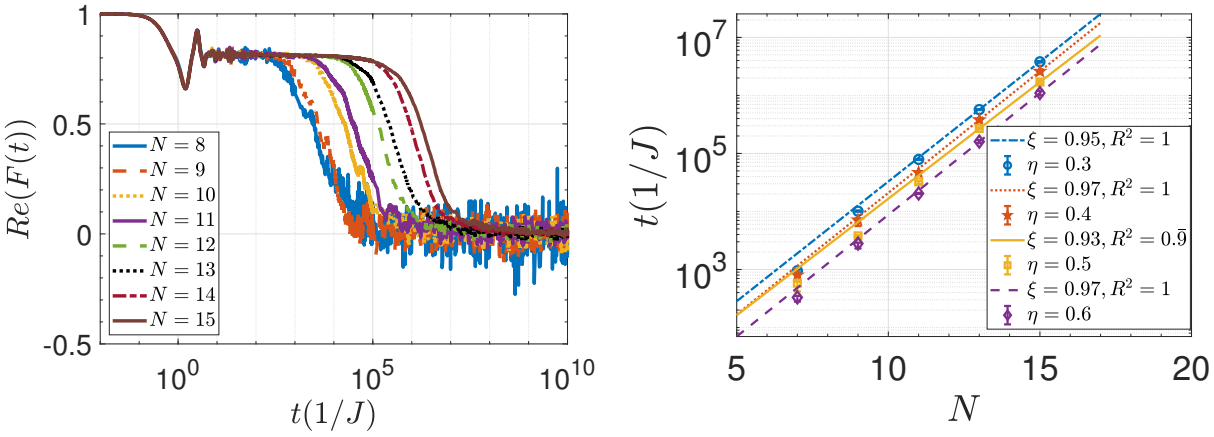

(a) (b)

Figure D.8: (a) Coherence times of the edge spins based on OTOC at $\Delta/J = -2$, deep in the topologically non-trivial phase $h/J = 0.3$ and (b) the system-size scaling of the coherence times in (a). Note that different curves correspond to different threshold values η where we look for the times that provide $F(t) = \eta$. ξ is the exponent in the exponential scaling and all of them are around $\xi \sim 1$.

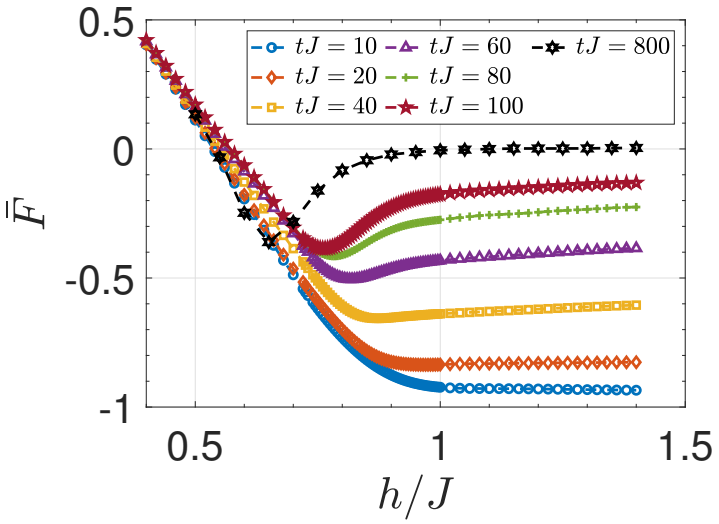

Figure D.9: Demonstration of the time-dependence of the phase diagram for the model with $\Delta/J = -0.1$ at $N = 14$ system size. Blue circles, orange diamonds, yellow squares, purple triangles, green pluses, red pentagrams and black hexagrams stand for $tJ = 10, 20, 40, 60, 80, 100, 800$, respectively.

while increasing the averaging time from $tJ = 10$ to later times causes the phase diagram to change significantly. Hence in the short-time limit, the coherence times of the prescrambling plateau are significantly contributed not only by the diagonal contribution, but also the off-diagonal contribution. This additional contribution, that is specific to OTOC, in fact survives until very long times, e.g. $t \gtrsim 2 \times 10^3$ (Fig. 5.8b in main text). However, farther away from the non-interacting limit the off-diagonal contribution vanishes faster, whereas the diagonal contribution remains for longer times.

We mark the ground state phase transition point in the model with $\Delta/J = -2$ via (i) minimizing the energy gap at the transition point; and (ii) Binder cumulant. We first present (i): The scaling parameters for the transition point read $h_c \sim N^{-1.2467} + 3.7746$ where the transition point in the thermodynamic limit is found $h_c^{\infty} = 3.7746$ with $R^2 = 0.9997$. The scaling parameters for the energy gap read $\Delta E \sim N^{-0.9775}$ with $R^2 = 0.9999$. So the system-size scaling exponent for the energy gap is close to -1. See Figs. D.10 for the scaling figures.

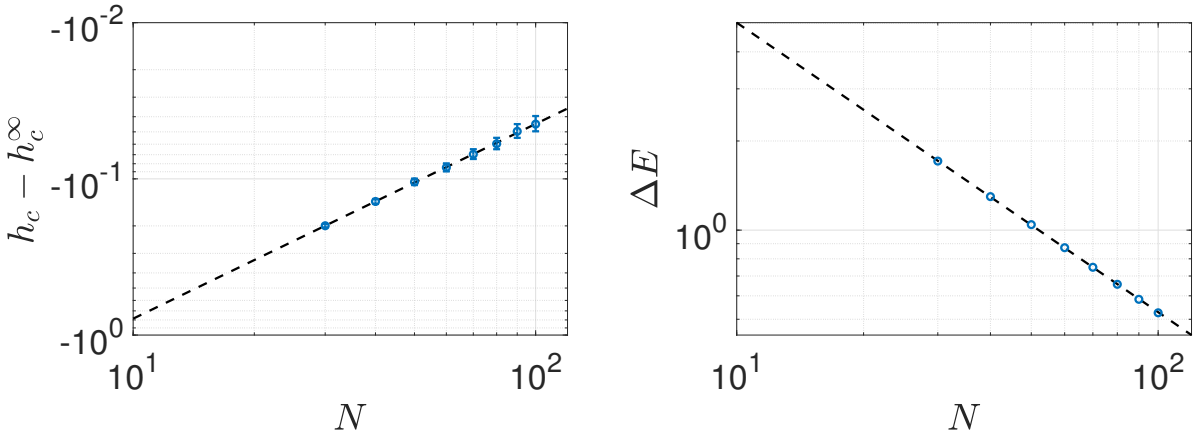

(a) (b)

Figure D.10: The scaling parameters for the ground state phase transition of the model with $\Delta/J = -2$, calculated via DMRG. (a) The system-size scaling of the critical point, giving $h_c^\infty = 3.7746$ in the thermodynamic limit. (b) The system-size scaling of the energy gap, giving an exponent of ~ -1 and showing that the gap closes in the thermodynamic limit.

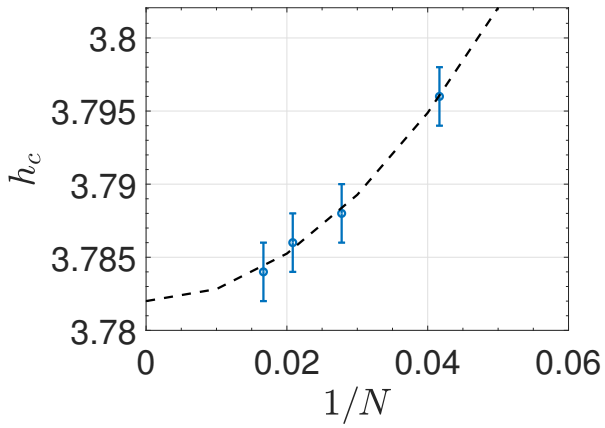

Figure D.11: The Binder cumulant calculated for the Ising model with $\Delta/J = -2$. The system size scaling gives $h_c^\infty = 3.782$.

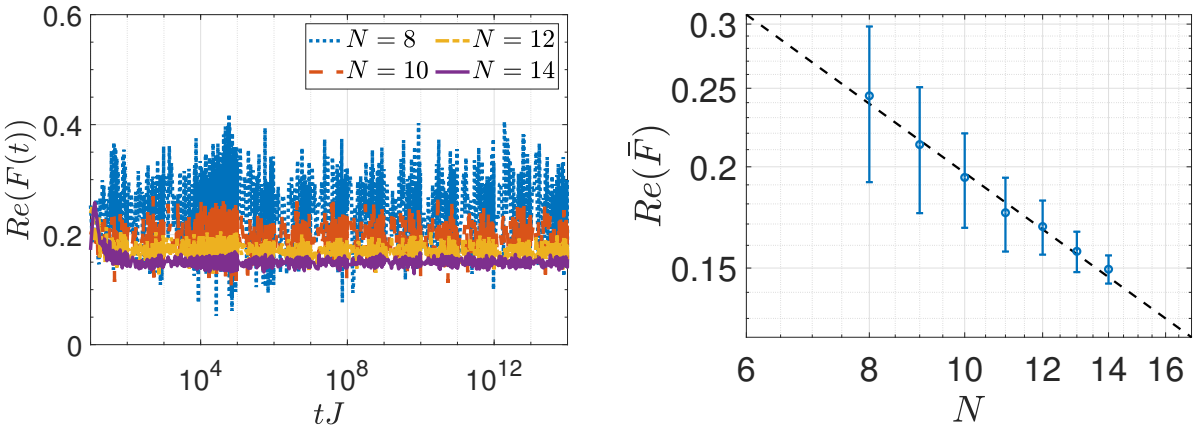

(a) (b)

Figure D.12: (a) The saturation value for long times and different system sizes ($N = 8$ to $N = 14$) are plotted for the gapless phase of the XXZ model. (b) The system size scaling of the saturation value where the error bars show the extend of the oscillations around the average of the signals in (a). The scaling has a form of $Re(\bar{F}) \propto N^{-\xi}$ where $\xi \sim 0.9$.

(ii) Fig. D.11 shows the system size scaling of Binder cumulant,

$$U = \frac{3}{2}\left(1 - \frac{1}{3}\frac{\langle S_z^4 \rangle}{\langle S_z^2 \rangle^2}\right), \tag{D.13}$$

where $S_z = \sum_i^N \sigma_i^z$, the total magnetization operator. This method marks the phase boundary as $h_c^\infty = 3.782$.

D.6 Further results on the XXZ model

Fig. D.12 shows long-time dynamics of OTOC in the gapless phase of the XXZ model and how the time-average of this signal scales with the system size. We see the scaling has a form of $Re(\bar{F}) \propto N^{-\xi}$ where $\xi \sim 0.9$. Hence in the thermodynamic limit we expect $\bar{F} \to 0$ in the gapless phase.

Fig. D.13 shows prescrambling time scales exponentially increase with the system size, a similar figure to Fig. 5.8d in the main text, however much closer to the transition boundary. The exponential increase in system size implies that the scrambling is a finite-size effect,

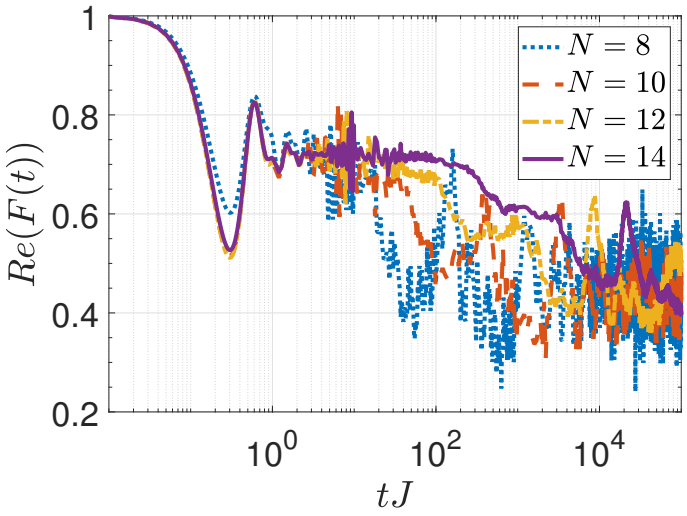

Figure D.13: The coherence times of prescrambling in the gapped phase of the XXZ model, $J_z/J = 5$ for different system sizes. The exponential increase in the prescrambling time intervals with the system size suggests that the scrambling seen is a finite-size effect.

hence in thermodynamic limit, prescrambling plateau should persist, giving $\bar{F} \neq 0$ in the topologically non-trivial gapped phase.

Appendix E

Probing Criticality in the Transient Quench Dynamics

E.1 Observation of Dynamical Quantum Phase Transitions in a Spinor Condensate

The following experimental procedure is followed by the experimentalists in Ref. [221]. They produce a spin-1 BEC of 1.3×10^5 sodium atoms via an all-optical procedure similar to Ref. [370]. A longitudinal polar (LP) state, c.f. Sec. 1.1.2, with $\overline{\rho_0} = 1$ is chosen as the initial state, because it is the ground state of the model Hamiltonian at $q_i/h = 42.3$ Hz with h being the Planck constant. To fully polarize atoms to $|F = 1, m_F = 0\rangle$ state, they hold the BEC under a large magnetic field gradient for 5 ms to eliminate the $|m_F = \pm 1\rangle$ atoms [371]. They then slowly turn off the gradient in 50 ms and hold the atoms for another 300 ms to sufficiently equilibrate the system. This method efficiently produces an LP state of up to 1×10^5 atoms.

A DPT is observed after a sudden quench of the quadratic Zeeman energy q. Similar to Ref. [250, 372, 373], they tune q via a microwave dressing field, i.e. $q = q_B + q_M$ with q_B (q_M) representing the quadratic Zeeman energy induced by a magnetic field (a microwave dressing

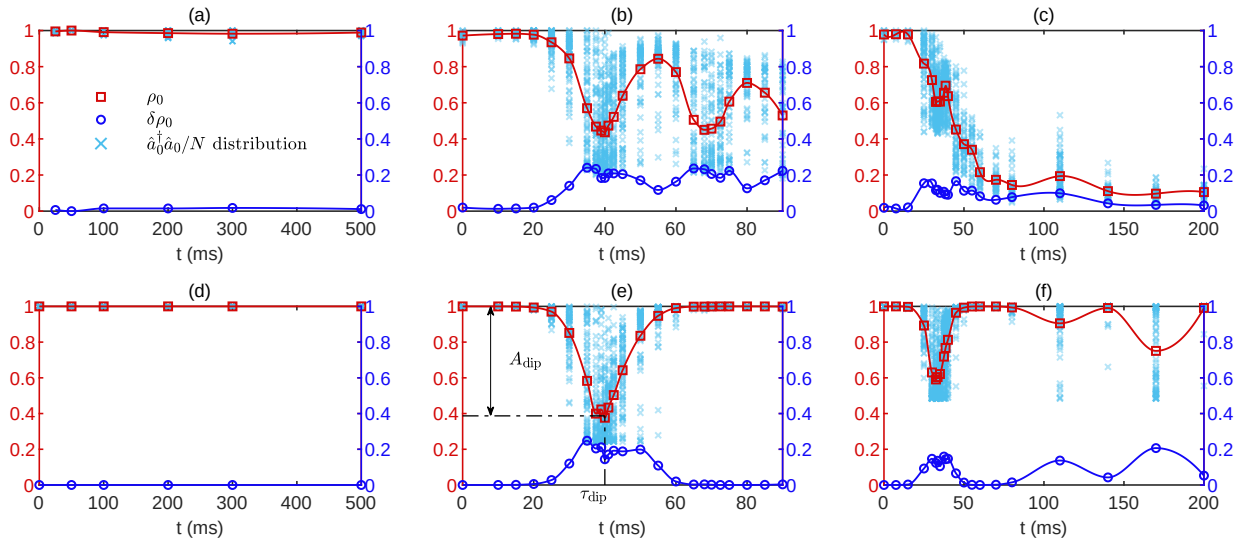

Figure E.1: Quench dynamics of $\overline{\rho_0}$ in the lab and the corresponding theoretical predictions derived from numerical simulations of the quench dynamics at three different q_f/c_1 (see text). Panels (a), (b), and (c) represent the experimental results at $c_1/h = 31\,\mathrm{Hz}$ and $q_f/c_1 = 0.65$, -0.48, and -0.97, respectively. Panels (d), (e), and (f) correspond to numerical simulations at $q_f/c_1 = 0.65$, -0.48, and -0.97, respectively. They repeat the experiments and simulations 80 times under each condition. The crosses on the background show the measurement results from these repeated experiments (upper panel) or Monte Carlo simulations (lower panel). The squares denote the average value $\overline{\rho_0}(t)$ from these 80 measurements and the circles denote the corresponding standard deviations.

field). The value of q_B is always positive for antiferromagnetic spin-1 sodium BECs, while q_M can be tuned to any value from $-\infty$ to $+\infty$ by changing the frequency or the intensity of the applied microwave pulses [372].

To probe quench dynamic after the initial LP state preparation at q_i in a fixed magnetic field, they suddenly turn on a microwave dressing field to abruptly change q_i to $q_f = q_i + q_M$. After holding the spinor gas at q_f for a given time t, they measure the fractional populations ρ_{m_F} via the standard Stern-Gerlach absorption imaging technique. To experimentally determine $\overline{\rho_0}(t)$, they repeat the same experiments 80 times and measure the entire evolution $\rho_0(t)$ for every realization. The time evolution of ρ_0 from each of these 80 repeated experiments, as well as their mean value $\overline{\rho_0}(t)$ and the standard deviations $\delta\rho_0(t)$ are shown in Figs. E.1(a-c) for three typical q_f. Note that the large variation of the observed ρ_0 at certain q_f and t for different rounds of experiments is not due to the experimental imperfection, but it is an intrinsic feature of quench dynamics related to the DPT. At this q_f and t, the dynamical state is far from the ground state and involves a superposition of many eigenstates of the final Hamiltonian, so ρ_0 has large intrinsic quantum fluctuations. To put this experimental result into the context, they also numerically calculate the time evolution of the model Hamiltonian (6.2), and the corresponding results are shown in Figs. E.1(d-f). To compare theory and experiments, they show the theoretical distribution of ρ_0 under 80 repetitions of measurements using Monte Carlo sampling. Through numerically diagonalizing of the model Hamiltonian (6.2), they obtain theoretical probability distribution of ρ_0, labeled as $f(\rho_0)$ for some q_f and t. They numerically sample ρ_0 80 times based on $f(\rho_0)$. This operation mimics the experimental procedure.

The time evolution of $\overline{\rho_0}$ has qualitatively different behaviors in three different regions of q_f. When $q_f > 0$ as shown in Figs. E.1(a) and E.1(d), $\overline{\rho_0}(t)$ always stays very close to 1 with a negligible variation $\delta\rho_0(t)$. The experimental results appear to agree well with theory in this region. When q_f/c_1 is negative but not too small (Figs. E.1(b) and E.1(e)), $\overline{\rho_0}(t)$ begins to oscillate and the $\rho_0(t)$ distribution shows quite large fluctuations. The experimental results

coincide with the theoretical prediction in the short time region of $t \lesssim \tau_{\rm dip}$, but deviates significantly during the subsequent evolution. This can be attributed to the breakdown of the SMA for the atomic motional state: the atoms in this case are significantly in the excited states of the spin Hamiltonian and their energy can relax to the motional state through the spin-dependent collisions, and thus invalidate the prediction from the single mode Hamiltonian (6.2) in the long time dynamics. When q_f/c_1 becomes even more negative (Figs. E.1(c) and E.1(f)), although the theory based on Eq. (6.2) still predicts oscillations, the energy relaxation to the motional state dominates the measurement results. The spin state approaches the transverse polar state, c.f. Sec. 1.1.2, with $\overline{\rho_0} = 0$, the ground state of the Hamiltonian at this negative q_f, through the relaxation; and spin oscillations are barely visible in quench dynamics for this case. The above observations show that it is important to detect the DPT with short time probes, e.g. transient temporal regime, and keep q_f in a region not too far from the phase transition point at $q_c = 0$.

E.2 Dynamical crossover in the transient quench dynamics of short-range transverse field Ising models

E.2.1 Periodic vs. open boundaries

In this section, we demonstrate how the spin operator (longitudinal magnetization per site) in the middle of an open chain exhibits exponential decay comparable with a spin operator at an arbitrary site in a periodic chain. Fig. E.2 compares the nonequilibrium responses of these two spins and as observed, the responses match with each other until the finite-size effects appear. This is reasonable, because a spin in the middle of the chain is equally distant to both edges, and hence it should exhibit behavior closest to a spin in a periodic chain. Therefore, based on this equivalence we can argue that the middle spin of an open chain behaves similar to total magnetization in exhibiting an exponential decay. This is simply

because the total magnetization is a sum over all spin operators σ_i^z.

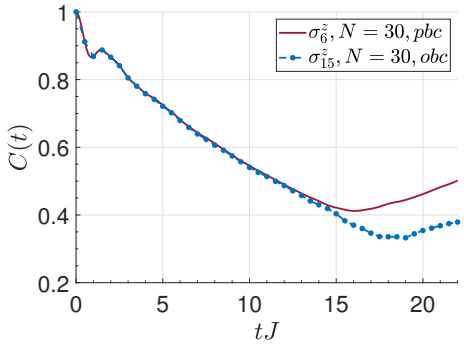

Figure E.2: $C(t)$ nonequilibrium response of the middle spin of an open chain $N = 30$, σ_{15}^z (blue-dotted) and a spin at an arbitrary location σ_6^z in a periodic chain $N = 30$ (red-solid).

E.2.2 Mapping to noninteracting fermions in quench dynamics

We map the integrable TFIM to noninteracting fermionic model in 1D via the transformation [193] as also discussed in Chapter 5,

$$\begin{aligned} \sigma_i^z &= -\prod_{j<i}\left(1-2c_j^\dagger c_j\right)\left(c_i+c_i^\dagger\right), \\ \sigma_i^x &= 1-2c_i^\dagger c_i, \\ \sigma_i^y &= -i\prod_{j<i}\left(1-2c_j^\dagger c_j\right)\left(c_i-c_i^\dagger\right), \end{aligned} \tag{E.1}$$

to obtain the noninteracting Hamiltonian

$$H = -J\sum_i\left(c_i^\dagger c_{i+1}+c_{i+1}^\dagger c_i+c_i^\dagger c_{i+1}^\dagger+c_{i+1}c_i-2hc_i^\dagger c_i\right). \tag{E.2}$$

One can immediately see that calculating the dynamical evolution of a bulk spin $\langle\sigma_i^z(t)\rangle$ in the noninteracting picture brings a string of operators and is not really tractable. Hence we

instead calculate equal-time two-point correlators and invoke the cluster theorem [116],

$$\left\langle \sigma_i^z(t)\sigma_{i+N/2}^z(t)\right\rangle \sim \left\langle \sigma_i^z(t)\right\rangle \left\langle \sigma_{i+N/2}^z(t)\right\rangle . \tag{E.3}$$

Cluster theorem holds in the lightcone, meaning for a time interval up until two sites i and $i+N/2$ start getting correlated with each other due to operator spreading. The time when the theorem breaks down can be estimated based on the maximum quasiparticle velocities v_q, $t < \Delta x/(2v_q)$ where $\Delta x = N/2$ is the distance between two spins that are selected symmetrically around the symmetry center of a periodic chain in Eq. (E.3). Since each site in a periodic chain experiences identical dynamical response due to translational symmetry, one can write

$$\langle \sigma_i^z(t)\rangle = \sqrt{\left\langle \sigma_i^z(t)\sigma_{i+N/2}^z(t)\right\rangle}. \tag{E.4}$$

Therefore, we need to calculate equal-time two-point correlators. Via introducing auxiliary operators $\Phi_i^{\pm} = c_i^{\dagger} \pm c_i$, one can write

$$\left\langle \sigma_i^z(t)\sigma_{i+N/2}^z(t)\right\rangle = \langle C_2(t)\rangle = \phi_i^-(t)\left(\prod_{j=i+1}^{i+N/2-1}\phi_j^+(t)\phi_j^-(t)\right)\ \phi_{i+N/2}^+(t). \tag{E.5}$$

This is, in fact, the expectation value of the so-called string order parameter (SOP) [315]. It can be calculated by invoking Wick's theorem, which allows one to re-express the above expectation value as a sum over products of elementary contractions, which in turn is the Pfaffian of an appropriately constructed antisymmetric matrix $T(t)$ i.e. $\langle C_2(t)\rangle = |\mathrm{Pf}(T(t))|$ [116, 193]. Although this is in general a complex number, it follows from (E.3) that for $t < t_l$ we actually have $(C(t))^2 \in \mathbb{R}$ so that we may compute $C(t) = |\mathrm{Pf}(T(t))|^{1/2} = |\sqrt{\det(T(t))}|^{1/2}$. This is advantageous since it is numerically more efficient to calculate determinants as compared to Pfaffians. To construct the matrix $T(t)$ we only need to calculate all possible elementary two-point contractions $\langle \phi_a^p(t)\phi_b^q(t)\rangle$ where

$p, q = \pm$ and $i \leq a \leq b \leq i + N/2$. Additionally we need to incorporate the mechanism of sudden quench in this picture. For this, we mainly follow the procedure outlined in Ref. [211]. Let us briefly review this procedure here.

Since we would like to quench from a polarized state, this quench point corresponds to $h_i = 0$ where h_i is the transverse field of the initial Hamiltonian in quench procedure. Therefore, we first solve the initial Hamiltonian H_i,

$$H_i = \sum_k E_k^i \alpha_k^\dagger \alpha_k, \tag{E.6}$$

where E_k and α_k are the single particle eigenenergies and eigenstates, respectively. The solution reads in general terms,

$$\begin{pmatrix} \alpha \\ \alpha^\dagger \end{pmatrix} = \begin{pmatrix} G_i & F_i \\ F_i & G_i \end{pmatrix} \begin{pmatrix} c_i \\ c_i^\dagger \end{pmatrix}, \tag{E.7}$$

where $c_i = (c_1, c_2, \cdots, c_N)^T$ and similarly for the creation operator $c_i^\dagger$. Note that one can work in this Bogoliubov-de Gennes (BdG) basis with the size doubled similar to Chapter 5, however here we work with the block matrices G and F [374] which is computationally more efficient. By solving the eigensystem of

$$[(A_i - B_i)(A_i + B_i)] \left|\Phi_k^i\right\rangle = (E_k^i)^2 \left|\Phi_k^i\right\rangle, \tag{E.8}$$

we obtain the eigenenergies E_k^i and eigenvectors $|\Phi_k^i\rangle$. Here A_i and B_i are the nearest neighbor hopping and the pairing terms in the Hamiltonian, respectively, so that the Hamiltonian could be written as,

$$H_i = \begin{pmatrix} A_i & B_i \\ B_i^\dagger & -A_i \end{pmatrix}, \tag{E.9}$$

in $(c\, c^\dagger)^T$ basis. Then we use the eigensystem $(E_k^i, |\Phi_k^i\rangle)$ to find

$$\left|\Psi_k^i\right\rangle = \frac{1}{E_k^i}\left[\left\langle\Phi_k^i\right|(A_i - B_i)\right]^T. \tag{E.10}$$

Now we can calculate the G_i and F_i in terms of $|\Phi_k^i\rangle$ and $|\Psi_k^i\rangle$. Noting that

$$\begin{aligned}\Phi_i &= \left[\left|\Phi_1^i\right\rangle\ \left|\Phi_2^i\right\rangle\cdots\left|\Phi_N^i\right\rangle\right],\\ \Psi_i &= \left[\left|\Psi_1^i\right\rangle\ \left|\Psi_2^i\right\rangle\cdots\left|\Psi_N^i\right\rangle\right],\end{aligned}$$

The block matrices follow

$$G_i = \frac{1}{2}\left(\Phi_i^T + \Psi_i^T\right),\ F_i = \frac{1}{2}\left(\Phi_i^T - \Psi_i^T\right). \tag{E.11}$$

A similar procedure follows for the final Hamiltonian H_f with

$$\begin{pmatrix}\beta\\ \beta^\dagger\end{pmatrix} = \begin{pmatrix}G_f & F_f\\ F_f & G_f\end{pmatrix}\begin{pmatrix}c_f\\ c_f^\dagger\end{pmatrix}, \tag{E.12}$$

and corresponding Φ_f and Ψ_f. Based on the pairs of block matrices, we calculate the transfer matrices,

$$\begin{aligned}T_1 &= G_f G_i^T + F_f F_i^T,\\ T_2 &= G_f F_i^T + F_f G_i^T.\end{aligned}$$

Now we want to calculate the Pfaffian matrix elements, ${}_\alpha\langle\psi_0|\left[\phi_a^p\phi_b^q\right]_\beta|\psi_0\rangle_\alpha$ where subscripts imply in which basis we have the states and the operators. Since we would like to make use of $\alpha|\psi_0\rangle_\alpha = 0$, we write $[\phi_a^p\phi_b^q]_\beta$ in the α basis.

$$\left[\phi_b^\pm\right]_\beta|\psi_0\rangle_\alpha \;=\; \left[c_b^\dagger(t) \pm c_b(t)\right]_\beta|\psi_0\rangle_\alpha = \left[\left(G_f^T \pm F_f^T\right)\left(e^{i\mathcal{E}t}T_1 \pm e^{-i\mathcal{E}t}T_2\right)\alpha^\dagger\right]_b|\psi_0\rangle_\alpha,$$

where $\mathcal{E}$ is a diagonal matrix with eigenenergies of the final Hamiltonian as the entries, $\mathcal{E} = \text{diag}[E_1^f\ E_2^f \cdots E_N^f]$. Based on this formulation, we construct matrices $\mathcal{M}_q(t)$ in an explicit form,

$$\begin{aligned} \mathcal{M}_+(t) &= \Phi_f \left(e^{-i\mathcal{E}t} T_1 + e^{i\mathcal{E}t} T_2\right), \\ \mathcal{M}_-(t) &= \left(T_1^T e^{i\mathcal{E}t} - T_2^T e^{-i\mathcal{E}t}\right) \Psi_f^T, \end{aligned} \tag{E.13}$$

to utilize in the following contractions,

$$\begin{aligned} \left\langle \phi_a^+(t)\phi_b^+(t)\right\rangle &= [\mathcal{M}_+(t)\mathcal{M}_+(t)^\dagger]_{ab}, \\ \left\langle \phi_a^-(t)\phi_b^-(t)\right\rangle &= -[\mathcal{M}_-^\dagger(t)\mathcal{M}_-(t)]_{ab}, \\ \left\langle \phi_a^+(t)\phi_b^-(t)\right\rangle &= [\mathcal{M}_+(t)\mathcal{M}_-(t)]_{ab}, \\ \left\langle \phi_a^-(t)\phi_b^+(t)\right\rangle &= -[\mathcal{M}_-^\dagger(t)\mathcal{M}_+^\dagger(t)]_{ab}. \end{aligned} \tag{E.14}$$

Now we can construct the Pfaffian matrix $T(t)$ at time t with the matrix elements $T_{ks}(t) = \langle \phi_a^p(t)\phi_b^q(t)\rangle$ where $1 \le k < s \le 2\Delta x$, $p = +(-)$ for k even(odd) and $q = +(-)$ for s even(odd). The relation between parameters a, b and k, s reads $a = i + \lfloor k/2 \rfloor$ and $b = i + \lfloor s/2 \rfloor$, because $i \le a \le b \le i + N/2$. Having constructed $T(t)$, one can then extract $\langle C(t)\rangle = |\sqrt{\det T(t)}|^{1/2}$, as discussed below Eq. (E.5).

E.2.3 Vanishing dynamical order for one-point observables

Here we compare the nonequilibrium responses of a one-point observable and an OTOC, defined at the same site, middle of an open chain and quenched from a polarized state $|\psi_0\rangle = |\uparrow\uparrow \ldots \uparrow\rangle$. OTOC is defined as, $F(t) = \langle\psi_0|\, \sigma_r^z(t)\sigma_r^z\sigma_r^z(t)\sigma_r^z\, |\psi_0\rangle$.

Fig. E.3a compares $F(t)$ and $C(t)$ for different system sizes N computed via time-dependent density matrix renormalization group (t-DMRG) at transverse field $h/J = 0.5$ in a time interval of $t = N$. When we apply a temporal cutoff of $t = N$, for OTOC, we

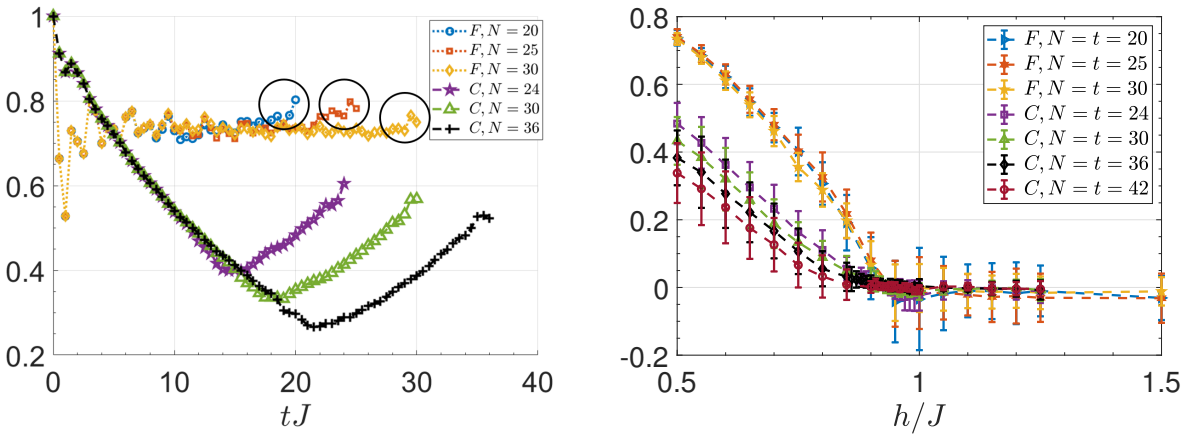

(a) (b)

Figure E.3: (a) Single-site observable $C(t)$ and OTOC $F(t)$, both defined at a single site, for different system sizes N for integrable TFIM at $h/J = 0.5$; (b) A system-size dependent temporal cutoff is applied to $C(t)$ and $F(t)$ for a time interval of $t = N$ resulting in $\bar{C}$ and $\bar{F}$ with respect to control parameter h/J.

observe that the dynamical order persists indefinitely resulting in a well-defined dynamical phase boundary for the time-average or long-time saturation value $\bar{F}$ in Fig. E.3b. Note that at $t \sim N$, $F(t)$ in Fig. E.3a starts to demonstrate finite-size effects, illustrated with black circles, which justifies the argument that $t \sim N$ is a sufficiently long-time limit $t \to \infty$ for chosen system sizes. With the same reasoning, one can plot $C(t)$ in a time interval of $t = N$ in Fig. E.3a and observe the decay of initial magnetization which dramatically becomes more pronounced as the system size increases, resulting in featureless long-time dynamics as well as a vanishing DPT-I boundary for $\bar{C}$ as seen in Fig. E.3b. The error bars in Fig. E.3b are 1σ standard deviation of the nonequilibrium response in time (due to oscillations) around the average of the response.

E.2.4 Comparison between fixed and parametric temporal cutoffs in the open chain

In this section, we plot the difference between rescaled observable values with different choices of temporal cutoffs: (i) fixed α and parametric $2\alpha/v_q$ (ii) two fixed cutoffs in integrable TFIM.

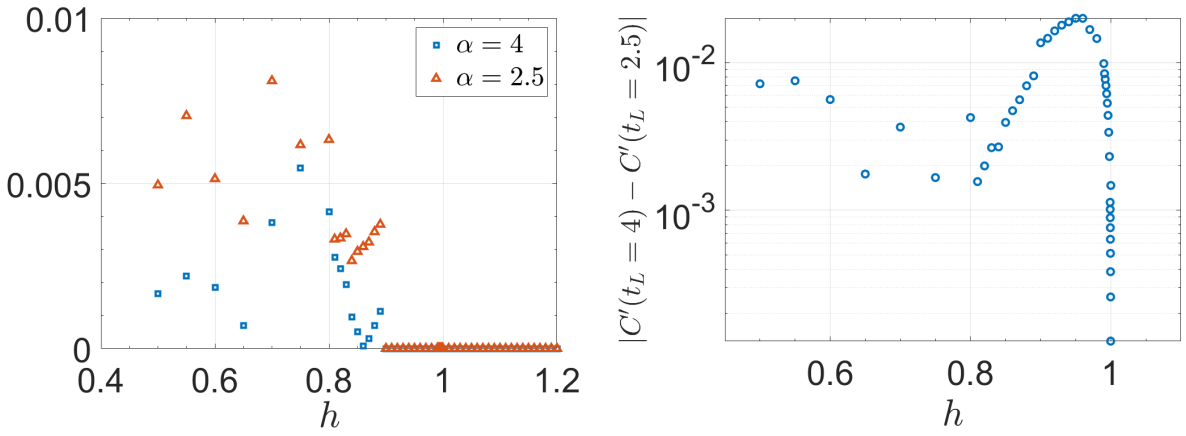

(a) (b)

Figure E.4: (a) The differences between rescaled observables with two different temporal cutoffs, parametric $2\alpha/v_q$ and fixed α for different α values (see legend). (b) The difference between the rescaled observables with two different fixed temporal cutoffs.

Even though these are clearly distinct temporal cutoffs, the differences are bounded for all h/J values in the dynamically-ordered regime and more importantly the differences steadily decrease as we approach the crossover boundary. Fig. E.4a demonstrates the differences between rescaled observable values generated with two types of temporal cutoffs for different α values. They are exactly zero in the vicinity of the crossover. This is likely because two types of temporal cutoffs converge to each other as we approach the crossover boundary. Fig. E.4b shows the difference between rescaled observable values for two fixed temporal cutoffs. In Fig. 7.2 in the main text, these differences seem to be the largest. Here we explicitly plot the difference and show that it steadily decreases as we approach the crossover boundary.

E.2.5 Equilibrium QPT for the nonintegrable TFIM

In this section, we present the equilibrium phase transition boundary via both an analysis of ground state energy gap and Binder ratio for the nonintegrable TFIM with $\Delta/J = -1$. Figs. E.5a-E.5b shows the determination of the phase boundary via energy gap analysis. We find that the equilibrium transition happens at $h_c \sim 2.463$ and the scaling exponent of the

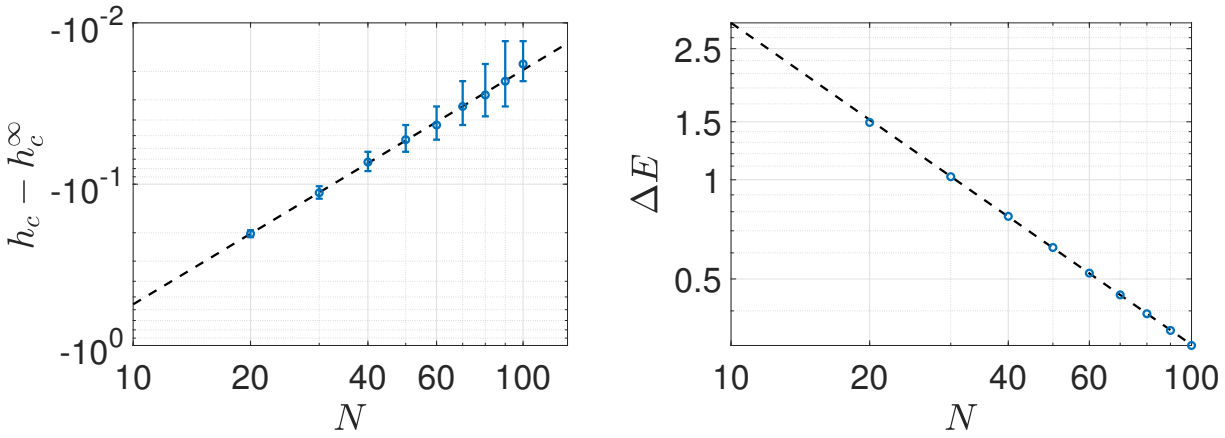

(a) (b)

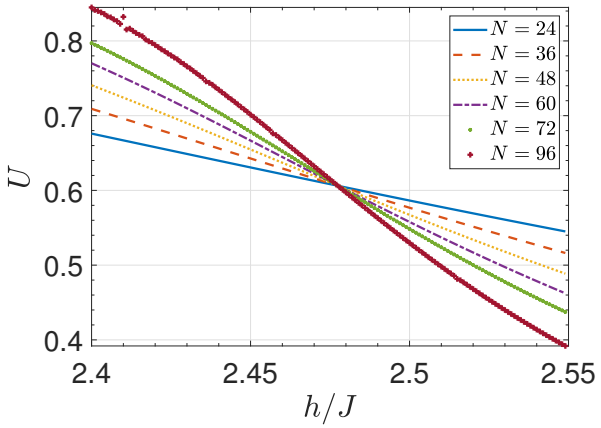

(c)

Figure E.5: (a-b) Ground state energy gap analysis with respect to system size N to determine the equilibrium QPT. (a) The critical point is marked as $h_c^\infty = 2.463$ in thermodynamic limit via scaling analysis. (b) Energy gap ΔE closes as we approach the QPT. The scaling exponent is $\Delta E = N^{-1}$. (c) Binder cumulant U for different system sizes ranging between $N = 24 - 96$, all crossing at $h_c^\infty = 2.477 \pm 0.001$.

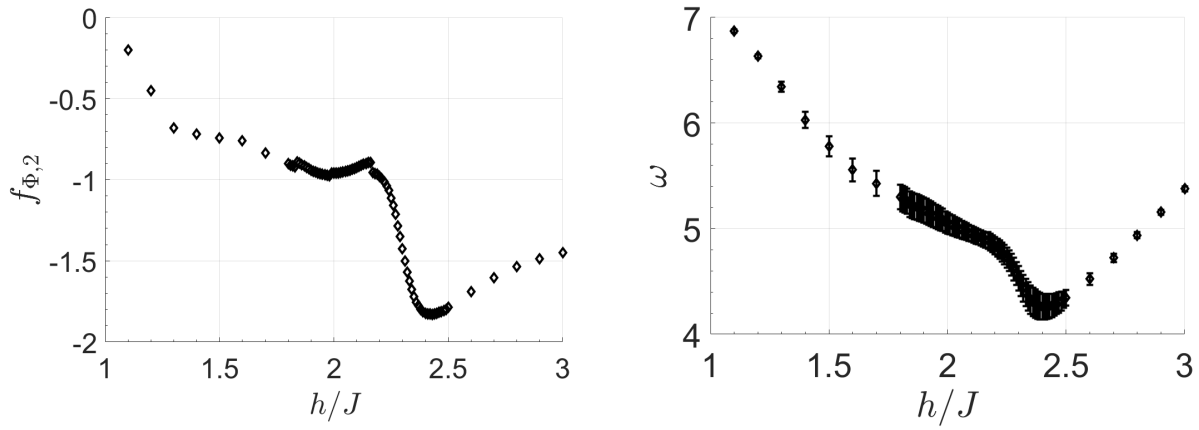

(a) (b)

Figure E.6: (a) The decay rate $f_{\Phi,2}$ and (b) the angular frequency ω of the fit function for the dynamics of nonintegrable TFIM at $\Delta/J = -1$.

energy gap closing is $\delta \sim -1$. Further, we compute the Binder cumulant in Fig. E.5c,

$$U = \frac{3}{2}\left(1 - \frac{1}{3}\frac{\langle S_z^4 \rangle}{\langle S_z^2 \rangle^2}\right), \tag{E.15}$$

where $S_z = \sum_i^N \sigma_i^z$, the total magnetization operator. This method marks the phase boundary as $h_c^\infty = 2.477 \pm 0.001$. The equilibrium transition points determined by these two different methods are very close.

E.2.6 Error bar calculations

The error bars in Figs. 6.9b, 6.9c and 6.13c are calculated via error propagation and in Figs. 7.3a, 6.11a and 6.13a, they are 1σ error bars computed via the confidence intervals of the fits. C_0 is fixed parameter in Eq. (6.9). In the case where one uses γ_1 parameter in the rescaling expression instead of $C(t^*)$ data, the free parameter γ_1 brings an uncertainty of $\Delta\gamma_1$ that can be computed via the confidence intervals of the fit. Based on the data points, one can have an uncertainty from t_L too: Δt denotes this uncertainty which is calculated as the difference between t_L and the available data point. Hence, we can calculate the propagation

of error as,

$$E^2 = \left(\frac{\partial \mathrm{OP}}{\partial t}\right)^2 (\Delta t)^2 + \left(\frac{\partial \mathrm{OP}}{\partial \gamma_1}\right)^2 (\Delta \gamma_1)^2, \tag{E.16}$$

where OP stands for rescaled observable, or in other words the dynamical OP-like quantity. Note that if one uses the rescaling method (i) for nonintegrable TFIM, additional terms should be added to the expression. The terms in the expression above reads

$$\begin{aligned} \frac{\partial \mathrm{OP}}{\partial \gamma_1} &= -\frac{C(t)^{1/t}}{t} \gamma_1^{-1/t-1}. \\ \frac{\partial \mathrm{OP}}{\partial t} &= -t^{-2} \left(\frac{C(t)}{\gamma_1}\right)^{1/t} \log\left(\frac{C(t)}{\gamma_1}\right). \end{aligned}$$

E.2.7 The rest of the fit parameters of the nonintegrable TFIM

In this appendix section, we plot the decay rate $f_{\Phi,2}$ and angular frequency ω with respect to h/J based on the fit function utilized for the nonintegrable TFIM. Fig. E.6 shows these fit parameters. Interestingly, both plots dip around $h/J \sim 2.41$. Whether these parameters could signal crossover physics is a question for future research.

Appendix F

Dynamical Criticality in the Quasi-Stationary Regimes

F.1 Methods

For the method on mapping to noninteracting fermions and how we utilize cluster theorem, see Appendix Sec. E.2.2. The only difference concerning the current Appendix is that we apply the method to open-boundary chains and spins close to boundaries, $r \ll N/2$. Therefore the cluster theorem reads [116],

$$\left\langle \sigma_r^z(t)\sigma_{N-r+1}^z(t)\right\rangle \sim \left\langle \sigma_r^z(t)\right\rangle \left\langle \sigma_{N-r+1}^z(t)\right\rangle . \tag{F.1}$$

Hence, the parameters read $t_l = \Delta x/(2v_q)$ where $\Delta x = N-2r+1$ is the distance between two spins that are equidistant from the symmetry center of an open-boundary chain in Eq. (F.1), which is the middle of the chain. For such symmetrically placed sites, the non-equilibrium response is the same and one can thus write

$$\left\langle \sigma_r^z(t)\right\rangle = \sqrt{\left\langle \sigma_r^z(t)\sigma_{N-r+1}^z(t)\right\rangle} \equiv \left\langle C_r(t)\right\rangle . \tag{F.2}$$

Therefore, we can extract the dynamical evolution of a bulk spin at site r from the equal-time two-point correlators of sites r and $N-r+1$.

F.1.1 Mean-field theory (MFT) Analysis

The next nearest-neighbor (NNN) term in the TFIM Hamiltonian reads in the fermionic picture as,

$$\begin{aligned} &= \Delta \sum_r \left(c_r - c_r^\dagger\right)\left(1 - 2c_{r+1}^\dagger c_{r+1}\right)\left(c_{r+2} + c_{r+2}^\dagger\right), \\ &= -\Delta \sum_r \left(c_r^\dagger - c_r\right)\left(1 - 2c_{r+1}^\dagger c_{r+1}\right)\left(c_{r+2} + c_{r+2}^\dagger\right), \\ &= -\Delta \sum_r \phi_r^- \phi_{r+1}^+ \phi_{r+1}^- \phi_{r+2}^+, \end{aligned} \tag{F.3}$$

where $\Delta < 0$ and $\phi_r^\pm$ stand for the auxiliary fermions of type-I or -II.

In Hartree-Fock expansion, we assume $|\Delta| \ll |J|$ where J is the nearest-neighbor coupling strength, and write Eq. (F.3) as

$$\begin{aligned} &= \Delta \sum_r \Big[\left\langle \phi_r^- \phi_{r+1}^+ \right\rangle_{t\to\infty} \phi_{r+1}^- \phi_{r+2}^+ + \phi_r^- \phi_{r+1}^+ \left\langle \phi_{r+1}^- \phi_{r+2}^+ \right\rangle_{t\to\infty} - \phi_r^- \left\langle \phi_{r+1}^+ \phi_{r+1}^- \right\rangle_{t\to\infty} \phi_{r+2}^+ \\ &- \left\langle \phi_r^- \phi_{r+2}^+ \right\rangle_{t\to\infty} \phi_{r+1}^+ \phi_{r+1}^- \Big]. \end{aligned} \tag{F.4}$$

Here the $\langle\cdot\rangle_{t\to\infty}$ means that we calculate the free fermion problem and obtain the correlators in the infinite-time limit (instead of ground state which would be for the static problem). In our numerics we treat the largest time point allowed by the cluster theorem as the asymptotically infinite time limit. The quench MFT formalism was previously applied to two-point correlators in a periodic chain [210]. Note that for an open-boundary chain, one needs to carefully take the edges of the chain into account based on Eq. (F.4). Using the above expansion, we obtain an effective mean field Hamiltonian which has slightly stronger nearest-neighbor (NN) coupling compared to the free problem, as well as new NNN cou-

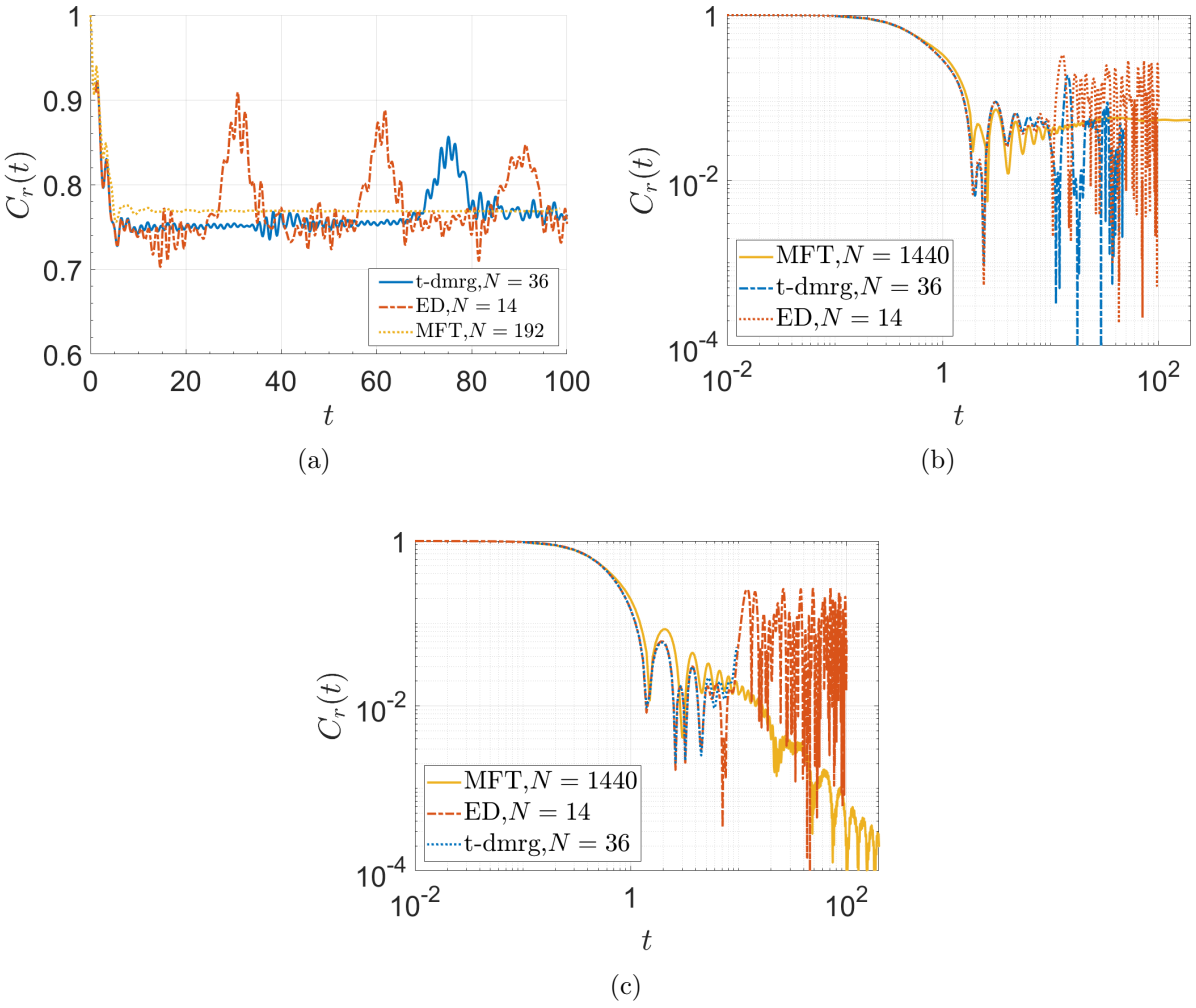

Figure F.1: Benchmarking mean field theory (MFT) analysis. All subfigures compare the results of MFT, t-DMRG and exact diagonalization (ED) results (see individual legends for system size information) for $C_{r=3}(t)$. The external fields are (a) $h = 0.5$, (b) $h = 1.1$ and (c) $h = 1.2$. In all, the MFT nonequilibrium response matches well with the nonequilibrium responses of the exact methods.

plings. Further, the effective chemical potential slightly decreases, which is reasonable when we think about how the critical point shifts to favor order, e.g. for $\Delta = -0.1$, $h_c \sim 1.16$ [210].

Based on these equations, we can calculate a quench phase diagram for the interacting problem in the mean field picture as shown in the main text. Fig. F.1 shows comparisons between MFT, t-DMRG and exact diagonalization (ED) results at different $h = 0.5$, $h = 1.1$ and $h = 1.2$, where the QCP is $h_c \sim 1.16$. We observe that the MFT analysis can even capture the correct frequency of the oscillations early times and the general trend of the nonequilibrium response successfully. However, MFT does not completely match with the exact methods, which is expected since MFT analysis is an approximate method that averages out the interactions.

F.1.2 t-DMRG calculations

We utilize the ITensor environment [300] to construct our matrix product states (MPS) and Trotter decomposition for the time evolution of the MPS. We set the maximum bond dimension as 100 of the resulting compressed MPS and the initial truncation error cutoff for the compression of the MPS as $\epsilon \sim 10^{-8}$. The truncation error cutoff is adaptive: As the maximum bond dimension is reached for the resulting MPS, the error cutoff increases systematically up until a hard error threshold of $\epsilon \sim 10^{-5}$ to be able to access longer times. Setting a maximum allowed bond dimension thus introduces an error which grows with time. Consequently, we are confined to early times for which the above interval of the error thresholds is satisfied.

F.2 The quasi-stationary regime in long-range interacting TFIM

The quasi-stationary temporal regime also emerges in the long-range hard-boundary TFIM with power-law decaying interactions. This boundary effect on the long-range TFIM has

been previously noticed in the context of prethermalization [340]. Here we provide numerical evidence for this boundary effect. All data presented in this section was obtained from TEBD (time-evolving block decimation).

The Hamiltonian for the long-range TFIM reads,

$$H = -\sum_{r,r'} J(r,r')\sigma_r^z\sigma_{r'}^z + h\sum_r \sigma_r^x, \tag{F.5}$$

where $J(r,r') = J/|r-r'|^\alpha$. In the limit where $\alpha = 0$, the model becomes integrable with all-to-all interactions, e.g. LMG model; whereas in the limit of $\alpha \to \infty$ the model reduces to short-range NN TFIM. When $\alpha = 10$, which is effectively a short-range TFIM with power-law decaying interactions, we reproduce the results in the main text for the TFIM with nearest-neighbor couplings and $J = 1$. Fig. F.2a shows that a spin close to the boundary develops a quasi-stationary regime whereas the spin in the middle of the chain does not. These nonequilibrium responses are compared to the total magnetization (green-dotted line), whose behavior in the long-time limit is not conclusive based on the data. When α decreases to $\alpha = 4$ and $\alpha = 3$, the quasi-stationary regime still survives for $C_{r=6}(t)$, up to some oscillations. We note that the nonintegrable short-range TFIM also develops such oscillations in the quasi-stationary regime, as demonstrated in the main text. Chapter Sec. 6.2 found a decaying nonequilibrium response for the spin in the middle of an open-boundary chain in the nonintegrable short-range TFIM with next-nearest neighbor interactions. Similarly, it also seems that the spin in the middle of the chain tends to decay in our results for the long-range TFIM with power-law decaying interactions. When $\alpha = 2$, the model becomes truly long-ranged and we do not observe a quasi-stationary regime in any of the spins. In fact the spins close to the boundary and in the middle of the chain behave quite similarly. This result points to the importance of locality in the Hamiltonian to observe the quasi-stationary temporal regime in spins close to the boundary, confirming the role of chain geometry rather than integrability.

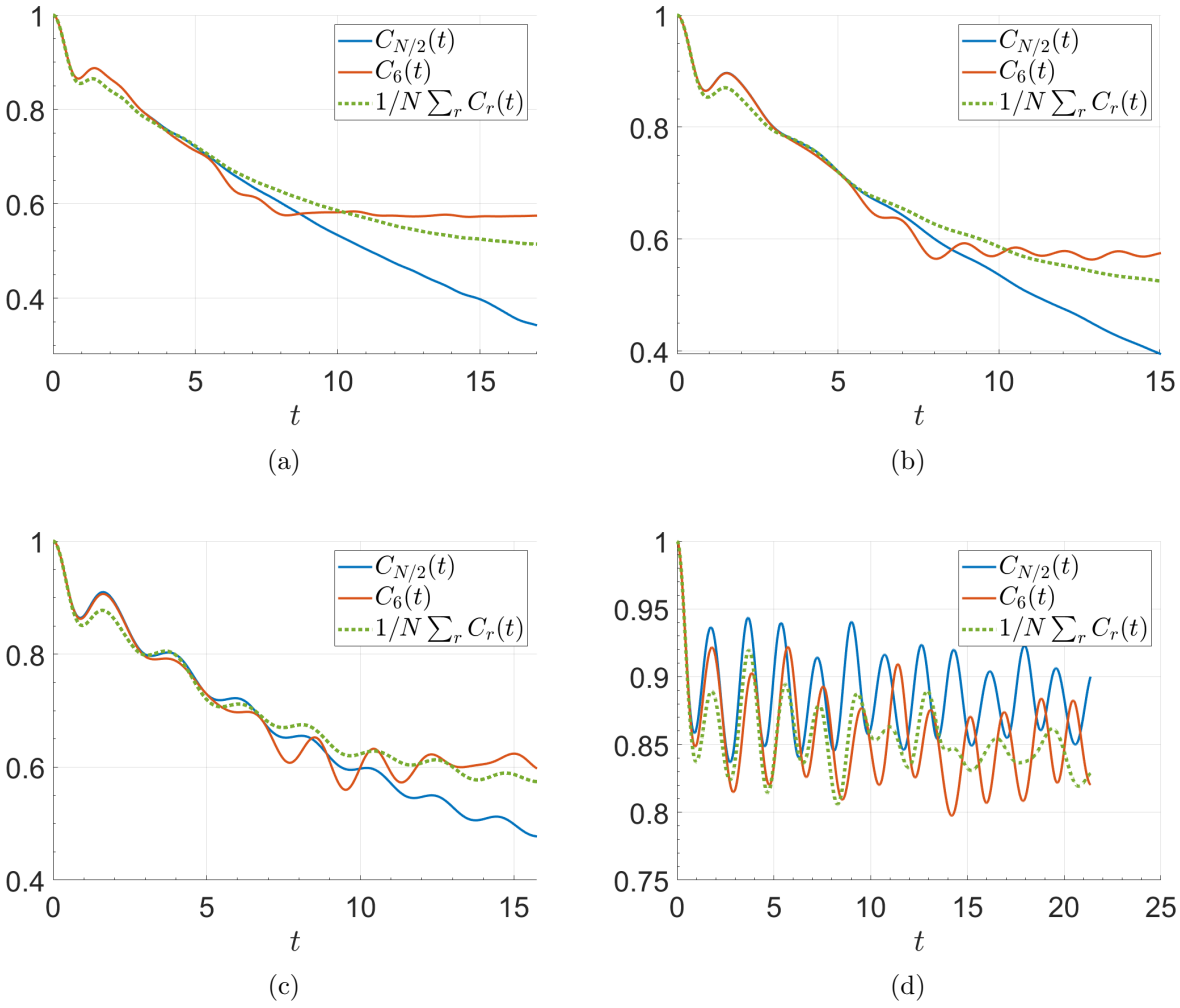

Figure F.2: Nonequilibrium responses of $\sigma^z_{N/2}$ (spin in the middle of the chain), σ^z_6 (spin close to the boundary) and the total magnetization, when (a) $\alpha = 10$, (b) $\alpha = 4$, (c) $\alpha = 3$ and (d) $\alpha = 2$.

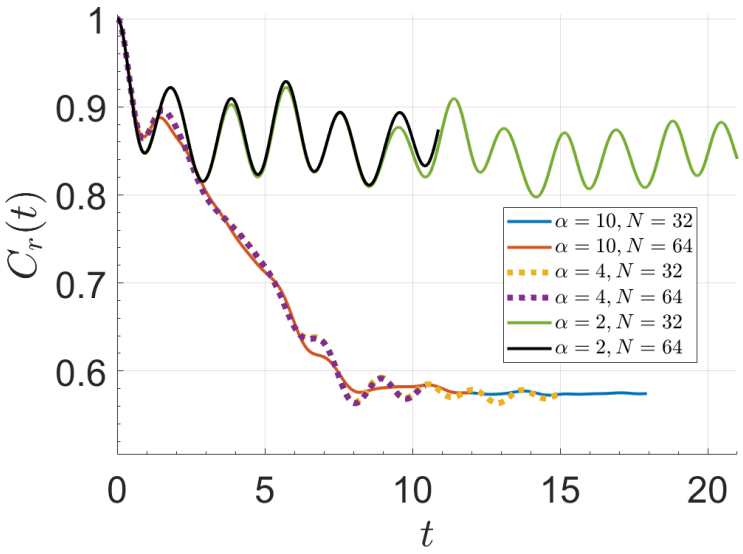

Figure F.3: The nonequilibrium responses of $C_{r=6(t)}$ for different α and different system sizes (see legend).

To demonstrate that the quasi-stationary temporal regime is not a finite-size effect, we show in Fig. F.3 the nonequilibrium responses of $C_{r=6}(t)$, a spin close to the boundary, for different system sizes and different α. For a given α, one can determine the time at which finite-size effects kick in by observing when the data for different system sizes $N = 32 - 64$ no longer overlap. Note that, for $\alpha = 10$ and $\alpha = 4$, the quasi-stationary regime develops before the finite-size effects appear.

F.3 Numerical evidence on quasi-stationary regime not being related to strong-zero modes

In this section, we plot the coherence times of edge magnetization (Fig. F.4c), as well as the magnetization of a bulk spin σ_3^z (Fig. F.4a) with respect to time for different interaction strengths Δ. An important evidence of strong zero modes is the presence of resonances, which would result in a non-monotonous trend of the steady-state value with respect to Δ [115]. The absence of such a behavior can be seen in Figs. F.4a and F.4c. Additionally, we provide

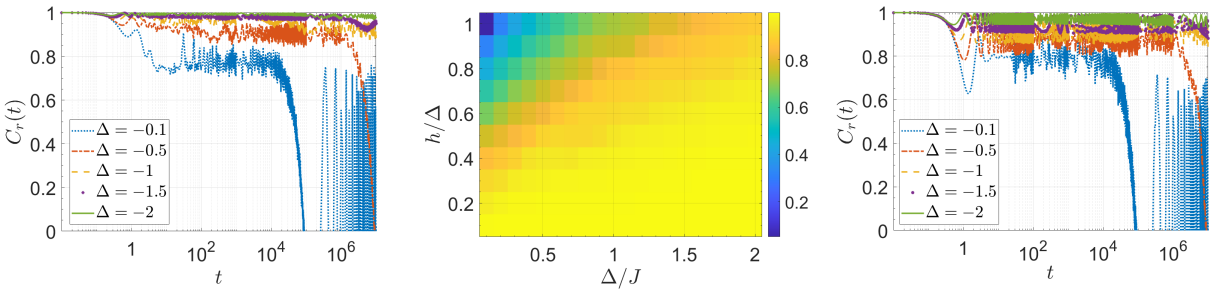

Figure F.4: Exact diagonalization results for the coherence time of (a-b) $C_{r=3}(t)$ and (c) $C_{r=1}(t)$ at a system size of $N = 14$. (a) and (c) depict certain nonintegrable models (see legend), whereas (b) gives a two-dimensional color plot of the long-time value of the quasi-stationary regime with respect to external field h and the interaction strength Δ. There is no non-monotonic behavior in the plot, demonstrating that the quasi-stationary regime is not caused by strong-zero modes.

a 2D plot of the long-time steady state value of $C_{r=3}(t)$ with respect to the external field strength h and the interaction strength Δ. The behavior is monotonous everywhere between $0 < h < 1$ and $0 < \Delta < 2$, which allows us to exclude the physics of strong zero modes as a possible explanation of the quasi-stationary temporal regime observed in the open-boundary chains.

We also compare the spatial profiles of the single-site magnetization at a fixed time — determined according to the breakdown of the cluster theorem t_l — with that of a Majorana edge mode $\gamma^1 = \phi_1^+$ (see Secs. F.1 and F.4 for the details of the temporal cutoffs in the study). For h in the ordered phase and $r \ll N/2$, where $N = 480$ is set for concreteness, this time corresponds to the quasi-stationary regime, and hence the single-site order parameter value is compared with the probability of the edge mode being found at r. As is evident from Fig. F.5, the spatial profiles for the magnetization decay exponentially in space, which is expected [128]. However, we observe that the decay rate of an edge mode and of magnetization at the same h differ by at least two orders of magnitude (red-diamonds vs. blue-circles, respectively). Their spatial profiles coincide perfectly at $r = 1$, which is the boundary of the chain, and start to differ as r increases. This is further evidence that the leakage of a zero mode into the bulk of the chain, alone, cannot explain the presence of a quasi-stationary

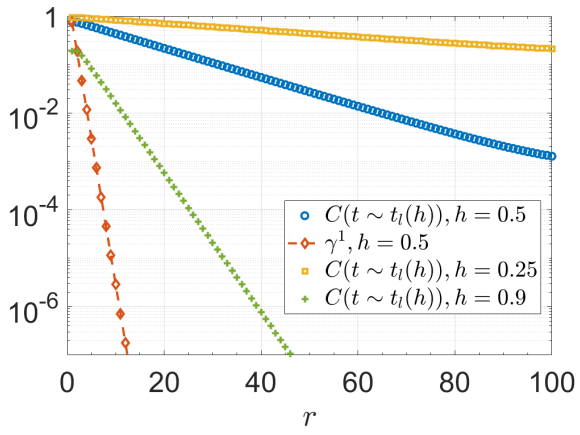

Figure F.5: The spatial profiles of the edge mode $\gamma^1 = \phi_1^+$ at $h = 0.5$ (red-diamonds) and of single-site magnetization for different h (see legend) at a fixed long time that is denoted as t_l meaning the lightcone time, which is set as the infrared cutoff, see Sec. F.4. The system size is $N = 480$.

temporal regime of bulk single-site observables. Fig. F.5 also compares the spatial profiles of magnetization at different h, showing them to decay faster for external fields close to the DCP.

F.4 Temporal cutoffs

There are two relevant temporal cutoffs in our results: i) ultraviolet (short-time, short-distance) cutoff and ii) infrared (long-time, long-distance) cutoff as explained in Sec. 6.2. We set the infrared cutoff as being a parametric cutoff due to the application of the cluster theorem (see Sec. F.1), and we test here whether our results depend on the choice of ultraviolet cutoff.

The results in the main text are produced with a fixed ultraviolet (UV) cutoff of $t^* = 10$ for all h. However, none of our results depend on the choice of ultraviolet cutoff: Figs. F.6, Figs. F.7 and F.8 all show the same qualitative behavior for single-site dynamical phase diagrams for various choices of ultraviolet cutoff. Figs. F.6 complement the $t^* = 10$ data of the main text by showing the single-site phase diagrams of the observables at $r = 3, 9, 12$. Figs. F.7 exhibit another fixed temporal cutoff of $t^* = 20$, whereas Figs. F.8 demonstrate the

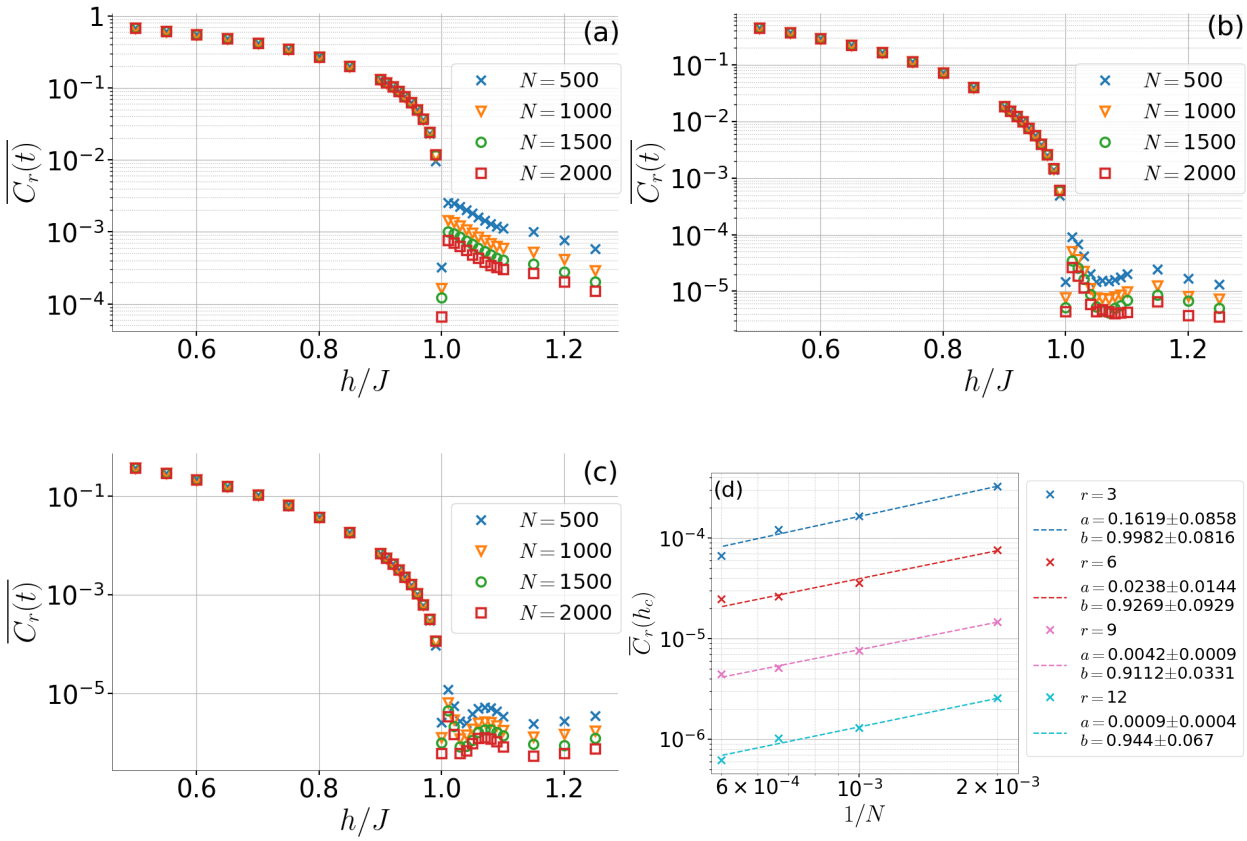

Figure F.6: The single-site dynamical phase diagrams with an ultraviolet temporal cutoff of $t^* = 10$ for (a) $C_{r=3}(t)$, (b) $C_{r=9}(t)$ and (c) $C_{r=12}(t)$. (d) The system size scaling of the single-site magnetization at the critical point h_c with cutoff $t^* = 10$. Downward trend can be seen with $N^{-\gamma}$ where $\gamma \sim 1$.

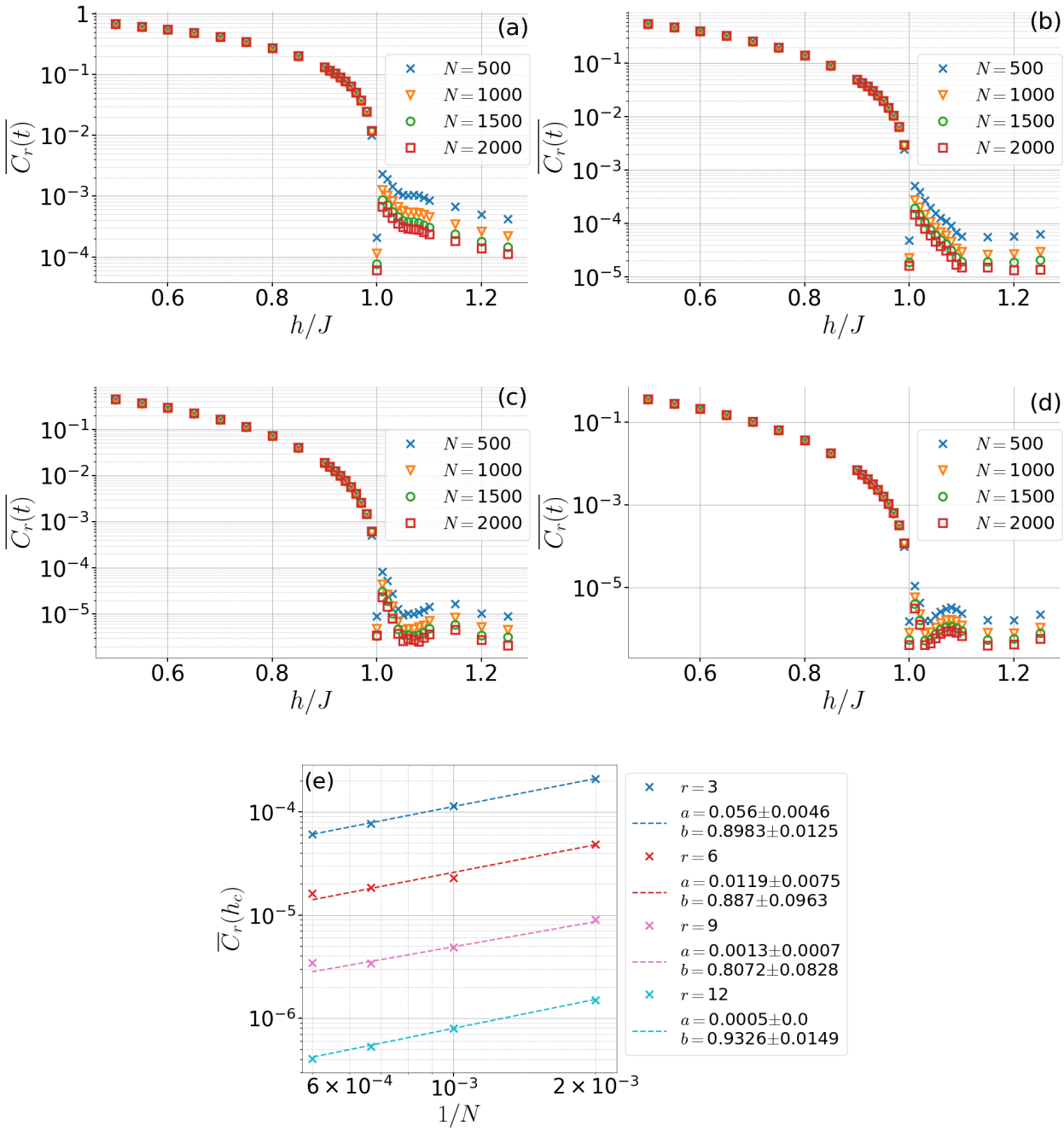

Figure F.7: The single-site dynamical phase diagrams with an ultraviolet temporal cutoff of $t^* = 20$ for (a) $C_{r=3}(t)$, (b) $C_{r=6}(t)$, (c) $C_{r=9}(t)$ and (d) $C_{r=12}(t)$. The behavior is qualitatively the same with the results of $t^* = 10$. (e) The system size scaling of the single-site magnetization at the critical point h_c with cutoff $t^* = 20$. Downward trend can be seen with $N^{-\gamma}$ where $\gamma \sim 1$.

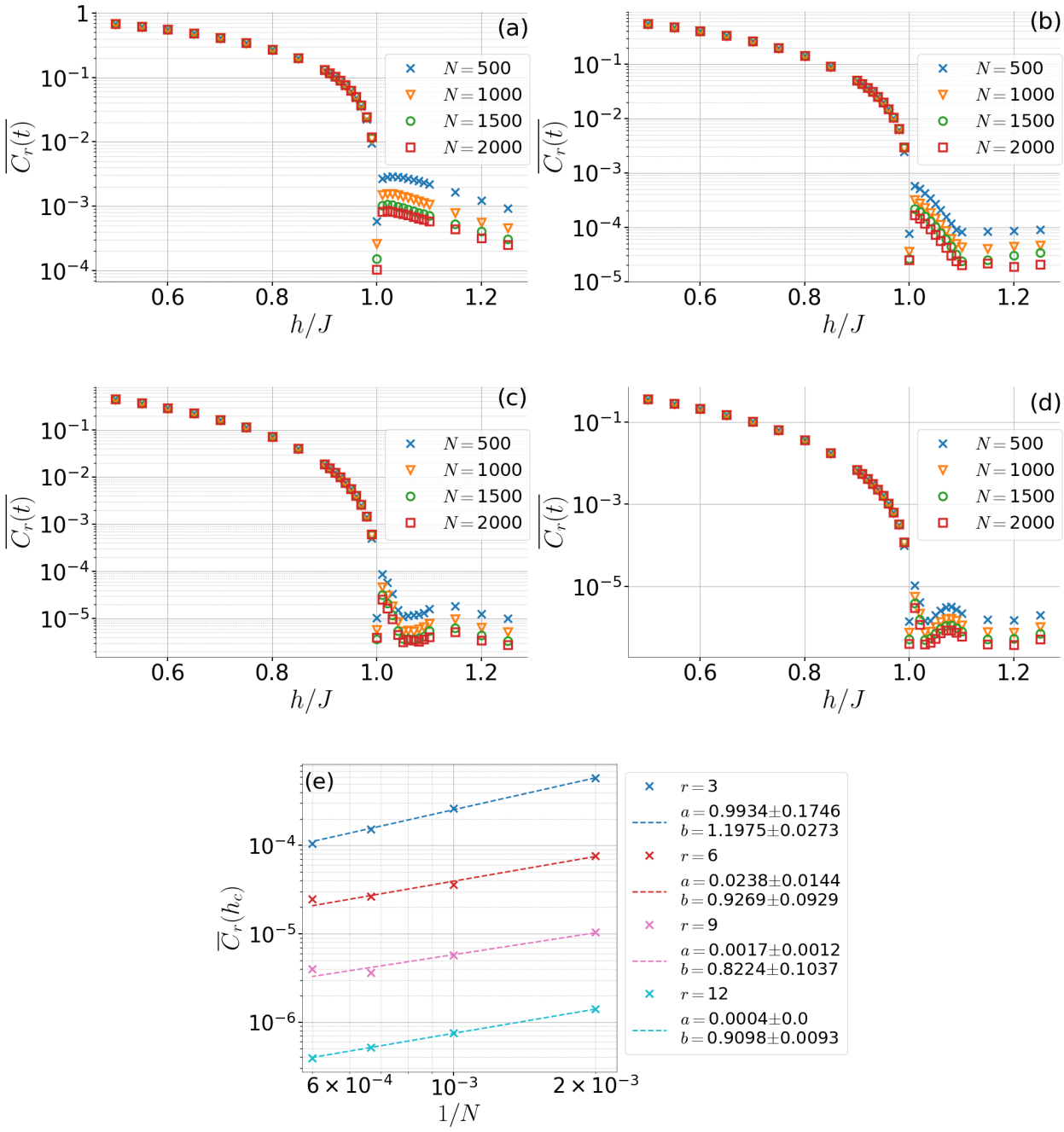

Figure F.8: The single-site dynamical phase diagrams with an ultraviolet temporal cutoff of $t^* = 2\alpha\Delta x/v_q$ where $\Delta x = r - 1$ with r being the single-site observable location and α is a tuning parameter for (a) $C_{r=3}(t)$, (b) $C_{r=6}(t)$, (c) $C_{r=9}(t)$ and (d) $C_{r=12}(t)$. The behavior is qualitatively the same with the results of other cutoffs. In all subfigures $\alpha = 2$. (e) The system size scaling of the single-site magnetization at the critical point h_c with cutoff $t^* = 2\alpha\Delta x/v_q$ and $\alpha = 2$. Downward trend can be seen with $N^{-\gamma}$ where $\gamma \sim 1$. t_{reflect} in the plot is the same with t^*.

obs.	cutoff	β	cutoff	β
σ_1^z		1.2972 ± 0.0018		1.2925 ± 0.0016
σ_3^z		1.3006 ± 0.0017		1.2948 ± 0.0016
σ_6^z	$t^* = 10$	1.3201 ± 0.0046	$t^* = 20$	1.3106 ± 0.0038
σ_9^z		1.3478 ± 0.0069		1.3263 ± 0.0032
σ_{12}^z		1.3331 ± 0.0056		1.3456 ± 0.0057

Table F.1: Fit parameters for the universal scaling law with different ultraviolet temporal cutoffs, part I.

results of a parametric temporal cutoff for all studied sites. This parametric UV cut-off is determined as follows: We roughly estimate the onset of the quasi-stationary regime as the time required for the quasiparticles to reflect back from the closest edge to the observation site. Therefore, the estimate can be mathematically stated as, $t^* = 2\alpha\Delta x/v_q$ where the distance $\Delta x = r - 1$ is the distance between the observation site, $r = 3, 6, 9, 12$ and the closest edge site, $r' = 1$, in our case. The parameter α is a tuning parameter, as our analytical formula is only an estimate. In fact we find that $\alpha = 2$ presents phase diagrams qualitatively the same with others for all r that we studied.

Additionally, in all cases the single-site magnetization at the critical point h_{dc} scales with similar exponents in a power-law fashion, $N^{-\gamma}$ where $\gamma \sim 1$. These fits can be seen in Figs. F.6d, F.7e and F.8e. Although the choice of cutoff slightly affects this exponent, it does not change the fact that there is a decreasing trend of the magnetization at h_{dc} with system size. This is a numerical evidence for the presence of a DCP.

Finally, we test the presence of the universal scaling in the vicinity of the transition when we change the ultraviolet cutoff.

Tables F.1 and F.2 provides all fit parameters for the exponent β in the integrable TFIM performed with different temporal cutoffs, either fixed or parametric, with the latter denoted as *parm* in the table. All exponents are very similar and around $\beta \sim 4/3$.

obs.	cutoff	β	cutoff	β
σ_1^z	parm, $\alpha = 1$	1.2931 ± 0.0018	parm, $\alpha = 2$	1.2931 ± 0.0018
σ_3^z		1.3011 ± 0.0016		1.3024 ± 0.0016
σ_6^z		1.3154 ± 0.0047		1.3201 ± 0.0046
σ_9^z		1.3455 ± 0.007		1.3527 ± 0.0067
σ_{12}^z		1.3359 ± 0.0053		1.3443 ± 0.0057

Table F.2: Fit parameters for the universal scaling law with different ultraviolet temporal cutoffs, part II.

observable	β
σ_1^z	1.3092 ± 0.0059
σ_6^z	1.3257 ± 0.0079
σ_{12}^z	1.3184 ± 0.0067

Table F.3: Fit parameters for the universal scaling law with a different initial state.

F.5 Independency of the results from the initial states

In this section, we change the initial state to the ground state of an initial Hamiltonian with $h_i = 0.1$, and test whether any of our results depend on the initial state. Figs. F.9 show the single-site dynamical phase diagrams computed with this initial state. We do not observe a change in the qualitative behavior. The single-site magnetization at the critical point still decreases with increasing system size.

We also test whether the scaling in the vicinity of the transition changes in Fig. F.10. The fit parameters for some observables in the vicinity of the transition is given in Table F.3 all of which demonstrates a dynamical critical exponent of $\beta \sim 4/3$. Based on this observation, we demonstrate in Fig. F.11 the collapse of the nonequilibrium responses of the system at $r = 6$ for different initial states $h_i = 0$ and $h_i = 0.1$. This collapse is achieved by utilizing the nonuniversal fit parameters in the scaling functions: $\bar{C}'_{r,h_i}(h_n) = a_{r,h_i} h_n^\beta$ and $\bar{C}'_{r',h'_i}(h_n) = a_{r',h'_i} h_n^\beta$ and hence the scaling factor reads $\bar{C}'_{r,h_i}(h_n)/\bar{C}'_{r',h'_i}(h_n) = a_{r,h_i}/a_{r',h'_i}$, i.e., $\tilde{C}_r(t) = C_r(t) a_{r,h_i}/a_{r,h'_i}$ in Fig. F.11.

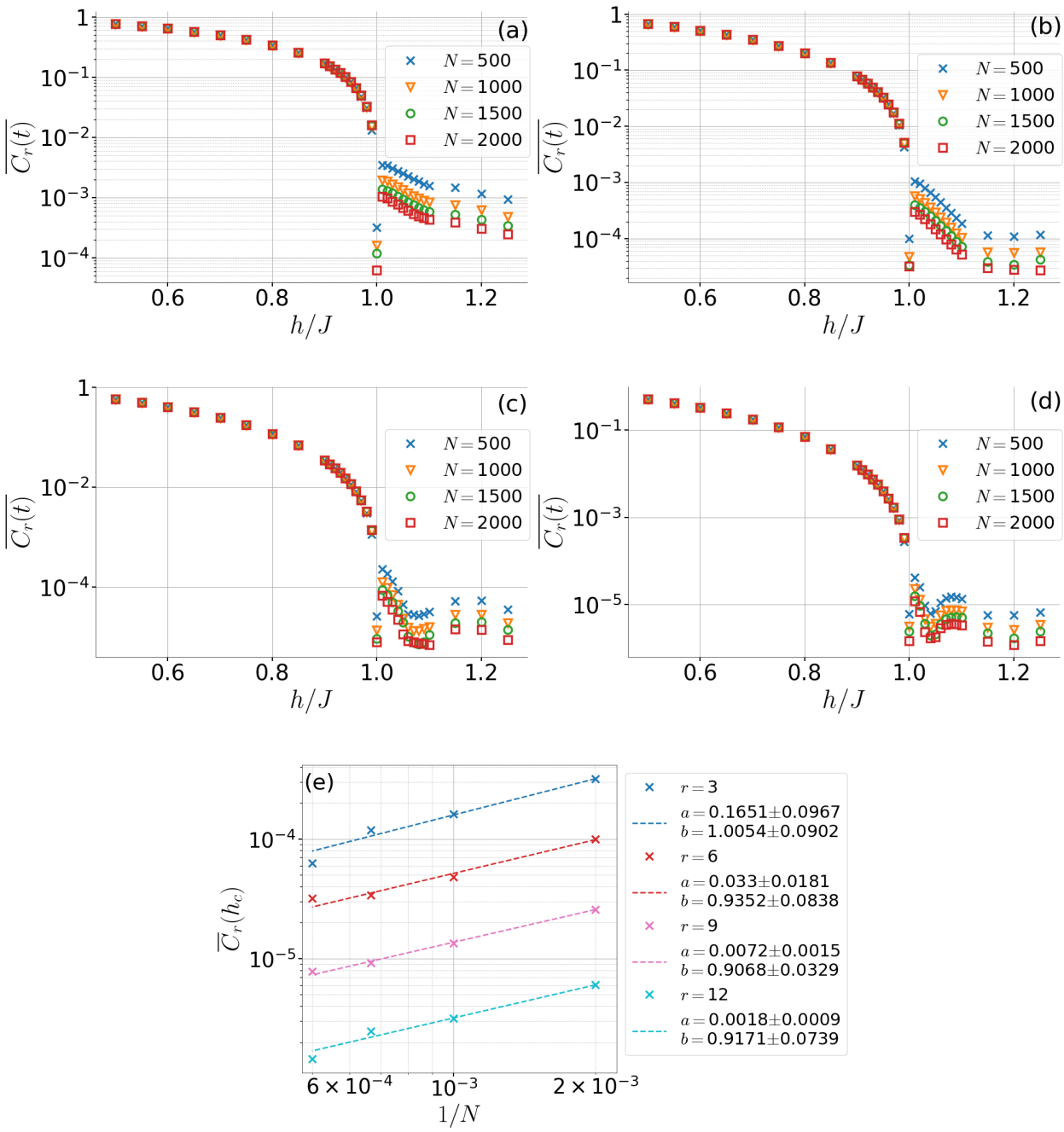

Figure F.9: The single-site dynamical phase diagrams with an initial state as the ground state of an initial Hamiltonian with $h_i = 0.1$ and an ultraviolet temporal cutoff of $t^* = 10$ for (a) $C_{r=3}(t)$, (b) $C_{r=6}(t)$, (c) $C_{r=9}(t)$ and (d) $C_{r=12}(t)$. The behavior is qualitatively the same as the results of $h_i = 0$. (e) The system size scaling of the single-site magnetization at the critical point h_c with cutoff $t^* = 10$. Downward trend can be seen with $N^{-\gamma}$ where $\gamma \sim 1$.

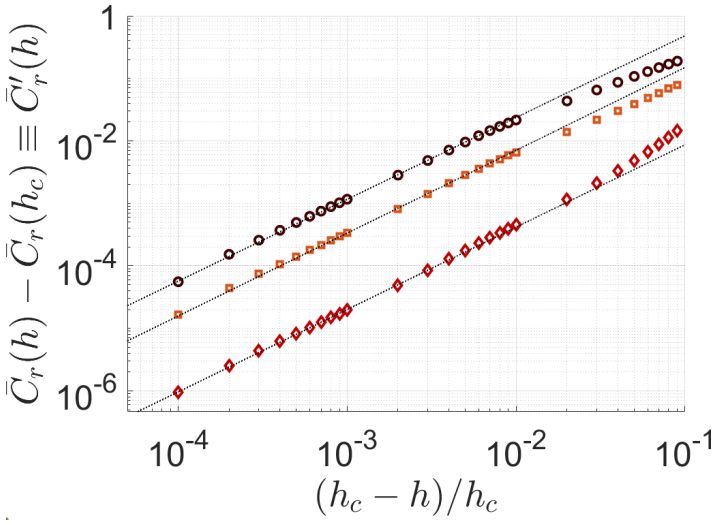

Figure F.10: The scaling behavior in the vicinity of the transition for $r = 1$, $r = 6$ and $r = 12$ in descending order when the initial state is the ground state of $h_i = 0.1$. All scaling exponents are $\beta \sim 4/3$.

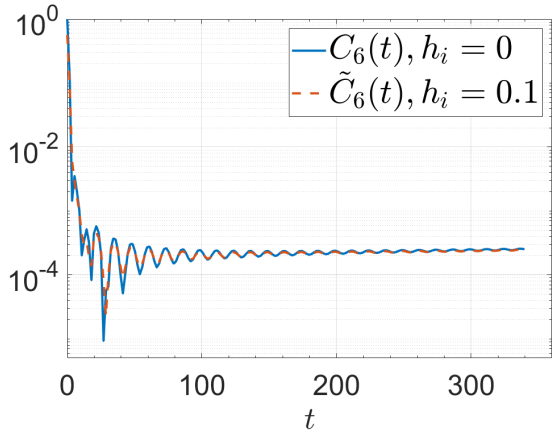

Figure F.11: $C_{r=6}(t)$ for quenches from $h_i = 0$ (blue-solid) or $h_i = 0.1$ (dashed-red) to $h = 0.999$ where the latter is rescaled to collapse on the other according to the fitted power-laws discussed in the main text. Rescaled quantity is denoted by tilde.

F.5.1 Analytical expression for the edge magnetization in the vicinity of the transition

In this subsection we show that the quasi-stationary value of the edge magnetization does not change its dynamical scaling in the vicinity of the transition. We remind the reader that this scaling is different from the dynamical universal scaling that we numerically observed in the vicinity of the transition. This is because of the divergent relaxation times which means that the times accessible to computation and experiment are still within the relaxation regime when we are in the close vicinity of the transition. The analytical expression for the quasi-stationary value of the edge magnetization in the dynamically-ordered phase is,

$$C^{qs}_{r=1}(h, h_i) = \frac{(1-h^2)(1-h_i)^{1/2}}{1-hh_i}, \tag{F.6}$$

for $h, h_i < 1$. Let us rewrite it in terms of the reduced control parameter, h_n,

$$C^{qs}_{r=1}(h_n, h_i) = \frac{(2-h_n)h_n(1-h_i)^{1/2}}{1+(h_n-1)h_i}. \tag{F.7}$$

In the vicinity of the transition, $h_n \to 0$, we can expand this expression and find up to the third order in h_n and h_i

$$\begin{aligned}
C^{qs}_{r=1}(h_n \to 0, h_i) &= a_1(h_i)h_n + a_2(h_i)h_n^2 + a_3(h_i)h_n^3 + \cdots, && \text{(F.8)}\\
a_1(h_i) &= 2 + h_i + \frac{3}{4}h_i^2 + \frac{5}{8}h_i^3 + \cdots, && \text{(F.9)}\\
a_2(h_i) &= -1 - \frac{5}{2}h_i - \frac{27}{8}h_i^2 - \frac{65}{16}h_i^3 + \cdots, && \text{(F.10)}\\
a_3(h_i) &= h_i + \frac{7}{2}h_i^2 + \frac{55}{8}h_i^3 + \cdots. && \text{(F.11)}
\end{aligned}$$

Therefore, one can see that $C^{qs}_{r=1}(h_n) \propto h_n$ in the vicinity of the transition, $h_n \to 0$ regardless of the choice of initial state. The initial state only changes the coefficient in front of h_n, which is known to be nonuniversal. Based on the observation that the edge magnetization

also exhibits $\beta \sim 4/3$ in its relaxation regime to the quasi-stationary value, it is possible that the rest of the single-site observables close enough to the boundary will also experience a similar scaling ~ 1 in their quasi-stationary regime. This is yet to be discovered, most likely analytically.

We note that the form of the fit function for the quasi-stationary regime of the edge magnetization is the same as Eq. (F.6), and hence the scaling in the vicinity of the transition is the same as well. Let us show this briefly,

$$C^{qs}_{r=1}(h_n) = \alpha(h_{dc}^{\beta} - (h_{dc} - h_n)^{\beta}), \tag{F.12}$$

$$\lim_{h_n \to 0} C^{qs}_{r=1}(h_n) = \alpha\beta h_{dc}^{\beta-1} h_n - \frac{1}{2}\alpha(\beta-1)\beta h_{dc}^{\beta-2} h_n^2 + \cdots . \tag{F.13}$$

We note that for a different initial state the general trend will remain the same, but that the coefficients α and β might change. In such a case, the scaling in the vicinity of the transition should remain the same as well.

F.6 Nonequilibrium response in the close vicinity of the transition

In this section we plot the nonequilibrium response in the close vicinity of the transition, to demonstrate that the dynamics slow down *critically* so that the onset of a quasi-stationary regime diverges as we move closer to the critical point. This naturally implies that the dynamical critical exponents that we probe in the vicinity of the transition are of nonequilibrium type, instead of equilibrium which could have been so if we were probing the quasi-stationary regime in the close vicinity. Fig. F.12a and F.12b show the nonequilibrium responses of edge magnetization and bulk magnetization at $r = 6$, respectively. (i) The first observation is that the nonequilibrium responses in the vicinity of the transition exhibit a very similar trend for both cases up to different time-average values (solid-black lines). We already presented

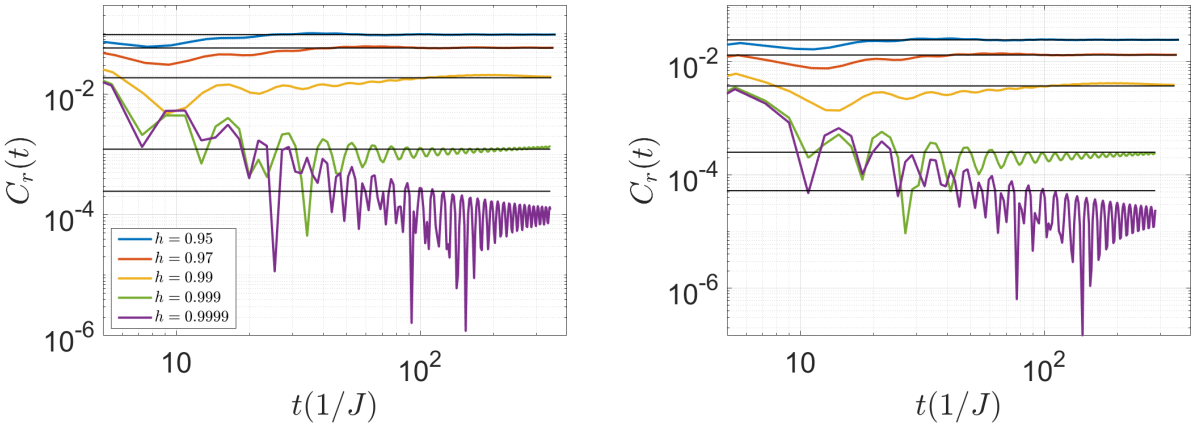

Figure F.12: The nonequilibrium response of integrable TFIM in the vicinity of the transition (see legend) for (a) the edge magnetization and (b) bulk $r = 6$ magnetization at system size $N = 1440$. The solid-black lines are the time-average with a fixed UV temporal cutoff of $t^* = 10$.

the collapse of nonequilibrium responses of different sites in the main text. (ii) As we move closer to the critical point, we observe that the onset of the quasi-stationary regime diverges: This effect starts to be visible from $h = 0.99$. Therefore, the time-average of the signal no longer matches perfectly with the magnetization value of the quasi-stationary regime, which is beyond accessible simulation times in these figures. We note that it is also around this value of h where we observe the onset of universal scaling appearing with $\beta \sim 4/3$ (see for instance Fig. 3a of the main text). We do not study the dynamical scaling closer than $h_n = 10^{-4}$ (purple), as it is not completely clear whether the dynamics relax to a quasi-stationary regime past this point due to constrained simulation time for a system size of $N = 1440$. Nevertheless, the allowed parameter regime still demonstrates a robust exponent of $\beta \sim 4/3$. In the future, one can extend the simulation time by increasing the system size further and thus test the dynamical critical exponent closer to the critical point.

In this section, we also plot the nonequilibrium response at the DCP which coincides with the QCP (Fig. F.13a), as well as in the dynamically-disordered phase at $h = 1.1$ (Fig. F.13b). One notices the power-law decay of the envelope of the nonequilibrium response, which

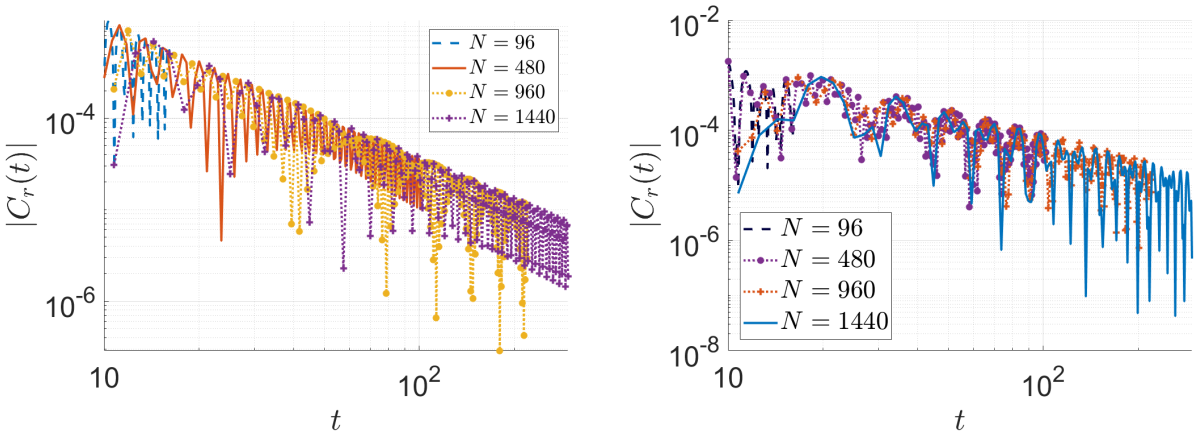

Figure F.13: The nonequilibrium response of integrable TFIM (a) at DCP $h = 1$ and (b) in the dynamically-disordered phase $h = 1.1$ for $r = 6$ magnetization at various system sizes (see legends).

suggests that there is no quasi-stationary regime appearing in the accessible times.

F.7 Details on the near-integrable model and the associated fit functions

We plot the nonequilibrium responses of our near-integrable model with $\Delta = -0.1$ for h past the DCP in Fig. F.14. This plot should be compared with Fig. 4c of the main text. One can observe the emergence of long wavelength oscillations as we pass the dynamical critical point, which is helpful in determining the DCP. This is because, such behavior of long wavelength oscillations is a characteristic of the disordered dynamical phase. One can also notice that the envelope of the nonequilibrium response in the dynamically-disordered phase decays in a power-law fashion, suggesting the absence of a quasi-stationary regime. Similar behavior is observed in the integrable TFIM (see Sec. F.6).

Table F.4 presents the fitting parameters for the dynamical scaling law in the vicinity of the transition for the near-integrable model for different sites $r \ll N/2$. For all sites we find a similar exponent of $\beta \sim 4/3$, which matches that found in the integrable model.

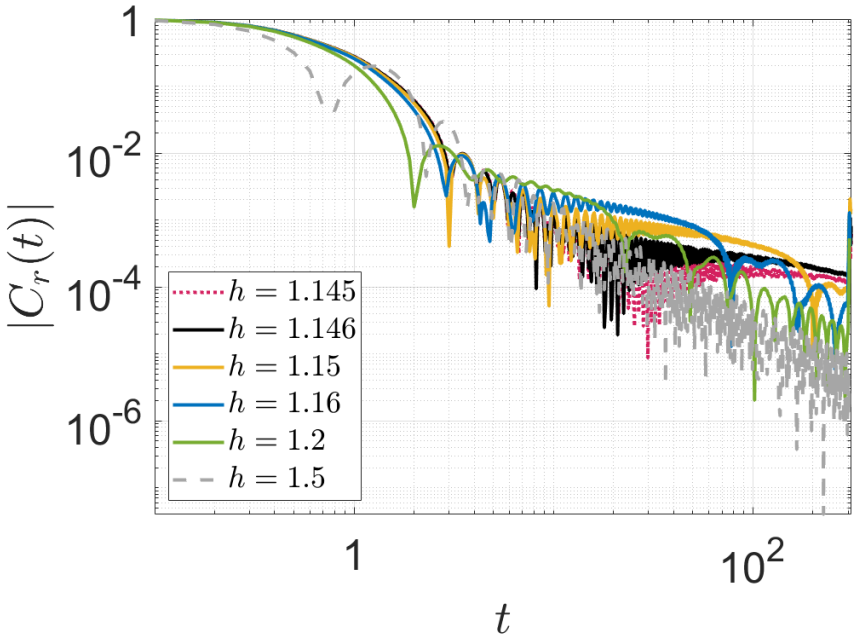

Figure F.14: Mean-field nonequilibrium responses of a near-integrable model with $\Delta = -0.1$ past the DCP (see legend) at a system size of $N = 1440$.

We also study the system size scaling at the DCP with different ultraviolet cutoffs t^*, all of which gives similar exponents $\bar{C}_r(h_c) \propto N^{-\gamma}$ where $\gamma \sim 0.7$. Table F.5 summarizes the fit parameters for some temporal cutoffs t^*.

When applying the cluster theorem to the MFT data of this weakly-interacting non-integrable TFIM, one needs to estimate the lightcone (correlation) velocity of the model. While for the integrable TFIM this velocity is analytically known, this is not true when we introduce nonintegrability to the model. Here we approximate a quasiparticle velocity based

observable	β
σ_1^z	1.3378 ± 0.0043
σ_3^z	1.3568 ± 0.0039
σ_6^z	1.3537 ± 0.0038
σ_9^z	1.3647 ± 0.0023
σ_{12}^z	1.3618 ± 0.0132

Table F.4: Fit parameters for the scaling law of the near-integrable model in the vicinity of the transition.

cutoff	σ_1^z, γ	σ_3^z, γ	σ_6^z, γ
$t^* = 10$	0.6842 ± 0.0437	0.6973 ± 0.052	0.7003 ± 0.0505
$t^* = 15$	0.6957 ± 0.0449	0.6865 ± 0.0492	0.6710 ± 0.0448

Table F.5: Fit parameters for the system-size scaling of single-site observable at $r = 1, 3, 6$ at the DCP.

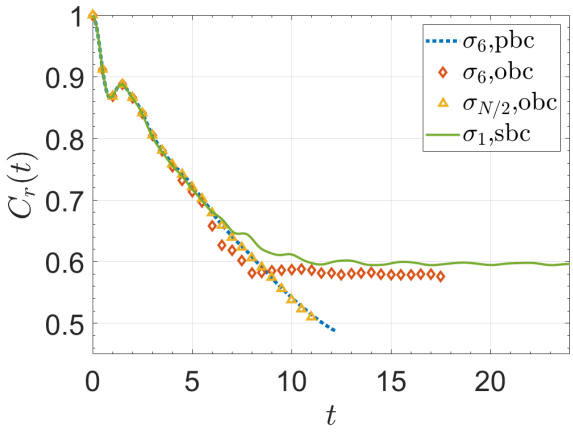

Figure F.15: Different boundary conditions are compared for the integrable TFIM at $h = 0.5$ and system size $N = 24$. One can obtain a quasi-stationary regime with smooth boundary conditions too.

on the analytical prediction of the integrable TFIM: $v_q = 2h$ for $h \leq h_c$ and $v_q = 2h_c$ for $h > h_c$. Since this is only an approximation, we sometimes exceed the time when the cluster theorem breaks down. This is because distant sites of the chain become correlated with one another (see Sec. F.1). This time can be observed with a recurrence attempt in the figures both in the main text and the supplementary, which is also a sign of finite-size effects.

F.8 Robustness of the quasi-stationary regime

In this section, we show that the quasi-stationary temporal regime emerges not only when we introduce hard boundaries [337], but also smooth boundaries. A smooth boundary condition can be applied by smoothly turning off the Hamiltonian parameters towards the edges of the chain [341]. Fig. F.15 shows the single-site nonequilibrium responses of the integrable

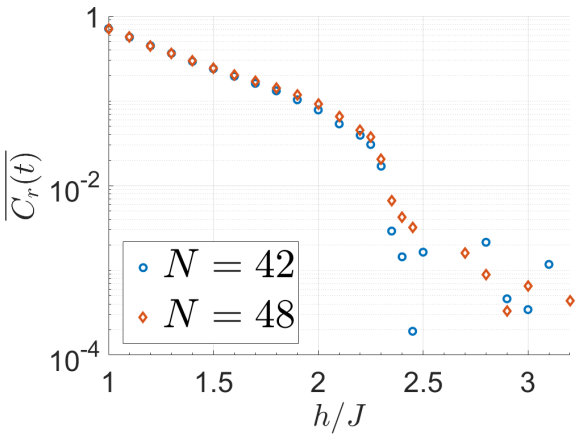

Figure F.16: The dynamic order profile of the nonintegrable TFIM with $\Delta = -1$ in logarithmic scale.

TFIM with hard boundarieas (red-diamonds), smooth boundaries (green-solid) and periodic boundary condition (blue-dotted). As shown in Sec. 6.2, the middle of a hard-boundary chain (yellow triangles) acts like an arbitrary site in a periodic chain.

We thus conclude that the quasi-stationary regime is robust against altering the boundary conditions, so long as they remain open. This provides further evidence that the stationary regime is a result of the geometry of the chain rather than of the zero modes.

F.9 t-DMRG results in detail

Finally, in Fig. F.16 we show the data of Fig. 5b of the main text in logarithmic scale to demonstrate why this data is insufficient to claim the presence of a dynamical phase transition (DPT) in the nonintegrable TFIM with strong integrability breaking. We remind the reader that the interaction strength is set to $\Delta = -1$ and the results are obtained via t-DMRG (see Sec. F.1). Although the dynamic order tends to increase with increasing system size in the dynamically-ordered regime and hence demonstrates a persistent dynamic order, it is not clear where the transition really happens. The DCP is expected to happen either before or at the QCP, which is at $h_c \sim 2.46J$ for this model. Longer simulations times, with sufficiently high precision, are needed in order to decide whether this crossover is actually a

DPT.

Bibliography

[1] S. Berryman, *Democritus*, in *The Stanford Encyclopedia of Philosophy*, E.N. Zalta, ed., Metaphysics Research Lab, Stanford University (2016).

[2] J. Dalton, *A New System of Chemical Philosophy*, vol. 1 of *Cambridge Library Collection - Physical Sciences*, Cambridge University Press (2010), 10.1017/CBO9780511736391.

[3] A. Einstein, *Über die von der molekularkinetischen theorie der wärme geforderte bewegung von in ruhenden flüssigkeiten suspendierten teilchen*, *Annalen der Physik* **322** (1905) 549 [https://onlinelibrary.wiley.com/doi/pdf/10.1002/andp.19053220806].

[4] J.J. Thomson, *Xl. cathode rays*, *The London, Edinburgh, and Dublin Philosophical Magazine and Journal of Science* **44** (1897) 293 [https://doi.org/10.1080/14786449708621070].

[5] E. Rutherford, *Lxxix. the scattering of α and β particles by matter and the structure of the atom*, *The London, Edinburgh, and Dublin Philosophical Magazine and Journal of Science* **21** (1911) 669 [https://doi.org/10.1080/14786440508637080].

[6] M. Planck, *On the law of distribution of energy in the normal spectrum*, *Annalen der physik* **4** (1901) 1.

[7] A. Einstein, *Über einem die erzeugung und verwandlung des lichtes betreffenden heuristischen gesichtspunkt*, *Annalen der physik* **4** (1905) .

[8] N.B.D. phil., *Xxxvii. on the constitution of atoms and molecules*, *The London, Edinburgh, and Dublin Philosophical Magazine and Journal of Science* **26** (1913) 476 [https://doi.org/10.1080/14786441308634993].

[9] L. De Broglie, *Ondes et mouvements*, vol. 1, Gauthier-Villars (1926).

[10] E. Schrödinger, *Quantisierung als eigenwertproblem*, *Annalen der Physik* **386** (1926) 109 [https://onlinelibrary.wiley.com/doi/pdf/10.1002/andp.19263861802].

[11] M. Born, *Quantenmechanik der stoßvorgänge*, *Zeitschrift für Physik* **38** (1926) 803.

[12] W. Heisenberg, *Über den anschaulichen inhalt der quantentheoretischen kinematik und mechanik*, in *Original Scientific Papers Wissenschaftliche Originalarbeiten*, pp. 478–504, Springer (1985).

[13] M. Born, W. Heisenberg and P. Jordan, *Zur quantenmechanik. ii.*, *Zeitschrift für Physik* **35** (1926) 557.

[14] P.A.M. Dirac, *The principles of quantum mechanics*, no. 27, Oxford university press (1981).

[15] C. Kittel, *Introduction to solid state physics* (1976).

[16] Bose, *Plancks Gesetz und Lichtquantenhypothese*, *Zeitschrift fur Physik* **26** (1924) 178.

[17] P. Jordan and E. Wigner, *Über das Paulische Äquivalenzverbot*, *Zeitschrift fur Physik* **47** (1928) 631.

[18] G.D. Mahan, *Many Particle Physics, Third Edition*, Plenum, New York (2000).

[19] K. Huang, *Statistical Mechanics*, John Wiley & Sons (1987).

[20] A. Leggett, *Quantum Liquids: Bose condensation and Cooper pairing in condensed-matter systems*, vol. 9780198526438, Oxford University Press (Jan., 2008), 10.1093/acprof:oso/9780198526438.001.0001.

[21] C.J. Pethick and H. Smith, *Bose–Einstein Condensation in Dilute Gases:*, Cambridge University Press, Cambridge, 2 ed. (003, 2008), 10.1017/CBO9780511802850.

[22] B.A. Bernevig and T.L. Hughes, *Topological Insulators and Topological Superconductors*, Princeton University Press (2013).

[23] I. Buluta and F. Nori, *Quantum simulators*, *Science* **326** (2009) 108.

[24] I.M. Georgescu, S. Ashhab and F. Nori, *Quantum simulation*, *Rev. Mod. Phys.* **86** (2014) 153.

[25] E. Altman, K.R. Brown, G. Carleo, L.D. Carr, E. Demler, C. Chin et al., *Quantum simulators: Architectures and opportunities*, *PRX Quantum* **2** (2021) 017003.

[26] D. Jaksch and P. Zoller, *The cold atom hubbard toolbox*, *Annals of Physics* **315** (2005) 52.

[27] M. Lewenstein, A. Sanpera and V. Ahufinger, *Ultracold Atoms in Optical Lattices: Simulating quantum many-body systems*, Oxford University Press (2012).

[28] R. Blatt and C.F. Roos, *Quantum simulations with trapped ions*, *Nature Physics* **8** (2012) 277.

[29] C. Monroe, W.C. Campbell, L.-M. Duan, Z.-X. Gong, A.V. Gorshkov, P.W. Hess et al., *Programmable quantum simulations of spin systems with trapped ions*, *Rev. Mod. Phys.* **93** (2021) 025001.

[30] A.A. Houck, H.E. Türeci and J. Koch, *On-chip quantum simulation with superconducting circuits*, *Nature Physics* **8** (2012) 292.

[31] A. Aspuru-Guzik and P. Walther, *Photonic quantum simulators*, *Nature physics* **8** (2012) 285.

[32] J. Eisert, M. Friesdorf and C. Gogolin, *Quantum many-body systems out of equilibrium*, *Nature Physics* **11** (2015) 124.

[33] J.-S. Caux and J. Mossel, *Remarks on the notion of quantum integrability*, *Journal of Statistical Mechanics: Theory and Experiment* **2011** (2011) P02023.

[34] L. D'Alessio, Y. Kafri, A. Polkovnikov and M. Rigol, *From quantum chaos and eigenstate thermalization to statistical mechanics and thermodynamics*, *Advances in Physics* **65** (2016) 239 [1509.06411].

[35] T. Mori, T.N. Ikeda, E. Kaminishi and M. Ueda, *Thermalization and prethermalization in isolated quantum systems: a theoretical overview*, *Journal of Physics B Atomic Molecular Physics* **51** (2018) 112001 [1712.08790].

[36] A.J. Short, *Equilibration of quantum systems and subsystems*, *New Journal of Physics* **13** (2011) 053009.

[37] P. Bocchieri and A. Loinger, *Quantum recurrence theorem*, *Phys. Rev.* **107** (1957) 337.

[38] J.M. Deutsch, *Quantum statistical mechanics in a closed system*, *Phys. Rev. A* **43** (1991) 2046.

[39] M. Srednicki, *Chaos and quantum thermalization*, *Phys. Rev. E* **50** (1994) 888.

[40] M. Rigol, V. Dunjko and M. Olshanii, *Thermalization and its mechanism for generic isolated quantum systems*, *Nature* **452** (2008) 854.

[41] F.J. Dyson, *Statistical theory of the energy levels of complex systems. i*, *Journal of Mathematical Physics* **3** (1962) 140 [https://doi.org/10.1063/1.1703773].

[42] V.E. Kravtsov, *Random matrix theory: Wigner-Dyson statistics and beyond. (Lecture notes of a course given at SISSA (Trieste, Italy))*, *ArXiv e-prints* (2009) [0911.0639].

[43] R. Nandkishore and D.A. Huse, *Many-body localization and thermalization in quantum statistical mechanics*, *Annual Review of Condensed Matter Physics* **6** (2015) 15.

[44] E.H. Lieb and D.W. Robinson, *The finite group velocity of quantum spin systems*, *Communications in Mathematical Physics* **28** (1972) 251.

[45] J. Zinn-Justin, *Quantum Field Theory and Critical Phenomena; 4th ed.*, Internat. Ser. Mono. Phys., Clarendon Press, Oxford (2002), 10.1093/acprof:oso/9780198509233.001.0001.

[46] X.-L. Qi and S.-C. Zhang, *Topological insulators and superconductors*, *Reviews of Modern Physics* **83** (2011) 1057–1110.

[47] B.A. Bernevig, *Topological insulators and topological superconductors*, Princeton university press (2013).

[48] M. Peskin, *An introduction to quantum field theory*, CRC press (2018).

[49] S. Sachdev, *Quantum Phase Transitions*, Cambridge University Press (1999).

[50] J.J. Sakurai and J. Napolitano, *Modern Quantum Mechanics*, Cambridge University Press, 2 ed. (2017), 10.1017/9781108499996.

[51] H. Lipkin, N. Meshkov and A. Glick, *Validity of many-body approximation methods for a solvable model: (i). exact solutions and perturbation theory*, *Nuclear Physics* **62** (1965) 188.

[52] F.J. Dyson, *Existence of a phase-transition in a one-dimensional ising ferromagnet*, *Communications in Mathematical Physics* **12** (1969) 91.

[53] A.Y. Kitaev, *Unpaired Majorana fermions in quantum wires*, *Physics Uspekhi* **44** (2001) 131 [cond-mat/0010440].

[54] A. Einstein, *Quantentheorie des einatomigen idealen Gases. (German) [Quantum theory of monatomic ideal gases]*, *Sitzungsberichte der Preussischen Akademie der Wissenschaften, Physikalisch-mathematische Klasse* **??** (1924) 261.

[55] C. Foot, *Atomic physics*, Oxford University Press, USA (2005).

[56] M.H. Anderson, J.R. Ensher, M.R. Matthews, C.E. Wieman and E.A. Cornell, *Observation of bose-einstein condensation in a dilute atomic vapor*, *Science* **269** (1995) 198 [http://science.sciencemag.org/content/269/5221/198.full.pdf].

[57] K.B. Davis, M.O. Mewes, M.R. Andrews, N.J. van Druten, D.S. Durfee, D.M. Kurn et al., *Bose-einstein condensation in a gas of sodium atoms*, *Phys. Rev. Lett.* **75** (1995) 3969.

[58] A.J. Leggett, *Bose-einstein condensation in the alkali gases: Some fundamental concepts*, *Rev. Mod. Phys.* **73** (2001) 307.

[59] J.D. Jackson, *Classical electrodynamics; 2nd ed.*, Wiley, New York, NY (1975).

[60] D.M. Stamper-Kurn and M. Ueda, *Spinor bose gases: Symmetries, magnetism, and quantum dynamics*, *Rev. Mod. Phys.* **85** (2013) 1191.

[61] C.K. Law, H. Pu and N.P. Bigelow, *Quantum spins mixing in spinor bose-einstein condensates*, *Phys. Rev. Lett.* **81** (1998) 5257.

[62] M. Greiner, O. Mandel, T. Esslinger, T.W. Hänsch and I. Bloch, *Quantum phase transition from a superfluid to a Mott insulator in a gas of ultracold atoms*, *Nature* **415** (2002) 39.

[63] M.P.A. Fisher, P.B. Weichman, G. Grinstein and D.S. Fisher, *Boson localization and the superfluid-insulator transition*, *Phys. Rev. B* **40** (1989) 546.

[64] D. Jaksch, C. Bruder, J.I. Cirac, C.W. Gardiner and P. Zoller, *Cold bosonic atoms in optical lattices*, *Phys. Rev. Lett.* **81** (1998) 3108.

[65] F. Franchini, ed., *An Introduction to Integrable Techniques for One-Dimensional Quantum Systems*, vol. 940 of *Lecture Notes in Physics, Berlin Springer Verlag*, 2017. 10.1007/978-3-319-48487-7.

[66] A. Polkovnikov, K. Sengupta, A. Silva and M. Vengalattore, *Colloquium*, *Rev. Mod. Phys.* **83** (2011) 863.

[67] C. Gogolin and J. Eisert, *Equilibration, thermalisation, and the emergence of statistical mechanics in closed quantum systems*, *Reports on Progress in Physics* **79** (2016) 056001 [1503.07538].

[68] W.H. Zurek, U. Dorner and P. Zoller, *Dynamics of a quantum phase transition*, *Phys. Rev. Lett.* **95** (2005) 105701.

[69] B. Damski and W.H. Zurek, *Dynamics of a quantum phase transition in a ferromagnetic bose-einstein condensate*, *Phys. Rev. Lett.* **99** (2007) 130402.

[70] J. Dziarmaga, *Dynamics of a quantum phase transition and relaxation to a steady state*, *Advances in Physics* **59** (2010) 1063 [https://doi.org/10.1080/00018732.2010.514702].

[71] A. del Campo and W.H. Zurek, *Universality of phase transition dynamics: Topological defects from symmetry breaking*, *International Journal of Modern Physics A* **29** (2014) 1430018 [https://doi.org/10.1142/S0217751X1430018X].

[72] M. Anquez, B.A. Robbins, H.M. Bharath, M. Boguslawski, T.M. Hoang and M.S. Chapman, *Quantum kibble-zurek mechanism in a spin-1 bose-einstein condensate*, *Phys. Rev. Lett.* **116** (2016) 155301.

[73] A. Sala, D.L. Núñez, J. Martorell, L. De Sarlo, T. Zibold, F. Gerbier et al., *Shortcut to adiabaticity in spinor condensates*, *Phys. Rev. A* **94** (2016) 043623.

[74] J.v. Neumann, *Beweis des ergodensatzes und desh-theorems in der neuen mechanik*, *Zeitschrift für Physik* **57** (1929) 30.

[75] H.B. Callen, *Thermodynamics and an introduction to thermostatistics; 2nd ed.*, Wiley, New York, NY (1985).

[76] W. THOMSON, *The kinetic theory of the dissipation of energy*, in *The Kinetic Theory of Gases*, pp. 350–361 DOI [https://www.worldscientific.com/doi/pdf/10.1142/9781848161337_0016].

[77] E. ZERMELO, *On a theorem of dynamics and the mechanical theory of heat*, in *The Kinetic Theory of Gases*, pp. 382–391 DOI [https://www.worldscientific.com/doi/pdf/10.1142/9781848161337_0020].

[78] L. BOLTZMANN, *Reply to zermelo's remarks on the theory of heat*, in *The Kinetic Theory of Gases*, pp. 392–402 DOI [https://www.worldscientific.com/doi/pdf/10.1142/9781848161337_0021].

[79] J.C. Maxwell, *Tait's "thermodynamics" 1*, *Nature* **17** (1878) 278.

[80] J.L. Lebowitz, *Statistical mechanics: A selective review of two central issues*, *Rev. Mod. Phys.* **71** (1999) S346.

[81] J.L. Lebowitz, *Boltzmann's entropy and time's arrow*, *Physics Today* **46** (1993) 32 [https://doi.org/10.1063/1.881363].

[82] R.B. Griffiths, *Statistical irreversibility: classical and quantum.*, in *Physical Origins of Time Asymmetry*, pp. 147–159, Jan., 1994.

[83] J.L. Lebowitz, *From time-symmetric microscopic dynamics to time-asymmetric macroscopic behavior: An overview*, 0709.0724.

[84] S. Popescu, A.J. Short and A. Winter, *Entanglement and the foundations of statistical mechanics*, *Nature Physics* **2** (2006) 754.

[85] S. Goldstein, J.L. Lebowitz, R. Tumulka and N. Zanghì, *Canonical typicality*, *Phys. Rev. Lett.* **96** (2006) 050403.

[86] M. Kollar and M. Eckstein, *Relaxation of a one-dimensional mott insulator after an interaction quench*, *Phys. Rev. A* **78** (2008) 013626.

[87] M. Rigol, *Breakdown of thermalization in finite one-dimensional systems*, *Phys. Rev. Lett.* **103** (2009) 100403.

[88] M. Rigol, *Quantum quenches and thermalization in one-dimensional fermionic systems*, *Phys. Rev. A* **80** (2009) 053607.

[89] H. Tasaki, *From quantum dynamics to the canonical distribution: General picture and a rigorous example*, *Phys. Rev. Lett.* **80** (1998) 1373.

[90] P. Reimann, *Foundation of statistical mechanics under experimentally realistic conditions*, *Phys. Rev. Lett.* **101** (2008) 190403.

[91] N. Linden, S. Popescu, A.J. Short and A. Winter, *Quantum mechanical evolution towards thermal equilibrium*, *Phys. Rev. E* **79** (2009) 061103.

[92] A.J. Short and T.C. Farrelly, *Quantum equilibration in finite time*, *New Journal of Physics* **14** (2012) 013063.

[93] H. Kim and D.A. Huse, *Ballistic spreading of entanglement in a diffusive nonintegrable system*, *Phys. Rev. Lett.* **111** (2013) 127205.

[94] R. Islam, R. Ma, P.M. Preiss, M.E. Tai, A. Lukin, M. Rispoli et al., *Measuring entanglement entropy in a quantum many-body system*, *Nature* **528** (2015) 77.

[95] A. Widera, F. Gerbier, S. Fölling, T. Gericke, O. Mandel and I. Bloch, *Coherent collisional spin dynamics in optical lattices*, *Phys. Rev. Lett.* **95** (2005) 190405.

[96] M.-S. Chang, C.D. Hamley, M.D. Barrett, J.A. Sauer, K.M. Fortier, W. Zhang et al., *Observation of spinor dynamics in optically trapped* ^{87}Rb *bose-einstein condensates*, *Phys. Rev. Lett.* **92** (2004) 140403.

[97] W. Zhang, D.L. Zhou, M.-S. Chang, M.S. Chapman and L. You, *Coherent spin mixing dynamics in a spin-1 atomic condensate*, *Phys. Rev. A* **72** (2005) 013602.

[98] M.-S. Chang, Q. Qin, W. Zhang, L. You and M.S. Chapman, *Coherent spinor dynamics in a spin-1 bose condensate*, *Nature physics* **1** (2005) 111.

[99] F. Liu, R. Lundgren, P. Titum, G. Pagano, J. Zhang, C. Monroe et al., *Confined quasiparticle dynamics in long-range interacting quantum spin chains*, *Phys. Rev. Lett.* **122** (2019) 150601.

[100] H. Bernien, S. Schwartz, A. Keesling, H. Levine, A. Omran, H. Pichler et al., *Probing many-body dynamics on a 51-atom quantum simulator*, *Nature* **551** (2017) 579.

[101] C.J. Turner, A.A. Michailidis, D.A. Abanin, M. Serbyn and Z. Papić, *Weak ergodicity breaking from quantum many-body scars*, *Nature Physics* **14** (2018) 745.

[102] M. Serbyn, D.A. Abanin and Z. Papić, *Quantum many-body scars and weak breaking of ergodicity*, 2011.09486.

[103] S. Choi, J. Choi, R. Landig, G. Kucsko, H. Zhou, J. Isoya et al., *Observation of discrete time-crystalline order in a disordered dipolar many-body system*, *Nature* **543** (2017) 221.

[104] K. Sacha and J. Zakrzewski, *Time crystals: a review*, *Reports on Progress in Physics* **81** (2017) 016401.

[105] D.V. Else, B. Bauer and C. Nayak, *Prethermal phases of matter protected by time-translation symmetry*, *Phys. Rev. X* **7** (2017) 011026.

[106] A. Syrwid, J. Zakrzewski and K. Sacha, *Time crystal behavior of excited eigenstates*, *Phys. Rev. Lett.* **119** (2017) 250602.

[107] R.V. Jensen and R. Shankar, *Statistical behavior in deterministic quantum systems with few degrees of freedom*, *Phys. Rev. Lett.* **54** (1985) 1879.

[108] M. Rigol, V. Dunjko, V. Yurovsky and M. Olshanii, *Relaxation in a completely integrable many-body quantum system: An ab initio study of the dynamics of the highly excited states of 1d lattice hard-core bosons*, *Phys. Rev. Lett.* **98** (2007) 050405.

[109] L. Vidmar and M. Rigol, *Generalized gibbs ensemble in integrable lattice models*, *Journal of Statistical Mechanics: Theory and Experiment* **2016** (2016) 064007.

[110] T.N. Ikeda, Y. Watanabe and M. Ueda, *Finite-size scaling analysis of the eigenstate thermalization hypothesis in a one-dimensional interacting bose gas*, *Phys. Rev. E* **87** (2013) 012125.

[111] V. Alba, *Eigenstate thermalization hypothesis and integrability in quantum spin chains*, *Phys. Rev. B* **91** (2015) 155123.

[112] V. Dunjko and M. Olshanii, *Thermalization from the perspective of eigenstate thermalization hypothesis*, in *Annual Review of Cold Atoms and Molecules*, pp. 443–471, WORLD SCIENTIFIC (2013).

[113] H. Kim, T.N. Ikeda and D.A. Huse, *Testing whether all eigenstates obey the eigenstate thermalization hypothesis*, *Phys. Rev. E* **90** (2014) 052105.

[114] G. Biroli, C. Kollath and A.M. Läuchli, *Effect of rare fluctuations on the thermalization of isolated quantum systems*, *Phys. Rev. Lett.* **105** (2010) 250401.

[115] J. Kemp, N.Y. Yao, C.R. Laumann and P. Fendley, *Long coherence times for edge spins*, *Journal of Statistical Mechanics: Theory and Experiment* **6** (2017) 063105 [1701.00797].

[116] P. Calabrese, F.H.L. Essler and M. Fagotti, *Quantum quench in the transverse field ising chain: I. time evolution of order parameter correlators*, *Journal of Statistical Mechanics: Theory and Experiment* **2012** (2012) P07016.

[117] A. Einstein et al., *On the electrodynamics of moving bodies*, *Annalen der physik* **17** (1905) 891.

[118] M.B. Hastings and T. Koma, *Spectral gap and exponential decay of correlations*, *Communications in mathematical physics* **265** (2006) 781.

[119] B. Nachtergaele, Y. Ogata and R. Sims, *Propagation of correlations in quantum lattice systems*, *Journal of statistical physics* **124** (2006) 1.

[120] S. Bravyi, M.B. Hastings and F. Verstraete, *Lieb-robinson bounds and the generation of correlations and topological quantum order*, *Phys. Rev. Lett.* **97** (2006) 050401.

[121] A.M. Läuchli and C. Kollath, *Spreading of correlations and entanglement after a quench in the one-dimensional bose–hubbard model*, *Journal of Statistical Mechanics: Theory and Experiment* **2008** (2008) P05018.

[122] P. Hauke and L. Tagliacozzo, *Spread of correlations in long-range interacting quantum systems*, *Phys. Rev. Lett.* **111** (2013) 207202.

[123] M. Kliesch, C. Gogolin and J. Eisert, *Lieb-robinson bounds and the simulation of time-evolution of local observables in lattice systems*, in *Many-Electron Approaches in Physics, Chemistry and Mathematics: A Multidisciplinary View*, V. Bach and L. Delle Site, eds., (Cham), pp. 301–318, Springer International Publishing (2014), DOI.

[124] Z.-X. Gong, M. Foss-Feig, S. Michalakis and A.V. Gorshkov, *Persistence of locality in systems with power-law interactions*, *Phys. Rev. Lett.* **113** (2014) 030602.

[125] M. Foss-Feig, Z.-X. Gong, C.W. Clark and A.V. Gorshkov, *Nearly linear light cones in long-range interacting quantum systems*, *Phys. Rev. Lett.* **114** (2015) 157201.

[126] M. Cheneau, P. Barmettler, D. Poletti, M. Endres, P. Schauß, T. Fukuhara et al., *Light-cone-like spreading of correlations in a quantum many-body system*, *Nature* **481** (2012) 484–487.

[127] R. Geiger, T. Langen, I.E. Mazets and J. Schmiedmayer, *Local relaxation and light-cone-like propagation of correlations in a trapped one-dimensional bose gas*, *New Journal of Physics* **16** (2014) 053034.

[128] P. Calabrese and J. Cardy, *Time dependence of correlation functions following a quantum quench*, *Phys. Rev. Lett.* **96** (2006) 136801.

[129] L. Villa, J. Despres and L. Sanchez-Palencia, *Unraveling the excitation spectrum of many-body systems from quantum quenches*, *Phys. Rev. A* **100** (2019) 063632.

[130] D.J. Luitz and Y. Bar Lev, *Information propagation in isolated quantum systems*, *Phys. Rev. B* **96** (2017) 020406.

[131] S. Sahu, S. Xu and B. Swingle, *Scrambling dynamics across a thermalization-localization quantum phase transition*, *Phys. Rev. Lett.* **123** (2019) 165902.

[132] S. Xu and B. Swingle, *Accessing scrambling using matrix product operators*, *Nature Physics* **16** (2020) 199.

[133] Y. Sekino and L. Susskind, *Fast scramblers*, *Journal of High Energy Physics* **10** (2008) 065 [0808.2096].

[134] N. Lashkari, D. Stanford, M. Hastings, T. Osborne and P. Hayden, *Towards the fast scrambling conjecture*, *Journal of High Energy Physics* **4** (2013) 22 [1111.6580].

[135] B. Swingle, *Quantum information scrambling: Boulder lectures*, Boulder School for Condensed Matter and Materials Physics: Quantum Information (2018), https://boulderschool.yale.edu/sites/default/files/files/qi_boulder.pdf.

[136] D. Huse, *Many-body quantum dynamics*, Maglab Theory Winter School (2018), https://nationalmaglab.org/images/news_events/searchable_docs/winterschool/2018/Theory_2018_huse1.pdf.

[137] B. Swingle, *Unscrambling the physics of out-of-time-order correlators*, *Nature Phys.* **14** (2018) 988.

[138] M.J. Klug, M.S. Scheurer and J. Schmalian, *Hierarchy of information scrambling, thermalization, and hydrodynamic flow in graphene*, *Phys. Rev. B* **98** (2018) 045102.

[139] Y. Huang, Y.-L. Zhang and X. Chen, *Out-of-time-ordered correlators in many-body localized systems*, *Annalen der Physik* **529** 1600318.

[140] J. Maldacena, S.H. Shenker and D. Stanford, *A bound on chaos*, *Journal of High Energy Physics* **2016** (2016) 106.

[141] D.A. Roberts and B. Swingle, *Lieb-robinson bound and the butterfly effect in quantum field theories*, *Physical review letters* **117** (2016) 091602.

[142] K. Hashimoto, K. Murata and R. Yoshii, *Out-of-time-order correlators in quantum mechanics*, *Journal of High Energy Physics* **10** (2017) 138 [1703.09435].

[143] A.A. Patel, D. Chowdhury, S. Sachdev and B. Swingle, *Quantum butterfly effect in weakly interacting diffusive metals*, *Physical Review X* **7** (2017) 031047.

[144] E.B. Rozenbaum, S. Ganeshan and V. Galitski, *Lyapunov exponent and out-of-time-ordered correlator's growth rate in a chaotic system*, *Physical review letters* **118** (2017) 086801.

[145] A.I. Larkin and Y.N. Ovchinnikov, *Quasiclassical Method in the Theory of Superconductivity*, *Soviet Journal of Experimental and Theoretical Physics* **28** (1969) 1200.

[146] B. Swingle, G. Bentsen, M. Schleier-Smith and P. Hayden, *Measuring the scrambling of quantum information*, *Phys. Rev. A* **94** (2016) 040302.

[147] G. Zhu, M. Hafezi and T. Grover, *Measurement of many-body chaos using a quantum clock*, *Phys. Rev. A* **94** (2016) 062329.

[148] N.Y. Yao, F. Grusdt, B. Swingle, M.D. Lukin, D.M. Stamper-Kurn, J.E. Moore et al., *Interferometric Approach to Probing Fast Scrambling*, *ArXiv e-prints* (2016) [1607.01801].

[149] N. Yunger Halpern, *Jarzynski-like equality for the out-of-time-ordered correlator*, *Phys. Rev. A* **95** (2017) 012120.

[150] A. Bohrdt, C.B. Mendl, M. Endres and M. Knap, *Scrambling and thermalization in a diffusive quantum many-body system*, *New Journal of Physics* **19** (2017) 063001 [1612.02434].

[151] N. Yunger Halpern, B. Swingle and J. Dressel, *Quasiprobability behind the out-of-time-ordered correlator*, *Phys. Rev. A* **97** (2018) 042105.

[152] J. Dressel, J.R. González Alonso, M. Waegell and N. Yunger Halpern, *Strengthening weak measurements of qubit out-of-time-order correlators*, *Phys. Rev. A* **98** (2018) 012132.

[153] B. Vermersch, A. Elben, L.M. Sieberer, N.Y. Yao and P. Zoller, *Probing scrambling using statistical correlations between randomized measurements*, *Phys. Rev. X* **9** (2019) 021061.

[154] P.D. Blocher, S. Asaad, V. Mourik, M.A.I. Johnson, A. Morello and K. Mølmer, *Measuring out-of-time-ordered correlation functions without reversing time evolution*, 2003.03980.

[155] B. Sundar, *Proposal to measure out-of-time-ordered correlations using bell states*, 2020.

[156] M. Gärttner, J. Bohnet, A. Safavi-Naini, M. L. Wall, J. J. Bollinger and A. Rey, *Measuring out-of-time-order correlations and multiple quantum spectra in a trapped ion quantum magnet*, .

[157] J. Li, R. Fan, H. Wang, B. Ye, B. Zeng, H. Zhai et al., *Measuring out-of-time-order correlators on a nuclear magnetic resonance quantum simulator*, *Phys. Rev. X* **7** (2017) 031011.

[158] K.X. Wei, C. Ramanathan and P. Cappellaro, *Exploring localization in nuclear spin chains*, *Phys. Rev. Lett.* **120** (2018) 070501.

[159] K.A. Landsman, C. Figgatt, T. Schuster, N.M. Linke, B. Yoshida, N.Y. Yao et al., *Verified quantum information scrambling*, *Nature* **567** (2019) 61–65.

[160] B. Chen, X. Hou, F. Zhou, P. Qian, H. Shen and N. Xu, *Detecting the out-of-time-order correlations of dynamical quantum phase transitions in a solid-state quantum simulator*, *Applied Physics Letters* **116** (2020) 194002 [https://doi.org/10.1063/5.0004152].

[161] X. Nie, B.-B. Wei, X. Chen, Z. Zhang, X. Zhao, C. Qiu et al., *Experimental observation of equilibrium and dynamical quantum phase transitions via out-of-time-ordered correlators*, *Phys. Rev. Lett.* **124** (2020) 250601.

[162] C. Xiao, Z. Tianci, H.D. A. and F. Eduardo, *Out-of-time-order correlations in many-body localized and thermal phases*, *Annalen der Physik* **529** 1600332.

[163] A. Chan, A. De Luca and J.T. Chalker, *Solution of a minimal model for many-body quantum chaos*, *Phys. Rev. X* **8** (2018) 041019.

[164] C.W. von Keyserlingk, T. Rakovszky, F. Pollmann and S.L. Sondhi, *Operator hydrodynamics, otocs, and entanglement growth in systems without conservation laws*, *Phys. Rev. X* **8** (2018) 021013.

[165] S. Pappalardi, A. Russomanno, B. Žunkovič, F. Iemini, A. Silva and R. Fazio, *Scrambling and entanglement spreading in long-range spin chains*, *Phys. Rev. B* **98** (2018) 134303.

[166] A. Chan, A. De Luca and J.T. Chalker, *Eigenstate correlations, thermalization, and the butterfly effect*, *Phys. Rev. Lett.* **122** (2019) 220601.

[167] B. Swingle and D. Chowdhury, *Slow scrambling in disordered quantum systems*, *Phys. Rev. B* **95** (2017) 060201 [1608.03280].

[168] R. Fan, P. Zhang, H. Shen and H. Zhai, *Out-of-time-order correlation for many-body localization*, *Science Bulletin* **62** (2017) 707 .

[169] R.-Q. He and Z.-Y. Lu, *Characterizing many-body localization by out-of-time-ordered correlation*, *Physical Review B* **95** (2017) 054201 [1608.03586].

[170] D. Basko, I. Aleiner and B. Altshuler, *Metal–insulator transition in a weakly interacting many-electron system with localized single-particle states*, *Annals of Physics* **321** (2006) 1126.

[171] V. Oganesyan and D.A. Huse, *Localization of interacting fermions at high temperature*, *Phys. Rev. B* **75** (2007) 155111.

[172] M. Žnidarič, T.c.v. Prosen and P. Prelovšek, *Many-body localization in the heisenberg xxz magnet in a random field*, *Phys. Rev. B* **77** (2008) 064426.

[173] A. Pal and D.A. Huse, *Many-body localization phase transition*, *Phys. Rev. B* **82** (2010) 174411.

[174] M. Serbyn, Z. Papić and D.A. Abanin, *Quantum quenches in the many-body localized phase*, *Phys. Rev. B* **90** (2014) 174302.

[175] M. Schreiber, S.S. Hodgman, P. Bordia, H.P. Lüschen, M.H. Fischer, R. Vosk et al., *Observation of many-body localization of interacting fermions in a quasirandom optical lattice*, *Science* **349** (2015) 842.

[176] J. Smith, A. Lee, P. Richerme, B. Neyenhuis, P.W. Hess, P. Hauke et al., *Many-body localization in a quantum simulator with programmable random disorder*, *Nature Physics* **12** (2016) 907 [1508.07026].

[177] J.Z. Imbrie, *On many-body localization for quantum spin chains*, *Journal of Statistical Physics* **163** (2016) 998.

[178] P.W. Anderson, *Absence of diffusion in certain random lattices*, *Phys. Rev.* **109** (1958) 1492.

[179] E. Iyoda and T. Sagawa, *Scrambling of quantum information in quantum many-body systems*, *Phys. Rev. A* **97** (2018) 042330.

[180] C.-J. Lin and O.I. Motrunich, *Out-of-time-ordered correlators in a quantum ising chain*, *Phys. Rev. B* **97** (2018) 144304.

[181] M. Heyl, F. Pollmann and B. Dóra, *Detecting equilibrium and dynamical quantum phase transitions in ising chains via out-of-time-ordered correlators*, *Phys. Rev. Lett.* **121** (2018) 016801.

[182] T. Xu, T. Scaffidi and X. Cao, *Does scrambling equal chaos?*, *Phys. Rev. Lett.* **124** (2020) 140602.

[183] H. Shen, P. Zhang, R. Fan and H. Zhai, *Out-of-time-order correlation at a quantum phase transition*, *Phys. Rev. B* **96** (2017) 054503.

[184] B.-B. Wei, G. Sun and M.-J. Hwang, *Dynamical scaling laws of out-of-time-ordered correlators*, *Phys. Rev. B* **100** (2019) 195107.

[185] Q. Wang and F. Pérez-Bernal, *Probing an excited-state quantum phase transition in a quantum many-body system via an out-of-time-order correlator*, *Phys. Rev. A* **100** (2019) 062113.

[186] Z.-H. Sun, J.-Q. Cai, Q.-C. Tang, Y. Hu and H. Fan, *Out-of-time-order correlators and quantum phase transitions in the rabi and dicke models*, *Annalen der Physik* **532** (2020) 1900270.

[187] C.B. Dağ, L.-M. Duan and K. Sun, *Topologically induced prescrambling and dynamical detection of topological phase transitions at infinite temperature*, *Phys. Rev. B* **101** (2020) 104415.

[188] R.J. Lewis-Swan, S.R. Muleady and A.M. Rey, *Detecting out-of-time-order correlations via quasiadiabatic echoes as a tool to reveal quantum coherence in equilibrium quantum phase transitions*, *Phys. Rev. Lett.* **125** (2020) 240605.

[189] S. Bandyopadhyay, A. Polkovnikov and A. Dutta, *Observing dynamical quantum phase transitions through quasilocal string operators*, *Phys. Rev. Lett.* **126** (2021) 200602.

[190] K.-B. Huh, K. Ikeda, V. Jahnke and K.-Y. Kim, *Diagnosing first and second order phase transitions with probes of quantum chaos*, 2020.

[191] R.K. Shukla, G.K. Naik and S.K. Mishra, *Out-of-time-order correlation and detection of phase structure in floquet transverse ising spin system*, 2002.05986.

[192] L.D. Landau, *On the theory of phase transitions*, *Zh. Eksp. Teor. Fiz.* **7** (1937) 19.

[193] S. Sachdev, *Quantum Phase Transitions*, Cambridge University Press (2001).

[194] M. Greiner, O. Mandel, T.W. Hänsch and I. Bloch, *Collapse and revival of the matter wave field of a bose–einstein condensate*, *Nature* **419** (2002) 51.

[195] W.S. Bakr, J.I. Gillen, A. Peng, S. Fölling and M. Greiner, *A quantum gas microscope for detecting single atoms in a Hubbard-regime optical lattice*, *Nature* **462** (2009) 74 [0908.0174].

[196] A.M. Kaufman, M.E. Tai, A. Lukin, M. Rispoli, R. Schittko, P.M. Preiss et al., *Quantum thermalization through entanglement in an isolated many-body system*, *Science* **353** (2016) 794.

[197] J. Zhang, G. Pagano, P.W. Hess, A. Kyprianidis, P. Becker, H. Kaplan et al., *Observation of a many-body dynamical phase transition with a 53-qubit quantum simulator*, *Nature* **551** (2017) 601.

[198] T. Mori, T.N. Ikeda, E. Kaminishi and M. Ueda, *Thermalization and prethermalization in isolated quantum systems: a theoretical overview*, *Journal of Physics B: Atomic, Molecular and Optical Physics* **51** (2018) 112001.

[199] M. Heyl, A. Polkovnikov and S. Kehrein, *Dynamical Quantum Phase Transitions in the Transverse-Field Ising Model*, *Phys. Rev. Lett.* **110** (2013) 135704 [1206.2505].

[200] N. Tsuji, M. Eckstein and P. Werner, *Nonthermal antiferromagnetic order and nonequilibrium criticality in the hubbard model*, *Phys. Rev. Lett.* **110** (2013) 136404.

[201] P. Jurcevic, H. Shen, P. Hauke, C. Maier, T. Brydges, C. Hempel et al., *Direct observation of dynamical quantum phase transitions in an interacting many-body system*, *Phys. Rev. Lett.* **119** (2017) 080501.

[202] N. Fläschner, D. Vogel, M. Tarnowski, B.S. Rem, D.-S. Lühmann, M. Heyl et al., *Observation of dynamical vortices after quenches in a system with topology*, *Nature Physics* **14** (2018) 265.

[203] B. Sciolla and G. Biroli, *Quantum quenches, dynamical transitions, and off-equilibrium quantum criticality*, *Phys. Rev. B* **88** (2013) 201110.

[204] E. Nicklas, M. Karl, M. Höfer, A. Johnson, W. Muessel, H. Strobel et al., *Observation of scaling in the dynamics of a strongly quenched quantum gas*, *Phys. Rev. Lett.* **115** (2015) 245301.

[205] A. Chiocchetta, M. Tavora, A. Gambassi and A. Mitra, *Short-time universal scaling in an isolated quantum system after a quench*, *Phys. Rev. B* **91** (2015) 220302.

[206] V. Gurarie, *Dynamical quantum phase transitions in the random field ising model*, *Phys. Rev. A* **100** (2019) 031601.

[207] D. Trapin, J.C. Halimeh and M. Heyl, *Unconventional critical exponents at dynamical quantum phase transitions in a random Ising chain*, 2005.06481.

[208] C. Kollath, A.M. Läuchli and E. Altman, *Quench dynamics and nonequilibrium phase diagram of the bose-hubbard model*, *Phys. Rev. Lett.* **98** (2007) 180601.

[209] M. Karl, H. Cakir, J.C. Halimeh, M.K. Oberthaler, M. Kastner and T. Gasenzer, *Universal equilibrium scaling functions at short times after a quench*, *Phys. Rev. E* **96** (2017) 022110.

[210] P. Titum, J.T. Iosue, J.R. Garrison, A.V. Gorshkov and Z.-X. Gong, *Probing ground-state phase transitions through quench dynamics*, *Phys. Rev. Lett.* **123** (2019) 115701.

[211] P. Uhrich, N. Defenu, R. Jafari and J.C. Halimeh, *Out-of-equilibrium phase diagram of long-range superconductors*, *Phys. Rev. B* **101** (2020) 245148.

[212] A. Haldar, K. Mallayya, M. Heyl, F. Pollmann, M. Rigol and A. Das, *Signatures of quantum phase transitions after quenches in quantum chaotic one-dimensional systems*, 2020.

[213] F.J. Gómez-Ruiz, J.J. Mendoza-Arenas, F.J. Rodríguez, C. Tejedor and L. Quiroga, *Universal two-time correlations, out-of-time-ordered correlators, and leggett-garg inequality violation by edge majorana fermion qubits*, *Phys. Rev. B* **97** (2018) 235134.

[214] M. Heyl, *Dynamical quantum phase transitions: a review*, *Reports on Progress in Physics* **81** (2018) 054001.

[215] B. Sciolla and G. Biroli, *Quantum quenches and off-equilibrium dynamical transition in the infinite-dimensional bose-hubbard model*, *Phys. Rev. Lett.* **105** (2010) 220401.

[216] A.A. Zvyagin, *Dynamical quantum phase transitions (review article)*, *Low Temperature Physics* **42** (2016) 971 [https://doi.org/10.1063/1.4969869].

[217] B. Žunkovič, M. Heyl, M. Knap and A. Silva, *Dynamical quantum phase transitions in spin chains with long-range interactions: Merging different concepts of nonequilibrium criticality*, *Phys. Rev. Lett.* **120** (2018) 130601.

[218] C.B. Dağ, S.-T. Wang and L.-M. Duan, *Classification of quench-dynamical behaviors in spinor condensates*, *Phys. Rev. A* **97** (2018) 023603.

[219] C.B. Dağ and L.-M. Duan, *Detection of out-of-time-order correlators and information scrambling in cold atoms: Ladder-XX model*, *Phys. Rev. A* **99** (2019) 052322.

[220] C.B. Dağ, K. Sun and L.-M. Duan, *Detection of quantum phases via out-of-time-order correlators*, *Phys. Rev. Lett.* **123** (2019) 140602.

[221] H.-X. Yang, T. Tian, Y.-B. Yang, L.-Y. Qiu, H.-Y. Liang, A.-J. Chu et al., *Observation of dynamical quantum phase transitions in a spinor condensate*, *Phys. Rev. A* **100** (2019) 013622.

[222] C.B. Dağ and K. Sun, *Dynamical crossover in the transient quench dynamics of short-range transverse-field ising models*, *Phys. Rev. B* **103** (2021) 214402.

[223] C.B. Dağ, P. Uhrich and J.C. Halimeh, *Probing equilibrium and dynamical criticality through single-site observables*, 2105.05986.

[224] C.B. Dağ, W. Niedenzu, O.E. Müstecaplıoğlu and G. Kurizki, *Multiatom quantum coherences in micromasers as fuel for thermal and nonthermal machines*, *Entropy* **18** (2016) .

[225] C.B. Dağ, W. Niedenzu, F. Ozaydin, O.E. Müstecaplıoğlu and G. Kurizki, *Temperature control in dissipative cavities by entangled dimers*, *The Journal of Physical Chemistry C* **123** (2019) 4035 [https://doi.org/10.1021/acs.jpcc.8b11445].

[226] A. Tuncer, M. Izadyari, C.B. Dağ, F. Ozaydin and Ö.E. Müstecaplıoğlu, *Work and heat value of bound entanglement*, *Quantum Information Processing* **18** (2019) 1.

[227] R. Kokkoniemi, T. Ollikainen, R.E. Lake, S. Saarenpää, K.Y. Tan, J.I. Kokkala et al., *Flux-tunable phase shifter for microwaves*, *Scientific reports* **7** (2017) 1.

[228] P. Eugenio and C. Dag, *Dmrg study of strongly interacting $\mathbb{Z}_2$ flatbands: a toy model inspired by twisted bilayer graphene*, *SciPost Physics Core* **3** (2020) .

[229] O. Fialko and D.W. Hallwood, *Isolated quantum heat engine*, *Phys. Rev. Lett.* **108** (2012) 085303.

[230] O. Fialko, *Quantum heat baths satisfying the eigenstate thermalization hypothesis*, *Phys. Rev. E* **92** (2015) 022104.

[231] C. Neill, P. Roushan, M. Fang, Y. Chen, M. Kolodrubetz, Z. Chen et al., *Ergodic dynamics and thermalization in an isolated quantum system*, *Nature Physics* **12** (2016) 1037 [1601.00600].

[232] D.A. Huse, R. Nandkishore, V. Oganesyan, A. Pal and S.L. Sondhi, *Localization-protected quantum order*, *Phys. Rev. B* **88** (2013) 014206.

[233] E. Fermi, J. Pasta and S. Ulam*Document LA-1940* (May 1955) .

[234] M. Tabor, *Chaos and integrability in nonlinear dynamics: an introduction*, Wiley-Interscience publication, Wiley (1989).

[235] D.R. Romano and E.J.V. de Passos, *Population and phase dynamics of $f = 1$ spinor condensates in an external magnetic field*, *Phys. Rev. A* **70** (2004) 043614.

[236] E.T. Jaynes, *Information theory and statistical mechanics*, *Phys. Rev.* **106** (1957) 620.

[237] C. Gogolin, M.P. Müller and J. Eisert, *Absence of thermalization in nonintegrable systems*, *Phys. Rev. Lett.* **106** (2011) 040401.

[238] S.R. Manmana, S. Wessel, R.M. Noack and A. Muramatsu, *Strongly correlated fermions after a quantum quench*, *Phys. Rev. Lett.* **98** (2007) 210405.

[239] N. Shiraishi and T. Mori, *Systematic construction of counterexamples to the eigenstate thermalization hypothesis*, *Phys. Rev. Lett.* **119** (2017) 030601.

[240] V.A. Yurovsky and M. Olshanii, *Memory of the initial conditions in an incompletely chaotic quantum system: Universal predictions with application to cold atoms*, *Phys. Rev. Lett.* **106** (2011) 025303.

[241] E. Canovi, D. Rossini, R. Fazio, G.E. Santoro and A. Silva, *Quantum quenches, thermalization, and many-body localization*, *Phys. Rev. B* **83** (2011) 094431.

[242] F. Evers and A.D. Mirlin, *Anderson transitions*, *Rev. Mod. Phys.* **80** (2008) 1355.

[243] M. Scully and M. Zubairy, *Quantum Optics*, Cambridge University Press (1997).

[244] S. Will, T. Best, U. Schneider, L. Hackermüller, D.-S. Lühmann and I. Bloch, *Time-resolved observation of coherent multi-body interactions in quantum phase revivals*, *Nature* **465** (2010) 197.

[245] H. Pu, C. Law and N. Bigelow, *Complex quantum gases: spinor bose–einstein condensates of trapped atomic vapors*, *Physica B: Condensed Matter* **280** (2000) 27 .

[246] H. Pu, C.K. Law, S. Raghavan, J.H. Eberly and N.P. Bigelow, *Spin-mixing dynamics of a spinor bose-einstein condensate*, *Phys. Rev. A* **60** (1999) 1463.

[247] L.E. Sadler, J.M. Higbie, S.R. Leslie, M. Vengalattore and D.M. Stamper-Kurn, *Spontaneous symmetry breaking in a quenched ferromagnetic spinor bose–einstein condensate*, *Nature* **443** (2006) 312.

[248] Z. Zhang and L.-M. Duan, *Generation of massive entanglement through an adiabatic quantum phase transition in a spinor condensate*, *Phys. Rev. Lett.* **111** (2013) 180401.

[249] W. Zhang, S. Yi and L. You, *Mean field ground state of a spin-1 condensate in a magnetic field*, *New Journal of Physics* **5** (2003) 77.

[250] J. Jiang, L. Zhao, M. Webb and Y. Liu, *Mapping the phase diagram of spinor condensates via adiabatic quantum phase transitions*, *Phys. Rev. A* **90** (2014) 023610.

[251] S. Yi, O.E. Müstecaplıoğlu, C.P. Sun and L. You, *Single-mode approximation in a spinor-1 atomic condensate*, *Phys. Rev. A* **66** (2002) 011601.

[252] X.-Y. Luo, Y.-Q. Zou, L.-N. Wu, Q. Liu, M.-F. Han, M.K. Tey et al., *Deterministic entanglement generation from driving through quantum phase transitions*, *Science* **355** (2017) 620.

[253] Y. Liu, S. Jung, S.E. Maxwell, L.D. Turner, E. Tiesinga and P.D. Lett, *Quantum phase transitions and continuous observation of spinor dynamics in an antiferromagnetic condensate*, *Phys. Rev. Lett.* **102** (2009) 125301.

[254] T.M. Hoang, H.M. Bharath, M.J. Boguslawski, M. Anquez, B.A. Robbins and M.S. Chapman, *Adiabatic quenches and characterization of amplitude excitations in a continuous quantum phase transition*, *Proceedings of the National Academy of Sciences* **113** (2016) 9475.

[255] M. Kardar, *Statistical Physics of Particles*, Cambridge University Press (2007).

[256] M. Srednicki, *Thermal fluctuations in quantized chaotic systems*, *Journal of Physics A: Mathematical and General* **29** (1996) L75.

[257] F. Haake, *Quantum Signatures of Chaos*, Physics and astronomy online library, Springer (2001).

[258] J.M. Magán, *Random free fermions: An analytical example of eigenstate thermalization*, *Phys. Rev. Lett.* **116** (2016) 030401.

[259] M. Heyl, *Dynamical quantum phase transitions: a review*, *ArXiv e-prints* (2017) [1709.07461].

[260] A.Y. Kitaev, *A simple model of quantum holography*, *KITP Lectures* (2015) .

[261] S.H. Shenker and D. Stanford, *Black holes and the butterfly effect*, *Journal of High Energy Physics* **2014** (2014) 67 [1306.0622].

[262] D.J. Luitz and Y. Bar Lev, *Emergent locality in systems with power-law interactions*, *ArXiv e-prints* (2018) [1805.06895].

[263] I. Bloch, J. Dalibard and W. Zwerger, *Many-body physics with ultracold gases*, *Rev. Mod. Phys.* **80** (2008) 885.

[264] W.C. Campbell, J. Mizrahi, Q. Quraishi, C. Senko, D. Hayes, D. Hucul et al., *Ultrafast gates for single atomic qubits*, *Phys. Rev. Lett.* **105** (2010) 090502.

[265] J. Lim, H.-G. Lee, S. Lee, C.-Y. Park and J. Ahn, *Ultrafast Ramsey interferometry to implement cold atomic qubit gates*, *Scientific Reports* **4** (2014) 5867.

[266] T. Barnes, E. Dagotto, J. Riera and E.S. Swanson, *Excitation spectrum of heisenberg spin ladders*, *Phys. Rev. B* **47** (1993) 3196.

[267] S.P. Strong and A.J. Millis, *Competition between singlet formation and magnetic ordering in one-dimensional spin systems*, *Phys. Rev. Lett.* **69** (1992) 2419.

[268] M.T. Batchelor, X.W. Guan, N. Oelkers and Z. Tsuboi, *Integrable models and quantum spin ladders: comparison between theory and experiment for the strong coupling ladder compounds*, *Advances in Physics* **56** (2007) 465 [cond-mat/0512489].

[269] A. Tribedi and I. Bose, *Spin-$\frac{1}{2}$ heisenberg ladder: Variation of entanglement and fidelity measures close to quantum critical points*, *Phys. Rev. A* **79** (2009) 012331.

[270] E. Dagotto and T.M. Rice, *Surprises on the way from one- to two-dimensional quantum magnets: The ladder materials*, *Science* **271** (1996) 618 [http://science.sciencemag.org/content/271/5249/618.full.pdf].

[271] E. Dagotto, *Experiments on ladders reveal a complex interplay between a spin-gapped normal state and superconductivity*, *Reports on Progress in Physics* **62** (1999) 1525.

[272] M. Žnidarič, *Coexistence of diffusive and ballistic transport in a simple spin ladder*, *Phys. Rev. Lett.* **110** (2013) 070602.

[273] B. Damski, J. Zakrzewski, L. Santos, P. Zoller and M. Lewenstein, *Atomic bose and anderson glasses in optical lattices*, *Phys. Rev. Lett.* **91** (2003) 080403.

[274] L. Fallani, J.E. Lye, V. Guarrera, C. Fort and M. Inguscio, *Ultracold atoms in a disordered crystal of light: Towards a bose glass*, *Phys. Rev. Lett.* **98** (2007) 130404.

[275] E. Jané, G. Vidal, W. Dür, P. Zoller and J.I. Cirac, *Simulation of quantum dynamics with quantum optical systems*, *eprint arXiv:quant-ph/0207011* (2002) [quant-ph/0207011].

[276] P. Hayden, D.W. Leung and A. Winter, *Aspects of generic entanglement*, *Communications in Mathematical Physics* **265** (2006) 95.

[277] D.J. Luitz and Y.B. Lev, *The ergodic side of the many-body localization transition*, *Annalen der Physik* **529** (2017) 1600350 [1610.08993].

[278] J. Emerson, Y.S. Weinstein, M. Saraceno, S. Lloyd and D.G. Cory, *Pseudo-random unitary operators for quantum information processing*, *science* **302** (2003) 2098.

[279] M. Azzouz, L. Chen and S. Moukouri, *Calculation of the singlet-triplet gap of the antiferromagnetic heisenberg model on a ladder*, *Phys. Rev. B* **50** (1994) 6233.

[280] I. Kukuljan, S. Grozdanov and T. Prosen, *Weak quantum chaos*, *Phys. Rev. B* **96** (2017) 060301 [1701.09147].

[281] S. Ray, S. Sinha and K. Sengupta, *Signature of Chaos and Delocalization in a Periodically Driven Many Body System : An Out-of-Time-Order Correlation Study*, *ArXiv e-prints* (2018) [1804.01545].

[282] T. Iadecola and M. Znidaric, *Exact localized and ballistic eigenstates in disordered chaotic spin ladders and the Fermi-Hubbard model*, *ArXiv e-prints* (2018) arXiv:1811.07903 [1811.07903].

[283] K. Agarwal, E. Altman, E. Demler, S. Gopalakrishnan, D.A. Huse and M. Knap, *Rare-region effects and dynamics near the many-body localization transition*, *Annalen der Physik* **529** 1600326.

[284] J. Eisert, M. van den Worm, S.R. Manmana and M. Kastner, *Breakdown of quasilocality in long-range quantum lattice models*, *Phys. Rev. Lett.* **111** (2013) 260401.

[285] M. Mezei and D. Stanford, *On entanglement spreading in chaotic systems*, *Journal of High Energy Physics* **2017** (2017) 65 [1608.05101].

[286] T.S. Nunner and T. Kopp, *Jordan-wigner approach to dynamic correlations in spin ladders*, *Phys. Rev. B* **69** (2004) 104419.

[287] A.J. Daley, H. Pichler, J. Schachenmayer and P. Zoller, *Measuring entanglement growth in quench dynamics of bosons in an optical lattice*, *Phys. Rev. Lett.* **109** (2012) 020505.

[288] C. Zhang, S.L. Rolston and S. Das Sarma, *Manipulation of single neutral atoms in optical lattices*, *Physical Review A* **74** (2006) 042316 [quant-ph/0605245].

[289] J.H. Lee, E. Montano, I.H. Deutsch and P.S. Jessen, *Robust site-resolvable quantum gates in an optical lattice via inhomogeneous control*, *Nature Communications* **4** (2013) 2027 [1306.0603].

[290] M. Aldous, J. Woods, A. Dragomir, R. Roy and M. Himsworth, *Carrier frequency modulation of an acousto-optic modulator for laser stabilization*, *Opt. Express* **25** (2017) 12830.

[291] L. Isenhower, E. Urban, X.L. Zhang, A.T. Gill, T. Henage, T.A. Johnson et al., *Demonstration of a neutral atom controlled-not quantum gate*, *Phys. Rev. Lett.* **104** (2010) 010503.

[292] A.M. Kaufman, B.J. Lester, M. Foss-Feig, M.L. Wall, A.M. Rey and C.A. Regal, *Entangling two transportable neutral atoms via local spin exchange*, *Nature* **527** (2015) 208 [1507.05586].

[293] Z.-H. Sun, J.-Q. Cai, Q.-C. Tang, Y. Hu and H. Fan, *Out-of-time-order correlators and quantum phase transitions in the Rabi and Dicke model*, *arXiv e-prints* (2018) arXiv:1811.11191 [1811.11191].

[294] M. Srednicki, *The approach to thermal equilibrium in quantized chaotic systems*, *Journal of Physics A Mathematical General* **32** (1999) 1163 [cond-mat/9809360].

[295] M. Srednicki, *Thermal Fluctuations in Quantized Chaotic Systems*, in *eprint arXiv:chao-dyn/9511001*, Nov., 1995.

[296] S. Sugiura and A. Shimizu, *Thermal pure quantum states at finite temperature*, *Phys. Rev. Lett.* **108** (2012) 240401.

[297] Y. Huang, F.G.S.L. Brandão and Y.-L. Zhang, *Finite-size scaling of out-of-time-ordered correlators at late times*, *Phys. Rev. Lett.* **123** (2019) 010601.

[298] V.L. Berezinskiĭ, *Destruction of Long-range Order in One-dimensional and Two-dimensional Systems having a Continuous Symmetry Group I. Classical Systems*, *Soviet Journal of Experimental and Theoretical Physics* **32** (1971) 493.

[299] J.M. Kosterlitz and D.J. Thouless, *Long range order and metastability in two dimensional solids and superfluids. (Application of dislocation theory)*, *Journal of Physics C Solid State Physics* **5** (1972) L124.

[300] *ITensor Library (version 2.0.11) http://itensor.org* .

[301] L.-M. Duan, E. Demler and M.D. Lukin, *Controlling spin exchange interactions of ultracold atoms in optical lattices*, *Phys. Rev. Lett.* **91** (2003) 090402.

[302] P. Reimann, *Typicality for generalized microcanonical ensembles*, *Phys. Rev. Lett.* **99** (2007) 160404.

[303] D.V. Else, P. Fendley, J. Kemp and C. Nayak, *Prethermal strong zero modes and topological qubits*, *Phys. Rev. X* **7** (2017) 041062.

[304] J. Berges, S. Borsányi and C. Wetterich, *Prethermalization*, *Phys. Rev. Lett.* **93** (2004) 142002.

[305] X.-G. Wen, *Colloquium: Zoo of quantum-topological phases of matter*, *Rev. Mod. Phys.* **89** (2017) 041004.

[306] S. Roy, R. Moessner and A. Das, *Locating topological phase transitions using nonequilibrium signatures in local bulk observables*, *Phys. Rev. B* **95** (2017) 041105.

[307] Y. Wang, *Detecting topological phases via survival probabilities of edge majorana fermions*, *Phys. Rev. E* **98** (2018) 042128.

[308] M.D. Caio, N.R. Cooper and M.J. Bhaseen, *Quantum quenches in chern insulators*, *Phys. Rev. Lett.* **115** (2015) 236403.

[309] J. Yu, *Phase vortices of the quenched haldane model*, *Phys. Rev. A* **96** (2017) 023601.

[310] Y. Hu, P. Zoller and J.C. Budich, *Dynamical buildup of a quantized hall response from nontopological states*, *Phys. Rev. Lett.* **117** (2016) 126803.

[311] N. Fläschner, D. Vogel, M. Tarnowski, B.S. Rem, D.-S. Lühmann, M. Heyl et al., *Observation of dynamical vortices after quenches in a system with topology*, *Nature Physics* **14** (2018) 265.

[312] L. D'Alessio and M. Rigol, *Dynamical preparation of Floquet Chern insulators*, *Nature Communications* **6** (2015) 8336 [1409.6319].

[313] M. McGinley and N.R. Cooper, *Classification of topological insulators and superconductors out of equilibrium*, *Phys. Rev. B* **99** (2019) 075148.

[314] A. Kitaev, *Periodic table for topological insulators and superconductors*, *AIP Conference Proceedings* **1134** (2009) 22.

[315] J.C. Budich and M. Heyl, *Dynamical topological order parameters far from equilibrium*, *Phys. Rev. B* **93** (2016) 085416.

[316] M. Schmitt and S. Kehrein, *Dynamical quantum phase transitions in the kitaev honeycomb model*, *Phys. Rev. B* **92** (2015) 075114.

[317] A. Kitaev and J. Preskill, *Topological entanglement entropy*, *Phys. Rev. Lett.* **96** (2006) 110404.

[318] M. Levin and X.-G. Wen, *Detecting topological order in a ground state wave function*, *Phys. Rev. Lett.* **96** (2006) 110405.

[319] H.-C. Jiang, Z. Wang and L. Balents, *Identifying topological order by entanglement entropy*, *Nature Physics* **8** (2012) 902 [1205.4289].

[320] Y. Kawaguchi and M. Ueda, *Spinor bose–einstein condensates*, *Physics Reports* **520** (2012) 253 .

[321] C. Gerving, T. Hoang, B. Land, M. Anquez, C. Hamley and M. Chapman, *Non-equilibrium dynamics of an unstable quantum pendulum explored in a spin-1 bose–einstein condensate*, *Nature communications* **3** (2012) 1.

[322] Y. Liu, E. Gomez, S.E. Maxwell, L.D. Turner, E. Tiesinga and P.D. Lett, *Number fluctuations and energy dissipation in sodium spinor condensates*, *Phys. Rev. Lett.* **102** (2009) 225301.

[323] E.M. Bookjans, A. Vinit and C. Raman, *Quantum phase transition in an antiferromagnetic spinor bose-einstein condensate*, *Phys. Rev. Lett.* **107** (2011) 195306.

[324] M. Eckstein, M. Kollar and P. Werner, *Thermalization after an interaction quench in the hubbard model*, *Phys. Rev. Lett.* **103** (2009) 056403.

[325] J.C. Halimeh, V. Zauner-Stauber, I.P. McCulloch, I. de Vega, U. Schollwöck and M. Kastner, *Prethermalization and persistent order in the absence of a thermal phase transition*, *Phys. Rev. B* **95** (2017) 024302.

[326] J.C. Halimeh and V. Zauner-Stauber, *Dynamical phase diagram of quantum spin chains with long-range interactions*, *Phys. Rev. B* **96** (2017) 134427.

[327] F.H.L. Essler, S. Evangelisti and M. Fagotti, *Dynamical correlations after a quantum quench*, *Phys. Rev. Lett.* **109** (2012) 247206.

[328] P. Calabrese, F.H.L. Essler and M. Fagotti, *Quantum quench in the transverse-field ising chain*, *Phys. Rev. Lett.* **106** (2011) 227203.

[329] S. Sachdev and A.P. Young, *Low temperature relaxational dynamics of the ising chain in a transverse field*, *Phys. Rev. Lett.* **78** (1997) 2220.

[330] D. Rossini, A. Silva, G. Mussardo and G.E. Santoro, *Effective thermal dynamics following a quantum quench in a spin chain*, *Phys. Rev. Lett.* **102** (2009) 127204.

[331] P. Barmettler, M. Punk, V. Gritsev, E. Demler and E. Altman, *Relaxation of antiferromagnetic order in spin-1/2 chains following a quantum quench*, *Phys. Rev. Lett.* **102** (2009) 130603.

[332] T. Tian, H.-X. Yang, L.-Y. Qiu, H.-Y. Liang, Y.-B. Yang, Y. Xu et al., *Observation of dynamical quantum phase transitions with correspondence in an excited state phase diagram*, *Phys. Rev. Lett.* **124** (2020) 043001.

[333] P. Calabrese and J. Cardy, *Evolution of entanglement entropy in one-dimensional systems*, *Journal of Statistical Mechanics: Theory and Experiment* **2005** (2005) P04010.

[334] Z. Wang, M. Foss-Feig and K.R.A. Hazzard, *Bounding the finite-size error of quantum many-body dynamics simulations*, *arXiv e-prints* (2020) arXiv:2009.12032 [2009.12032].

[335] A. Clauset, C.R. Shalizi and M.E.J. Newman, *Power-law distributions in empirical data*, *SIAM Review* **51** (2009) 661 [https://doi.org/10.1137/070710111].

[336] J. Lang, B. Frank and J.C. Halimeh, *Concurrence of dynamical phase transitions at finite temperature in the fully connected transverse-field ising model*, *Phys. Rev. B* **97** (2018) 174401.

[337] F. Iglói and H. Rieger, *Quantum relaxation after a quench in systems with boundaries*, *Phys. Rev. Lett.* **106** (2011) 035701.

[338] J.C. Halimeh, D. Trapin, M.V. Damme and M. Heyl, *Local measures of dynamical quantum phase transitions*, 2010.07307.

[339] Z.-X. Gong and L.-M. Duan, *Prethermalization and dynamic phase transition in an isolated trapped ion spin chain*, *New Journal of Physics* **15** (2013) 113051.

[340] B. Neyenhuis, J. Zhang, P.W. Hess, J. Smith, A.C. Lee, P. Richerme et al., *Observation of prethermalization in long-range interacting spin chains*, *Science Advances* **3** (2017) e1700672 [1608.00681].

[341] M. Vekić and S.R. White, *Smooth boundary conditions for quantum lattice systems*, *Phys. Rev. Lett.* **71** (1993) 4283.

[342] J.C. Halimeh, M. Van Damme, V. Zauner-Stauber and L. Vanderstraeten, *Quasiparticle origin of dynamical quantum phase transitions*, *Phys. Rev. Research* **2** (2020) 033111.

[343] M. Rautenberg and M. Gärttner, *Classical and quantum chaos in a three-mode bosonic system*, *Phys. Rev. A* **101** (2020) 053604.

[344] P. Feldmann, C. Klempt, A. Smerzi, L. Santos and M. Gessner, *Interferometric order parameter for excited-state quantum phase transitions in bose-einstein condensates*, *Phys. Rev. Lett.* **126** (2021) 230602.

[345] Z.-H. Sun, J. Cui and H. Fan, *Characterizing the many-body localization transition by the dynamics of diagonal entropy*, *Phys. Rev. Research* **2** (2020) 013163.

[346] S.-S. Li, Z.-Y. Ge and H. Fan, *Localization of rung pairs in a hard-core bose-hubbard ladder*, *Phys. Rev. A* **102** (2020) 062409.

[347] H. Gharibyan, M. Hanada, S.H. Shenker and M. Tezuka, *Onset of random matrix behavior in scrambling systems*, *Journal of High Energy Physics* **2018** (2018) 1.

[348] A. Chan, A. De Luca and J. Chalker, *Spectral statistics in spatially extended chaotic quantum many-body systems*, *Physical review letters* **121** (2018) 060601.

[349] D.V. Vasilyev, A. Grankin, M.A. Baranov, L.M. Sieberer and P. Zoller, *Monitoring quantum simulators via quantum nondemolition couplings to atomic clock qubits*, *PRX Quantum* **1** (2020) 020302.

[350] D.J. Yates, A.G. Abanov and A. Mitra, *Lifetime of almost strong edge-mode operators in one-dimensional, interacting, symmetry protected topological phases*, *Phys. Rev. Lett.* **124** (2020) 206803.

[351] T. Rakovszky, P. Sala, R. Verresen, M. Knap and F. Pollmann, *Statistical localization: From strong fragmentation to strong edge modes*, *Phys. Rev. B* **101** (2020) 125126.

[352] A. Nahum, S. Vijay and J. Haah, *Operator spreading in random unitary circuits*, *Phys. Rev. X* **8** (2018) 021014.

[353] V. Khemani, A. Vishwanath and D.A. Huse, *Operator spreading and the emergence of dissipative hydrodynamics under unitary evolution with conservation laws*, *Phys. Rev. X* **8** (2018) 031057.

[354] T. Rakovszky, F. Pollmann and C.W. von Keyserlingk, *Diffusive hydrodynamics of out-of-time-ordered correlators with charge conservation*, *Phys. Rev. X* **8** (2018) 031058.

[355] R.A. Hart, P.M. Duarte, T.-L. Yang, X. Liu, T. Paiva, E. Khatami et al., *Observation of antiferromagnetic correlations in the hubbard model with ultracold atoms*, *Nature* **519** (2015) 211.

[356] A. Mazurenko, C.S. Chiu, G. Ji, M.F. Parsons, M. Kanász-Nagy, R. Schmidt et al., *A cold-atom fermi–hubbard antiferromagnet*, *Nature* **545** (2017) 462.

[357] D. Bluvstein, A. Omran, H. Levine, A. Keesling, G. Semeghini, S. Ebadi et al., *Controlling quantum many-body dynamics in driven rydberg atom arrays*, *Science* **371** (2021) 1355.

[358] S. Ebadi, T.T. Wang, H. Levine, A. Keesling, G. Semeghini, A. Omran et al., *Quantum phases of matter on a 256-atom programmable quantum simulator*, 2012.12281.

[359] G. Semeghini, H. Levine, A. Keesling, S. Ebadi, T.T. Wang, D. Bluvstein et al., *Probing topological spin liquids on a programmable quantum simulator*, 2104.04119.

[360] K.v. Klitzing, G. Dorda and M. Pepper, *New method for high-accuracy determination of the fine-structure constant based on quantized hall resistance*, *Phys. Rev. Lett.* **45** (1980) 494.

[361] K. Von Klitzing, *The quantized hall effect*, *Reviews of Modern Physics* **58** (1986) 519.

[362] S.M. Girvin, *Course 2: The Quantum Hall Effect: Novel Excitations and Broken Symmetries*, in *Topological Aspects of Low Dimensional Systems*, A. Comtet, T. Jolicoeur, S. Ouvry and F. David, eds., vol. 69, p. 53, Jan., 1999 [cond-mat/9907002].

[363] D. Tong, *Lectures on the Quantum Hall Effect*, University of Cambridge (2016).

[364] C.L. Kane and E.J. Mele, *Z_2 topological order and the quantum spin hall effect*, *Phys. Rev. Lett.* **95** (2005) 146802.

[365] M.Z. Hasan and C.L. Kane, *Colloquium: Topological insulators*, *Rev. Mod. Phys.* **82** (2010) 3045.

[366] X.-L. Qi and S.-C. Zhang, *Topological insulators and superconductors*, *Rev. Mod. Phys.* **83** (2011) 1057.

[367] E. Altman. private communication.

[368] P. Hayden, D.W. Leung and A. Winter, *Aspects of Generic Entanglement*, *Communications in Mathematical Physics* **265** (2006) 95 [quant-ph/0407049].

[369] M.P. Zaletel, R.S.K. Mong, C. Karrasch, J.E. Moore and F. Pollmann, *Time-evolving a matrix product state with long-ranged interactions*, *Phys. Rev. B* **91** (2015) 165112.

[370] J. Jiang, L. Zhao, M. Webb, N. Jiang, H. Yang and Y. Liu, *Simple and efficient all-optical production of spinor condensates*, *Phys. Rev. A* **88** (2013) 033620.

[371] C. Käfer, R. Bourouis, J. Eurisch, A. Tripathi and H. Helm, *Ejection of magnetic-field-sensitive atoms from an optical dipole trap*, *Phys. Rev. A* **80** (2009) 023409.

[372] L. Zhao, J. Jiang, T. Tang, M. Webb and Y. Liu, *Dynamics in spinor condensates tuned by a microwave dressing field*, *Phys. Rev. A* **89** (2014) 023608.

[373] F. Gerbier, A. Widera, S. Fölling, O. Mandel and I. Bloch, *Resonant control of spin dynamics in ultracold quantum gases by microwave dressing*, *Phys. Rev. A* **73** (2006) 041602.

[374] E. Lieb, T. Schultz and D. Mattis, *Two soluble models of an antiferromagnetic chain*, *Annals of Physics* **16** (1961) 407.